Fundamental Mechanisms of Pulsed Laser Ablation of Biological Tissue

by

Douglas Albagli

B.A., Physics, Colgate University, 1987

SUBMITTED TO THE DEPARTMENT OF PHYSICS
IN PARTIAL FULFILLMENT OF THE REQUIREMENTS
FOR THE DEGREE

DOCTOR OF PHILOSOPHY

at the

MASSACHUSETTS INSTITUTE OF TECHNOLOGY

August, 1994

Signature of Author _____
Department of Physics
August 5, 1994

Certified by _____
Michael S. Feld
Professor of Physics
Thesis Supervisor

Accepted by _____
Professor George F. Koster
Chairman, Graduate Committee

Fundamental Mechanisms of Pulsed Laser Ablation of Biological Tissue

by

Douglas Albagli

Submitted to the Department of Physics on August 5, 1994 in partial fulfillment of the requirements for the Degree of Doctor of Philosophy in Physics.

Abstract

The ability to cut and remove biological tissue with short pulsed laser light, a process called laser ablation, has the potential to revolutionize many surgical procedures. Ablation procedures using short pulsed lasers are currently being developed or used in many fields of medicine, including cardiology, ophthalmology, dermatology, dentistry, orthopedics, and urology. Despite this, the underlying physics of the ablation process is not well understood. In fact, there is wide disagreement over whether the fundamental mechanism is primarily photothermal, photomechanical, or photochemical. In this thesis, both experimental and theoretical techniques are developed to explore this issue.

The photothermal model postulates that ablation proceeds through vaporization of the target material. The photomechanical model asserts that ablation is initiated when the laser-induced tensile stress exceeds the ultimate tensile strength of the target. I have developed a three dimensional model of the thermoelastic response of tissue to short pulsed laser irradiation which allows the time dependent stress distribution to be calculated given the optical, thermal and mechanical properties of the target. A complimentary experimental technique has been developed to verify this model, measure the needed physical properties of the tissue, and record the thermoelastic response of the tissue at the onset of ablation.

The results of this work have been widely disseminated to the international research community and have led to significant findings which support the photomechanical model of ablation of tissue. First, the energy deposited in tissue is an order of magnitude less than that required for vaporization. Second, unlike the one-dimensional thermoelastic model of laser-induced stress generation that has appeared in the literature, the full three-dimensional model predicts the development of significant tensile stresses on the surface of the target, precisely where ablation is observed to occur. Third, although the laser-induced temperature rise is modest, the magnitude of the stresses is sufficient to initiate mechanically destructive phenomenon. In hard materials, including

bone, a gradual weakening of material with each successive laser pulse is observed and correlated with the formation of permanent microcracks within the material. In meniscus, a representative soft tissue, the growth and collapse of mechanically destructive cavitation bubbles is observed.

Thesis Committee :

Supervisor : Michael S. Feld, Professor of Physics, M.I.T.

Readers : Toyoichi Tanaka, Professor of Physics, M.I.T.
George B. Benedek, Professor of Physics, M.I.T.
Irving Itzkan, Senior Research Scientist, M.I.T. Spectroscopy Lab.
Lev Perelman, Research Scientist, M.I.T. Spectroscopy Lab.
V.S. Letokhov, Institute of Spectroscopy, Russian Academy of Science, Troitsk, Russia

Acknowledgments

The work presented in this thesis was conducted at the George R. Harrison Spectroscopy Laboratory at M.I.T. It was funded through the National Institutes of Health support of the M.I.T. Laser Biomedical Resource Center. I have also been funded through a Lester Wolfe fellowship sponsored by the Spectroscopy Laboratory, for which I greatly appreciate.

I would like to thank my thesis committee for their guidance and participation. Professor Feld, my thesis supervisor, provided enthusiastic support throughout all the stages of this research. His continual guidance and overall perspective kept my research both well focussed and well directed. His approach towards physics and understanding complex problems has served as a model for me. Dr. Itzkan also provided invaluable support throughout my entire project. Besides providing day-to-day advice on almost any problem, his ideas are well represented throughout this entire thesis. Professors Tanaka, Benedek, and Letokhov provided additional guidance through my semi-annual thesis committee meetings.

I would also like to thank the other members of my research group. Dr. Lev Perelman has been instrumental in helping me with both the analytical and numerical methods of solving the thermoelastic wave equation. His expertise in theoretical physics has aided our effort to develop a quantitative model of the ablation process. Dr. Sargent Janes provided expertise in the area of experimental design and proposed the important idea of modulating one arm of the Michelson interferometer. Dr. Charles von Rosenberg attended my weekly group meetings for two years and was beneficial in interpretating the many experimental and theoretical results. Dr. Jonathan Schaffer provided overall guidance from a clinical perspective and specific guidance on the biological tissues bone and meniscus. He was also responsible for obtaining the human meniscus tissue samples.

Other staff members and students of the Spectroscopy Laboratory also provided valuable assistance. I worked closely with Dr. Joseph Izatt during the last two years of his thesis. Starting from ground zero, I learned about optics, lasers, biological tissue, experimental design, and oral presentation skills under his guidance. Gary Hayes also provided valuable support in operating and repairing laboratory equipment and the facilities necessary for running that equipment. Dr. Mike Otteson provided innumerable hours of his time to answer detailed, specific questions regarding experimental equipment. Bryan Banish, a UROP student, worked on an undergraduate thesis based on this project and took the lead role in studying meniscus. Marta Dark, the graduate student taking over this project, has worked closely with me over the past year. She has helped collect and analyze some of the most important data in this thesis from the interferometric surface monitoring apparatus. George Zonios helped with the Monte Carlo simulation reported in chpater 8. Finally, Dr. Ramachandra Dasari provided support in acquiring the facilities and equipment necessary to conduct this research effort.

I would especially like to thank my family. My parents, Maureen and Victor Albagli, have provided me with the skills and the ambition necessary to get to M.I.T. and the support to stay there. My in-laws, Jane and Ralph Hendrickson, have also provided unwavering support since I met them nearly eleven years ago. My brother, David Albagli, who was a graduate student and post-doc at M.I.T. during my stay, provided first hand advice on many aspects of this experience. Finally, I would like to thank my wife Lisa. Lisa has been there through every aspect of my journey : receiving my acceptance letter, moving from the Laboratory of Nuclear Science to the Spectroscopy Laboratory, passing my written and oral examinations, finding a research project, and writing my thesis. Her unwavering support and understanding, personal sacrifices, and uncompromising love throughout every day of this seven year experience will never be forgotten. As a fitting celebration of the love and commitment that my wife and I have built over the past seven years, our son Kyle was born on July 10, 1994.

Table of Contents

Chapter 3. An Introduction to Interferometric Surface Monitoring of Biological Tissue to Study Inertially Confined Ablation

Chapter 4. The Theory of Elasticity and the 1D Solution to the Thermoelastic Wave Equation

Chapter 5. Analytical 3D Steady-State Solution to the Thermoelastic Wave Equation.

Chapter 6. Numerical Time Dependent Solution to the Thermoelastic Wave Equation

Chapter 7. Development of an Interferometric Method for the Measurement of Laser Induced Stresses in Solids

Chapter 8. Application of Interferometric Surface Monitoring to Study the Physical Properties of Biological Tissue and the Initiation of Ablation

Chapter 9. Conclusions and Future Directions

References

List of Symbols

$A_{r,z}$	Stress functions
$B_{r,z}$	Stress functions
β	Thermal expansion coefficient, units per ^0C
C	Inertial confinement coefficient, unitless
C_ϕ	Stress function
C_l	Longitudinal speed of sound, units m/s
C_t	Transverse speed of sound, units m/s
C_V	Heat capacity at constant volume, units J / gm K
D	Optical penetration depth, units are distance
Δ	Grid spacing in numerical simulation, units are distance
Δt	Time step in numerical simulation, units are time
δ	Depth of ablation crater
dR	Work done by internal energy, units energy
ε	Total internal energy, units are energy
ε_c	Elastic component of the total internal energy, units are energy
ε_e	Electronic component of the total internal energy, units are energy
ε_T	Thermal component of the total internal energy, units are energy
E	Young's modulus
E_{th}	Energy per unit volume at the ablation threshold, units J/cm^3
F	Helmholtz free energy, units are energy
F_i	Force per unit volume, units are force
Φ	Thermoelastic displacement potential, unitless
Φ	Laser fluence, units mJ/mm^2
Φ_{th}	Fluence threshold for ablation, units mJ/mm^2
g	Anisotropy, unitless
g_0	Geometrical correction factor
Γ	Gruneisen coefficient, unitless
J_n	Bessel function of order n
K	Bulk modulus
k_1	Constant that describes the radial temperature profile, units are distance
κ	Thermal diffusivity, units mm^2/s
κ_T	Isothermal compressibility, units inverse pressure
L(r)	Radial profile of laser induced temperature
L_0	Radial profile constant, unitless
λ	Wavelength, units are distance
η	Heaviside step function
n	Numerical correction factor for laser profile, unitless
P	Pressure, units are pressure
P_c	Elastic component of the pressure, units are pressure
P_e	Electronic component of the pressure, units are pressure
P_i	Half-Period of interference pattern
P_r	Half-Period of reference interference pattern

List of Symbols (cont.)

P_T	Thermal component of the pressure, units are pressure
ψ	Love function
ρ	Density, units mass per unit volume
r	Radial coordinate, units are distance
$r_{1\text{-}4}$	Constants that describe the radial temperature profile, units are distance
R	Aspect ratio, unitless
R_c	Pressure relaxation coefficient, unitless
R_0	Initial radius of cavitation bubble, units are distance
S	Surface displacement, units are distance
$S_{0,3}$	Equilibrium surface displacement, units are distance
σ	Poisson ratio, unitless
σ_{ik}	Stress tensor, components have units of pressure
σ_{rr}	Radial component of the stress
$\sigma_{\phi\phi}$	Circumferential component of the stress
σ_{rz}	Shear component of the stress
σ_{zz}	Axial component of the stress
σ_{max}	Maximum value of laser-induced stress, units are pressure
t	Time coordinate, units time
t_c	Time for the collapse of cavitation bubbles, units are time
τ	Pulse duration of the laser, units are time
τ_c	Characteristic pressure dissipation time, units are time
τ_d	Characteristic thermal diffusion time, units are time
τ_m	Characteristic time for motion, units are time
T	Temperature, units ^{0}C
u_i	Thermoelastic displacement vector, units are distance
u_r	Radial displacement
u_z	Axial displacement
u_{ik}	Strain tensor, components are unitless
μ	Shear modulus
μ_a	Optical absorption coefficient, units are inverse distance
μ_s	Optical scattering coefficient, units are inverse distance
μ_s'	Effective optical scattering coefficient, units are inverse distance
v	Velocity, units m/s
v_{cc}	Corner cube velocity, units m/s
v_s	Average velocity of the sample surface
V	Specific volume, units are inverse density
w	Radius of laser beam, units are distance
z	Coordinate, represents distance into target surface

CHAPTER 1

Introduction to the Ablation of Biological Tissue

1.1 IMPORTANCE OF UNDERSTANDING THE ABLATION OF BIOLOGICAL TISSUE

The application of the laser to the cutting and removal of biological tissue, also known as laser ablation, has the potential to revolutionize many surgical procedures. This potential is rooted in three features : 1) the ability to produce short pulses of high intensity light; 2) the ability to deliver this light precisely to anywhere in the body; 3) the ability to selectively effect one tissue type over another. Experimental observations have shown that a single pulse of laser light with an intensity between 10^5 and 10^9 W/cm^2 incident on either "hard" (e.g. bone, tooth enamel, calcified plaque) or "soft" biological tissue, can lead to the precise removal of a known amount of tissue with minimal damage to the surrounding areas. Since laser light can be delivered precisely to an area as small as a few microns and transmitted through fiber optic cables to almost anywhere in the body, laser ablation has the potential for remote, minimally invasive, microsurgery. Furthermore, laser ablation offers the ability to selectively effect one type of tissue while leaving adjacent or overlying tissue unaltered. The laser tissue interaction is governed primarily by the absorption of light within the tissue. Since the absorption properties of tissue are highly wavelength dependent, selectivity can be obtained by an appropriate choice of laser

wavelength. Thus, for example, visible laser light can be transmitted through the cornea and lens to perform delicate surgery on the retina.

Ablation procedures using short pulsed lasers are currently being developed or used in many fields of medicine, including cardiology, ophthalmology, otolaryngology, dermatology, dentistry, orthopedics, urology, and gynecology. The procedures mentioned in the following paragraphs are intended to show the broad range of applications being studied and do not represent a comprehensive list.

The potential of the laser to reduce the number of heart attacks has been studied extensively. In a procedure called coronary laser angiosurgery, atherosclerotic plaque within the coronary arteries is removed via laser ablation. Although this procedure has tremendous potential, significant problems are still under investigation. This procedure is currently in clinical trials and its results have recently been reviewed by Deckelbaum [1994]. An advanced angiosurgery system, using a guidance system based on laser-induced fluorescence, is also under development at this laboratory [Feld et al., 1991].

In ophthalmology, pulsed laser systems are undergoing clinical trials for photorefractive keratectomy, a procedure where the controlled ablation of the cornea alters the shape of its surface in the precise way needed to correct near-sightedness [van Saarloos and Constable, 1993]. In otolaryngology, the use of pulsed lasers to perform surgery on the delicate bone in the middle ear is being explored [Schlenk et al., 1990]. In dermatology, the use of lasers for the removal of superficial epidermal lesions is being

investigated [Kaufmann and Hibst, 1989]. The ablation of enamel and dentin of human teeth is being studied for possible use in dental procedures [Li et al., 1992].

In orthopedics, a procedure called percutaneous laser discectomy is being developed to treat diseases of the intervertebral discs [Quigley et al., 1992]. The ablation of meniscus for arthroscopic knee surgery is under investigation [Buchelt et al., 1992]. In urology, fiber optic delivery of laser light is being used to ablate legions of superficial bladder carcinoma [Johnson, 1994]. This procedure is done on an outpatient setting and requires no anesthesia in contrast to electrosurgical removal which requires anesthesia and a 24-48 hour hospital stay. In a procedure called laser lithotripsy, laser light is used to fragment gallstones into small pieces which can be easily extracted [Spindel et al., 1992]. The use of fiber optic guided pulsed laser light is being tested in the area of gynecology to treat endometriosis [Duffy et al., 1992].

Although there are many clinical procedures involving laser ablation currently under development, in clinical trials, or in practice, the ablation process itself is not well understood. In fact, there is wide disagreement over whether the fundamental mechanism is a photothermal, photomechanical, or photochemical process. As clinical procedures become more advanced, a detailed knowledge of the ablation process will be essential in order to tailor the laser system to the specific procedure.

1.2 PAST WORK AT MIT

Earlier work devoted to studying the ablation of biological tissue was performed in our laboratory by Dr. Joseph A. Izatt and is described in detail in his Ph.D. thesis [Izatt, 1991b]. This work focused on an empirical characterization of the ablation process in order to guide the design of a clinical laser angiosurgery system to treat atherosclerosis. A brief summary of some important empirical results, obtained by Dr. Izatt and myself, is given below.

Under the right conditions, a short pulse of laser light incident on biological tissue causes an explosive removal of material from its surface. This process, called ablation, is strongly dependent on the laser irradiation parameters. The first step in an empirical characterization of ablation is to determine the effects of the laser irradiation conditions on the ablation process. The three most important parameters are the laser wavelength, fluence (energy per unit area), and intensity and are described in section 1.2.1. An experiment to study the temporal dependence of the dynamics of the ablation process is described in section 1.2.2.

1.2.1 Parametric Study of Laser Irradiation Conditions on Ablation

An extensive experimental study on the role of laser wavelength, fluence, and intensity in the ablation process of both "hard" (bone) and "soft" (aorta) biological tissue was performed. A wide array of lasers were used including a flash-pumped dye laser (λ = 295-590 nm), XeCl excimer laser (λ = 308 nm), Nd:YAG laser (third harmonic, λ = 355 nm), Alexandrite laser (Second harmonic, λ = 375 nm), Holmium YSGG laser (λ = 2.09 μm), and Hydrogen fluoride laser (λ = 2.7 to 2.9 μm). The duration of the laser pulses

ranged from 7.5 ns to 250 μsec. In all experiments, the laser tissue interaction was studied by irradiating the target sample with a number of laser pulses at a given fluence and wavelength. The tissue was then studied under a high power microscope to determine the effects of the laser irradiation.

Besides providing input for the design of a clinical system, the results of this experimental survey produced important information concerning the ablation process itself [Izatt et al., 1991a; Izatt 1991b; Izatt et al., 1990a]. One important result was the existence of a fluence threshold for the ablation process. For laser fluences below the fluence threshold, there were no visible effects on the target surface after laser irradiation. For fluences above the threshold, a crater was visible on the surface with a diameter roughly equal to the diameter of the incident laser beam. The depth of the crater depended both on the number of shots and difference between the fluence and the fluence threshold. If the number of shots is small (< 100) and the fluence is less than twice the threshold, both of these dependencies are linear.

The existence of a fluence threshold was a general feature of the laser tissue interaction, occurring in both "hard" and "soft" tissues at all wavelengths studied ranging from the ultraviolet, through the visible, and into the infrared. Although "soft" tissues could be ablated with either short pulses of light or continuous wave irradiation, "hard" tissues could only be ablated by short pulses [Izatt et al., 1990b]. Since the ability to ablate both kinds of tissue is of great importance, our research has concentrated on pulsed

lasers with duration between 7.5 ns and 250 μsec, which corresponds to irradiation intensities between 10^5 and 10^9 W/cm^2 on the tissue.

In order to study this important general feature in more detail, a quantitative determination of the fluence threshold as a function of laser wavelength was made in bone. In these experiments, the depth of the crater produced by laser irradiation at a given fluence was determined by measuring the vertical travel of the high power microscope between focusing on the top and the bottom of the crater. For each wavelength, the crater depth was plotted as a function of fluence. As qualitatively described above, the crater depths were zero for low fluences and then increased linearly above the threshold fluence. A quantitative determination of the fluence threshold was made by performing a least squares fit to the linear region of the data and determining the x-intercept.

The fluence thresholds showed a steady increase between λ = 308 nm (18 mJ/mm^2) and λ = 2.09 μm (295 mJ/mm^2). The lowest thresholds were obtained in the infrared between 2.7 and 2.9 μm (4-13 mJ/mm^2). This wide range of fluence thresholds can be explained by the optical properties of the tissue. The light distribution (and thus the energy density distribution) within the tissue is determined by the absorption and scattering properties of the material, which are wavelength dependent. The optical penetration depth, D, is equal to the depth at which the energy density has fallen by a factor 1/e. Using a spectrophotometer and an integrating sphere, the penetration depth in bone was determined as a function of wavelength in the ultraviolet and visible. It was found that the penetration depth was lowest in the ultraviolet and increased throughout

the visible, exactly as the fluence thresholds did. The penetration depth of the constituents of bone (water, collagen, hydroxyapatite) between 2.7 and 2.9 μm have been measured by other workers [Robertson and Williams, 1971; Yannas 1972; Pouchert 1967]. Due to the strong absorption by these components, the penetration depth is less than that in the ultraviolet and is consistent with the small fluence thresholds measured in this regime.

Another important parameter which can be obtained from the results of this study is the energy per unit volume within the tissue at the fluence threshold. This value provides important information on the mechanism of the ablation process. In particular, simple thermal models predict an energy density of several thousand J/cm^3, the amount needed to cause vaporization. An estimate of this parameter can be made by dividing the fluence threshold (energy per unit area needed to initiate ablation) by the penetration depth (depth at which this energy is distributed). At a wavelength of 355 nm, this estimate gives 180 J/cm^3 (for Φ_{th} = 36 mJ/mm^2 and D = 200 μm). Similar values are obtained at other wavelengths and for "soft" biological tissues. Thus the energy density present in biological tissue at the initiation of the ablation process is over an order of magnitude less than that required for vaporization. This anomaly has served as a starting point for this thesis.

1.2.2 Strobe Photography of Ablation

Information on the dynamic nature of the ablation process was obtained through strobe photography. In these experiments, two lasers were used simultaneously. The first laser used a short pulse (7.5 ns) of 355 nm light (Nd:YAG, third harmonic) to ablate a

sample of bone. The second laser (7.5 ns pulse duration, λ = 600 nm) was passed parallel to and slightly above the target and provided illumination for the strobe photography. Two separate imaging geometry's were used to photograph the results of the laser tissue interaction. The first geometry, called a scattergraph, collected the strobe light which was scattered at an angle of 90^0 and is useful for examining the size and position of the ejected material. The second geometry, called a shadowgraph, collected the unscattered strobe light. Although the debris cannot be studied in a shadowgraph due to diffraction effects, this geometry is sensitive to the second derivative of the index of refraction [Dubovik, 1981] and is therefore useful in determining whether blast waves are present.

The results from this experiment provided information on the dynamics of the ablation process. By electronically triggering the strobe pulse to fire at a fixed time after the ablation pulse, photographs of the debris ejection could be taken with a time resolution of less than 10 ns. The scattergraphs [see Izatt, 1991b] showed the explosive nature of the ablation process. As early as 50 ns after the ablation pulse, debris was clearly visible traveling away from the bone surface at speeds in excess of 600 m/s. The particulate debris ranged in size with an upper limit of about 50 μm. In addition, shadowgraphs showed the formation of a blast wave traveling ahead of the ejected debris with an initial velocity of several thousand meters per second.

In order to investigate the difference between ultraviolet and infrared ablation, this experiment was repeated using an infrared pulse to initiate ablation (pulse duration 350 ns, λ = 2.8 μm). The results of this experiment were strikingly similar to those obtained with

the ultraviolet laser. The strobe photographs showed small particulate debris traveling away from the bone surface at speeds in excess of 600 m/s.

Debris from both the ultraviolet and infrared ablation was collected and analyzed using a scanning electron microscope. In both cases, the size of the debris ranged from several hundred nanometers to a few tens of μm in diameter. The rough edges and non spherical shape of the debris implied that it had not melted and recondensed. Electron diffraction analysis identified the debris as consisting of calcium and phosphorous, in the same ratio as is found in calcium hydroxyapatite.

1.2.3 Summary

The empirical results discussed above supply important information on the ablation process. It was found that, for both "hard" and "soft" biological tissue, ablation is initiated when the laser fluence exceeds a fluence threshold. This fluence threshold was wavelength dependent and scaled with the penetration depth of the light within the tissue. The energy density within the tissue was found to be several hundred Joules per cubic centimeter. Strobe photography revealed that the ablation process of bone was explosive, leading to small particulates being ejected at velocities of several hundred meters per second. The explosive behavior was very similar at both ultraviolet and infrared wavelengths.

More importantly, these empirical results reveal a lack of understanding of the ablation process for short pulses. Although the photothermal model of ablation has been

successfully used to describe ablation with continuos wave irradiation, its predictions are not consistent with the results described above for short pulsed lasers. The energy density required to completely vaporize water is 2500 J/cm^3, an order of magnitude greater than the calculated energy density within the tissue at ablation threshold. The strobe photographs and SEM analysis of bone ablation also clearly show that the ejected material consists of unmelted, particulate matter.

These inconsistencies, which have also been discovered by other researchers, have led to numerous proposals for the ablation mechanism. These proposals can be grouped into three categories, photothermal, photomechanical and photochemical, and are discussed in the next section.

1.3 OVERVIEW OF RELATED WORK REPORTED IN THE LITERATURE

Just as in our early work, the early work on understanding the ablation of biological tissue published in the literature concentrated on an empirical characterization of this process. These studies focused on determining the relationship between the experimentally controlled parameters (laser wavelength, fluence, pulse duration, repetition rate, diameter, tissue type, etc.) and the observed outcomes (ablation threshold, tissue removal rate, zone of adjacent damage, biological response, etc.). Although the results of these studies have proven useful and have enabled clinical laser systems to be developed, a more advanced understanding of the ablation process is clearly needed and has been vigorously sought by many researchers in the field.

In order to understand the ablation of biological tissue, the fundamental physical process responsible for the initiation of ablation must be determined. Proposed mechanisms can be divided into three broad categories, photothermal, photomechanical, and photochemical.

1.3.1 The Photothermal Model of Ablation

The most basic form of the photothermal model postulates that ablation proceeds when a sufficient amount of energy has been delivered to the tissue to cause vaporization. In the case of continuous wave irradiation, a full analytical solution, including heat diffusion, has been published by Partovi et al. [1987] and supporting experimental data reported by Cothren et al. [1986].

For laser irradiation with short pulses, however, there are significant discrepancies between experimental results and a model based on vaporization. The most important discrepancy concerns the amount of energy within the tissue at the initiation of ablation. The heat of vaporization of water ("soft" biological tissue is 70 % water) is 2500 J/cm^3. Researchers have reported, however, that over a wide range of wavelengths from the near ultraviolet to the infrared (λ = 1.06 μm), the amount of energy within tissue at the initiation of ablation is only ~ 200 J/cm^3, an order of magnitude less than that required to cause vaporization [Oraevsky et al., 1991; Albagli et al., 1994]. For wavelengths near 2-3 μm, the energy density within tissue at ablation is within a factor of two of the heat of vaporization [Albagli et al., 1994].

One explanation for this discrepancy postulates that the optical properties of the tissue undergo laser induced dynamic changes. If the absorption or scattering were to dramatically increase so that the optical penetration depth was reduced by an order of magnitude, then the energy density near the surface would increase by a factor of ten and would be in agreement with an ablation model based on vaporization. There is little experimental evidence to support this claim. Ediger et al. [1993] studied the transmission of deep ultraviolet light (λ = 193 nm, τ = 14 ns) through thin samples of collagen (both hydrated and dehydrated) for both high laser fluences (above ablation threshold) and low fluences (50 times smaller). Most experimental results showed a permanent increase in the transmitted light through the sample. During ablation of the hydrated sample, however, a temporary decrease in the transmission occurred. This decrease, however, is caused by an increase of scattered light at the surface of the sample and not by an increase in the absorption coefficient [Pettit and Ediger, 1993]. Recent studies by Cilesiz and Welch [1993] and Pickering et al. [1993] at visible wavelengths have revealed only modest increases (1.1-2 times) in the absorption and effective scattering coefficients in aorta and myocardium, respectively, when these samples were slowly heated in water baths (100 ^{0}C and 75 ^{0}C, respectively). Note that these temperatures are higher than the laser-induced temperatures at the ablation threshold. In addition, recent experiments done by Torres et al. [1994] suggest that the experimental technique of measuring the optical coefficients with a spectrophotometer and integrating sphere overestimate the absorption coefficient.

As described above, there is little evidence that the optical penetration depth decreases by an order of magnitude throughout the ultraviolet, visible, and near infrared. In addition, there is strong experimental evidence that the penetration depth in tissue in the midinfrared increases significantly during laser irradiation. Experiments by Levine et al. [1989] and Valderrama et al. [1989] show that the absorption coefficient of cornea in the infrared (λ = 2.5 - 4.0 μm) decreases significantly as a function of temperature, as much as an order of magnitude for wavelengths near the absorption peak at 3.0 μm. Similar results have been reported for vascular tissue [Valderrama et al., 1990].

The temperature dependence of the absorption coefficient of water in the infrared has been known since 1925 [Collins, 1925]. Recent work by Cummings and Walsh [1993] have studied the dynamic change of the absorption coefficient near 3 μm in water and tissue phantoms and have shown that it is caused by a temperature-dependent change in the hydrogen bonding structure of water. In addition, when this dynamic behavior is applied to typical irradiation conditions for laser ablation at λ = 2.79 and λ = 2.94 μm, they found that the optical penetration of light actually increases by an order of magnitude. Other studies by Jansen et al. [1994] have also found significant increases in the optical penetration depth of water during irradiation from Ho:YAG, Ho:YSGG and Tm:YAG lasers at wavelengths between 1.85 and 2.15 μm. Since "soft" biological tissues contain 70 % water and water is the primary absorbing chromophore at these wavelengths, the dynamic changes in water explain the results for cornea and vascular tissue described above.

Thus, throughout the spectrum, the laser ablation of biological tissue is not consistent with a model based solely on vaporization. A photothermal explosion mechanism, based on a non-uniform heating of the irradiated tissue, has been proposed by Oraevsky, Esenaliev and Letokhov [1991b] to account for this observed anomaly. They propose that although the average energy density in tissue is low, if this energy is non-uniformly distributed, the peak energy density in certain microregions may be much higher. The elevated energy density in these regions may be caused by the size and distribution of the absorbing chromophores [Oraevsky et al., 1991] or by the non-uniform distribution of light caused by coherent scattering within the tissue [Golovlyov et al., 1993]. This can lead to the formation of overheated microcenters which undergo explosive boiling and lead to a mechanical removal of the entire irradiated region. Although changes in the energy density distribution within tissue caused by scattering and non-uniform absorption may be important, recent work by the same authors suggest that experimental results can be explained within the framework of an "acoustical" laser ablation model [Golovlyov and Letokhov, 1993]. This result will be discussed in the next section which describes the photomechanical model of ablation.

1.3.2 The Photomechanical Model of Ablation

As discussed above, a major drawback of the photothermal model of ablation is the experimental observation that the energy density within tissue at the ablation threshold is over an order of magnitude less than that required for vaporization. A model which does not have this drawback is the photomechanical model. The key ingredients in this model

of ablation are the laser induced stress and the mechanical properties of the tissue. It is postulated that ablation occurs when this stress exceeds the strength of the material, causing it to disassemble. The photomechanical model can therefore be studied by examining the laser-induced stresses and the role of the mechanical properties of the tissue.

Many researchers have found a strong correlation between the observed ablation characteristics of a tissue and its mechanical properties [Cummings and Walsh, 1993b; Jansen et al., 1993; Cummings and Walsh, 1992; Walsh and Deutsch, 1989; Zweig and Weber, 1987]. In the work by Cummings and Walsh, they examined the ablation characteristics of several different tissues which had vastly different mechanical properties (skin, artery, liver and cornea). An Erbium YSGG laser with a 250 μsec macropulse (consisting of 1 μsec micropulses) was used to initiate ablation. They found that the ejected tissue was not completely vaporized but rather was made up of particulates ranging in size from several microns to several hundred microns. In addition, the laser-tissue interaction caused extended damage to the surrounding tissue which could not be explained via simple thermal models. The observed damage to this tissue correlated well with the expected mechanical damage based on a detailed study of the differing compositions of the four tissue types. Finally, using a ballistic pendulum, the recoil momentum was measured and used to estimate the peak laser induced pressure. This pressure was found to be in the range of the mechanical strength of the tissue.

The calculation and measurement of laser induced stresses in solids [Bushnell and McCloskey, 1968] and liquids [Carome et al., 1964] were first done in the 1960's. Bushnell and McCloskey used the thermoelastic equations from the theory of elasticity in order to find the time dependent distribution of stresses within a material after absorption of a short pulse of laser light. It was assumed that the laser beam diameter was much greater than the penetration depth of the light within the target so that the calculations could be done in a one dimensional approximation. The temperature distribution created by the absorption of the laser light was also assumed to be a maximum on the surface and decay exponentially within the material. The results from the calculation showed that the initial stress distribution, which was entirely compressive, evolved into a traveling bipolar wave with both compressive and tensile components. The wave traveled at a velocity equal to the longitudinal speed of sound in the material. Experiments which measured the stress distribution in glass samples after irradiation with a 28 nsec pulse of light from a Q-switched ruby laser confirmed the theoretical predictions.

The formation of laser induced tensile stresses within a target material has significant implications for the photomechanical mechanism of ablation of biological tissue. It was well known in other fields that a transient tensile stress within a solid material can lead to the formation of microcracks and other defects [Anisimov et al., 1984]. If the stress exceeds the effective strength of the material, fracture and material ejection can occur. This process, called spallation, has been verified in metals with excellent agreement between experimental results and theoretical calculations [Tuler and Butcher, 1968]. In addition, transient tensile stresses in liquids can rupture the medium, causing a phenomena

known as cavitation. Cavitation, a dynamic process involving the growth and collapse of cavities within liquid, has been shown to be capable of damaging surrounding solid material [Knapp et al., 1970].

The process of spallation has been suggested as the mechanism for the laser ablation of biological tissue using short pulses and has been called photospall ablation to emphasize that the tensile stresses are induced by laser light [Dingus and Scammon, 1991a; 1991b]. Since then, many researchers have found evidence that fracture and cavitation play a role in the ablation process. Golovlyov and Letokhov [1993] studied the ablation of a homogenous aqueous solution with a Nd:YAG laser (λ = 1.06 μm, τ = 15 ns) and found that ablation takes place at laser energy fluences insufficient for the liquid under irradiation to boil away. They propose an acoustic model to explain the observed ejection of microdroplets at such low fluences. Paltauf et al. [1992] studied the ablation of an aqueous dye solution using strobe photography. In this experiment, they irradiated a solution with a known absorption coefficient with pulses from a Nd:YAG laser (pulse duration = 8 ns, λ = 1064 nm). Schlieren photography was performed with a second laser (pulse duration 8 ns, λ = 532 nm), which could be fired with a variable delay from the ablation pulse. These photographs provided a time history of events both below and above the solution surface. After irradiation with a single pulse of light with a fluence of 3.4 J/cm^2, cavitation bubbles were seen forming on a sub-microsecond time scale behind the traveling bipolar wave. Note that this fluence corresponds to a temperature rise of only 17 ^{0}C. At a fluence of 12 J/cm^2, the surface of the solution is completely disrupted and liquid droplets are accelerated away from the solution into the surrounding air. Thus,

for a laser-induced temperature of only 60 ^{0}C, material ejection (and thus ablation) is observed to occur in liquid. This experiment was repeated under identical conditions using a long pulsed Nd:YAG laser (pulse duration = 100 μs). It was found that no material ejection occurred until the laser-induced temperature rise exceeded 100 ^{0}C and vaporization was initiated.

Other evidence linking mechanical effects to the ablation process has been reported by Jacques et al. [1992]. In a similar experiment to the one described above, the effects of short pulsed irradiation (λ = 755 nm, pulse duration = 140 ns) of an aqueous dye solution were monitored using strobe photography. It was found that cavitation was initiated with temperature rises of only 3 ^{0}C, which corresponded to a stress of 8 bars. This value is in agreement with the reported threshold for creating cavitation within water [Knapp et al., 1970]. At higher fluences, corresponding to a peak temperature of only 55 ^{0}C material ejection was also recorded. In related work, Preisack et al. [1992] studied the ablation of vascular tissue by an excimer laser (λ = 308 nm, τ = 30 ns) and concluded that a mechanical fragmentation caused by cavitation was responsible for ablation.

Mechanical effects have also been observed in the ablation of "hard" biological tissue. Golovlyov and Letokhov [1993] studied the ejection and size distribution of microparticles during the ablation of bone with an XeCl laser (λ = 308 nm, τ = 30 ns) and concluded that the ablation mechanism was acoustical. Vickers et al. [1992] used an Er:YAG laser to ablate artificial dental stones and human teeth. Scanning electron micrographs of tooth enamel after laser irradiation showed the existence of circumferential

craze lines around the perimeter of the crater. A solution of the thermoelastic equations in a two dimensional geometry, predicts the formation of tensile circumferential stresses surrounding a laser irradiated region [Motamedi et al., 1992]. Calculations show that the predicted stress, under conditions where ablation is observed, is on the order of the ultimate tensile stress of tooth enamel.

Photoacoustic studies to measure the laser induced stress transients have been done on organic polymers [Dyer and Srinivasan, 1986], corneal tissue [Srinivasan et al., 1987; Dyer and Al-Dhahir, 1990] and vascular tissue [Cross et al., 1987; Cross et al., 1988]. In these experiments, thin filmed piezoelectric transducers were mounted on the back side of a thin piece of tissue. Transducers with fast response times (< 4 nanoseconds) were used. The front of the tissue was irradiated with a short pulse of light and the ensuing stress wave was recorded by the transducer. Experiments on vascular tissue using three different lasers (λ = 248 nm, τ = 8 ns; λ = 308 nm, τ = 10 ns; λ = 532, τ = 10 ns) all showed the expected bipolar stress wave at low fluences. At fluences above ablation threshold, the tensile part disappeared. This change was associated with the recoil momentum of the ablation products but may also be caused by the onset of cavitation. Similar results were found on corneal samples irradiated with short pulses at wavelengths of 193 nm, 248 nm, and 9.2 μm [Dyer and Al-Dhahir, 1990]. The measured stresses and the morphology of the resulting crater lead the authors to conclude that mechanical rupture plays an important part in the ablation at 9.2 μm and 248 nm. The authors also contend that the results at 193 nm imply a photochemical mechanism of ablation (discussed in the next section). Haase et al. [1993] also did photoacoustic studies on

vascular tissue at 308 nm (τ = 115 ns) and concluded that tissue fragmentation was an important mechanism for ablation.

In addition to studying the ablation process, this method has also been used for diagnostic procedures. Since the shape of the stress wave is related to the laser induced temperature distribution, it can be used to measure the optical properties of the target material. Recently, Oraevsky et al. [1993] have demonstrated the ability to extract both the absorption coefficient and the effective scattering coefficient in three different type of biological tissue (liver, prostrate, and vascular tissue) by studying the shape of the transient acoustic pulse. Other researchers have looked for changes in the acoustic stress transient to indicate when ablation has penetrated through one layer and reached a second layer of different mechanical properties [Reinisch and Ossoff, 1993].

Finally, stress transients associated with the formation of a plasma on the surface of the irradiated tissue have also been suggested as playing a role in the ablation process and causing damage to the surrounding tissue. Prince et al. [1988] studied the ablation of calcified plaque in human arteries using short pulses at visible wavelengths under conditions when plasma formation was present and concluded that a mechanical removal process was responsible. Other researchers have measured the formation of shock waves generated by laser-induced plasmas in order to understand their role in causing widespread damage in biological tissue [Doukas and Zweig, 1992; Zweig and Deutsch, 1992; Doukas et al., 1990]. The generation of stresses by plasma formation has also been modeled by Venugopalan et al. [1993].

1.3.3 The Photochemical Model of Ablation

The photochemical model of ablation has been proposed to explain the sharp cutting and lack of thermal damage found in the far ultraviolet ablation of biological tissue [Srinivasan, 1986]. In this model, termed ablative photodecomposition, it is proposed that the absorption of high energy photons (over 6 eV at λ = 193 nm) leads to a direct dissociation of molecular bonds in the material. Since the specific volume of the products of this photodecomposition is larger than what they replace, the pressure within the irradiated volume increases leading to an explosive expansion and ejection of molecular fragments. A theoretical model of this process in polymers has demonstrated that that this process can lead to material ejection at supersonic velocities, in agreement with experimental results [Garrison and Srinivasan, 1984]. Of particular interest is the ablation of the corneal surface and there have been a number of papers supporting this model in cornea for 193 nm irradiation [Kitai et al., 1991; Srinivasan et al., 1987].

Although there is evidence for the photochemical model of ablation at wavelengths below 200 nm, there is considerable evidence against it for all wavelengths above this. In a review article by Oraevsky, Esenaliev, and Letokhov [1991], it is pointed out that although single photons of 193 nm radiation can dissociate molecular bonds, multiphoton processes would be needed for near ultraviolet and visible irradiation. For two photon processes, many aspects of the ablation process should scale with the square of the laser intensity - a prediction not born out by experimental results in polymers or biological tissues. Some researchers have even questioned whether ablation in the deep ultraviolet is

a photochemical mechanism. Lane et al [1987] studied the ablation of skin at 248 nm and concluded that smooth cutting and minimal thermal damage could be explained by thermal and mechanical processes. Since this thesis concentrates on ablation in the near ultraviolet, visible and infrared, the photochemical model of ablation will not be considered any further.

1.4 OBJECTIVES, OUTLINE, AND ACCOMPLISHMENTS OF THIS THESIS

1.4.1 Objectives

As described above, laser ablation has great potential to assist or replace many surgical procedures. Despite this potential, and many years of basic research, the physical processes underlying the ablation process are not well understood. The purpose of this thesis is to advance the knowledge of the current understanding of the ablation process and in particular, to help develop a model of the fundamental mechanism of ablation which is consistent with experimental results. I believe that a detailed, physical model of ablation is necessary in order to develop advanced laser surgical procedures.

Experimental evidence supporting the important role of mechanical effects in the ablation process has been growing rapidly over the past several years (see section 1.3.2). Despite this, the photomechanical model of ablation is based on a simple, one-dimensional calculation of the laser-induced stresses first made in the 1960's and introduced to this field in 1991 [Dingus and Scammon, 1991a]. In addition, there is a serious discrepancy between the predictions of the model and experimental data. The basis of the

photomechanical mechanism is that laser induced tensile stresses cause mechanical effects (cavitation in liquids, microcrack formation in solids) which lead to the fracture, disassembly, and ejection of tissue fragments. Ablation craters caused by irradiation at wavelengths in the near ultraviolet, visible, and near infrared are typically several to several tens of microns deep while the optical penetration depth of light within the tissue is several hundred to several thousand microns. Thus, the effects of ablation are concentrated near the surface, even though the energy is distributed over a depth 10-100 times greater. This is not consistent with the one dimensional calculations of the stress distribution.

The time dependent laser-induced stress distribution within a material can be calculated from the theory of elasticity by solving the thermoelastic wave equation. Consider a pulsed laser incident on a non-scattering target. The absorption of the light will lead to an exponentially decaying temperature distribution as a function of depth within the target. For a short pulsed laser ($\tau < 10$ ns), this non-uniform temperature distribution serves as the initial conditions for the thermoelastic wave equation. The solution to this equation shows that initially, the stress distribution is compressive and is simply proportional to the temperature distribution. The stress distribution then evolves through traveling acoustic waves. In the one dimensional solution, a simple physical picture can be used to describe the complex evolution of the stress distribution. Consider the initial stress distribution (maximum value on the surface, decaying exponentially as a function of depth) as consisting of two equal amplitude waves which are traveling in opposite directions. As time progresses, one wave continues to travel into the material while the

other reaches the air-target interface. Due to the large acoustic impedance mismatch, this wave is reflected back into the material. In order to satisfy the boundary condition that the stress on a free surface is zero, the sign of the reflected wave is reversed and thus becomes a tensile stress. The stress distribution is then obtained by summing the three components (the non reflected wave traveling into the material, the reflected tensile wave traveling into the material, and the tail of this wave still traveling towards the surface). Although this solution leads to the formation of a significant tensile stress at depths equal to and greater than the optical penetration depth, the tensile stress at the surface is zero and near the surface is negligible.

Thus, there are major inconsistencies between experimental observations and both the photothermal and photomechanical models of ablation. In the thermal model, the predicted amount of energy needed to initiate ablation seems to be an order of magnitude higher than the measured value (section 1.3.2). Although the mechanical model may not suffer from this problem, it has several other problems. First, the tensile stress postulated to disassemble the tissue is absent at the surface, precisely where ablation is observed to occur. Second, there is no quantitative model which allows the time dependent stress distribution to be calculated for realistic (three dimensional) geometry's. Third, accurate calculations of the magnitude of the stresses are also limited by the lack of knowledge of the mechanical, optical, and thermal properties of biological tissue. Fourth, although there is substantial experimental evidence that mechanical processes play a role in ablation, the current experimental techniques give only limited information on that role (strobe

photography is limited to transparent media such as aqueous dye solutions and photoacoustic studies have been limited to one dimensional geometry's).

The objective of this thesis is to solve these problems so that the proposed models of ablation can be properly evaluated. First, the order of magnitude energy density discrepancy within the tissue at the initiation of ablation must be studied in much greater detail as a function of laser wavelength. This study will reveal whether this discrepancy can be explained through transient optical changes (since laser-induced changes in the optical properties of the tissue should be wavelength dependent) or if its a general, wavelength-independent feature of ablation (which suggests a nonthermal model of ablation). The results of this study, reviewed in the next section and described in chapter 2, show the latter and the development of experimental and theoretical technique to study the photomechanical model of ablation became the primary objective of this thesis.

In order to overcome the problems associated with the evaluation of the photomechanical model of ablation (described above), both experimental and theoretical techniques must be developed. First, a quantitative model which allows the time dependent stress distribution to be calculated for realistic (three dimensional) geometry's must be developed. Second, complimentary experimental techniques must be developed which either measure the stress directly or measure the optical, mechanical and thermal properties of the tissue which are necessary to calculate the stresses. The results from these should allow a more careful evaluation of the proposed photomechanical model. In

particular, the determination of whether tensile stresses form on the target surface, is a central question which must be answered.

Finally, any progress made on this important problem must be available to other researchers and physicians. Although this thesis will be available from the MIT libraries, I believe that it is essential that this work be widely disseminated to the research community through published papers and presentations at international conferences.

1.4.2. Outline and Accomplishments of This Thesis

The first objective of this thesis was to study the order of magnitude energy density discrepancy within the tissue at the initiation of ablation as a function of laser wavelength. This study is described in detail in chapter 2. The results of this study confirm that over a wide range of wavelengths from the near ultraviolet to the near infrared, the energy density needed to initiate ablation in both "hard" and "soft" biological tissue is consistently an order of magnitude less than that required for vaporization. Since the same effect is seen over such a wide range of wavelengths and tissues, it is highly unlikely that changes in the optical properties of the irradiated material can explain this universal effect since different chromophores are responsible for the absorption. Although the deposited energy is insufficient to cause vaporization, the laser induced stress (which is proportional to the energy density) reaches a value of several tens to hundreds of atmospheres which is high enough to cause mechanical effects. Thus this result lends support to the photomechanical model of ablation and emphasizes the need for detailed, quantitative calculations of this model.

The development of complimentary experimental and theoretical techniques to study the photomechanical model of ablation is first described in chapter 3. The experiment described in this chapter uses an interferometer to measure the laser induced time dependent thermoelastic expansion of biological tissue with sub-micron spatial resolution. A theoretical model, based on the hydrodynamic equations of motion, is used to predict the motion. A comparison of the measured and predicted motion yields important information regarding the tissues thermomechanical response to the laser irradiation. Although both the theoretical model and the experimental apparatus are subsequently replaced in later chapters, this chapter serves an important historical function. In particular, the methodology of comparing the measured thermomechanical motion of the tissue to the predicted motion which is established in this chapter, is a central concept in the rest of this thesis.

A quantitative theoretical model of the laser-induced stresses within an irradiated material is developed in chapters 4-6. In chapter 4, a brief review of the theory of elasticity and a derivation of the thermoelastic wave equation is given. A full time-dependent analytical solution of this equation is derived in a one dimensional geometry and is shown to be consistent with that found using the simple model described in chapter 3 in the appropriate limiting case. Although most of the work reported in this chapter was already reported in the literature, this chapter establishes the theoretical framework needed to find a three dimensional solution which has not been reported in the literature and is central to the objectives of this thesis.

In chapter 5, a quasi-steady state analytical solution to the thermoelastic wave equation in a three dimensional geometry is derived. This (quasi-steady state) solution is valid for times after acoustic wave propagation (typically 1 μs) but before significant thermal diffusion takes place (typically 100 ms). This solution provides several important findings which are qualitatively different from the predictions of the one dimensional theory. First, it shows that there are significant quasi-steady state stresses present within the target after the acoustic transients have died away. In the one dimensional case, these stresses were zero. Second, the three dimensional solution shows the existence of shear stresses which may also play a role in fracturing the material. Third, and most important, this solution predicts the existence of quasi-steady state tensile stresses on the surface of the target, a significant finding which supports the photomechanical model of ablation.

A full time-dependent solution to the thermoelastic wave equation in three dimensions is found in chapter 6 using numerical methods. This solution is checked extensively against both the one dimensional solution from chapter 4 and the three dimensional quasi-steady state solution from chapter 5 in the appropriate limiting cases. The results from this solution show that there are significant transient tensile stresses on the target surface and shear stresses near the target surface following laser irradiation. These results, combined with those from chapter 5, show that the major discrepancy between the photomechanical model and experimental observations was an artifact of the one dimensional model. In three dimensions, a complex coupling of different stress

components on the target surface lead to the formation of tensile stresses which are necessarily absent in one dimension.

Although the theoretical finding of surface tensile stresses is of great significance, two more issues must be resolved. First, experimental verification of the theoretical findings is required to show that they are both correct and complete. Second, the magnitude and distribution of laser-induced stresses cannot be determined without accurate values of the optical, mechanical, and physical properties of the tissue target. Both of these issues are resolved in chapter 7 which describes an interferometric technique which can measure the thermoelastic expansion of material with a spatial resolution of several nanometers on a nanosecond time scale. This technique is an improved version over that described in chapter 3. Experimental results for the laser-induced thermoelastic motion of glass and plastic samples confirm the accuracy of the theoretical model. In addition, the complex time dependent features of the surface motion allow one to determine the optical, mechanical, and thermal properties of the material which are necessary to calculate the stresses.

The application of this technique to study biological tissue is described in chapter 8. The interferometric measurements of the thermoelastic expansion of "hard" biological tissue (cortical bone) induced by sub ablation threshold laser irradiation show similar features to that found in the glass and plastic samples. Comparison of these features to the theoretical model allow the important optical, mechanical, and thermal properties of the tissue to be determined. In addition, deviations between experiment and theory show

the important influence of scattering. These deviations can be minimized by using a Monte Carlo technique to calculate the temperature distribution given the scattering properties of the medium. Experimental results near the ablation threshold confirm that the penetration depth does not decrease by a factor of ten.

By modifying the geometry of the experimental apparatus, the response of the target to laser pulses causing ablation can be monitored. In experiments done on clear plastic, the thermoelastic motion caused by near threshold pulses showed measurable deviations from the predicted motion. These deviations correlated with the formation of permanent microcracks within the target which were easily photographed. Subsequent pulses led to a fracturing and ejection of the surface material. Although the bone sample was not transparent and therefore could not be studied photographically, the thermoelastic motion of bone near and above threshold showed the same characteristic deviations that the plastic did. The calculated laser induced stresses associated with ablation for both materials were of the same order, although somewhat below, the static tensile strength of the material.

Preliminary data on the laser-induced thermoelastic expansion of "soft" biological tissue (human meniscus) is also presented in chapter 8. This data shows long-lived surface motions which are not predicted by the theory. A similar experiment on an aqueous dye solution shows the same results. The dynamics of this motion along with the small laser-induced temperatures (~ 5 ^{0}C) and moderate stresses (~ 20-30 bars) are all consistent with the formation, growth, and collapse of cavitation bubbles within the tissue. This is a

significant finding because the collapse of these bubbles is a mechanically destructive event and has been shown to be capable of damaging any surrounding solid material. Since the findings of chapter 2 show that ablation of soft biological tissue occurs at very low temperature, cavitation may play a major role in initiating ablation.

The major findings of this thesis are summarized in the final chapter. The experimental and theoretical evidence is shown to support a photomechanical model of ablation. In solids and "hard" biological tissue, this model is based on a weakening of the material due to the accumulation of microdefects caused by laser-induced stresses. In "soft" biological tissue, the material is damaged through the destructive effects associated with cavitation phenomena caused by laser-induced stresses. Experiments to investigate this proposed model are also suggested for future work.

The experimental apparatus developed in this work also has additional applications. These applications, including studying light propagation in turbid media and studying caviation in liquids, are briefly discussed in chapter 9.

The final objective of this thesis was to make its findings available to other researchers and physicians in the field. This work has been thoroughly disseminated to the research community in the forms of papers in refereed journals, oral and poster presentations at conferences, and written manuscripts in conference proceedings. I have authored five papers in refereed journals and co-authored two others papers, a book chapter, and four conference proceedings. I have presented posters on this work at the

Gordon Research Conference on Lasers in Medicine and Biology in Meriden, NH (July, 1990), the 1992 Gordon Conference in New London, NH (July 6-10), and at the Medical Free Electron Laser Symposium at the Wellman Laboratories of Photomedicine in Boston, MA (October 26-28, 1992). Oral presentations of this work were given at the 13th Annual Meeting of the American Society for Laser Medicine and Surgery (ASLMS) in New Orleans, LA (April 18-20, 1993), at a Modern Optics and Spectroscopy Seminar at MIT (December, 1993) and at the 14th Annual Meeting of ASLMS in Toronto, Ontario (April 8-10, 1994). Additional presentations of this work have been made by Dr. Irving Itzkan at the Second International Conference on Laser Ablation : Mechanisms and Applications-II in Knoxville, TN (April, 1993), the 6th Annual Proceedings of the IEEE Lasers and Electro-Optics Society (November, 1993), and the Gordon Conference on Lasers in Medicine and Biology in Meriden, NH (July 4-8, 1994) and by Dr. Lev Perelman at the International Society for Optical Engineering (SPIE) Conference entitled Laser-Tissue Interaction V, in Los Angeles, CA (January 24-28, 1994).

CHAPTER 2

Inertially Confined Ablation of Biological Tissue

2.1 OVERVIEW

An empirical study of the parameters affecting the laser ablation of biological tissue, described in chapter 1, uncovered an important experimental finding which has served as a starting point of the detailed examination of ablation described in the rest of this thesis. By measuring the fluence threshold and the optical penetration depth, the energy per unit volume needed to initiate ablation was determined and found to be significantly less than that required for vaporization, implying that another mechanism was responsible for short pulsed ablation.

This important, but preliminary finding and its ramifications are examined in more detail in this chapter. A host of experimental results reported in the literature for the fluence thresholds and optical penetration depths under different conditions have been analyzed. A calculation of the energy density in tissue at the onset of pulsed laser ablation reveals that, over a large range of wavelengths and tissue types, it is an order of magnitude lower than that needed for vaporization. This chapter will also demonstrate that under appropriate conditions of laser pulse duration and penetration depth, tremendous pressures can be generated in the tissue at energy densities well below vaporization.

The model of inertially confined ablation is developed to explain these experimental results. This model, which can be characterized as a photomechanical model, postulates that ablation is initiated when the laser-induced pressure ruptures the tissue and is qualitatively consistent with the data presented in this chapter. This photomechanical model will be developed in more detail in subsequent chapters.

The work described in this chapter was presented at a poster session at the 1992 Gordon Conference on Lasers in Medicine and Biology in New London, New Hampshire and was published in an article entitled "Inertially Confined Ablation of Biological Tissue" in the journal *Lasers in the Life Sciences* [Albagli et al., 1994a].

2.2 INTRODUCTION

The energy density in tissue needed to initiate the ablation process can be calculated from the optical properties of the tissue and the fluence threshold. The calculated energy density in aorta needed to initiate ablation at 308 nm is shown in figure 2-1. This figure, adapted from a paper in the literature [Gijsbers et al., 1990], is based on a Monte Carlo simulation using the experimentally measured optical coefficients (μ_a = 60 cm^{-1}, μ_s' = 63.2 cm^{-1}) of aorta at 308 nm. The incident beam in the simulation had a diameter of 200 μm. By multiplying the fluence contours obtained in the simulation by the absorption coefficient, and scaling the incident fluence of the laser up to the experimentally measured threshold for ablation (1.8 J/cm^2, [Taylor et al., 1987]), the energy density contours were obtained. Two assumptions have been made in this calculation: 1) the

optical properties of the tissue remain constant during the laser pulse; and 2) once absorbed, the energy is evenly distributed through the local tissue volume.

Figure 2-1 indicates that the energy density in the first 10 μm layer of tissue (a typical single shot ablation crater depth) is only 254 J/cm^3 - a factor of ten less than that needed for vaporization. Thus, a more detailed calculation confirms the preliminary finding described in chapter one and suggests that ablation is initiated by a different mechanism than vaporization.

2.3 TISSUE ENERGY DENSITY DURING ABLATION

Since the energy density in aorta at the 308 nm ablation threshold appears to be a factor of ten below that required for vaporization, we wished to determine the scope of this inconsistency by estimating the energy density in both aorta (a representative soft tissue) and beef shank bone (a representative hard tissue) for other wavelengths in the near ultraviolet and visible. The energy density in the tissue at ablation threshold can be estimated by dividing the fluence threshold by the penetration depth. For the case of 308 nm ablation of aorta, this experimentally determined estimate gives 270 J/cm^3, as compared to the calculated value of 254 J/cm^3 obtained from the Monte Carlo simulation.

Figure 2-2 shows a comparison between fluence thresholds of ablation (Φ_{th}) and the penetration depth of light (D) in beef shank bone. In a previous study we used beef shank bone as a model of calcified plaques in arteries and therefore had available a

substantial body of data to draw upon [Izatt et al., 1991a]. The penetration depth was obtained by performing total transmission and total reflection measurements of a thin piece of beef shank bone in an integrating sphere [Izatt, 1991b]. These measurements were used to determine the absorption coefficient (μ_a) and effective scattering coefficient (μ_s') as a function of wavelength [Izatt, 1991b; Van Gemert and Star, 1987]. The penetration depth was determined by :

$$D = \sqrt{\frac{1}{3\mu_a(\mu_a + \mu_s')}} \qquad [2\text{-}1]$$

The ablation thresholds used in figure 2-2 were reported by Izatt [1991a]. In this study, a XeCl excimer laser (308 nm), tripled Nd:YAG laser (355 nm), doubled Alexandrite laser (375 nm) and a flash lamp-pumped dye laser (450 - 590 nm) were used. Pulse durations were between 7.5 ns and 1.5 μsec. The ablation thresholds were found by plotting the crater depth produced as a function of the incident fluence and determining the x-intercept.

Figure 2-2 clearly shows a correlation between the ablation threshold and the penetration depth. The energy density in the tissue before ablation (Φ_{th} / D) thus remains relatively constant through this wavelength region with an approximate value of 200 J/cm^3. Oraevsky, Enseliev, and Letokhov [1991] present similar results for ablation of atherosclerotic plaque using a Q-switched Nd:YAG laser at wavelengths of 1064, 532, 355, and 266 nm. Using experimentally measured ablation thresholds and Monte Carlo modeling, they found that energy densities between 80 and 200 J/cm^3 were necessary to

initiate ablation. Ablation thresholds for aorta at 355 and 375 nm [Izatt, 1991b] and penetration depths at these wavelengths [Oraevsky et al, 1988] give similar values.

Thus, the surprisingly low energy density in tissue required for pulsed laser ablation occurs over a wide range of wavelengths as well as different type of tissues. Three explanations, based on the photothermal and photomechanical models described in chapter 1, have been suggested to explain this large discrepancy. The first explanation is that the optical properties of the tissue change during the laser ablation pulse to enhance the absorption. This increases the energy density in the first layer to 2500 J/cm^3 and ablation proceeds through vaporization, a photothermal effect. Such a change in optical properties should be highly variable with wavelength. As shown above, the energy density discrepancy persists at wavelengths in the near ultraviolet, visible, and infrared - making it extremely unlikely that a host of dynamic changes in the optical coefficients are responsible. Recent studies by Cilesiz and Welch [1993] and Pickering et al. [1993] have revealed modest (1.1 - 2 times) increases in the absorption and effective scattering coefficients at visible wavelengths in aorta and myocardium, respectively, when these samples were slowly heated in water baths (100°C and 75°C, respectively).

A second explanation is that of a non-homogeneous energy density distribution in the tissue due to the discrete nature of the absorbing chromophores and the lack of energy transfer mechanisms. This effect has been coupled with a photothermal explosion mechanism to explain the energy density discrepancy [Oraevsky et al, 1991]. In this

model, it is proposed that the fast formation of gas bubbles in the overheated tissue leads to an explosive boiling of the water in the tissue. This model may be more appropriate for picosecond laser pulses where there is no time for local redistribution of the energy during the laser pulse.

A third explanation, which does not require vaporization, is laser induced front surface spallation or photospall ablation [Dingus and Scammon, 1991a; 1991b]. In this model, the laser heats the tissue before it has time to expand - causing a large increase in pressure (compressive stress). The compressive stress, considered as two counter-propagating stress waves, produces a tensile stress wave after one of the waves reflects from the free surface of the air-tissue interface. If this stress exceeds the ultimate tensile stress of the tissue, spallation occurs and the top layer of tissue is ejected. Although this model correctly predicts that the energy density needed to initiate ablation can be significantly less than that for vaporization, a model based only on spallation is not consistent with a host of experimental results for the ablation of tissue in the near ultraviolet, visible, and infrared. For example, under spallation, the depth of the crater produced should be one to a few times larger than the optical penetration depth. As Oraevsky et al. [1991] point out though, experimental results show that the ablation crater depth is more than an order of magnitude less than the penetration depth at 355, 532, and 1064 nm. Quantitatively, the dependence of the fluence threshold on the pulse duration that spallation predicts is also inconsistent with experimental results. For example, for 308 nm ablation of aorta, the spallation model predicts that the fluence threshold should increase by more than a factor of five when the pulse duration is increased from 7 ns to

300 ns [Dingus and Scammon, 1991a], but experimental data shows only a 20% increase [Taylor et al., 1987]. Finally, since spallation depends on the reflection of the compressive stress wave from the acoustic mismatch at the surface, ablation thresholds should be significantly higher for tissues under liquid. However, experimental results have shown similar results for ablation under air and under water (ablation yields remain constant, ablation thresholds increase by only a factor of two [Izatt, 1991b]) at a variety of wavelengths, making it unlikely that completely different mechanisms are at work.

2.4 INERTIALLY CONFINED ABLATION

A review of the experimental evidence presented above shows, for a wide range of parameters, that the energy density in tissue during ablation is an order of magnitude less than that for vaporization. The model of inertially confined ablation proposed in this paper, like the spallation model, emphasizes the role of pressure in causing ablation at such a low energy density. An understanding of the thermodynamics of water is used to show how, under conditions of inertial confinement, this energy density can lead to the generation of a large pressure within the tissue and a tremendous pressure gradient near the surface. It is proposed that ablation occurs when these conditions exceed a certain threshold (which is dependent on the structural properties of the tissue). The relationship between fluence threshold, penetration depth, and pulse duration for a host of experiments reported in the literature is shown below to be consistent with this model.

2.4.1 Understanding the Thermodynamics of Water

Since soft biological tissues contain up to 70% water, understanding the thermodynamics of water is helpful in understanding tissue ablation. The thermodynamic properties of water are extremely well known. These properties, including the density, pressure, internal energy, entropy, enthalpy, and temperature have been tabulated over a wide range of values. Figure 2-3 was tabulated from the National Bureau of Standards and Nuclear Regulatory Commission Steam Tables [Haar et al, 1984]. This simplified figure shows only the most important parameters required for an understanding of the ablation process. On this plot of pressure vs internal energy, contours of constant temperature and density are displayed and the boundary of the phase change region is outlined with a bold line.

The conventional value of 2500 J/cm^3 used to describe vaporization of water applies to a constant pressure process. This process is illustrated in figure 2-3 by the horizontal path A-C. This path assumes that the conditions of the heating are such that the pressure remains constant. However, if the heating is rapid compared to the time of pressure relaxation mechanisms, the pressure will increase and the system will traverse a different thermodynamic path. In the extreme case of instantaneous heating, the volume (or density) of the system remains constant. To illustrate the difference between heating at constant pressure and heating at constant volume, consider paths A-B and A-D in figure 2-3. In path A-B, 300 J/cm^3 are slowly added to the water. The pressure remains constant at 1 bar while the temperature increases to 92°C and the density decreases to 0.964 gm/cm^3. In path A-D, 300 J/cm^3 are added to the water faster than the pressure

can relax. While the density remains constant at 1.0 gm/cm^3 and the temperature increases to 96^{o}C, the pressure rises to 900 bars. Note that the phase change boundary is never crossed and so it is meaningless to speak of "vaporization".

2.4.2 Inertially Confined Ablation in Tissue

The concept of inertially confined ablation is based on the generation of tremendous pressure that occurs while heating a substance at constant volume. In pulsed laser ablation of tissue, the energy can be supplied so rapidly that the material is inertially confined during the length of the laser pulse. A quantitative illustration of this can be seen in figure 2-4, which illustrates the temperature and pressure contours in aorta immediately after interacting with a 7 ns, 1.8 J/cm^2, 308 nm laser pulse. The contours were calculated from the energy density contours of figure 2-1 and the thermodynamic properties of water from figure 2-3, under the assumption of constant volume (since the energy is deposited in only 7 ns, the tissue is inertially confined and thus the constant density path (A-D) is traversed). It is important to note that we are only modeling the thermodynamic properties of aorta as water, the structural properties of aorta play a key role in the ablation process and must be considered separately.

As shown in figure 2-4, these assumptions predict a large stress generation in the tissue. More importantly, since the pressure just outside the surface must be one bar, there is a tremendous stress gradient near the surface of the tissue. Note that pressure is a scalar property of an isotropic fluid, while stress is a tensor property of a solid. For an

isotropic system, the three principal components of the stress tensor are equal to the negative of the pressure, and the non-diagonal components are zero. We use the calculation of pressure obtained from the thermodynamic properties of water to estimate the stress generated in the tissue, and the stress gradient to estimate the dynamic forces. The extreme stress gradient near the surface and the associated tensile stresses lead to dislocations between the layers of tissue and the nucleation and growth of microcracks, which can be modeled by solving the kinetic equation for the total volume of cracks [Anisimov et al., 1984]. Ablation occurs when these extreme laser-induced conditions exceed a threshold value (which is dependent on the structural properties of the tissue) and proceeds through a disassembly of the tissue at the microcracks and subsequent acceleration away from the crater due to the stress gradient. This "threshold value" for ablation may be more complicated than simply exceeding the ultimate tensile stress of the tissue, for example, Anisimov also points out that the prior existence and formation of microcracks can reduce the effective tensile strength. Efforts are currently underway to quantitatively study this disassembly of the tissue as well as the relationship between the stress generated, the structural properties of the tissue, and the fluence threshold.

2.4.3 Inertial Confinement in "Soft" Biological Tissue

In comparing this model to experimental data in the literature, it would be instructive to examine the energy density needed to initiate ablation when i) the laser pulse duration (τ) is short compared to the characteristic time for the laser-induced pressure to

dissipate (τ_c) and ii) $\tau > \tau_c$. The pressure dissipation time under these conditions is usually written as

$$\tau_c = \frac{D}{C_l} \qquad [2\text{-}2]$$

where D is the optical penetration depth and C_l is the longitudinal speed of sound (assumed equal to 1500 m/s in soft tissue).

Figure 2-5a is a plot of energy density in aorta at threshold versus a pressure relaxation coefficient (R_c). The energy density at threshold (E_{th}) was estimated by dividing the fluence threshold (Φ_{th}) by the penetration depth. The coefficient R_c is defined as the ratio of the pulse duration of the laser to the pressure dissipation time. A value of $R_c < 1$ indicates that the tissue is inertially confined during the laser pulse. The dotted line in figure 2-5a shows the predicted behavior based on a simple theoretical model which will be explained later (see Eq. 2-10).

Although the data in figure 2-5a is qualitatively consistent with the model of inertially confined ablation, the energy density needed to initiate ablation does not start to increase significantly until the laser pulse duration exceeds the pressure dissipation time by an order of magnitude ($R_c = 10$). This model, which assumes that pressure plays a key role in initiating ablation, predicts a sharp increase in the energy density at threshold when the pressure is able to dissipate significantly during the laser pulse ($R_c = 1$), a conclusion not born out by the data.

In order to understand this order of magnitude discrepancy, we must re-examine the pressure dissipation time (eq. 2-2) which was found by dividing a characteristic length (optical penetration depth) by a characteristic velocity (speed of sound). This speed is a parameter of the wave equation which can be derived from the coupled differential equations describing the conservation of mass, momentum, and energy and several approximations including the requirement that the strain be much smaller than unity (acoustic approximation). Although this approximation is valid for calcified biological tissue (e.g., for bone the maximum (breaking) strain is 0.015), soft biological tissue can exhibit strains as large as 1 before breaking. Thus, in considering the ablation of soft biological tissue where large laser-induced stresses produce significant strains, the acoustic approximation breaks down and stress dissipation cannot be described by an acoustic relaxation with a time constant as in eq. 2-2.

In order to model the pressure dissipation time in soft biological tissue under the conditions when the acoustic approximation fails, we have made an order of magnitude estimate for the value of the characteristic time for motion (τ_m). This time can be determined from the ratio of the penetration depth to the velocity of the material v, where it is assumed the energy deposited in the tissue is converted into kinetic energy (order ρv^2).

$$\tau_m = \sqrt{\frac{D^3 \rho}{\Phi}} = \sqrt{\frac{D^2 \rho}{E}} \qquad [2\text{-}3]$$

In analogy to the pressure relaxation coefficient R_c, an inertial confinement coefficient, C, can then be defined as the ratio of the laser pulse duration to this characteristic time. This non dimensional parameter has the same form as the self-similar parameter introduced by Sedov [1959] to analyze an intense explosion in a gas in a planar geometry. Zel'dovich and Raizer [1966,1967] discuss the use of this scaling parameter in cases when the speed of sound cannot be used to characterize a physical process.

Figure 2-5b is a plot of energy density in aorta at threshold versus the inertial confinement coefficient. The data in both figures 2-5a and 2-5b is qualitatively consistent with the model of inertially confined ablation. The data illustrates a trend of increasing energy density requirements with increasing pressure relaxation and inertial confinement coefficients. For low values (R_c or $C < 1$), the energy density needed to ablate is less than 300 J/cm^3 for a host of different lasers ranging from the strongly absorbing (248 nm, 15 μm penetration depth) to the weakly absorbing (1064 nm, 2.8 mm penetration depth). This trend of small energy densities occurs for over 3 orders of magnitude with these coefficients. As the assumption of inertial confinement breaks down (R_c or $C >> 1$), the energy density required to ablate aorta rises to 2000-3000 J/cm^3, the energy density required for vaporization. The data in figure 2-5b, however, is also quantitatively consistent with the model of inertially confined ablation. The energy density needed to initiate ablation starts to increase as C exceeds one. Thus, both the theoretical argument based on the breakdown of the acoustic approximation and experimental data from the literature support the use of the inertial confinement coefficient over the pressure relaxation coefficient for characterizing the ablation of aorta with short pulsed lasers.

The data required to construct figures 2-5a and 2-5b is summarized in Table 2-1. This table includes the wavelength, pulse duration, experimentally measured fluence threshold and penetration depth, calculated energy density, inertial confinement coefficient, pressure relaxation coefficient and reference for each data point. The reported spot sizes of the ablation threshold experiments varied between 0.25 and 1.8 mm, and no attempt was made to correct for these differences.

The result from a simple theoretical model is also shown in figures 2-5b (dotted line). In this model, it is assumed that the energy density required to initiate ablation remains constant for $C \leq 1$. The value of this constant threshold energy density is related to the stress conditions created by the energy deposition and the ability of the tissue to withstand these conditions (which will depend on the structural properties of the tissue). This value, $E_{th}^{C\leq 1}$, was determined from the average of the ten data points in figure 2-5b for which $C \leq 1$ and has a value of 192 J/cm^3. For $C > 1$, the threshold energy density, $E_{th}^{C>1}$, is higher because pressure relaxation effects now have time to compete with the pressure build up. To model this, consider a fraction of the pulse, with duration $\tau' < \tau$, which deposits an energy density of E' in the tissue. Although the entire pulse does not satisfy the conditions of inertial confinement (because $C > 1$), we can find τ' such that this portion of the pulse does satisfy the conditions of inertial confinement (i.e. the characteristic time associated with this fraction of the pulse must be equal to τ') :

$$\tau' = \sqrt{\frac{\rho D^2}{E'}} \qquad [2\text{-}4]$$

By the rectangular pulse assumption

$$E' = \frac{\tau'}{\tau} E_{th}^{C>1}. \qquad [2\text{-}5]$$

Eliminating τ' from these equations yields

$$E_{th}^{C>1} = C^{2/3} E' \qquad [2\text{-}6]$$

where

$$C = \tau \sqrt{\frac{E_{th}^{C>1}}{D^2 \rho}} \qquad [2\text{-}7]$$

is the inertial confinement coefficient as calculated for use in figure 2-5b.

If we now assume that the conditions reached in the time τ' are sufficient to initiate ablation of the tissue, then

$$E' = E_{th}^{C\leq 1}. \qquad [2\text{-}8]$$

Therefore,

$$E_{th}^{C>1} = C^{2/3} E_{th}^{C\leq 1}, \qquad [2\text{-}9]$$

which is the curve plotted in figure 2-5b. Because the energy density increase needed to achieve a given pressure increase is a function of initial temperature (as can be verified from the steam tables), the correct curve in figure 2-5b for C > 1 would rise less steeply due to the increase of temperature during the first part of the pulse. Also, the fact that the temporal profiles are Gaussian and not rectangular, will also cause the curve to rise less steeply. Proceeding in an analogous manner using the pressure relaxation coefficient, the theoretical value of the energy density needed to initiate ablation (see figure 2-5a) is :

$$E_{th}^{R>1} = R E_{th}^{R\leq 1} \qquad [2\text{-}10]$$

Two additional comments must be made concerning figures 2-5a and 2-5b. First, data points 16-22 are from a Co:MgF_2 laser (wavelength range 1.94 - 2.14 μm) and are shown with large horizontal error bars. The temporal profile of this laser pulse consisted of a train of 2 μs micropulses in a 100 μs macropulse. The endpoints of the error bars correspond to calculating the inertial confinement coefficient for both a 2 μs pulse and a 100 μs pulse. The situation is further complicated by the fact that this temporal profile changes as a function of wavelength.

Secondly, it should be noted that one data point (23), corresponding to HF ablation (2.78 μm), appears to be in the vaporization region with an ablation energy density equal to 2000 J/cm^3 and C greater than 100. This value is based on the 2 μm penetration depth of this wavelength in water. Experimental evidence from Levine et al. [1989] and Valderrama et al. [1990] suggests that the strong water absorption peak (near 3 μm) may change dramatically during the ablation process, increasing the penetration depth by an order of magnitude. If this is the case, HF ablation would only be depositing several hundred Joules per cubic centimeter in tissue and have an inertial confinement coefficient of about five. Thus, even this ablation may not proceed entirely through vaporization.

It is interesting to note that although, in certain cases, the path in pressure-energy space may not enter the phase change region during energy deposition (low C), the return

path may cross the phase boundary during the ensuing expansion. In describing a model for the ablation of skin at 248 nm, Lane et al. [1987] proposes that after the laser pulse creates a high pressure, high temperature fluid, an isentropic expansion occurs, converting thermal energy into kinetic energy directed away from the surface. During this expansion, the thermodynamic path may pass through the phase change region and form a mixture of vapor and condensate. However, for most of the data discussed in this paper (including the inertially confined ablation regime), there is not enough energy deposited into the tissue to enter the phase change region.

2.4.4 Inertial Confinement in "Hard" Biological Tissue

Figure 2-6 shows the energy density needed to initiate ablation in bone as a function of the pressure relaxation coefficient. The data required to make this figure is summarized in Table 2-2. This data clearly shows that energy densities of less than 200 J/cm^3 can initiate ablation at several different ultraviolet and near ultraviolet wavelengths. This data fits equally well when plotted against the inertial confinement coefficient. However, since the acoustic approximation is valid up to the breaking strain of bone, there is no compelling theoretical reason to abandon the pressure relaxation coefficient. The scarce amount of data available for this figure is due mainly to the lack of knowledge of the optical properties of the bone in the infrared and deep ultraviolet where the ablation thresholds are also known.

2.5 CONCLUSIONS

An analysis of the optical properties of biological tissue and the fluence threshold for laser ablation has revealed that the energy density in the tissue is an order of magnitude less than the amount needed for vaporization. This discrepancy exists at a wide range of wavelengths from the near ultraviolet to the visible and infrared, as well as to different tissue types (aorta, atherosclerotic plaque, and beef shank bone). Inertially confined ablation has been proposed to address this discrepancy. When a material is heated so quickly that inertial confinement prevents it from expanding, a large increase in pressure (or more correctly stress) occurs creating a tremendous stress gradient near the surface. Ablation consists of the disassembly of the tissue and subsequent acceleration of the debris away from the surface. This model correctly predicts the relationship between the ablation threshold, pulse duration, and optical penetration depth for a host of experiments reported in the literature.

The results from this chapter lend support to the photomechanical model of ablation. In order to examine this model in more detail, the physics of the laser-tissue interaction must be understood. In particular, the spatial and temporal distribution of the laser-induced stress must be calculated and compared to the mechanical strength of the sample and the details of the sample response must be examined experimentally. This approach is used in the subsequent chapters of this thesis.

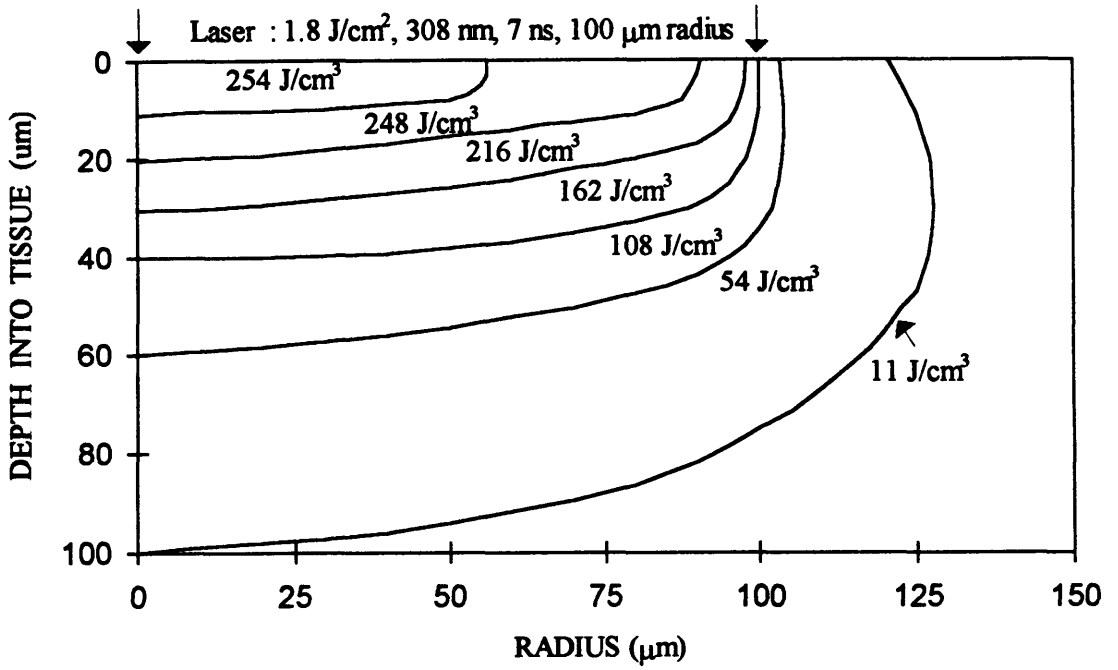

Figure 2-1. The maximum energy density in aorta at the 308 nm ablation threshold is only 254 J/cm^3, an order of magnitude less than that required for vaporization.

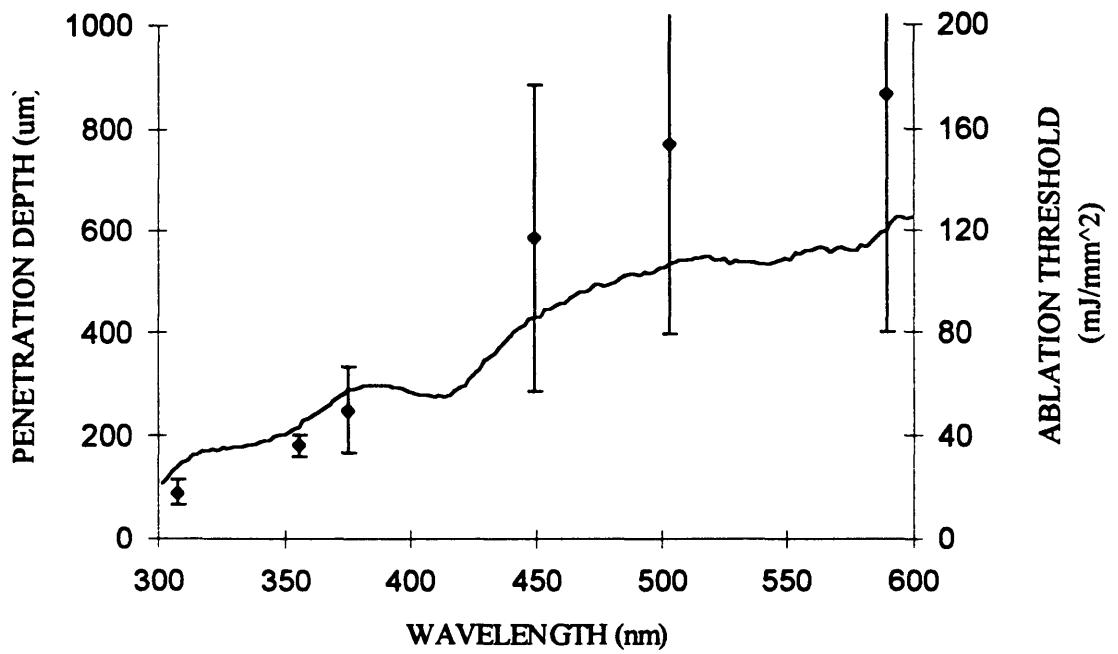

Figure 2-2. Since the fluence thresholds of pulsed ablation of beef shank bone (data points) tracks the penetration depth (solid line) as a function of wavelength, the ratio of these (energy density) remains constant. As in figure 2-1, this constant is an order of magnitude less than that required for vaporization.

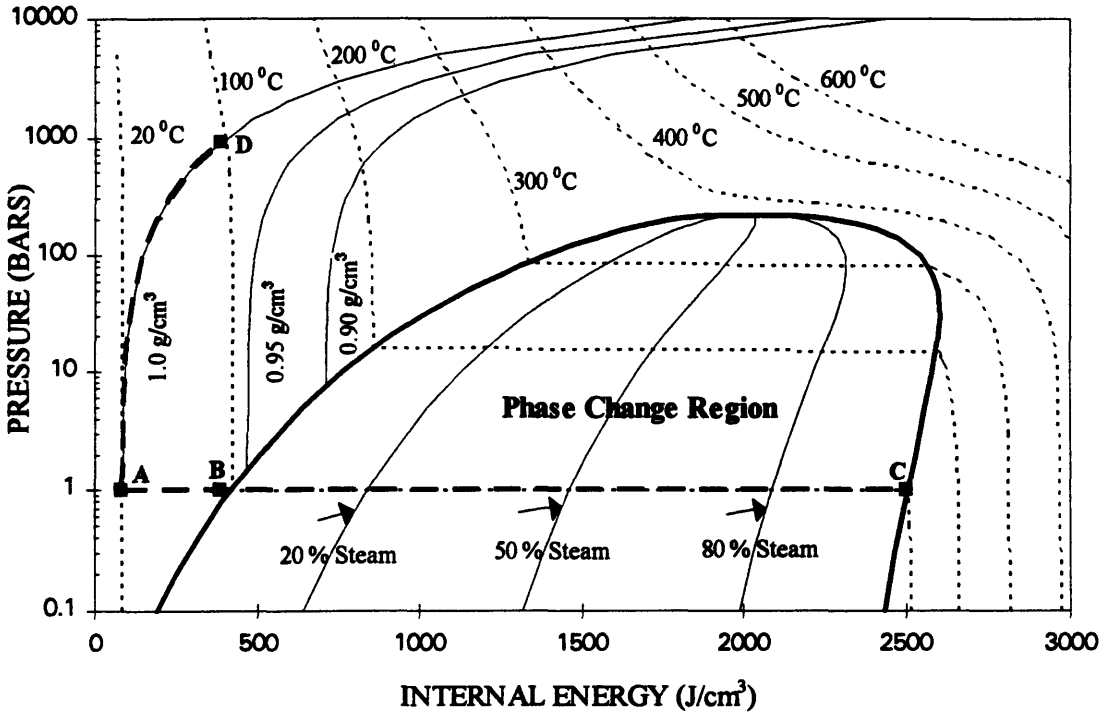

Figure 2-3. Although 2500 J/gm of internal energy are needed to vaporize water at constant pressure (path A-C), the addition of 300 J/gm of internal energy to water, at STP, in a constant volume process will increase the pressure to 900 bars (path A-D).

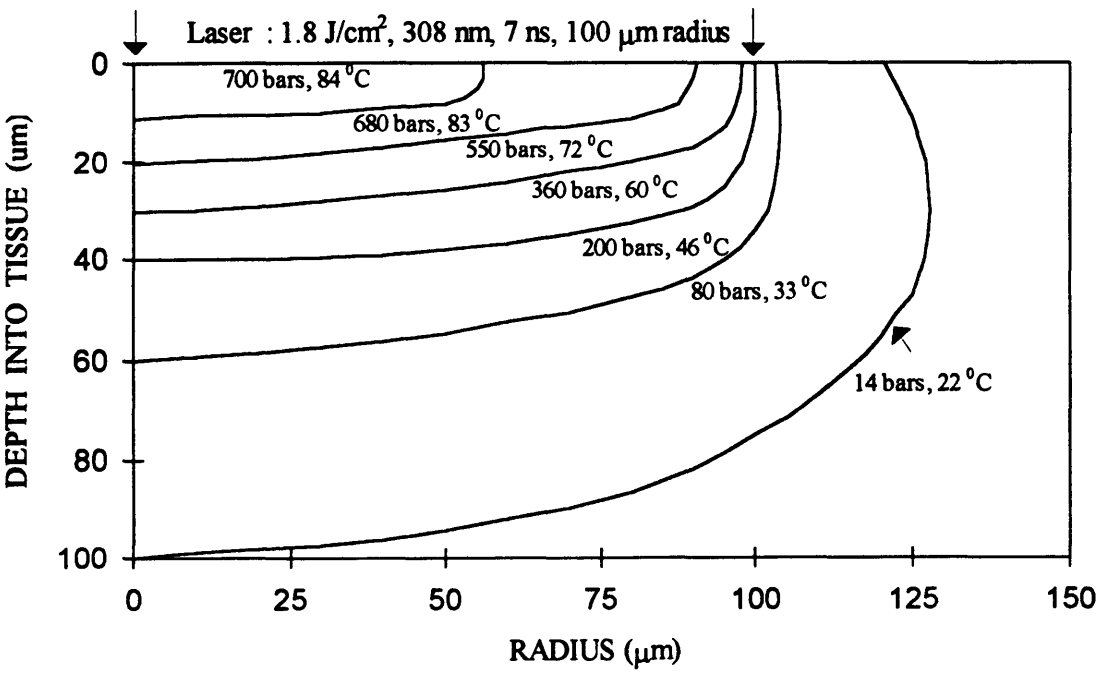

Figure 2-4. Although the energy density in aorta at the 308 nm ablation threshold is not sufficient for vaporization (see figure 2-1), the generation of a large stress and associated stress gradient causes the tissue to disassemble - leading to ablation without vaporization.

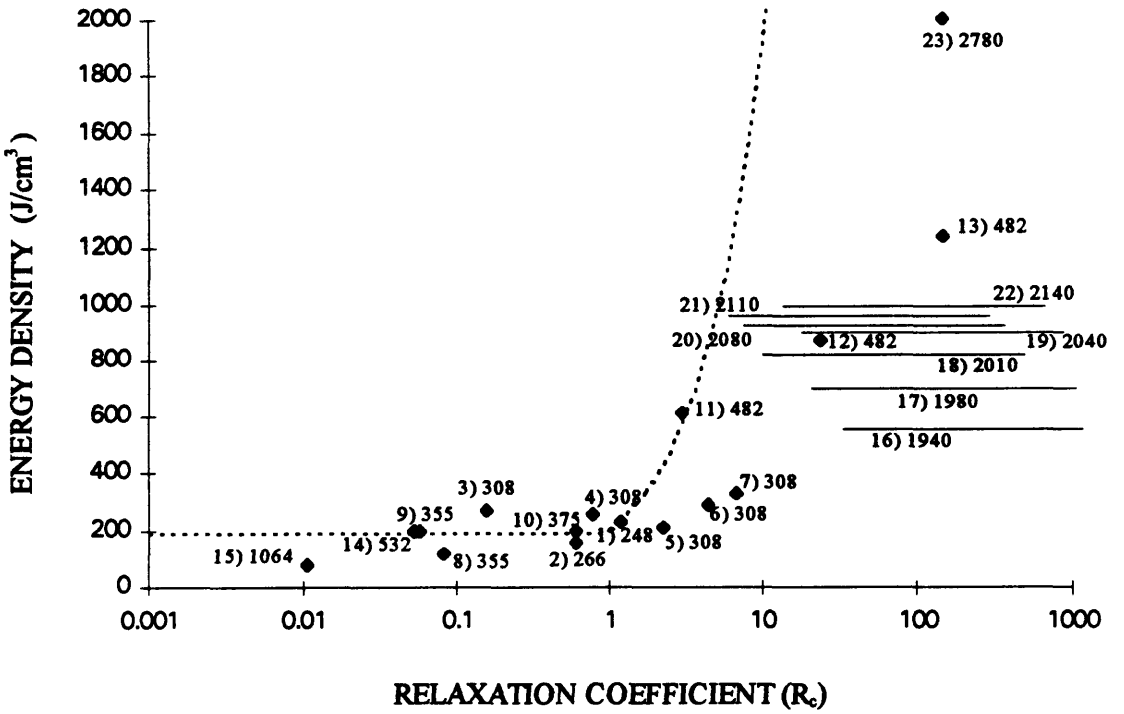

Figure 2-5a. Data from the literature, covering a wide array of wavelengths, supports the model of inertially confined ablation for aorta. When the tissue is inertially confined ($R \leq 1$), the energy density needed to initiate ablation is less than 300 J/cm^3. For R >> 1, the pressure build-up decreases and the energy density needed for ablation rises to the vaporization threshold (2500 J/cm^3). Quantitatively, there is an order of magnitude discrepancy between the predicted (R=1) and actual (R=10) transition points marking the end of inertially confined ablation.

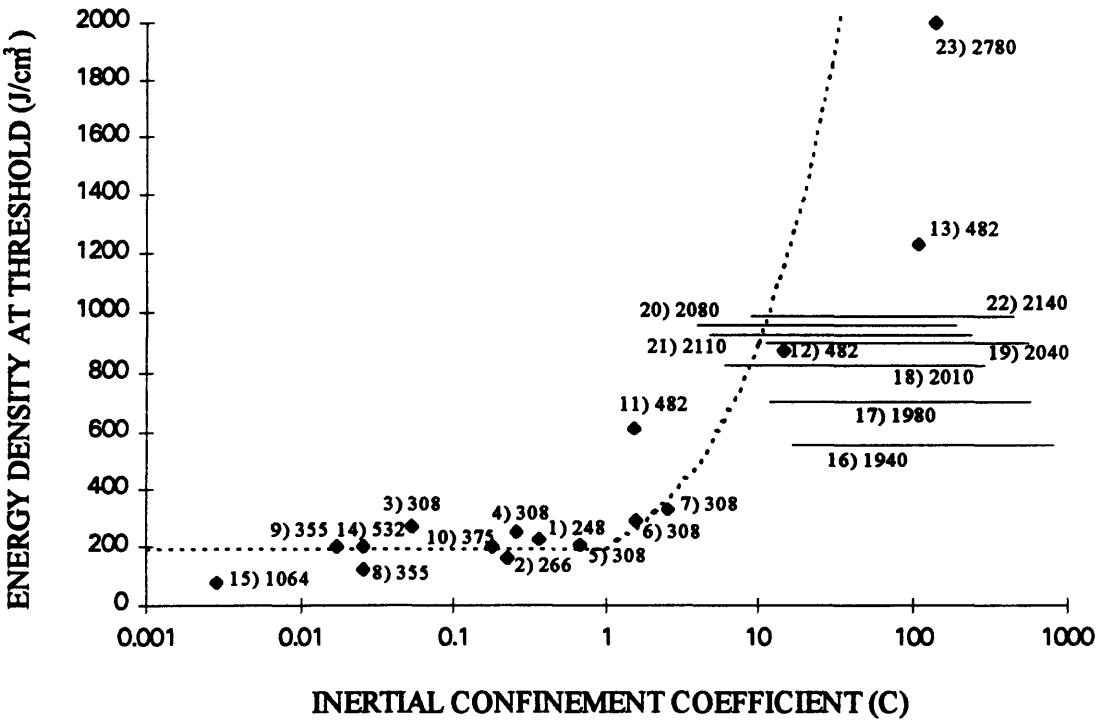

Figure 2-5b. When the data from figure 2-5a is replotted as a function of the inertial confinement coefficient (C), it is in quantitative agreement with the predicted transition value (C=1) for the end of inertially confined ablation.

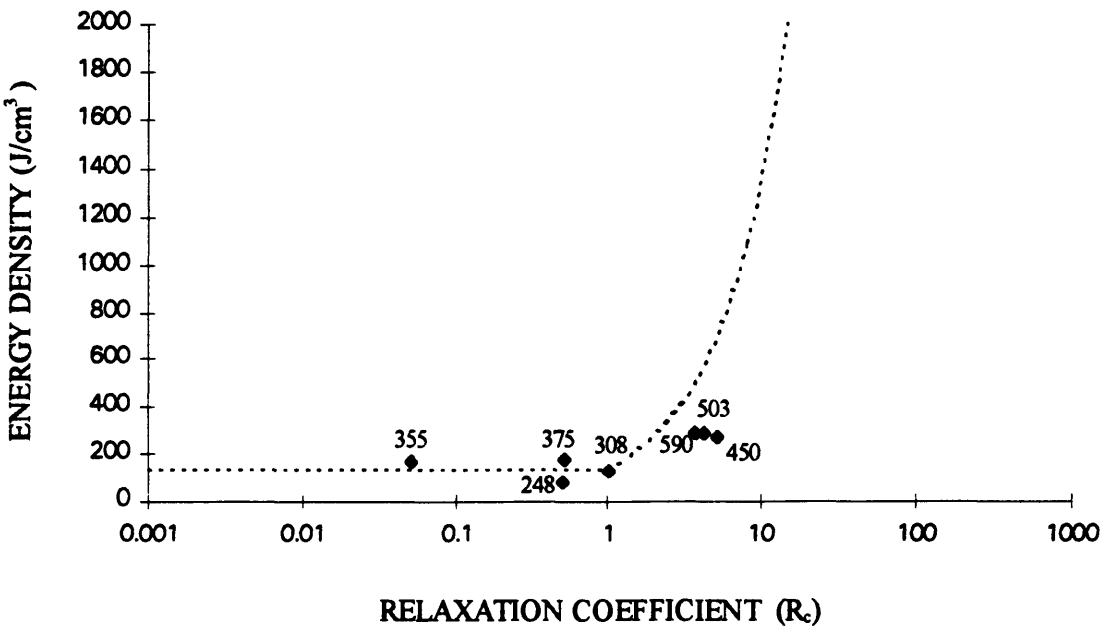

Figure 2-6. Since the acoustic approximation is valid for bone at the breaking strain, the energy density needed to initiate ablation should be governed by the relaxation coefficient (R_c). Data from the literature, including both ultraviolet and visible wavelengths, is consistent with the model of inertially confined ablation for bone.

Table 2-1. Laser Ablation Parameters for Aorta Used to Make Figures 2-5a and 2-5b.

Laser (harmonic)	λ (μm)	τ (μs)	Φ_{th} (J/cm^2)	D (μm)	E_{th} (J/cm^3)	C (τ/τ_m)	R (τ/τ_c)	Fig 5 label	Ref.
KrF	0.248	0.012	0.35	15.4 [a]	227	0.37	1.17	1)	I.[f]
Nd:YAG (4th)	0.266	0.01	0.8 [h]	25	160 [b]	0.23	0.60	2)	II. [c]
XeCl	0.308	0.007	1.8	67 [d]	269	0.054	0.16	3)	III.
		0.035	1.7	67	254	0.26	0.78	4)	IV. [c]
		0.1	1.4	67	209	0.68	2.24	5)	V. [c]
		0.2	1.96	67	292	1.61	4.48	6)	IV. [c]
		0.3	2.2	67	328	2.57	6.71	7)	III.
Nd:YAG (3rd)	0.355	0.01	4.0 [h]	182	120 [b]	0.026	0.08	8)	II. [c]
		0.007	3.6	182	198	0.017	0.06	9)	VI. [c]
Alexandrite (2nd)	0.375	0.1	5.0	250	200	0.18	0.6	10)	VI. [c]
Dye	0.482	1	30.5 [j]	500 [i]	610	1.56	3.0	11)	VII.
		8	43.6	500	872	14.9	24	12)	VII.
		50	61.7	500	1234	111	150	13)	VII.
Nd:YAG (2nd)	0.532	0.015	24 [h]	430	200 [b]	0.026	0.05	14)	II. [c]
Nd:YAG	1.064	0.02	45 [h]	2800	80 [b]	0.003	0.01	15)	II. [c]
Co:MgF_2	1.94	2-100 [g]	5	90 [e]	556	16.6-828	33-1670	16)	VIII.
	1.98	2-100	10	143	699	11.7-585	21-1050	17)	VIII.
	2.01	2-100	15	167	898	11.4-568	18-900	18)	VIII.
	2.04	2-100	22	222	991	9.0-448	14-680	19)	VIII.
	2.08	2-100	25	303	825	6.0-300	10-500	20)	VIII.
	2.11	2-100	37	400	925	4.8-240	7.5-380	21)	VIII.
	2.14	2-100	48	500	960	3.9-196	6-300	22)	VIII.
HF	2.78	0.2	0.4	2	2000	141	150	23)	IX.

Notes and References :

I. [Singleton et al., 1986] II. [Oraevsky et al., 1991] III. [Taylor et al., 1987]
IV. [Taylor et al., 1990] V. [Izatt et al., 1991a] VI. [Izatt, 1991b]
VII. [Prince et al., 1988] VIII. [Schomacker et al., 1991] IX. [Valderrama et al., 1990]

[a] [Furzikov, 1987] [b] Corr. for light scattering [c] atherosclerotic aorta
[d] [Gijsbers et al., 1990] [e] [Curcio and Petty, 1990] [f] human femoral artery
[g] micropulse- macropulse [h] [Esenaliev et al., 1989] [i] [Oraevsky et al., 1988]
[j] Thresholds are scaled by a factor obtained from comparing to a similar experiment [Izatt et al., 1991b] done without fiber optic delivery.

Table 2-2. Laser Ablation Parameters for Bone[a] Used to Make Figure 2-6.

Laser (harmonic)	λ (μm)	τ (μs)	Φ_{th} (J/cm^2)	D (μm)	E_{th} (J/cm^3)	R (τ/τ_c)	Fig 5 label	Ref.
KrF	0.248	0.02	0.5	60 [b]	83	0.50	1)	I
XeCl	0.308	0.1	1.8	146 [b]	123	1.03	2)	II.
Nd:YAG (3^{rd})	0.355	0.007	3.6	218 [b]	165	0.05	3)	II.
Alexandrite (2^{nd})	0.375	0.1	5.0	292 [b]	171	0.51	4)	II.
Dye	0.450	1.5	11.7	432 [b]	270	5.21	5)	II.
Dye	0.503	1.5	15.4	534 [b]	288	4.21	6)	II.
Dye	0.590	1.5	17.3	607 [b]	285	3.71	7)	II.

Notes and References :

I. [Li et al., 1991] II. [Izatt et al., 1991a]

[a] All experiments used beef shank bone except KrF (cat skull)

[b] [Izatt 1991b]

CHAPTER 3

An Introduction to Interferometric Surface Monitoring of Biological Tissue to Study Inertially Confined Ablation

3.1 OVERVIEW

The photomechanical model of inertially confined ablation postulates that, for short pulses, laser-induced stress initiates the ablation process (chapter 2). This model was developed to explain the experimental data from the literature which shows that the energy per unit volume within the tissue at ablation threshold is an order of magnitude less than that required for vaporization. If this energy is deposited in a short period of time, however, it leads to a significant production of stress within the tissue. This is the basis of the photomechanical model of ablation.

This chapter will explore the photomechanical model of ablation in more detail both experimentally and theoretically. Although both the experimental technique and theoretical model developed in this chapter will be replaced in later chapters, this work has an important historical value in demonstrating a viable methodology to study the laser-tissue interaction. In this chapter, a quantitative model, based on the hydrodynamic equation of motion, is developed to predict the laser-induced pressure distribution and the thermal expansion in an irradiated sample as a function of time. The results from this model are compared to experimental results obtained from an interferometric surface monitoring technique. In the experiment, a 7.5 ns pulse of 355 nm light was used to

irradiate bovine shank bone, human meniscus, and an aqueous dye solution under sub-threshold conditions. Interferometric monitoring of the tissue surface was used to determine its motion after laser irradiation. The surface movement of bone was qualitatively consistent with the theoretical predictions of the model. The movement of meniscus and an aqueous dye solution showed additional features which are consistent with the growth and collapse of cavitation bubbles.

This work was orally presented in part at the 13th Annual Meeting of the American Society for Laser Medicine and Surgery, April 18-20, 1993, New Orleans, La. and was published in an article entitled "Interferometric Surface Monitoring of Biological Tissue to Study Inertially Confined Ablation" in the journal *Lasers in Surgery and Medicine* [Albagli, 1994b].

As mentioned above, the results described in this chapter are mostly of historical significance and set the direction for the rest of this thesis. By quantitatively modeling the mechanical response of tissue to short pulses of sub-threshold laser irradiation and comparing the predicted behavior to the experimentally measured behavior, the photomechanical model of ablation can be examined in great detail This chapter demonstrates the usefulness of this methodology, which will be used in the remainder of this thesis. In chapters 4-6, the one dimensional hydrodynamic model developed in this chapter will be replaced by a three dimensional model based on the theory of elasticity. This theory was developed to describe the thermoelastic response of solid material and is more appropriate to our problem than the hydrodynamic formulation which is primarily

used to model liquids and gases. In chapters 7 and 8, an improved interferometric surface monitoring technique is used to collect data on the laser-induced surface movement of different materials, including biological tissues. These results are quantitatively compared to the three dimensional theory and important information on the photomechanical model of ablation is extracted.

3.2 INTRODUCTION

A review of experimental data in the literature reveals that over a wide range of wavelengths in the ultraviolet, visible, and infrared, the energy density needed to initiate ablation of some biological tissues (human aorta, bovine shank bone) with nanosecond duration laser pulses is an order of magnitude less than that required for vaporization [Albagli et al., 1994a; Oraevsky et al., 1991]. One explanation is that vaporization does not occur and that ablation is initiated when laser-induced stresses and stress gradients exceed some threshold value which is related to the mechanical properties of the tissue. This explanation has led to several models in the literature including laser-induced spallation [Dingus and Scammon, 1991a, 1991b] and inertially confined ablation [Albagli et al., 1994a, discussed in chapter 2], where high pressures are created because the tissue does not have time to expand during the short duration of the laser pulse. An experimental study to determine the role of laser-induced pressure and the mechanical properties of biological tissue should yield important information concerning the fundamental mechanisms of short pulsed (nanosecond - microsecond) laser ablation. An understanding of these mechanisms could have important implications in clinical ablation procedures.

The surface movement of tissue immediately after irradiation with a short pulse of laser light is intimately related to the distribution of absorbed energy, the instantaneous pressure generated by this energy, and the mechanical properties of the tissue. Measuring the surface movement for fluences both below and near the threshold can thus reveal information on these important aspects initiating the ablation process. We have developed an experimental technique to measure this movement and applied a physical model to describe it. The model is based on the equation of state and the coupled differential equations for the conservation of mass, momentum, and energy in a continuous medium. Experimentally, there are stringent requirements on the technique used to determine the surface displacement including the ability to measure sub-micron movements on a nanosecond time scale. Since interferometric techniques are well established at measuring small surface motions (e.g. [Barker and Hollenbach, 1972]), we built our surface monitoring tool based on a Michelson interferometer. Results for surface movements after laser irradiation are presented for bovine shank bone, human meniscus and an aqueous dye solution.

3.3 HYDRODYNAMIC EQUATION OF MOTION

In order to determine the role of laser-induced pressure generation in the ablation of biological tissue, a quantitative model of the process must be developed. Given the equation of state of a material, one can develop a hydrodynamic model based on the conservation of mass, momentum, and energy in a continuous media and solve for the pressure and density distributions as a function of time and space. The pressure

distribution is of considerable importance since laser-induced pressures are postulated as the mechanism of ablation. The integrated density distribution is related to the thermal expansion of the surface and can be compared to experimental measurements described in section 3.4.

In the calculation below, let us consider a one dimensional geometry with a space coordinate z ($z = 0$ at the air-tissue interface and increases into the tissue) and a time coordinate t (delta function laser pulse occurs at $t = 0$).

3.3.1 Equation of State

The total internal energy and pressure in a solid medium can each be expressed as the sum of three terms [Zeldovich and Raizer, 1967] :

$$\varepsilon = \varepsilon_c(\rho) + \varepsilon_T + \varepsilon_e$$

$$P = P_c(\rho) + P_T + P_e \qquad [3\text{-}1]$$

The first term in each equation, known as the elastic or cold component, is independent of the temperature. This component is related to the forces of interaction between the atoms in the medium and is only a function of the density. The elastic components are related via:

$$P_c = -\frac{d\varepsilon_c}{dV} \qquad [3\text{-}2]$$

where V is the specific volume (equal to the inverse density). The slope of the cold compression curve is related to the speed of sound in the material :

$$\left[\frac{\partial P_c}{\partial \rho}\right]_T \equiv \frac{1}{\kappa_T \rho} = C_l^2 \qquad [3\text{-}3]$$

where κ_T is the isothermal compressibility and C_l is the longitudinal speed of sound. The second terms in eq. 3-1 represent the thermal components of the internal energy and pressure and are proportional to the temperature :

$$\varepsilon_T = \varepsilon_{T_0} + \varepsilon_L = C_V(T_0 + T_L) \qquad [3\text{-}4]$$

$$P_T = \Gamma \rho \varepsilon_T \qquad [3\text{-}5]$$

where the subscript "L" represents the additional contribution from the laser, C_V is the heat capacity, T is the temperature, and Γ is the Grüneisen coefficient. The last terms in eq. 3-1 are related to the thermal excitation of electrons. These electronic terms can be dropped for temperatures below ten thousand degrees. Therefore the equation of state can be written as :

$$P = P_c(\rho) + \Gamma \rho \varepsilon_T \qquad [3\text{-}6]$$

3.3.2 Conservation Laws And The Acoustical Approximation

The equations representing the conservation laws in a continuous medium can be written in the form [Landau and Lifshitz, 1987] :

$$\frac{\partial \rho}{\partial t} + \vec{\nabla} \cdot \rho \vec{v} = 0 \qquad [3\text{-}7]$$

$$\frac{\partial \vec{v}}{\partial t} + \left(\vec{v} \cdot \vec{\nabla}\right)\vec{v} = \frac{-\vec{\nabla} P}{\rho} \qquad [3\text{-}8]$$

$$\frac{\partial}{\partial t}\left(\frac{\rho v^2}{2} + \rho\varepsilon\right) = -\vec{\nabla} \cdot \left[\rho \vec{v}\left(\varepsilon + \frac{P}{\rho} + \frac{v^2}{2}\right)\right] \qquad [3\text{-}9]$$

where v is the velocity and ε is the total internal energy per unit mass. The first equation, the equation of continuity, is derived by equating the change in density as a function of time with the flow of mass into and out of a fixed volume. The second equation, Euler's equation, is simply a restatement of Newton's law which relates force to acceleration in a continuous media. The conservation of energy, described by the third equation, is derived by equating the time rate of change of the kinetic and internal energy in a volume with the flow of that energy into and out of that volume.

Let us assume that the perturbations in density, internal energy and velocity caused by the laser-tissue interaction are small :

$$\rho(z,t) = \rho_o + \rho_L(z,t) \qquad \rho_o >> \rho_L$$

$$\varepsilon(z,t) = \varepsilon_o + \varepsilon_L(z,t) \qquad \varepsilon_o >> \varepsilon_L \qquad [3\text{-}10]$$

$$v(z,t) = 0 + v_L(z,t)$$

where the subscript zero refers to the initial tissue values and the subscript "L" refers to the small perturbations caused by the laser. In a gas, the conservation equations (eqs. 3-7

through 3-9) can be linearized and solved analytically in the acoustical approximation that the change in density and pressure are small compared to the external density and pressure [Morse and Ingard, 1968]. However in liquids and solids, the acoustic pressure is not small compared to the original pressure of one atmosphere. To lowest order, the ratio of the density change to the initial density can be expressed as [Morse and Ingard, 1968] :

$$\frac{\rho}{\rho_0} = P\kappa_T \qquad [3\text{-}11]$$

where P is the acoustic pressure. In a gas such as air where the compressibility is ~0.7 atm^{-1}, the acoustic pressure must be much smaller than the equilibrium pressure of one atmosphere in order for the density change to be small compared to the original density. In liquids or solids, however, the compressibility is ~10^{-5} to 10^{-6} atm^{-1} so the condition on the density is easily met even for acoustic pressures much larger than the equilibrium pressure.

Using these perturbation assumptions [eq. 3-10] and keeping only the lowest order terms, the equations representing the conservation of mass and momentum (eqs. 3-7 and 3-8) take the form :

$$\frac{\partial \rho_L}{\partial t} + \rho_0 \frac{\partial v_L}{\partial z} = 0 \qquad [3\text{-}12]$$

$$\frac{\partial v_L}{\partial t} + \frac{1}{\rho_o}\frac{\partial P}{\partial z} = 0 \qquad [3\text{-}13]$$

Dropping the two small terms (in velocity squared) and making use of eq. 3-1 and 3-4, the conservation of energy [eq. 3-9] can be written as :

$$\frac{\partial}{\partial t}[\rho\varepsilon_T]+\frac{\partial}{\partial t}[\rho\varepsilon_c]=-\rho_0\frac{\partial v_L}{\partial z}\left[\varepsilon+\frac{P}{\rho_0}\right]-v_L\left[\varepsilon\frac{\partial\rho_L}{\partial z}+\rho_0\left(\frac{\partial\varepsilon_L}{\partial z}+\frac{\partial\varepsilon_c}{\partial\rho}\frac{\partial\rho_L}{\partial z}\right)-\rho_0\frac{\partial v_L}{\partial t}\right] \qquad [3\text{-}14]$$

where eq. 3-13 has been used to obtain the last term. The last four terms may be dropped since each contain two small terms (v_L, ρ_L, ε_L). The second term on the left can be rewritten using eqs. 3-2 and 3-6 :

$$\frac{\partial}{\partial t}[\rho\varepsilon_c]=\varepsilon_c\frac{\partial\rho_L}{\partial t}+\rho_0\frac{\partial\varepsilon_c}{\partial\rho}\frac{\partial\rho_L}{\partial t}=\left[\varepsilon_c+\frac{P_c}{\rho_0}\right]\frac{\partial\rho_L}{\partial t}=\left[\varepsilon_c+\frac{P}{\rho_0}-\Gamma\varepsilon_T\right]\frac{\partial\rho_L}{\partial t} \qquad [3\text{-}15]$$

Substituting eq. 3-15 into 3-14 and making use of eq. 3-12 gives :

$$\frac{\partial}{\partial t}[\rho\varepsilon_T]=\varepsilon_T(\Gamma+1)\frac{\partial\rho_L}{\partial t} \qquad [3\text{-}16]$$

The equation of state (eq. 3-6) can be differentiated to yield :

$$\frac{\partial}{\partial t}[\rho\varepsilon_T]=\frac{1}{\Gamma}\left[\frac{\partial P}{\partial t}-\frac{\partial P_c(\rho)}{\partial\rho}\frac{\partial\rho_L}{\partial t}\right] \qquad [3\text{-}17]$$

Equating eq. 3-16 and 3-17 and using eq. 3-3, one obtains :

$$\frac{\partial P}{\partial t}-\left[C_l^2+\Gamma\varepsilon_T(\Gamma+1)\right]\frac{\partial\rho_L}{\partial t}=0 \qquad [3\text{-}18]$$

where the term in brackets represents the increasing speed of sound with temperature. Since this effect is small (for water and aluminum at 300 K, the second term is 5.9% and 6.0% of the first term respectively), the second term can be dropped to give

$$\frac{\partial}{\partial t}\left[P - C_l^2 \rho_L\right] = 0 \qquad [3\text{-}19]$$

Since the term in brackets is constant in time, it must be equal to its value at time zero, the initial laser-induced pressure distribution P_i. Thus eq. 3-19 can be written as :

$$P(z,t) - C_l^2 \rho_L(z,t) = P_i(z) \qquad [3\text{-}20]$$

Finally, the wave equation for pressure can be found by combining eqs. 3-12, 3-13 and 3-20 :

$$\frac{\partial^2 P(z,t)}{\partial t^2} - C_l^2 \frac{\partial^2 P(z,t)}{\partial z^2} = 0 \qquad [3\text{-}21]$$

3.3.3 Calculation of the Surface Expansion and the Pressure

Assuming the energy deposited by the laser is exponentially distributed in the target, the initial laser-induced pressure distribution can be written from eq. 3-5 as :

$$P_i(z) = \frac{\Gamma \Phi}{D} e^{-z/D} \qquad [3\text{-}22]$$

where Φ is the laser fluence and D is the effective optical penetration depth. Given the initial laser-induced pressure distribution in a medium, the resulting motion can be found

by solving eq. 3-20 and 3-21 subject to the boundary condition (an acoustic mismatch at the air-tissue interface) :

$$P(z,t) = \frac{\Gamma\Phi}{2D}\left[e^{-\left(\frac{z-C_l t}{D}\right)} + e^{-\left(\frac{z+C_l t}{D}\right)} \right] \quad for\ z \geq C_l t$$

$$P(z,t) = \frac{\Gamma\Phi}{2D}\left[e^{-\left(\frac{z+C_l t}{D}\right)} - e^{\left(\frac{z-C_l t}{D}\right)} \right] \quad for\ z < C_l t \qquad [3\text{-}23]$$

These expressions for the pressure represent traveling waves in the medium.

The surface displacement as a function of time, *S(t)*, can be found by integrating the strain:

$$S(t) = -\int_0^\infty \frac{\rho_L(z,t)}{\rho_0} dz = \int_0^\infty \frac{P_i(z) - P(z,t)}{\rho_0 C_l^2} dz \qquad [3\text{-}24]$$

where ρ_0 is the initial density and the minus sign has been introduced so that the direction of the surface displacement variable S is opposite that of the variable z. Performing the integration in eq. 3-24 then gives :

$$S(t) = S_0\left[1 - e^{-t/\tau_c}\right] \quad \text{where } S_0 = \frac{\Gamma\Phi}{\rho_0 C_l^2} \quad \text{and } \tau_c = \frac{D}{C_l} \qquad [3\text{-}25]$$

The parameter S_0, the steady-state surface movement, should be equal to the total thermal expansion. The Grüneisen coefficient can be written as [Zeldovich and Raizer, 1967] :

$$\Gamma = \frac{\beta C_l^2}{C_v} \qquad [3\text{-}26]$$

where C_v is the heat capacity at constant volume and β is the thermal expansion coefficient (note: although the notation for this coefficient is α in the Russian text [Zeldovich and Raizer, 1967], we use the more common symbol β to avoid confusion with the linear expansion coefficient). By expressing the fluence in terms of the laser-induced temperature increase (T_L), the steady-state surface movement can be written as :

$$S_0 = \beta D T_L \qquad [3\text{-}27]$$

which is the expected expression for total thermal expansion.

Although monitoring the surface movement of tissue after laser irradiation can yield important information about the ablation process, there are significant experimental difficulties involved. An estimate for the steady-state movement, S_0, and the characteristic time scale of this movement, τ_c, after tissue irradiation with a 7.5 ns, 355 nm laser pulse is summarized in Table 3-1. This estimate shows expected movements on the order of 1 μm on a time scale on the order of 100 ns. Since we are interested in studying the fundamental mechanisms behind the ablation process for fluences well below ablation threshold, we need to resolve displacements at least an order of magnitude less than the smallest expected displacement at fluence threshold. Thus, we need an experimental technique to measure the surface displacement of laser irradiated tissue with a spatial resolution of less than 100 nanometers and a time resolution of 10 nanoseconds. The technique that I have developed to achieve these values of resolution is based on an interferometer and is described in the next section.

3.4 EXPERIMENTAL TECHNIQUE OF INTERFEROMETRIC SURFACE MONITORING

A schematic of the interferometric surface monitoring technique is shown in figure 3-1. Light from a cw Helium Neon laser (632.8 nm) is electronically shuttered to a 6 millisecond pulse duration and passed to a 50/50 beamsplitter in a Michelson interferometer. In the reference arm, a 5 cm lens focuses the light onto a quartz flat. The 4% reflection from the surface of the quartz flat is recollimated by the lens and travels back toward the beamsplitter. The quartz plate is adjusted so that the reflected light is both collinear and coincident with the incident light. In the sample arm of the interferometer, the quartz flat is replaced by the target to be measured (e.g. biological tissue). An additional filter is placed in the reference arm to compensate for the lower specular reflection in the sample arm. The light from both arms of the interferometer is combined by the beamsplitter and directed towards a photomultiplier tube (RCA 1P28). An interference filter centered at 632.8 nm is used to filter out stray light. The signal from the photomultiplier tube is captured and digitized by a 500 MHz transient digitizer (Tektronix model 7912AD) and transferred to a computer for analysis.

The pump light in this experiment (i.e. the light of sufficient intensity to cause thermomechanical changes in the sample) is supplied by a frequency tripled Q-switched Nd:YAG laser (wavelength = 354.7 nm, pulse duration = 7.5 ns, beam diameter = 6 mm). Since the pulse duration of 7.5 ns is much less than the time scale of the movement, τ_c = 75-230 ns (see eq. 3-25, Table 3-1), we are in the inertially confined regime and our

assumption of instantaneous energy deposition in the theoretical model is valid. This light is passed through a 3 mm aperture and reimaged to a 750 μm spot on the target (concentric with the 100 μm HeNe probe beam). The laser energy is controlled via a half-wave plate and Glan polarizing prism. A portion of the beam is directed to a laser beam analyzer (Big Sky Software) for monitoring and to the photomultiplier tube for timing. A pulse generator (Stanford Research Systems, DG535) serves as the master clock and controls the triggering of the Nd:YAG laser, electronic shutter, and transient digitizer.

After the pump light is absorbed in the target, the subsequent pressure distribution will cause the surface of the target to move. For a surface movement equal to a quarter wavelength of the probe beam (158 nm), the path length difference in the two arms of the interferometer will change by a half wavelength, causing a change in the interference pattern in the photomultiplier tube (e.g. from total constructive interference to total destructive interference). Thus, a constant velocity movement of the surface will create a sinusoidal voltage signal where each full period (fringe) represents a surface displacement of 316 nm. This should be born in mind when interpreting the data.

The three targets used in this experiment were bovine shank bone, human meniscus, and an aqueous dye solution. The bovine shank bone samples were obtained no later than 2 days post-mortem. A razor blade was used to remove surface refuse and the periosteum from the cortical surface. The samples were then polished in a three step process which ended with a 0.05 μm grit alumina oxide polish. Samples were kept refrigerated in a moist environment until use. Human meniscus samples were obtained no

later than 3 days post-mortem. Samples were kept frozen at -80°C until use. During use, the tissue was placed in a Petri dish filled with saline. The surface of the tissue, which was just above the surface of the saline, was kept dry by using tissue paper to absorb any water on the surface. The aqueous dye solution consisted of water and 7.53 g/L of $FeCl_3$. This concentration was chosen to give a 200 μm penetration depth (which was measured with a spectrophotometer).

3.5 RESULTS

With proper alignment of the interferometer, significant single shot interference fringes were obtained from the specular reflections from all three targets (bone, meniscus, and an aqueous solution). The amplitude of the signals of 30-50 mV was more than an order of magnitude greater than the noise (< 3 mV). Interference fringes were always present on a millisecond time scale due to random vibrations throughout the experimental setup. Since all experiments were performed on a time scale of less than 10 μs, the only effect of these fringes was to determine the initial phase of the interference. All results are from single pulses of sub-ablation threshold laser light.

3.5.1 Bone

Some experimental results for beef shank bone are shown in figure 3-2a and 3-2b. The timing pulse (a portion of the 355 nm pump pulse directed into the detector to indicate the exact time of the laser-tissue interaction) can be seen as the first downward spike at 180 ns in both figures. Figure 3-2a shows the surface movement of the bone after

irradiation with 4.3 mJ/mm^2. The flat signal for the first 180 ns shows that there is no surface movement on this time scale due to any vibrations before the pump pulse strikes the tissue. The change in signal amplitude after the timing pulse indicates surface motion caused by the laser-tissue interaction. By 1.2 μs, all motion has stopped and the surface remains at its new equilibrium level. Experiments verify that the surface remains at this new equilibrium for at least 20 μs, as theoretically expected (surface recession due to thermal cooling takes place on a millisecond time scale). At a fluence of 7.2 mJ/mm^2 (figure 3-2b), a similar but greater motion is seen. Note that this fluence is well below the ablation threshold (see Table 3-1). Depending on the initial path length difference in the two arms (which changes from shot to shot due to vibrations in the system), surface movement may lead to an initial increase (figure 3-2a) or decrease (figure 3-2b) in signal voltage.

The data collected with the interferometric surface monitoring technique has been compared to the theoretical surface movements derived in section 3.3.3. For beef shank bone, the surface movement was qualitatively consistent with the predictions. Since the total movement for these sub-ablation threshold fluences was less than one half fringe, this movement can only be estimated. For this experiment, the PMT voltage ranged from 25-60 mV. Thus a voltage change of 35 mV represents one half fringe of motion which corresponds to 158 nm. In figure 2-2a, the signal starts at 46 mV, moves up the maximum 60 mV, and then back to 58 mV which corresponds to 72 nm of motion (16/35 times 158 nm). In figure 2-2b, the signal starts at 48 mV, moves down to the minimum 25 mV and then back to 29 mV which corresponds to 122 nm of motion (27/35 times 158 nm). The

predicted motion is 120-200 nm for Φ = 4.3-7.2 mJ/mm^2 (see eq. 3-25 and Table 3-1). The time scale for motion, τ_c (eq. 3-25), can be estimated from figures 3-2a and 3-2b and is found to be approximately equal to 150 ns. Thus both the time scale and the amplitude of the surface movement are qualitatively consistent with theoretical predictions (given in Table 3-1).

3.5.2 Meniscus and Water

Figure 3-3a shows the surface movement of meniscus after irradiation with 8.6 mJ/mm^2. The downward spike at 340 ns is the timing pulse. As with bone, the surface movement starts immediately after the pump pulse. A half fringe of motion (158 nm) has occurred within 70 ns. The data shows a surprising and unexpected phenomenon. In figure 3-3a, the width of the fringes increases between 0.4-1.1 μs but then decreases between 1.1-2.0 μs. Thus the surface decelerates until 1.1 μs and then begins to accelerate again. The fact that the signal voltage increases after 1.1 μs, instead of continuing to decrease to the minimum level of 37 mV, reveals that the surface motion has changed direction.

Using the fringe pattern in figure 3-3a, the motion of the surface for meniscus was determined as a function of time after the absorption of the laser pulse and is plotted in figures 3-3b. Based on the argument put forth in the previous paragraph, the motion after 760 ns (1100 - 340) is represented as a contraction of the surface. The peak expansion at this fluence was nearly 800 nm. Note that the fluence used in this experiment is significantly lower than the ablation threshold.

At a lower pump fluence of 4.3 mJ/mm^2, a similar but lesser motion is detected (figure 3-4a). This data, as well as all meniscus data, also has a direction reversal in the surface movement. For this fluence, this point occurs at 0.85 μs. The temporal location of this turning point was very reproducible at a given fluence and increased as the fluence increased. The actual surface motion as a function of time is shown in figure 3-4b. For this case, the peak expansion was nearly 500 nm.

The experimental results for the surface movement of meniscus were not consistent with the predictions from the model. The predicted characteristic time scale of movement, τ_c, should be ~ 230 ns (Table 3-1) but the actual movement continued for several microseconds. The surface level was predicted to approach its new equilibrium value exponentially (eq. 3-25) but instead showed periods of deceleration and acceleration with a change in direction between the two.

In order to determine the source of this anomaly, the experiment was repeated on an aqueous dye solution ($FeCl_3$ dissolved in water). Since meniscus is roughly 70 % water and 30 % structural protein, the results from this experiment should show which of these components is responsible for this unexpected deviation. The surface motion of the aqueous dye solution was very similar to the motion of the meniscus tissue. Figure 3-5a shows the motion of this solution after irradiation with 9 mJ/mm^2. The pump pulse is barely visible on this time scale but can be seen as the 4 mV shoulder at 0.46 μs. After three fringes of motion (950 nm), there is a turning point at 2.1 μs followed by at least

two more fringes of motion. As with meniscus, the turning points occurred in all the data and the temporal locations were reproducible at a fixed fluence, and increased with increasing fluence. Using the data in figures 3-5a, the surface motion of the aqueous dye solution was determined as a function of time and is plotted in figures 3-5b.

The experimental results for the surface movement of the aqueous dye solution showed the same anomalies as the data from the meniscus samples, implying that the source of this discrepancy is the water itself. The predicted time scale of movement, based on parameters accurately known for water, is 133 ns but the actual movement continued for many microseconds. In addition, the total displacement was significantly greater than the theoretically predicted value. These deviations between experiment and theory are caused by cavitation phenomena and are discussed in the next section.

3.6 CAVITATION

Cavitation is a dynamic phenomena related to the growth and collapse of cavities within a liquid [Knapp et al., 1970]. If a tensile wave is propagated through a liquid, the liquid will rupture and cavities will form if the amplitude of the stress exceeds the tensile strength of the liquid. The dynamics of cavities created by this process will be determined by the external liquid pressure, surface tension at the cavity-liquid interface, and internal vapor pressure of the cavity. After the stress wave has passed, the external pressure returns to normal and the cavitation bubbles will collapse. It is important to note that the collapse of cavitation bubbles near a solid surface have been found to damage all types of

solids including metal, rubber, plastic, glass, quartz, concrete, and others [Knapp et al., 1970].

We propose that the presence of these additional features in the data for the aqueous dye solution is the result of cavitation. The laser-induced temperature and pressure can be estimated from the steam tables [Haar et al., 1984]. For the range of fluences in the experiment, the predicted temperature rise is 5-20^{0}C and the predicted pressure rise is 25-130 bars. Half of this peak pressure (compressive stress) will generate a tensile stress as the wave is reflected from the acoustic mismatch at the air-solution interface. Since cavitation can be induced in water with tensile stresses as small as 9 bars [Knapp et al., 1970], it should be present in our experiment. In fact, under experimental conditions similar to ours, cavitation bubbles have been recorded with strobe photography after irradiation with an 8 ns laser pulse [Paltauf et al., 1992]. At similar peak energy densities, the formation and growth of cavitation bubbles was photographed on a sub-microsecond time scale. Since water is highly incompressible, the appearance of bubbles with negligible density must manifest itself as an expansion of the surface. The manifestation will take place through pressure and density waves and thus will operate on a time scale determined by the spatial extent of the phenomenon and the speed of sound (~ 100 ns). Thus initial surface motion will be caused by a combination of thermoelastic expansion and the growth of cavitation bubbles.

The phenomena of cavitation is also consistent with the existence of the turning points in the data. The time scale of the collapse for an empty bubble in water was first calculated by Lord Rayleigh [1917] and can be written in the form [Knapp et al., 1970] :

$$t_c \cong 0.92 R_0 \sqrt{\frac{\rho}{P_0}} \qquad [3\text{-}27]$$

where R_0 is the initial radius of the bubble, and P_0 is the initial surrounding pressure. Assuming an initial radius of 10-50 μm (an estimate consistent with strobe photography [Paltauf et al., 1992]), the predicted time scale for the collapse of the bubble (using eq. 3-27) is 1-5 μs. Our experimental data shows 1-5 μs of movement after the apparent inflection points. As with the growth of the cavitation bubbles, their collapse will produce pressure and density waves through the material which will manifest themselves as a downward surface movement on a time scale of ~ 100 ns.

After the collapse of the cavitation bubbles, the height of the surface will return to the originally predicted steady-state value S_0. The time scales for surface tension, gravity, and thermal cooling to affect the surface level are 30 μs, 100 μs, and 100 ms, respectively, therefore none of these will have a significant effect on time scales of less than 10 μs. Thus it should be possible to measure the equilibrium value S_0 after the collapse of the cavitation bubbles. All our data indicates that the number of fringes after the turning point is always less than the number before it (e.g. see figure 3-5a). Although more data is needed in this time regime to make a quantitative comparison, the difference between the

two roughly corresponds to the predicted surface movement of a few hundred nanometers (figure 3-5b).

The data from the meniscus tissue was very similar to that from the aqueous dye solution. As mentioned above, the same additional features (i.e. the long time scale of surface movement and the change in direction of that movement) were present in both cases. This implies that cavitation is taking place within the meniscus tissue. Using the penetration depth at 355 nm for meniscus from Table 3-1 and the fluence used in figure 3-3b, the predicted laser-induced temperature increase can be estimated by :

$$T_L = \frac{1}{\rho C_V}\frac{\Phi}{D} \approx 6\ ^{0}C \qquad [3\text{-}28]$$

Thus, as with the aqueous dye solution, it is the tensile stress which is causing cavitation. Ultrasound-induced cavitation phenomena within biological tissue has been reported for over 30 years [Hynynen, 1991]. Other cavitation phenomena, where significant heating takes place, has been studied in the laser ablation of arterial tissue in saline [van Leeuwen et al., 1992] and blood fields [de la Torre and Gregory, 1992; van Leeuwen et al., 1993] above the tissue. The results from our study indicate that cavitation within the meniscus tissue itself, under the conditions where laser-induced tensile stresses are produced but no significant heating takes place, plays an important role in the events initiating the ablation process.

3.7 CONCLUSIONS

This chapter has demonstrated that the technique of interferometric surface monitoring can be used to study the photomechanical model of ablation of biological tissue. The technique uses an interferometer to measure the surface movement of tissue after it has been irradiated with a short pulse of laser light. The results are compared to a theoretical model which establishes the relationship of this movement to important optical and mechanical properties of the tissue. A laser interferometric technique has been developed to measure these surface movements. The surface movement of bone, meniscus, and an aqueous dye solution were monitored after irradiation with a 7.5 ns, 355 nm pump pulse. The results for bone were qualitatively consistent with the theoretical model presented in this paper, showing sub-micron movements on a one hundred nanosecond time scale. The surface movement of the meniscus tissue and the aqueous dye solution showed additional effects which are consistent with cavitation phenomena. This data points to the important role of cavitation, within the tissue itself, in the ablation process of meniscus and perhaps other soft biological tissues.

This chapter establishes an important methodology for quantitatively examining the photomechanical model of laser ablation of biological tissue. Significant improvements are needed, however, to accomplish this. First, the theory must be extended to describe the behavior of solids in three dimensions instead of liquids in one dimension. Second, the experimental technique must be improved in two ways. In order to get quantitative data on bone, the spatial resolution must be reduced to $\sim$ 10 nm. As shown in this chapter, counting fringes is not adequate when the total movement represents less than one fringe.

Second, the experimental apparatus needs to be modified so that it is sensitive to the direction of movement as well as the magnitude. The extension of the theory and improvement in the experiment are discussed in the upcoming chapters.

Table 3-1. Estimate of surface displacement parameters for tissue after irradiation with a short pulse of 355 nm light at the threshold fluence.

Parameter	Beef Shank Bone (Sample "Hard" Tissue)	Human Meniscus (Sample "Soft" Tissue)
D	220 μm [a]	350 μm [b]
C_l	3000 m/s [c]	1500 m/s [d]
τ_c	**75 ns**	**230 ns**
Γ	~ 0.5	~ 0.1 [d]
Φ_{th}	36 mJ/mm^2 [e]	30 mJ/mm^2 [b]
ρ	2000 kg/m^3 [c]	1000 kg/m^3
S_0	**~ 1.0 μm**	**~ 1.3 μm**

a [Albagli et al., 1994a]

b [Banish, 1993]

c [Cowin, 1989]

d estimated to be the same as water

e [Izatt et al., 1991a]

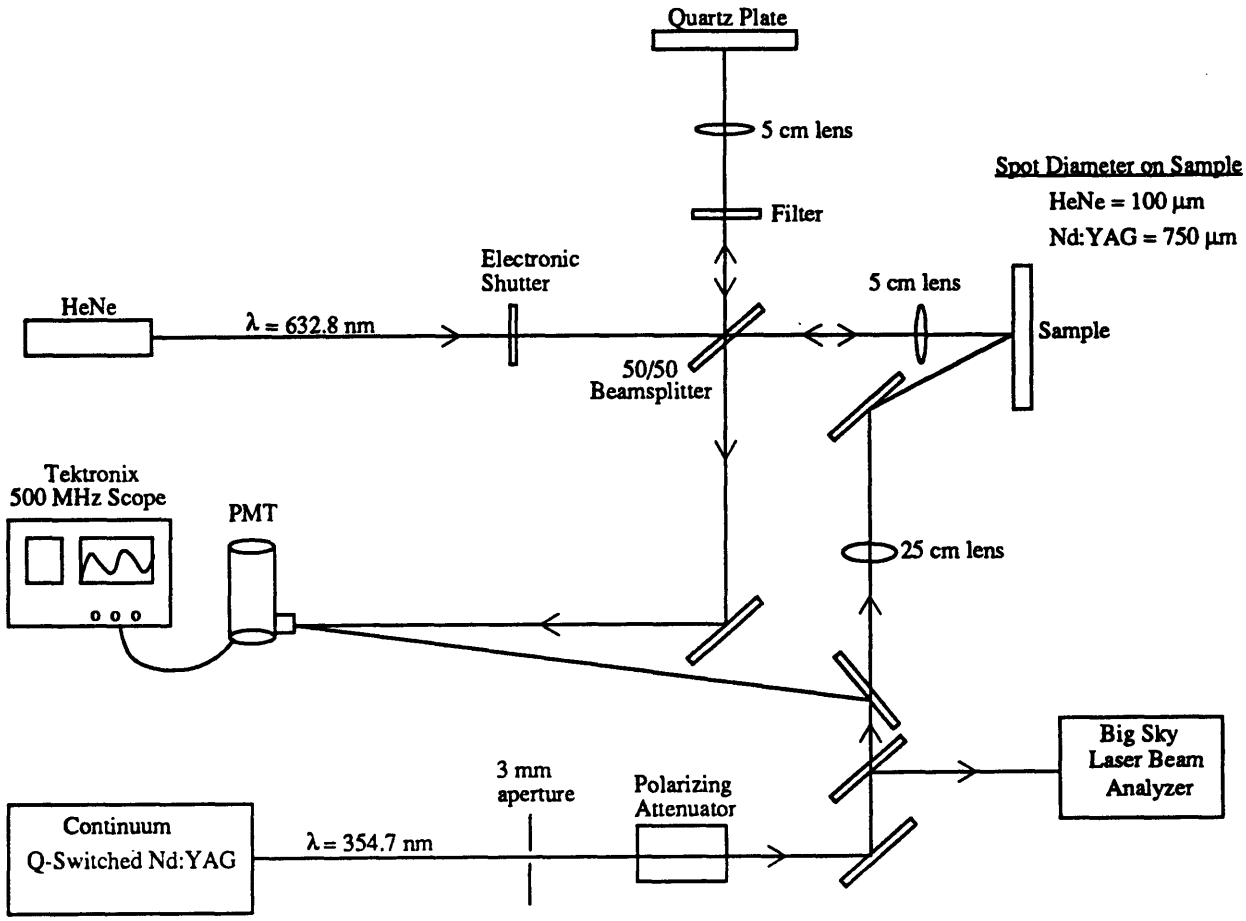

Figure 3-1. A schematic of the interferometric surface monitoring technique. This pump-probe technique uses a 7.5 ns, 355 nm pulse of light to excite the tissue sample and a Michelson interferometer to measure the laser-induced tissue surface movement.

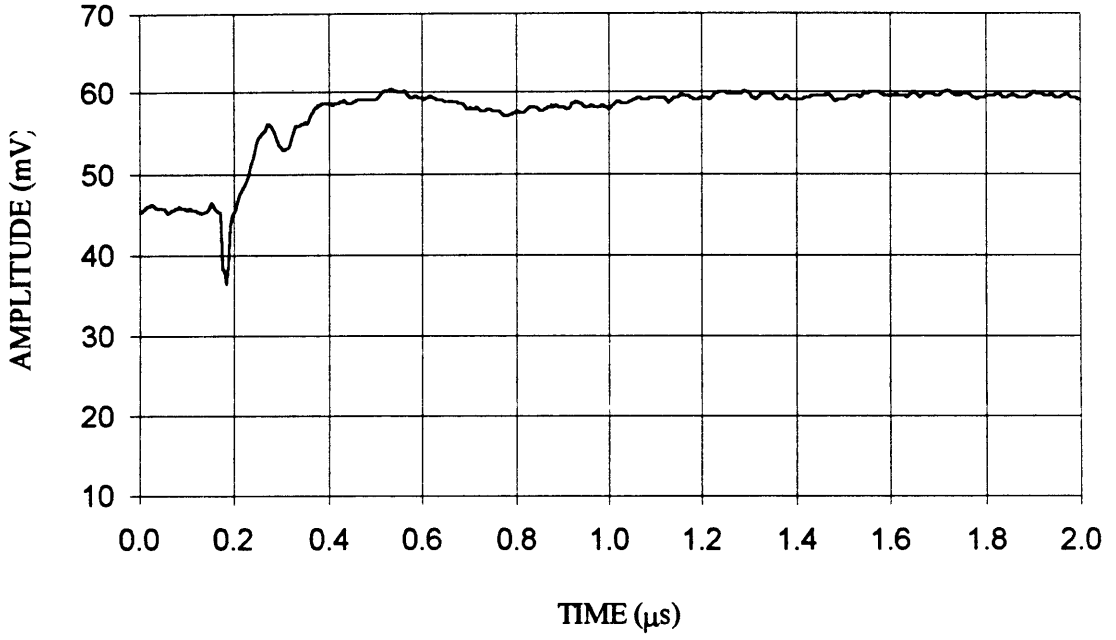

Figures 3-2a. The output signal from the PMT shows a constant voltage until a 4.3 mJ/mm^2, 355 nm pulse strikes the bone surface at 180 ns. After absorbing the laser pulse, the surface expansion causes a change in the signal voltage. It is calculated that this change represents a movement of 72 nm with a time constant of 150 ns, in qualitative agreement with theoretical predictions.

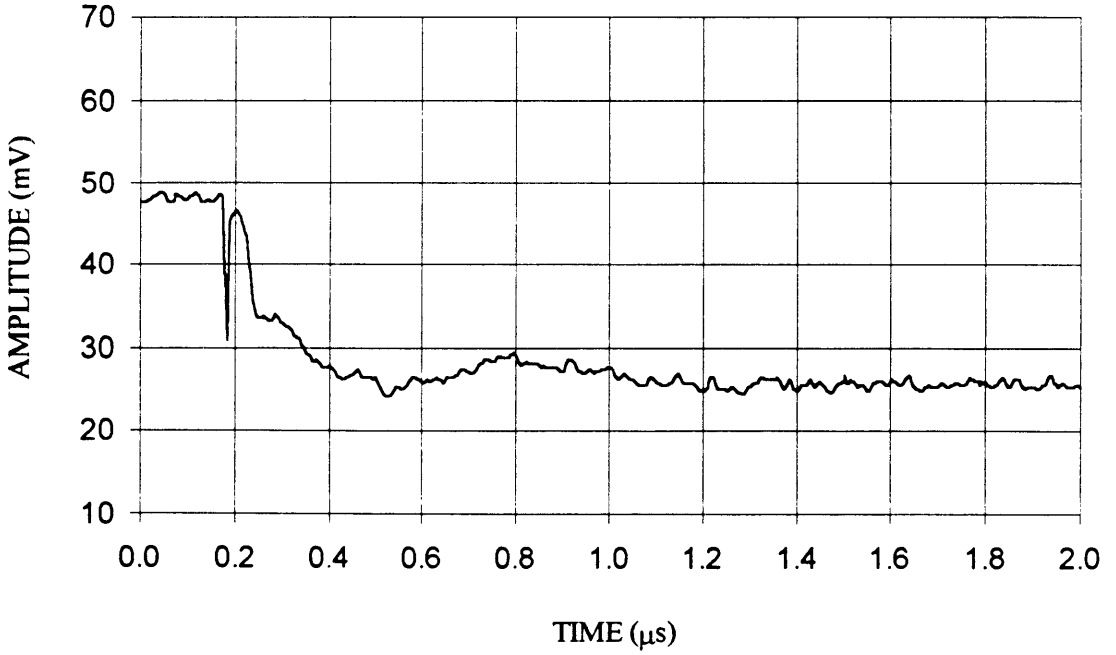

Figures 3-2b. After irradiation with a 7.2 mJ/mm^2 pulse of light, the surface of the beef shank bone moves 122 nm. By 1.2 μs, the surface has reached a new equilibrium position.

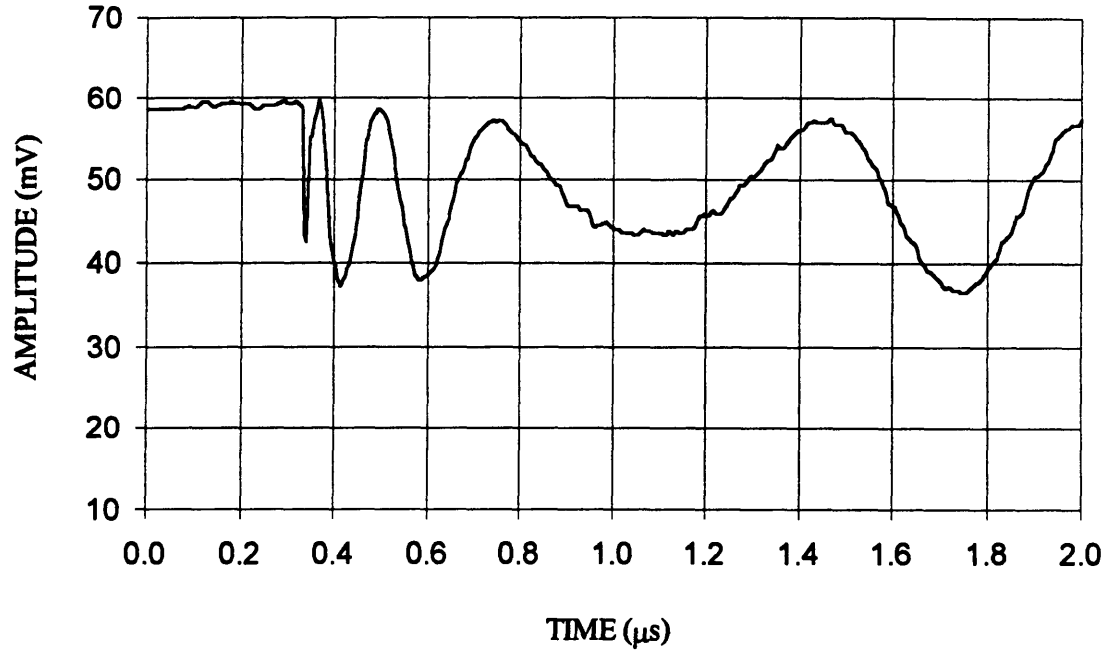

Figure 3-3a. The interference fringes caused by the surface movement of meniscus after irradiation with 8.6 mJ/mm^2 of 355 nm light fired at 340 ns. The target expands until 1.1 μs and then appears to contract. This behavior is not consistent with the theoretical model described earlier

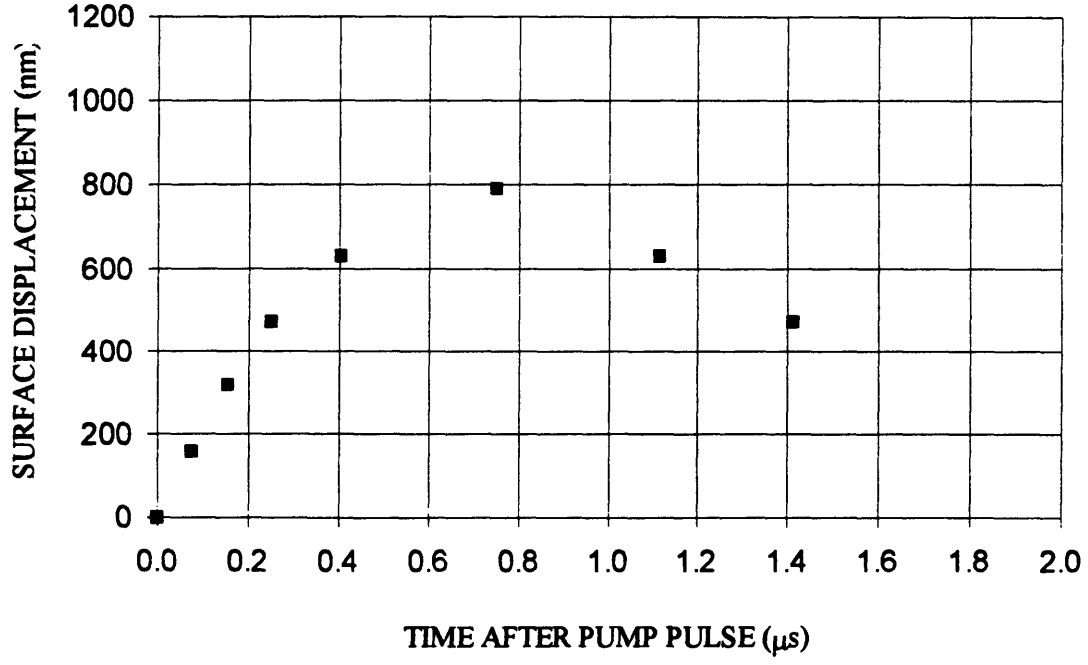

Figure 3-3b. Since each interference fringe corresponds to a half-wavelength of motion (316 nm), the data presented in figures 3-3a can be converted to the actual surface movement as a function of time as plotted here.

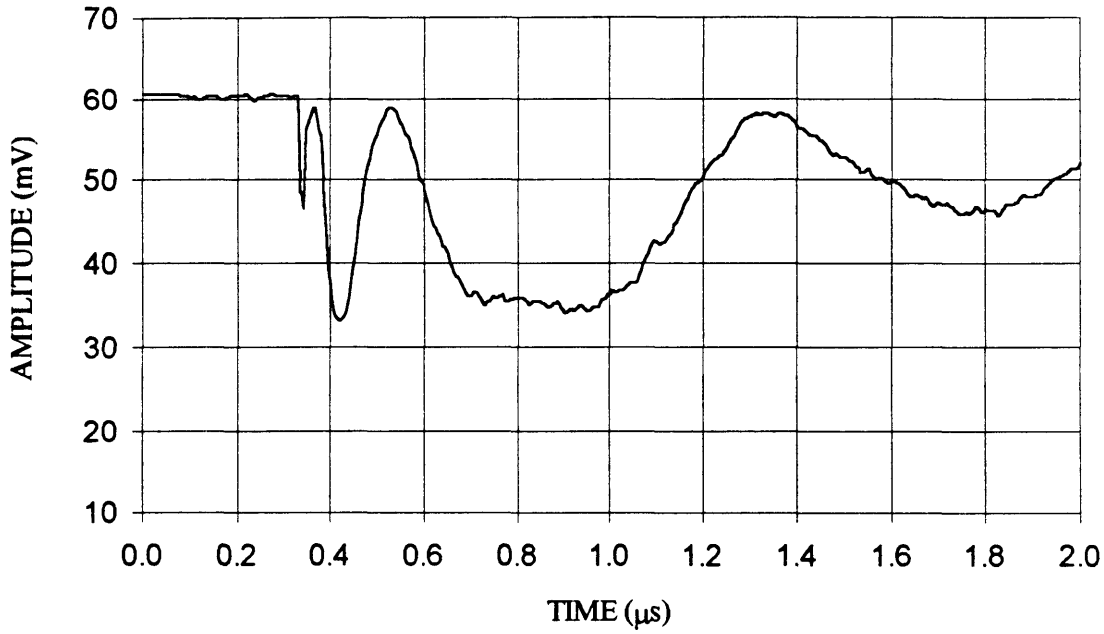

Figure 3-4a. The interference fringes caused by the surface movement of meniscus after irradiation with 4.3 mJ/mm^2 of 355 nm light fired at 340 ns. The target expands until 850 ns and then appears to contract. This behavior is not consistent with the theoretical model described earlier.

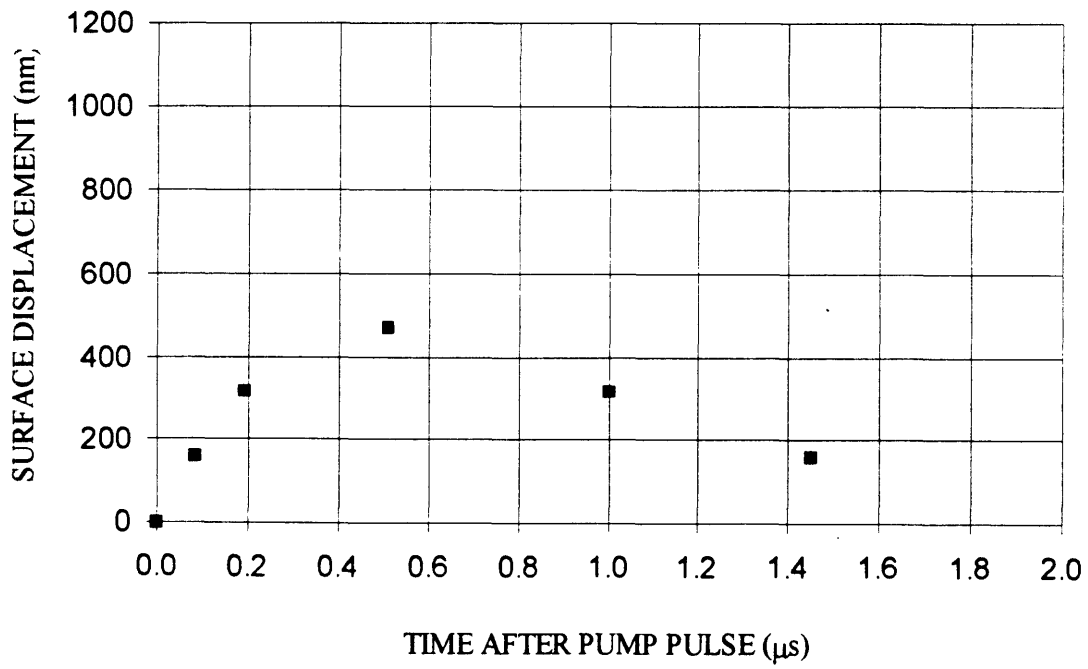

Figure 3-4b. Since each interference fringe corresponds to a half-wavelength of motion (316 nm), the data presented in figures 3-4a can be converted to the actual surface movement as a function of time as plotted here.

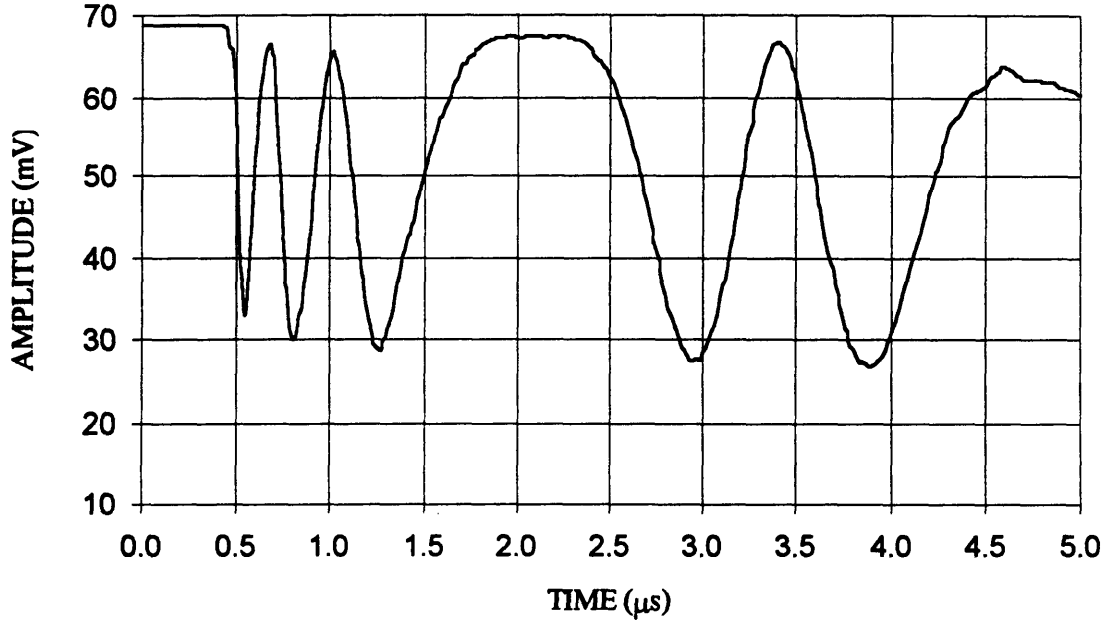

Figure 3-5a. The interference fringes caused by the surface movement of an aqueous solution after irradiation with 9.0 mJ/mm^2 of 355 nm light fired at 460 ns. The target expands until 2.1 μs and then appears to contract. This behavior is not consistent with the theoretical model described earlier

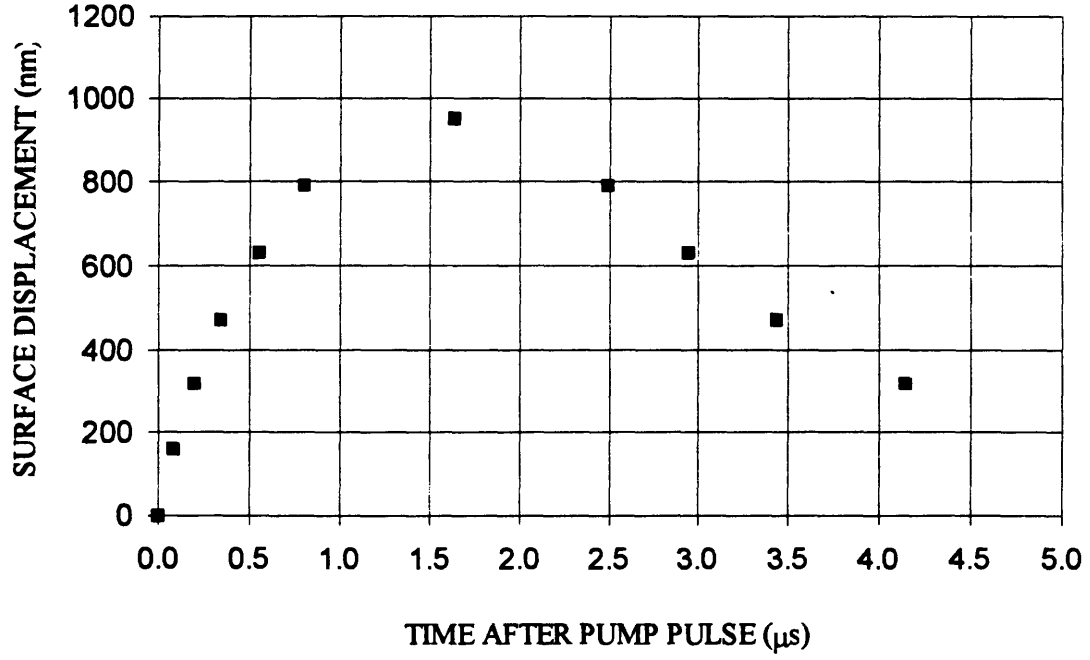

Figure 3-5b. Since each interference fringe corresponds to a half-wavelength of motion (316 nm), the data presented in figures 3-5a can be converted to the actual surface movement as a function of time as plotted here.

CHAPTER 4

The Theory of Elasticity and the 1D Solution to the Thermoelastic Wave Equation

4.1 OVERVIEW

In order to evaluate the photomechanical model of ablation, a quantitative model of the tissue response to the laser irradiation must be developed. In the previous chapter, a model based on the hydrodynamic equations of motion was developed. In this chapter, the theory of elasticity will be used to develop a model, based on the thermoelastic wave equation, which is more appropriate for biological tissue.

A full time dependent solution of the thermoelastic wave equation has been obtained for the laser-induced heating of a sample in a one dimensional geometry. This solution shows that the sample will undergo thermoelastic expansion and the surface will exponentially approach a new equilibrium position. The time constant of this expansion is governed by the ratio of how deeply the laser light penetrates to the speed of sound in the sample. Although this solution has the same functional form as the hydrodynamic solution obtained in the last chapter, there is an important additional multiplicative constant. The stress distributions predicted by the two models also have similar forms but differ by this same constant. In the special case where the sample is a liquid, this constant is unity and the two models are in agreement. For solids and biological tissue, however, the value of

this constant ranges from 0.33 to 1. Therefore to quantitatively model the thermoelastic response of biological tissue, it is essential to use a model based on the theory of elasticity.

The predictions from this model also show that the laser-induced stress distribution, which initially is entirely compressive, evolves into a traveling bipolar wave with both tensile and compressive components. Although the formation of tensile stresses is an important ingredient in the photomechanical model, the spatial location of these tensile stresses is not consistent with experiment observations of material rupture. This inconsistency will be resolved in chapters 5 and 6 when the full three dimensional nature of the problem is considered.

4.2 INTRODUCTION

In the previous chapter, a theoretical model based on the hydrodynamic equations of motion was developed in order to calculate the response of a material to the absorption of a short pulse of laser light. This model was based on the equation of state of the material and the conservation of mass, momentum, and energy in a continuous media. Although this theoretical framework is appropriate for fluids (liquids and gases), the theory of elasticity was developed specifically for solids. The basic equations in this framework were established by Cauchy and Poisson in the 1820's and are reviewed in section 4.3. In this framework, the scalar quantity of pressure is replaced by the rank 2 stress tensor. The strain, which is related to derivatives of the displacements, is also established as a rank 2 tensor. Using thermodynamics and the conservation of energy, the

stress tensor can be expressed in terms of the strain tensor. The thermoelastic wave equation is derived by combining the stress-strain relation with Newton's law.

In section 4.4, the thermoelastic wave equation is solved in a one dimensional geometry. It is assumed that the laser pulse is a delta function in time and that it creates an exponentially decreasing temperature profile within the sample with a 1/e depth given by D, the optical penetration depth. The solutions for the laser-induced surface movement and the stress distribution are compared to the results from the previous chapter in section 4.4.4

4.3 THEORY OF ELASTICITY

The review of the theory of elasticity in this section comes mainly from the text by Landau and Lifshitz [1986].

4.3.1 Strain Tensor

Let x_i and x_i' be the coordinates of a point in a solid before and after deformation. Then

$$u_i = x_i' - x_i \qquad [4\text{-}1]$$

is defined as the displacement vector. Specifying the displacement vector as a function of coordinates completely determines the deformation of the body. Consider two points in a solid. The distance between them before and after deformation is :

$$dl = \sqrt{dx_1^2 + dx_2^2 + dx_3^2} \qquad dl' = \sqrt{dx_1'^2 + dx_2'^2 + dx_3'^2} \qquad [4\text{-}2]$$

Writing $$du_i = \frac{\partial u_i}{\partial x_k} dx_k \qquad [4\text{-}3]$$

the distance between two points after deformation can be written as :

$$dl'^2 = dl^2 + 2\frac{\partial u_i}{\partial x_k} dx_i dx_k + \frac{\partial u_i}{\partial x_k}\frac{\partial u_i}{\partial x_l} dx_k dx_l \qquad [4\text{-}5]$$

where repeated indices indicate summation. The second term on the right can be written in the symmetric form

$$2\frac{\partial u_i}{\partial x_k} dx_i dx_k = \left(\frac{\partial u_i}{\partial x_k} + \frac{\partial u_k}{\partial x_i}\right) dx_i dx_k \qquad [4\text{-}6]$$

Therefore eq. 4-5 can now be written in the form :

$$dl'^2 = dl^2 + 2u_{ik} dx_i dx_k \qquad [4\text{-}7]$$

$$u_{ik} = \frac{1}{2}\left(\frac{\partial u_i}{\partial x_k} + \frac{\partial u_k}{\partial x_i} + \frac{\partial u_l}{\partial x_i}\frac{\partial u_l}{\partial x_k}\right) \qquad [4\text{-}8]$$

is the strain tensor. For small deformations, the last term can be neglected. It can be shown that the sum of the diagonal components of the strain tensor is equal to the relative volume change.

4.3.2 Stress Tensor

The total force on a small portion of a body can be described by a volume integral :

$$T_i = \int F_i dV \qquad [4\text{-}10]$$

If each component of the force per unit volume can be written as the divergence of a vector, one can use the divergence theorem to transform the volume integral into a surface integral. Since the total force can be written as a volume integral of a vector, the force per unit volume vector must be written as the divergence of a rank 2 tensor. Thus

$$F_i = \frac{\partial \sigma_{ik}}{\partial x_k} \qquad and \quad \int F_i dV = \oint \sigma_{ik} df_k \qquad [4\text{-}11]$$

where σ_{ik} is called the stress tensor. As can be seen from eq. 4-11, the i^{th} component of the force on the surface element df is given by $\sigma_{ik} df_k$.

4.3.3 Relationship of Stress and Strain Tensor

For a reversible process, the change in internal energy can be expressed as :

$$d\varepsilon = TdS - dR \qquad [4\text{-}12]$$

where TdS is the heat acquired by the unit volume and dR is the work done by the internal stresses. The work done by the internal stresses can be found by multiplying the force by the displacement and integrating over the volume :

$$\int \delta R dV = \int \frac{\partial \sigma_{ik}}{\partial x_k} \delta u_i dV \qquad [4\text{-}13]$$

Integrating by parts and using the definition of the strain tensor (eq. 4-8) yields :

$$\delta R = -\sigma_{ik} \delta u_{ik} \qquad [4\text{-}14]$$

Substituting this expression into the thermodynamic relation described by eq. 4-12 gives :

$$d\varepsilon = TdS + \sigma_{ik}du_{ik} \qquad [4\text{-}15]$$

which is the fundamental thermodynamic relation for deformed bodies. Expressing this in terms of the Helmholtz free energy, F = ε - TS, yields :

$$dF = -SdT + \sigma_{ik}du_{ik} \qquad and \quad \sigma_{ik} = \left(\partial F/\partial u_{ik}\right)_T \qquad [4\text{-}16]$$

Therefore, the relationship between the stress and strain tensors can be determined if the free energy as a function of the strain tensor is known.

Consider an expansion of the free energy in a power series of the strain tensor. Let us consider as the initial state a solid at an ambient temperature T_a with no external forces on it. For this solid at a temperature T (still with no forces acting on it), the stress tensor will be zero and the strain tensor will be due entirely to the deformation due to its increased temperature $T-T_a$. From eq. 4-16 , this means the free energy will have a linear term proportional to the strain tensor. There can only be one linear scalar quantity formed from the components of the tensor u_{ik}, the sum of its diagonal components u_{ll}. For a small temperature change, we can assume that the coefficient of this term is simply proportional to the temperature difference. Writing this constant as $-K\beta$, the first two terms of the free energy are then :

$$F(T) = F_0(T) - K\beta(T - T_a)u_{ll} \qquad [4\text{-}17]$$

There can be two second order terms since two independent scalars can be formed from a symmetric rank 2 tensor. The free energy can then be written as :

$$F(T) = F_0(T) - K\beta(T - T_a)u_{ll} + \frac{1}{2}\lambda u_{ii}^2 + \mu u_{ik}^2 \qquad [4\text{-}18]$$

where the two new constants are called the Lame coefficients. It is more convenient to choose another combination of independent scalars from the strain tensor. Consider the identity

$$u_{ik} = \left(u_{ik} - \frac{1}{3}\delta_{ik}u_{ll}\right) + \frac{1}{3}\delta_{ik}u_{ll} \qquad [4\text{-}19]$$

Since the sum of the diagonal elements in the first term is zero, there is no volume change associated with it. This is known as pure shear. The second term, which only has diagonal elements is known as hydrostatic compression. Choosing two new scalars based on eq. 4-19, the free energy can be written as :

$$F(T) = F_0(T) - K\beta(T - T_a)u_{ll} + \mu\left(u_{ik} - \frac{1}{3}\delta_{ik}u_{ll}\right)^2 + \frac{1}{2}K{u_{ll}}^2 \qquad [4\text{-}20]$$

where K is known as the bulk modulus and μ is called the shear modulus.

The relationship between the stress and strain tensor can now be found by differentiating the free energy at constant temperature :

$$dF = Ku_{ll}du_{ll} - K\beta(T - T_a)du_{ll} + 2\mu\left(u_{ik} - \frac{1}{3}\delta_{ik}u_{ll}\right)d\left(u_{ik} - \frac{1}{3}\delta_{ik}u_{ll}\right) \qquad [4\text{-}21]$$

Thus the stress tensor can be written as :

$$\sigma_{ik} = \left(\frac{\partial F}{\partial u_{ik}}\right)_T = K u_{ll}\delta_{ik} - K\beta(T - T_a)\delta_{ik} + 2\mu\left(u_{ik} - \frac{1}{3}\delta_{ik}u_{ll}\right) \qquad [4\text{-}22]$$

For free thermal expansion of a body, internal stresses must be zero. Setting the stress tensor equal to zero, we see the strain tensor must only have diagonal components and :

$$u_{ll} = \beta(T - T_a) \qquad [4\text{-}23]$$

Since the sum of the diagonal components of the strain tensor is equal to the relative change in volume, we see the beta is simply the thermal expansion coefficient.

The stress tensor can also be expressed in terms of the constants E and σ which are called Young's Modulus and Poisson's ratio where :

$$E = \frac{9K\mu}{(3K + \mu)} \qquad \sigma = \frac{(3K - 2\mu)}{2(3K + \mu)} \qquad [4\text{-}24]$$

Poisson's ratio is equal to the ratio of transverse compression to longitudinal extension and varies between 0 and 0.5. The stress tensor can now be written as :

$$\sigma_{ik} = \frac{E}{1+\sigma}\left(u_{ik} + \frac{\sigma}{1-2\sigma}u_{ll}\delta_{ik}\right) - \frac{E\beta T_L}{3(1-2\sigma)}\delta_{ik} \qquad [4\text{-}25]$$

where the temperature increase ($T-T_a$) has been replaced by T_L since, in our case, this will be a laser-induced temperature increase. In component form :

$$\sigma_{xx} = \frac{E}{(1+\sigma)(1-2\sigma)}\left[(1-\sigma)u_{xx} + \sigma(u_{yy} + u_{zz}) - \frac{(1+\sigma)}{3}\beta T_L\right]$$

$$\sigma_{yy} = \frac{E}{(1+\sigma)(1-2\sigma)}\left[(1-\sigma)u_{yy} + \sigma(u_{xx} + u_{zz}) - \frac{(1+\sigma)}{3}\beta T_L\right]$$

$$\sigma_{zz} = \frac{E}{(1+\sigma)(1-2\sigma)}\left[(1-\sigma)u_{zz} + \sigma(u_{xx} + u_{yy}) - \frac{(1+\sigma)}{3}\beta T_L\right]$$

$$\sigma_{xy} = \frac{E}{1+\sigma}u_{xy} \qquad \sigma_{xz} = \frac{E}{1+\sigma}u_{xz} \qquad \sigma_{yz} = \frac{E}{1+\sigma}u_{yz} \qquad [4\text{-}26]$$

4.3.4 Thermoelastic Wave Equation

The equations of motion can be found by equating the internal stress force to the product of the acceleration and density :

$$\rho\frac{\partial^2 u_i}{\partial t^2} = \frac{\partial \sigma_{ik}}{\partial x_k} \qquad [4\text{-}27]$$

Substituting in the general expression for the stress tensor (eq. 4-25) gives :

$$\rho\frac{\partial^2 u_i}{\partial t^2} = \frac{E}{1+\sigma}\left(\frac{\partial u_{ik}}{\partial x_k} + \frac{\sigma}{1-2\sigma}\frac{\partial u_{ll}}{\partial x_i}\right) - \frac{E\beta}{3(1-2\sigma)}\frac{\partial T_L}{\partial x_i} \qquad [4\text{-}28]$$

Substituting the general expression for the strain tensor (eq. 4-9) gives :

$$\rho\frac{\partial^2 u_i}{\partial t^2} = \frac{E}{1+\sigma}\left(\frac{1}{2}\frac{\partial^2 u_i}{\partial x_k^2} + \frac{1}{2}\frac{\partial^2 u_k}{\partial x_i \partial x_k} + \frac{\sigma}{1-2\sigma}\frac{\partial^2 u_l}{\partial x_i \partial x_l}\right) - \frac{E\beta}{3(1-2\sigma)}\frac{\partial T_L}{\partial x_i} \qquad [4\text{-}29]$$

This can be simplified to :

$$\rho\frac{\partial^2 u_i}{\partial t^2} = \frac{E}{2(1+\sigma)}\frac{\partial^2 u_i}{\partial x_k^2} + \frac{E}{2(1+\sigma)(1-2\sigma)}\frac{\partial^2 u_l}{\partial x_i \partial x_l} - \frac{E\beta}{3(1-2\sigma)}\frac{\partial T_L}{\partial x_i} \qquad [4\text{-}30]$$

In vector notation, this takes the form

$$\rho\frac{\partial^2 \mathbf{u}}{\partial t^2} = \frac{E}{2(1+\sigma)}\nabla^2\mathbf{u} + \frac{E}{2(1+\sigma)(1-2\sigma)}\nabla(\nabla\cdot\mathbf{u}) - \frac{E\beta}{3(1-2\sigma)}\nabla T_L \qquad [4\text{-}31]$$

Therefore finding the displacement vector which satisfies eq. 4-31 completely specifies the deformation of a solid as a function of time. For boundary value problems, the surface of a solid must satisfy :

$$\sigma_{ik} n_k = P_i \qquad [4\text{-}32]$$

where **n** is a unit vector outward normal to the surface and **P** is the external force per unit area.

4.4 ONE DIMENSIONAL SOLUTION TO THE THERMOELASTIC WAVE EQUATION

The thermoelastic wave equation (eq. 4-31) describes the thermoelastic response of a solid material to a given temperature distribution. As can be seen from this equation, it is the gradient of the temperature distribution which serves as the driving term for the wave equation. We are interested in the particular problem of a non uniform temperature distribution created by the absorption of a short pulse of laser light. Although we are

interested in the full time dependent solution of the thermoelastic wave equation in a three dimensional geometry, due to the complexity of this coupled differential equation the first step is to find the one dimensional solution. This solution provides important insights and will also be used in chapter 6 to help verify the full three dimensional solution.

Consider a laser beam of infinite extent which strikes a solid and is exponentially absorbed with penetration depth D, creating an exponentially decreasing temperature profile. In this one dimensional calculation, displacement is only in the z direction and depends only on the z coordinate. With these assumptions, the thermoelastic wave equation (eq. 4-31) becomes :

$$\frac{\partial^2 u_z}{\partial t^2} = C_l^2 \frac{\partial^2 u_z}{\partial z^2} + \frac{E\beta T_0}{3D\rho(1-2\sigma)} e^{\frac{-z}{D}} \qquad where\ C_l^2 = \frac{E(1-\sigma)}{\rho(1+\sigma)(1-2\sigma)} \qquad [4\text{-}33]$$

Consider a solution of the form :

$$u_z(z,t) = \Psi(z,t) + A(z) \qquad [4\text{-}34]$$

Substituting this into eq. 4-33 yields

$$\frac{\partial^2 \Psi}{\partial t^2} - C_l^2 \frac{\partial^2 \Psi}{\partial z^2} = C_l^2 \frac{\partial^2 A}{\partial z^2} + \frac{E\beta T_0}{3D\rho(1-2\sigma)} e^{\frac{-z}{D}} \qquad [4\text{-}35]$$

4.4.1 Particular and Homogeneous Solutions

The general solution for the displacement can be found by adding the particular solution for A which makes the right hand side of eq. 4-35 vanish to the general solution

of the remaining wave equation. Equating the right hand side to zero and changing the partial derivative to a full derivative, one can write :

$$A = -\int dz \int dz \frac{E\beta T_0}{3D\rho C_l^2(1-2\sigma)} e^{\frac{-z}{D}} \qquad [4\text{-}36]$$

Performing the integration yields

$$A(z) = \frac{-\beta T_0 D}{a} e^{\frac{-z}{D}} + c_1 z + c_2 \qquad where\ a = \frac{3(1-\sigma)}{1+\sigma} \qquad [4\text{-}37]$$

Equation 4-35 is now

$$\frac{\partial^2 \Psi}{\partial t^2} - C_l^2 \frac{\partial^2 \Psi}{\partial z^2} = 0 \qquad [4\text{-}38]$$

The general solution of this wave equation can be found by separation of variables :

$$\Psi(z,t) = \left(a_1 e^{-k_1 z} + a_2 e^{k_1 z}\right)\left(a_3 e^{-k_1 C_l t} + a_4 e^{k_1 C_l t}\right) \qquad [4\text{-}39]$$

The general solution for the displacement can be found from eqs. 4-37 and 4-39 :

$$u_z = \frac{-\beta T_0 D}{a} e^{\frac{-z}{D}} + c_1 z + c_2 + c_3 e^{-k_1(z+C_l t)} + c_4 e^{-k_1(z-C_l t)} + c_5 e^{k_1(z-C_l t)} + c_6 e^{k_1(z+C_l t)} \qquad [4\text{-}40]$$

Since the displacement must be bounded for all z, and equal to zero at infinity, we have :

$$u_z = \frac{-\beta T_0 D}{a} e^{\frac{-z}{D}} + c_3 e^{-k_1(z+C_l t)} + c_5 e^{k_1(z-C_l t)} \qquad for\ z \le C_l t \qquad [4\text{-}41]$$

$$u_z = \frac{-\beta T_0 D}{a} e^{\frac{-z}{D}} + c_3 e^{-k_1(z+C_l t)} + c_4 e^{-k_1(z-C_l t)} \qquad for\ z \geq C_l t \qquad [4\text{-}42]$$

4.4.2 Applying the Initial and Boundary Conditions

The initial conditions are that the displacement must equal zero at time equal zero. Applying this condition, eqs. 4-41 and 4-42 become :

$$0 = \frac{-\beta T_0 D}{a} + c_3 + c_5 \qquad for\ z \leq C_l t \qquad [4\text{-}43]$$

$$0 = \frac{-\beta T_0 D}{a} e^{\frac{-z}{D}} + e^{-k_1 z}\left(c_3 + c_4\right) \qquad for\ z \geq C_l t \qquad [4\text{-}44]$$

The boundary condition , given be eq. 4-32, is that the zz component of the stress tensor must equal zero at z equal to zero. Using Eq 4-26, this can be expressed as

$$\left.\frac{\partial u_z}{\partial z}\right|_{z=0} = \frac{\beta T_0}{a} \qquad [4\text{-}45]$$

Applying the boundary condition to eq. 4-41 gives :

$$\frac{\beta T_0}{a} = \frac{\beta T_0}{a} - k_1 e^{-k_1 C_l t}\left(c_3 - c_5\right) \qquad for\ z \leq C_l t \qquad [4\text{-}46]$$

Thus eqs. 4-41 and 4-42 now take the form :

$$u_z = \frac{\beta T_0 D}{2a}\left[e^{-k_1(z+C_l t)} + e^{k_1(z-C_l t)} - 2e^{\frac{-z}{D}}\right] \qquad for\ z \leq C_l t \qquad [4\text{-}47]$$

$$u_z = c_3 e^{-\frac{(z+C_l t)}{D}} + c_4 e^{-\frac{(z-C_l t)}{D}} - \frac{-\beta T_0 D}{a} e^{\frac{-z}{D}} \qquad for\ z \geq C_s t$$

$$\text{where } c_3 + c_4 = \frac{\beta T_0 D}{a} \qquad [4\text{-}48]$$

Finally, since the displacement must be continuous at $z = C_l t$, eqs. 4-47 and 4-48 must be equal at this point :

$$\frac{\beta T_0 D}{2a}\left[e^{-2k_1 z} + 1 - 2e^{\frac{-z}{D}}\right] = c_3 e^{-\frac{2z}{D}} + c_4 - \frac{\beta T_0 D}{a} e^{\frac{-z}{D}} \qquad [4\text{-}49]$$

Equation 4-49 shows that c_3 and c_4 must be equal and that k_1 is the inverse of the penetration depth D.

4.4.3 The Displacement and Stress

The final expressions for the displacement can then be written as :

$$u_z = \frac{\beta T_0 D}{6} \frac{1+\sigma}{1-\sigma}\left[e^{-\frac{z+C_l t}{D}} + e^{\frac{z-C_l t}{D}} - 2e^{\frac{-z}{D}}\right] \qquad for\ z \leq C_l t \qquad [4\text{-}50]$$

$$u_z = \frac{\beta T_0 D}{6} \frac{1+\sigma}{1-\sigma}\left[e^{-\frac{z+C_l t}{D}} + e^{-\frac{z-C_l t}{D}} - 2e^{\frac{-z}{D}}\right] \qquad for\ z \geq C_l t \qquad [4\text{-}51]$$

The displacement as a function of time for a point on the surface and a point at one penetration depth is shown in figure 4-1. A point below the surface will initially move away from the surface and then reverse directions and move towards the surface. The time at which this reversal occurs is equal to the time for an acoustic wave starting at the surface to reach the point. For a point on the surface (figure 4-1), the movement is always

in the same direction. The surface movement, found by setting z = 0 in eq. 4-50, has a particularly simple form :

$$S(t) = \frac{S_0}{3}\frac{1+\sigma}{1-\sigma}\left[1 - e^{\frac{-t}{\tau_c}}\right]$$

where $S_0 = \beta T_0 D$ and $\tau_c = \frac{D}{C_l}$ [4-52]

The steady-state displacement can be found by letting the time approach infinity in eq. 4-50. This shows that the final shape of the displacement is simply related to the initial laser-induced temperature distribution (figure 4-2).

The stress can be found from the expressions for the displacement. In one dimension, the expression for the axial stress (eq. 4-26) simplifies to :

$$\sigma_{zz} = \rho C_l^2\left[\frac{\partial u_z}{\partial z} - \frac{1+\sigma}{3(1-\sigma)}\beta T_0 e^{-\frac{z}{D}}\right] \qquad [4\text{-}53]$$

The expression for the derivative of the displacement can be found from eqs. 4-50,51 :

$$\frac{\partial u_z}{\partial z} = -\frac{\beta T_0}{6}\frac{1+\sigma}{1-\sigma}\left[e^{-\frac{z+C_l t}{D}} - e^{\frac{z-C_l t}{D}} - 2e^{\frac{-z}{D}}\right] \qquad for\ z \le C_l t \qquad [4\text{-}54]$$

$$\frac{\partial u_z}{\partial z} = -\frac{\beta T_0}{6}\frac{1+\sigma}{1-\sigma}\left[e^{-\frac{z+C_l t}{D}} + e^{-\frac{z-C_l t}{D}} - 2e^{\frac{-z}{D}}\right] \qquad for\ z \ge C_l t \qquad [4\text{-}55]$$

Substituting these expressions into eq. 4-53 and using the characteristic time for motion τ_c (eq. 4-52) gives the final expression for the stress :

$$\sigma_{zz} = -\frac{\sigma_{max}}{2}\left[e^{-\frac{z}{D}-\frac{t}{\tau_c}} - e^{\frac{z}{D}-\frac{t}{\tau_c}}\right] \qquad for\ z \le C_l t \qquad [4\text{-}56]$$

$$\sigma_{zz} = \frac{\sigma_{max}}{2}\left[e^{-\frac{z}{D}-\frac{t}{\tau_c}} + e^{-\frac{z}{D}+\frac{t}{\tau_c}}\right] \qquad for\ z \ge C_l t \qquad [4\text{-}57]$$

where

$$\sigma_{max} = \frac{1+\sigma}{3(1-\sigma)}\rho C_l^2 \beta T_0 \qquad [4\text{-}58]$$

The stress as a function of depth, z, is plotted for several different times in figure 4-3. Initially, the stress is an exponentially decaying function which is proportional to the initial temperature distribution. The stress is entirely compressive (plotted as negative values in figure 4-3). This stress distribution can be considered as the sum of two identical traveling waves moving in opposite directions. When one of the waves reaches the surface, it will be completely reflected and will change from a compressive to a tensile stress. Mathematically, this follows directly from the boundary condition that the stress must be equal to zero on the free surface (see eq. 4-32). At a later time, the amplitude of the compressive wave has decreased while the amplitude of the tensile wave has increased. Finally, the stress distribution forms a bipolar wave where the compressive and tensile components have equal amplitudes. Note that the wave front moves with the velocity C_l.

Since the basis of the photomechanical model of ablation is the laser-induced stress, an analytical expression for the stress distribution as a function of time (eqs. 4-56 and 4-57) is valuable. As shown in figure 4-3, the initial laser-induced compressive stress evolves into a tensile stress. Although the generation of tensile stress is essential to the photomechanical model, the spatial location of this stress is not in agreement with experimental observations of failure. These observations show that ablation occurs near the surface ($z << D$) while the predicted tensile stress in the one dimensional model do not become significant until deep within the sample ($z \sim D$). The discrepancy will be remedied in chapters 5 and 6 when the three dimensional nature of the problem is considered.

4.4.4 Comparison to the Hydrodynamic Solution

Expressions for the surface movement and stresses caused by the absorption of a short pulse of laser light have been obtained using the theory of elasticity (section 4.4.3) and the hydrodynamic equations of motion (section 3.3.3). It will be instructive to compare the results. The expressions for the surface displacements are (see eqs. 3-25, 3-27, and 4-52) :

$$S(t) = S_0\left[1 - e^{\frac{-t}{\tau_c}}\right] \qquad \text{Hydrodynamic Formulation} \quad [4\text{-}59]$$

$$S(t) = \frac{S_0}{3}\frac{1+\sigma}{1-\sigma}\left[1 - e^{\frac{-t}{\tau_c}}\right] \qquad \text{Theory of Elasticity} \quad [4\text{-}60]$$

These expressions differ by a correction factor which is a function of the Poisson ratio. The Poisson ratio is defined as the ratio of the transverse compression to the longitudinal extension and has a value between 0 and 0.5 for all substances [Landau and Lifshitz, 1986]. The bulk modulus, or modulus of compression (K), can be expressed as :

$$K = \frac{E}{3(1-2\sigma)} \qquad [4\text{-}61]$$

Combining this with the expression for the longitudinal sound velocity (eq. 4-33) yields an expression for the correction factor :

$$\frac{1+\sigma}{3(1-\sigma)} = \frac{K}{\rho C_l^2} \qquad [4\text{-}62]$$

For water at 20^0C, K is 2.183 x 10^9 N/m^2 [Weast, 1983], ρ is 998.23 Kg/m^3, and C_l is 1483 m/s [Haar et al., 1984]. Substituting these values into eq. 4-62 yields a correction factor of one which corresponds to a Poisson ratio of 0.5. Thus the expression for the displacement is identical in the two theoretical formulations in the limiting case that the Poisson ratio is at a maximum value, as is the case for liquids. In solids, the Poisson ratio takes on values less than 0.5, corresponding to a coupling of displacements and stresses in different dimensions, and the formalism based on the theory of elasticity must be used.

The expressions for the stress distribution using the hydrodynamic formulation (see eq. 3-23) and the theory of elasticity (see eqs. 4-56 and 4-57) are :

$$\frac{\Gamma\Phi}{2D}$$ Hydrodynamic Formulation [4-63]

$$\frac{\sigma_{max}}{2}$$ Theory of Elasticity [4-64]

Using the expression for the Gruneisen coefficient (eq. 3-26) and expressing the energy per unit volume (Φ/D) as a function of the temperature ($\rho C_V T$), eq. 4-63 can be written as:

$$\frac{\Gamma\Phi}{2D} = \frac{\rho C_l^2 \beta T_0}{2} = \frac{\sigma_{max}}{2}\frac{3(1-\sigma)}{1+\sigma} \qquad [4\text{-}65]$$

Thus, the expressions for the stress from the theory of elasticity and the hydrodynamic formulation differ by the same factor that the displacements differ.

4.5 CONCLUSIONS

In order to evaluate the photomechanical model of ablation, a quantitative model of the tissue response to the laser irradiation must be developed. Using the theory of elasticity, equations for the laser-induced displacement and the stresses have been found in a one dimensional geometry. These equations have been compared to the solutions using the hydrodynamic equations of motion derived in the previous chapter. The two solutions have the same functional form and differ only my a multiplicative constant related to the Poisson ratio. Although this constant is one for water, it ranges from 0.33 to 1 for solids.

The model shows that although the initial laser-induced stress is compressive, the boundary condition at the free surface leads to the formation of a bipolar acoustic

traveling wave which has both compressive and tensile components. The maximum tensile stress achieved at each point increases as a function of depth up to a value equal to one half of the initial compressive stress. The value and location of the tensile stresses is extremely important since it is postulated that the tensile stresses are responsible for rupturing the material. Although this one dimensional model does show the formation of tensile stresses, they are deep within the sample, not near the surface where ablation is observed to occur. As will be shown in the next two chapters, this discrepancy disappears when the full three dimensional nature of the problem is considered.

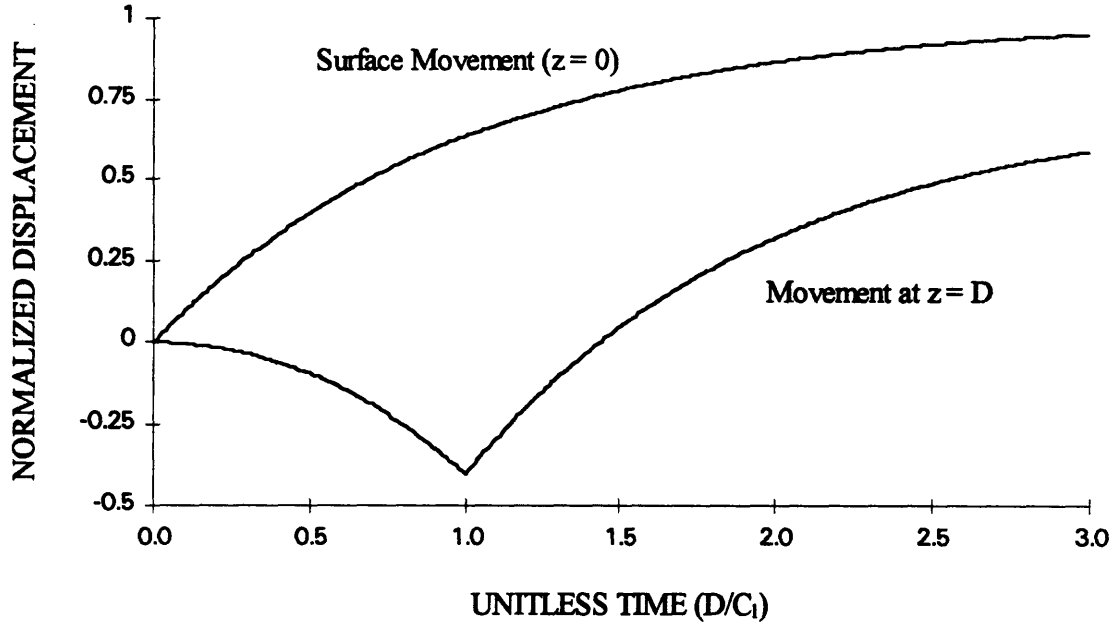

Figure 4-1. The normalized surface displacement as a function of a unitless time shows a steady expansion. At a depth D, a point originally moves away from the surface, and then begins to moves towards the surface.

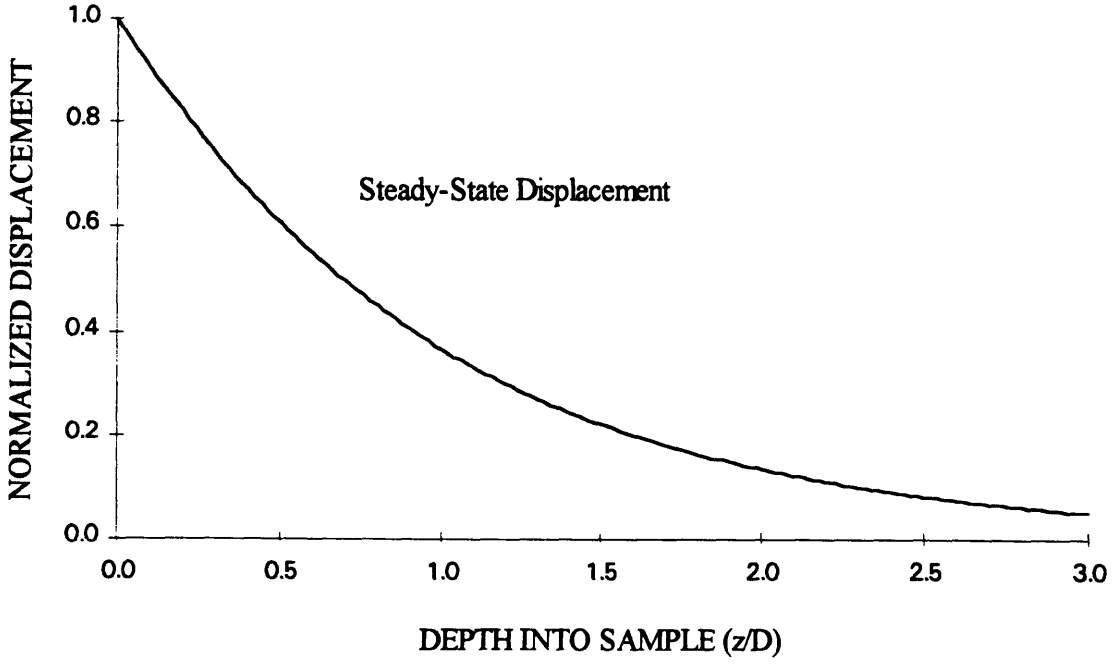

Figure 4-2. At long times, the sample reaches an equilibrium distribution which is related to the original temperature distribution. The sample will remain in this shape until thermal diffusion dissipates the energy.

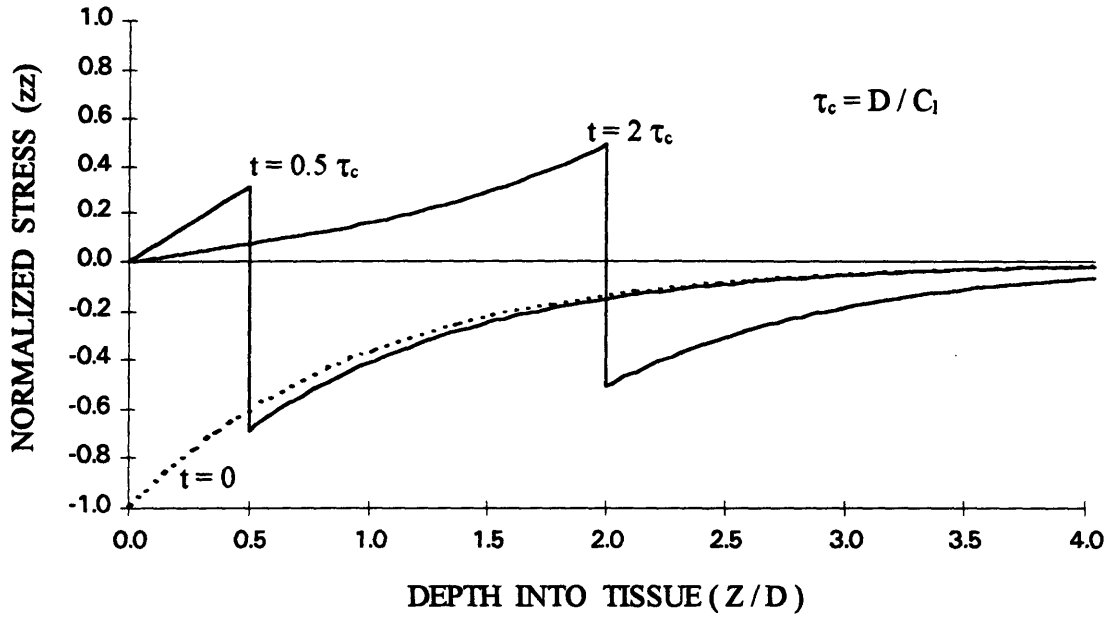

Figure 4-3. The normalized axial stress as a function of depth into the sample and unitless time. Initially, the stress is compressive (negative) and is proportional to the laser-induced temperature distribution. Due to the boundary conditions on the surface, this distribution evolves into a bipolar wave with both compressive and transient components.

CHAPTER 5

Analytical 3D Steady-State Solution to the Thermoelastic Wave Equation

5.1 OVERVIEW

The photomechanical model asserts that ablation is initiated when the laser-induced stresses exceed the strength of the material in question. Although one-dimensional calculations have shown that short pulsed lasers can create significant transient tensile stresses in target materials (chapter 4), the stresses last for only a few nanoseconds and the spatial location of the peak stresses is not consistent with experimental observations of material failure in biological tissues. Using the theory of elasticity, we have derived analytical expressions for the thermoelastic stresses and deformations in an axially symmetric three-dimensional solid body caused by the absorption of laser light. The full three-dimensional solution includes three stresses, radial, circumferential and shear, which are necessarily absent in the simple one-dimensional solution. These stresses have long-lived components which exist for eight orders of magnitude longer in time than the acoustic transients, an important point when the details of dynamic fracture are considered. Many important qualitative features are revealed including the spatial location of the peak stresses which is more consistent with experimental observations of failure.

This work has been accepted for publication in the journal *Medical Physics* in an article entitled " Laser-Induced Thermoelastic Deformation : A Three Dimensional Solution and its Application to the Ablation of Biological Tissue" [Albagli et al., 1994c].

5.2 INTRODUCTION

For ablation using short pulsed lasers ($\tau < 10$ μs), there is evidence that photomechanical effects play the most significant role in ablation [Albagli et al., 1994a; Itzkan et al., 1994] and there are several simple one dimensional photomechanical models described in the literature including laser-induced spallation [Dingus and Scammon 1991a, 1991b] and inertially confined ablation [Albagli et al., 1994a, 1994b] (chapter 2). In the models of ablation, it is postulated that the laser-induced stresses exceed the strength of the irradiated material. When the laser pulse enters the target, scattering and absorption take place, creating non-uniform temperature and stress distributions within the target. In simple 1D calculations ([Bushnell and McCloskey, 1968] and chapter 4), the initial stress is compressive but can lead to the development of both compressive and tensile acoustic traveling waves. Since most materials, including biological tissues, are weaker in tension [Duck, 1990], it has been conjectured that the tensile acoustic traveling wave causes the material to rupture, a process known as laser-induced spallation. For example, it has been shown that spallation plays an important role in the ablation of metals [Tuler and Butcher, 1968]. This assumption is not consistent with experimental results in biological tissues

since observed failure occurs at and near the surface, while the amplitude of the acoustic tensile wave becomes significant an order of magnitude deeper into the target.

The inconsistency between the predictions of the 1D spallation model and experimental observations is due to important features left out of this calculation. In addition to the axial stress considered in the 1D spallation model, there are three other important stresses (radial, circumferential and shear) which must be considered in a three-dimensional (3D) geometry. The acoustic components of these stresses are transient and propagate away with the speed of sound, and therefore remain in the region for short times. Unlike in the 1D case, however, in the 3D case there are also long-lived quasi-steady state thermoelastic components of the stresses which eventually dissipate by thermal diffusion. We shall calculate the quasi-steady state stresses and show that they are smaller but of the same order of magnitude as the transient stresses. Since these quasi-steady state stresses persist for many orders of magnitude longer in time than the transient stresses, they can play a significant role in the ablation process. When these important features are taken into account, the inconsistencies in the predictions of the photomechanical model of ablation are removed.

The theory of elasticity can be used to predict the deformations and stresses caused by a laser-induced non-uniform temperature distribution. We define the aspect ratio, R, as the ratio of the characteristic half width of the temperature distribution to the characteristic depth. If R is very large compared to unity (the case of plane stress), the thermoelastic equations simplify dramatically and the solution can be found in a standard

textbook [Boley and Weiner, 1985]. Recently the plane stress solution has been applied to laser ablation in dentistry to compare the peak laser-induced radial and circumferential stresses at threshold to the known strength of tooth enamel [Motamedi at al., 1992]. For most biomedical applications, however, R is near unity. For these cases, the solution to the complete three-dimensional thermoelastic equations is required. The solution is presented in the next section for a temperature distribution which decays exponentially in the axial direction and has either a Gaussian or "top-hat" radial distribution.

5.3 DERIVATION OF 3D ANALYTICAL SOLUTION

5.3.1 Fundamental Equations of Thermoelasticity

Consider a plane semi-infinite homogeneous material with its surface at z = 0, and an axially symmetric non-uniform temperature distribution T(r,z). The thermoelastic displacement equations in cylindrical coordinates are [Sokolnikoff, 1956] :

$$F_r = \rho \frac{\partial^2 u_r}{\partial t^2} = \frac{\partial \sigma_{rr}}{\partial r} + \frac{\partial \sigma_{rz}}{\partial z} + \frac{\sigma_{rr} - \sigma_{\phi\phi}}{r} \qquad [5\text{-}1]$$

$$F_z = \rho \frac{\partial^2 u_z}{\partial t^2} = \frac{\partial \sigma_{zz}}{\partial z} + \frac{\partial \sigma_{zr}}{\partial r} + \frac{\sigma_{zr}}{r} \qquad [5\text{-}2]$$

where F_r and F_z are the total forces per unit volume in the r and z directions, ρ is the density, u_r and u_z are the displacements in the r and z directions, and σ_{ik} is the ik component of the stress tensor. The general expression for the stress tensor in cylindrical coordinates for an isotropic, homogeneous medium subjected to a axially symmetric temperature field T(r,z) is [Landau and Lifshitz, 1986] :

$$\sigma_{zr} = \sigma_{rz} = \frac{E}{(1+\sigma)} u_{rz}$$

$$\sigma_{rr} = M\left[(1-\sigma)u_{rr} + \sigma(u_{\phi\phi} + u_{zz}) - \frac{1+\sigma}{3}\beta T(r,z)\right]$$

$$\sigma_{zz} = M\left[(1-\sigma)u_{zz} + \sigma(u_{rr} + u_{\phi\phi}) - \frac{1+\sigma}{3}\beta T(r,z)\right] \qquad [5\text{-}3]$$

$$\sigma_{\phi\phi} = M\left[(1-\sigma)u_{\phi\phi} + \sigma(u_{rr} + u_{zz}) - \frac{1+\sigma}{3}\beta T(r,z)\right]$$

where $$M = \frac{E}{(1+\sigma)(1-2\sigma)}, \qquad [5\text{-}4]$$

E is Young's modulus, σ is the Poisson ratio, β is the thermal expansion coefficient (equal to three times the linear expansion coefficient) and u_{ik} is the strain tensor. There should be no confusion between the Poisson ratio and the stress tensor since the former has no subscripts. Similarly, the displacement vector has one subscript and the strain tensor two. For small strains and axial symmetry, the expression for the strain tensor is [Landau and Lifshitz, 1986] :

$$u_{zz} = \frac{\partial u_z}{\partial z} \qquad u_{rr} = \frac{\partial u_r}{\partial r}$$

$$u_{rz} = \frac{1}{2}\left(\frac{\partial u_z}{\partial r} + \frac{\partial u_r}{\partial z}\right) \qquad u_{\phi\phi} = \frac{u_r}{r} \qquad [5\text{-}5]$$

The differential equation for the displacement vector can be found by substituting eqs. 5-3 and 5-5 into eqs. 5-1 and 5-2 [Landau and Lifshitz, 1986] :

$$\rho\frac{\partial^2\mathbf{u}}{\partial t^2}-\frac{E}{2(1+\sigma)}\nabla^2\mathbf{u}-\frac{M}{2}\nabla(\nabla\cdot\mathbf{u})=\frac{-E\beta}{3(1-2\sigma)}\nabla T(r,z) \qquad [5\text{-}6]$$

This is the thermoelastic wave equation which was derived in chapter 4 (eq. 4-31). We will consider the steady-state solution when the displacement vector is no longer a function of time (first term in eq. 5-6 is zero). Note that the response of the medium is driven by the gradient of the temperature distribution. The boundary conditions at the free surface are [Landau and Lifshitz, 1986] :

$$\sigma_{zz}\big|_{z=0}=0 \qquad \text{and} \qquad \sigma_{rz}\big|_{z=0}=0 \qquad [5\text{-}7]$$

5.3.2 Transformation of the Wave Equation Using Scalar Potentials

The general steady-state solution to equation 5-6 is the sum of a particular solution of the inhomogeneous equation plus a general solution of the homogeneous equation ($\nabla T(r,z)=0$). In the following, single bars over a variable indicate the contribution from the inhomogeneous equation and double bars from the homogeneous equation. A very effective solution technique is to transform the vector equations into scalar equations using potentials.

5.3.2.1 Transformation of the Steady State Inhomogeneous Equation

Goodier [1937] introduced the thermoelastic displacement potential Φ, where :

$$\bar{u}_z=\frac{\partial\Phi}{\partial z} \qquad \bar{u}_r=\frac{\partial\Phi}{\partial r} \qquad [5\text{-}8]$$

Substituting this potential into eq. 5-6 in the steady state gives a Poisson equation :

$$\nabla^2\Phi = N\,T(r,z) \qquad [5\text{-}9]$$

where $$N = \frac{1+\sigma}{3(1-\sigma)}\beta \qquad [5\text{-}10]$$

Solving this equation for Φ for the given temperature distribution allows the calculation of the in-homogeneous parts of the displacement vector (from eq. 5-8) and the stresses (from eq. 5-3) [Nowacki, 1962] :

$$\overline{\sigma_{rz}} = \frac{E}{1+\sigma}\frac{\partial^2\Phi}{\partial r\,\partial z} \qquad \overline{\sigma_{rr}} = \frac{E}{1+\sigma}\left(\frac{\partial^2\Phi}{\partial r^2} - \nabla^2\Phi\right)$$

$$\overline{\sigma_{zz}} = \frac{E}{1+\sigma}\left(\frac{\partial^2\Phi}{\partial z^2} - \nabla^2\Phi\right) \qquad \overline{\sigma_{\theta\theta}} = \frac{E}{1+\sigma}\left(\frac{1}{r}\frac{\partial\Phi}{\partial r} - \nabla^2\Phi\right) \qquad [5\text{-}11]$$

5.3.2.2 Transformation of the Steady State Homogeneous Equation

The steady state homogeneous equation is (eq. 5-6 with $\partial^2\mathbf{u}/\partial t^2 = 0$ and $\nabla T(r,z) = 0$) :

$$\frac{E}{2(1+\sigma)}\nabla^2\mathbf{u} + \frac{M}{2}\nabla(\nabla\cdot\mathbf{u}) = 0 \qquad [5\text{-}12]$$

Love [1923] showed that this equation can be transformed into the biharmonic equation :

$$\nabla^2\nabla^2\psi = 0 \qquad [5\text{-}13]$$

where ψ is called the Love function. The displacements and stresses in terms of ψ are [Nowacki, 1962] :

$$\overline{\overline{u_z}} = \frac{1}{1-2\sigma}\left[2(1-\sigma)\nabla^2 - \frac{\partial^2}{\partial z^2}\right]\psi \qquad \overline{\overline{u_r}} = -\frac{1}{1-2\sigma}\frac{\partial^2 \psi}{\partial r\,\partial z} \qquad [5\text{-}14]$$

and :

$$\overline{\overline{\sigma_{rz}}} = M\frac{\partial}{\partial r}\left[(1-\sigma)\nabla^2 - \frac{\partial^2}{\partial z^2}\right]\psi \qquad \overline{\overline{\sigma_{rr}}} = M\frac{\partial}{\partial z}\left[\sigma\nabla^2 - \frac{\partial^2}{\partial r^2}\right]\psi$$

$$\overline{\overline{\sigma_{zz}}} = M\frac{\partial}{\partial z}\left[(2-\sigma)\nabla^2 - \frac{\partial^2}{\partial z^2}\right]\psi \qquad \overline{\overline{\sigma_{\phi\phi}}} = M\frac{\partial}{\partial z}\left[\sigma\nabla^2 - \frac{1}{r}\frac{\partial}{\partial r}\right]\psi \qquad [5\text{-}15]$$

The complete solution for the displacements and stresses is obtained by summing the contributions :

$$u_i = \overline{u_i} + \overline{\overline{u_i}} \qquad [5\text{-}16]$$

$$\sigma_{ik} = \overline{\sigma_{ik}} + \overline{\overline{\sigma_{ik}}} \qquad [5\text{-}17]$$

5.3.3 Solution of the Wave Equation for a Laser-Induced Temperature Profile

5.3.3.1 Solution of the Steady State Inhomogeneous Equation

Consider a laser beam with a top-hat radial profile (of radius w) incident on a target with its surface at z = 0, as shown in figure 5-1 (the solution for a Gaussian radial profile will be discussed in section 5.2.4). The absorption of the laser light will create a

non-uniform temperature distribution within the target. Assuming the laser light is attenuated exponentially within the target with a characteristic "1/e" depth D, called the optical penetration depth, the temperature distribution can be written as :

$$T(r,z) = T_0 \eta(w-r)\left[e^{-z/D}\eta(z) - e^{z/D}\eta(-z)\right] \qquad [5\text{-}18]$$

where η(x) is the Heaviside step function and has the value 1 for x greater than zero, 0.5 for x equal to zero, and zero for x less than zero. This temperature distribution employs a virtual (or image) distribution in negative z-space to clamp the surface of the medium, z = 0, at zero temperature.

The Poisson equation (eq. 9) can be solved with a given temperature distribution using integral transforms [Nowacki, 1962]. The temperature distribution, eq. 5-18, can be expressed in integral form by means of the following identities [Gradshteyn and Ryzhik, 1965] :

$$\int_0^\infty \frac{\lambda}{1+\lambda^2}\sin\left(\frac{\lambda z}{D}\right)d\lambda = \frac{\pi}{2}\left[e^{-z/D}\eta(z) - e^{z/D}\eta(-z)\right] \qquad [5\text{-}19]$$

$$\int_0^\infty RJ_1(Ry)J_0\left(\frac{yr}{D}\right)dy = \eta(w-r) \qquad [5\text{-}20]$$

where R = w / D. Thus :

$$T(r,z) = \frac{2T_0}{\pi}\int_0^\infty\int_0^\infty \frac{\lambda RJ_1(Ry)}{1+\lambda^2}\sin\left(\frac{\lambda z}{D}\right)J_0\left(\frac{yr}{D}\right)dyd\lambda \qquad [5\text{-}21]$$

The solution to the Poisson equation can immediately be written down :

$$\Phi(r,z) = -ND^2 \frac{2T_0}{\pi} \int_0^\infty \int_0^\infty \frac{\lambda R J_1(Ry)}{(1+\lambda^2)(y^2+\lambda^2)} \sin\left(\frac{\lambda z}{D}\right) J_0\left(\frac{yr}{D}\right) dy d\lambda \qquad [5\text{-}22]$$

The integration over λ can be performed [Gradshteyn and Ryzhik, 1965] to give the expression for the potential as a single integral :

$$\Phi(r,z) = NT_0D^2 \int_0^\infty \frac{e^{-yz/D} - e^{-z/D}}{(y^2-1)} R J_1(Ry) J_0\left(\frac{yr}{D}\right) dy \qquad [5\text{-}23]$$

Using this potential, the components of the displacement vector take the form

$$\overline{u_z} = -NT_0D \int_0^\infty \frac{\left(ye^{-yz/D} - e^{-z/D}\right)}{(y^2-1)} R J_1(Ry) J_0\left(\frac{yr}{D}\right) dy \qquad [5\text{-}24]$$

$$\overline{u_r} = -NT_0D \int_0^\infty \frac{y\left(e^{-yz/D} - e^{-z/D}\right)}{(y^2-1)} R J_1(Ry) J_1\left(\frac{yr}{D}\right) dy \qquad [5\text{-}25]$$

and the stresses take the form

$$\overline{\sigma_{rz}} = P \int_0^\infty \frac{y\left(ye^{-yz/D} - e^{-z/D}\right)}{(y^2-1)} R J_1(Ry) J_1\left(\frac{yr}{D}\right) dy \qquad [5\text{-}26]$$

$$\overline{\sigma_{rr}} = -P \int_0^\infty \left[\frac{\left(y^2e^{-yz/D} - e^{-z/D}\right)}{(y^2-1)} J_0\left(\frac{yr}{D}\right) - \frac{y^2\left(e^{-yz/D} - e^{-z/D}\right)}{(y^2-1)} \frac{J_1(yr/D)}{yr/D} \right] R J_1(Ry) dy \qquad [5\text{-}27]$$

$$\overline{\sigma_{zz}} = P \int_0^\infty \frac{y^2\left(e^{-yz/D} - e^{-z/D}\right)}{(y^2-1)} R J_1(Ry) J_0\left(\frac{yr}{D}\right) dy \qquad [5\text{-}28]$$

$$\overline{\sigma_{\phi\phi}} = -P\int_0^{\infty}\left[e^{-z/D}J_0\left(\frac{yr}{D}\right)+\frac{y^2\left(e^{-yz/D}-e^{-z/D}\right)}{\left(y^2-1\right)}\frac{J_1(yr/D)}{yr/D}\right]RJ_1(Ry)dy \qquad [5\text{-}29]$$

where $$P=\frac{E\beta T_0}{3(1-\sigma)} \qquad [5\text{-}30]$$

5.3.3.2 Solution of the Steady State Homogeneous Equation

The general solution of the biharmonic equation in cylindrical coordinates can be written as [Nowacki, 1962] :

$$\psi=\int_0^{\infty}\left(A_1+\frac{yz}{D}A_2\right)e^{-yz/D}J_0\left(\frac{yr}{D}\right)dy \qquad [5\text{-}31]$$

where A_1 and A_2 are arbitrary constants to be determined from the boundary conditions. Since $\overline{\sigma_{zz}}$ is zero on the surface (eq. 5-28), $\overline{\overline{\sigma_{zz}}}$ must also be zero on the surface in order to satisfy the boundary condition (eq. 5-7). Using eqs. 5-15 and 5-31 gives the result :

$$A_1=(2\sigma-1)A_2 \qquad [5\text{-}32]$$

Since $\overline{\sigma_{rz}}$ is not zero on the surface (eq. 5-26), $\overline{\overline{\sigma_{rz}}}$ must be equal to $-\overline{\sigma_{rz}}$ on the surface in order to satisfy the boundary condition (eq. 5-7). Using eqs. 5-15, 5-26 and 5-31 gives the condition :

$$A_2=NT_0(1-2\sigma)D^3\frac{RJ_1(Ry)}{y^2(y+1)} \qquad [5\text{-}33]$$

The components of the displacement vector for the homogeneous equation can then be found from the Love function from eq. 5-14 :

$$\overline{\overline{u_z}} = -NT_0D\int_0^\infty \frac{(1-2\sigma+yz/D)}{(y+1)} e^{-yz/D} RJ_1(Ry)J_0\left(\frac{yr}{D}\right)dy \qquad [5\text{-}34]$$

$$\overline{\overline{u_r}} = NT_0D\int_0^\infty \frac{(2-2\sigma-yz/D)}{(y+1)} e^{-yz/D} RJ_1(Ry)J_1\left(\frac{yr}{D}\right)dy \qquad [5\text{-}35]$$

and the stresses can be found from eq. 5-15 :

$$\overline{\overline{\sigma_{rz}}} = P\int_0^\infty \frac{y(-1+yz/D)e^{-yz/D}}{(y+1)} J_1\left(\frac{yr}{D}\right)RJ_1(Ry)dy \qquad [5\text{-}36]$$

$$\overline{\overline{\sigma_{rr}}} = P\int_0^\infty \frac{ye^{-yz/D}}{(y+1)}\left[\left(2-\frac{yz}{D}\right)J_0\left(\frac{yr}{D}\right)+\left(2\sigma-2+\frac{yz}{D}\right)\frac{J_1(yr/D)}{yr/D}\right]RJ_1(Ry)dy \qquad [5\text{-}37]$$

$$\overline{\overline{\sigma_{zz}}} = P\int_0^\infty \frac{(y^2z/D)e^{-yz/D}}{(y+1)} J_0\left(\frac{yr}{D}\right)RJ_1(Ry)dy \qquad [5\text{-}38]$$

$$\overline{\overline{\sigma_{\phi\phi}}} = P\int_0^\infty \frac{ye^{-yz/D}}{(y+1)}\left[2\sigma J_0\left(\frac{yr}{D}\right)-\left(2\sigma-2+\frac{yz}{D}\right)\frac{J_1(yr/D)}{yr/D}\right]RJ_1(Ry)dy \qquad [5\text{-}39]$$

5.3.3.3. Complete Solution for the Displacement and Stresses

Defining the dimensionless variables

$$r' = \frac{r}{D} \qquad z' = \frac{z}{D} \qquad [5\text{-}40]$$

and using eqs. 5-16, 5-24, 5-25, 5-34, and 5-35 gives, for the components of the displacements :

$$u_z = -\frac{1+\sigma}{3(1-\sigma)} D\beta T_0 \int_0^\infty \left[\frac{(1-2\sigma+yz')}{(y+1)} e^{-yz'} + \frac{\left(ye^{-yz'} - e^{-z'}\right)}{\left(y^2-1\right)} \right] RJ_1(Ry) J_0(yr')dy \qquad [5\text{-}41]$$

$$u_r = \frac{1+\sigma}{3(1-\sigma)} D\beta T_0 \int_0^\infty \left[\frac{(2-2\sigma-yz')}{(y+1)} e^{-yz'} - \frac{y\left(e^{-yz'} - e^{-z'}\right)}{\left(y^2-1\right)} \right] RJ_1(Ry) J_1(yr')dy \qquad [5\text{-}42]$$

These expressions for the r and z components of the displacements are verified by substitution back into the original thermoelastic wave equation (5-6) in the final section of this chapter (5.5).

The expressions for the stresses can be found from eqs. 5-17, 5-26 through 5-29, and 5-36 through 5-39 :

$$\sigma_{rz} = \frac{E\beta T_0}{3(1-\sigma)} \int_0^\infty \left[\frac{(-1+yz')e^{-yz'}}{(y+1)} + \frac{\left(ye^{-yz'} - e^{-z'}\right)}{\left(y^2-1\right)} \right] yJ_1(yr') RJ_1(Ry)dy \qquad [5\text{-}43]$$

$$\sigma_{rr} = \frac{E\beta T_0}{3(1-\sigma)} \int_0^\infty \left\{ \begin{array}{l} \left[\frac{y(2-yz')e^{-yz'}}{(y+1)} - \frac{\left(y^2 e^{-yz'} - e^{-z'}\right)}{\left(y^2-1\right)} \right] J_0(yr') + \\ \left[\frac{y(2\sigma-2+yz')e^{-yz'}}{(y+1)} + \frac{y^2\left(e^{-yz'} - e^{-z'}\right)}{\left(y^2-1\right)} \right] \frac{J_1(yr')}{yr'} \end{array} \right\} RJ_1(Ry)dy \qquad [5\text{-}44]$$

$$\sigma_{zz} = \frac{E\beta T_0}{3(1-\sigma)} \int_0^\infty \left[\frac{z' e^{-yz'}}{(y+1)} + \frac{\left(e^{-yz'} - e^{-z'}\right)}{\left(y^2-1\right)} \right] y^2 J_0(yr') R J_1(Ry) dy \qquad [5\text{-}45]$$

$$\sigma_{\phi\phi} = \frac{E\beta T_0}{3(1-\sigma)} \int_0^\infty \left\{ \begin{array}{l} \left[\frac{2\sigma y e^{-yz'}}{(y+1)} - e^{-z'} \right] J_0(yr') - \\ \left[\frac{y(2\sigma - 2 + yz')e^{-yz'}}{(y+1)} + \frac{y^2\left(e^{-yz'} - e^{-z'}\right)}{\left(y^2-1\right)} \right] \frac{J_1(yr')}{yr'} \end{array} \right\} R J_1(Ry) dy \qquad [5\text{-}46]$$

5.3.4 Solution for Other Radial Temperature Distributions

The solution obtained in the previous section was for a laser beam with a top-hat radial distribution. The solutions for another useful distribution, a Gaussian radial profile, can be easily obtained from the top-hat solution. Consider an initial temperature distribution of the form :

$$T(r,z) = T_0 e^{-r^2/w^2} \left[e^{-z/D} \eta(z) - e^{z/D} \eta(-z) \right] \qquad [5\text{-}47]$$

Given the integral [Gradshteyn and Ryzhik, 1965] :

$$\frac{w^2}{2} \int_0^\infty x e^{-w^2 x^2/4} J_0(rx) dx = e^{-r^2/w^2} \qquad [5\text{-}48]$$

the temperature distribution can be written in integral form and compared to the temperature distribution for a top-hat radial profile (eq. 5-21). After a change of variables y = xD, this becomes:

$$T(r,z)=\frac{2T_0}{\pi}\int_0^\infty\int_0^\infty\frac{\lambda R}{1+\lambda^2}\sin\left(\frac{\lambda z}{D}\right)J_0\left(\frac{yr}{D}\right)\left[\frac{Ry}{2}e^{-R^2y^2/4}\right]dyd\lambda \qquad \text{Gaussian} \quad [5\text{-}49]$$

$$T(r,z)=\frac{2T_0}{\pi}\int_0^\infty\int_0^\infty\frac{\lambda R}{1+\lambda^2}\sin\left(\frac{\lambda z}{D}\right)J_0\left(\frac{yr}{D}\right)\left[J_1(Ry)\right]dyd\lambda \qquad \text{Top-hat} \quad [5\text{-}21]$$

The top-hat temperature distribution differs from the Gaussian only by the replacement:

$$J_1(Ry)\Rightarrow\frac{Ry}{2}e^{-R^2y^2/4} \qquad [5\text{-}50]$$

Since this substitution into the initial temperature distribution (eq. 5-21) does not affect any of the subsequent steps in the derivation, the final displacements and stresses for an initial Gaussian radial distribution can be found directly from eqs. 5-41 through 5-46 with the substitution given by eq. 5-50.

Finally, the solution for an annular ring of width Δw can be found by subtracting the solution for a top-hat radial profile with radius w from the solution with radius $w+\Delta w$. The solution for any piecewise axially symmetric temperature distribution can then be constructed by summing annular rings with different amplitudes and radii.

5.4 APPLICATION TO THE PHOTOMECHANICAL MODEL OF ABLATION OF BIOLOGICAL TISSUE

5.4.1 Time Regimes of Laser-Induced Stresses

In studying the photomechanical model of ablation, one is interested in knowing the laser-induced stresses in a material as a function of time and space. This problem can be conveniently divided into three time regimes, governed by : 1) acoustic transients, 2) quasi-steady state thermoelastic stresses and 3) thermal diffusion.

5.4.1.1 Acoustic Transients

The absorption of the laser light produces an initial temperature and stress distribution in the material. For a short laser pulse (delta function in time) occurring at time equal zero, the initial stresses can be found from eq. 5-3 by setting the displacements equal to zero (since nothing has had time to move) :

$$\sigma_{rr,zz,\phi\phi}\Big|_{t=0} = \frac{-E}{3(1-2\sigma)}\beta T(r,z) \qquad \sigma_{max} = \frac{-E}{3(1-2\sigma)}\beta T_0 \qquad [5\text{-}51]$$

where the negative sign indicates a compressive stress. An estimate of this stress for bone (using the values [Duck, 1990] of E = 1.5×10^{10} Pa, $\sigma = 0.3$, $\beta/3 = 2.7 \times 10^{-5}$, $T_0 = 100^{\circ}C$) is $\sigma_{max} = 10^8$ Pa (1000 atm).

The full time dependent solution of eq. 5-6 results in longitudinal and transverse acoustic waves propagating with the speed of sound (C_l and C_t respectively). Thus the acoustic stress will decay exponentially on a time scale of (see section 4.4.3) :

$$\tau_a \approx \frac{\delta}{C_l} \qquad [5\text{-}52]$$

where δ is the depth of the region of interest. For the ablation of bone with near-ultraviolet wavelengths (300-400 nm), the typical single shot crater depth, δ, is about 3 μm [Izatt et al., 1991a]. For a speed of sound of 3000 m/s, this gives a decay time of 1 ns. In the one-dimensional theory, the initial compressive stress distribution develops into a traveling bipolar acoustic wave. Although the amplitude of the tensile stress component in this wave reaches a value of 0.5 σ_{max} deep within the target, the peak amplitude within the region of interest δ is only 0.015 σ_{max} (for δ = 3 μm, D = 200 μm).

5.4.1.2. Quasi-Steady State Thermoelastic Stresses

After the acoustic transients have decayed away, the system reaches equilibrium and the total forces in the r and z directions (eqs. 1 and 2) are zero. The individual stress components, however, are not zero (eqs. 5-1 and 5-2). These stresses, called the quasi-steady state thermoelastic stresses, are due to the non-uniform temperature distribution which still exists after the acoustic transients have decayed away. Expressions for these stresses were derived in section 5.2.3.3 and are plotted in figures 5-2 through 5-5 (using eqs. 5-43,5-44,5-46 and 5-50). In all figures, it is assumed that the Poisson ratio is equal to 0.25 (for most materials of interest, $0.1 < \sigma < 0.5$, [Duck 1990]). In order to compare these stresses to the transient stresses, they have been normalized to the peak transient stress, σ_{max} (eq. 5-51). Note that positive values refer to tension while negative values refer to compression.

Figure 5-2a shows the radial stress (σ_{rr}) as a function of radial position at the surface (z = 0) for a top-hat radial temperature distribution for several different aspect ratios. The surface radial stress is almost always compressive. Note that the peak value of compressive stress is a significant fraction (0.6) of the peak transient stress and occurs at the radius of the laser beam. The sharp jumps in the radial stress are a direct result of the discontinuous nature of the top-hat temperature distribution since the equations for the stress components contain a term proportional to the temperature (eq. 5-3). The radial stress for a Gaussian distribution is shown in figure 5-2b. Since the driving term in the thermoelastic equation of motion (eq. 5-6) is proportional to the gradient of the temperature, the stresses associated with the Gaussian temperature distribution will be smaller in magnitude and without abrupt changes. A corollary of this result is that sharp beam boundaries can be useful in enhancing ablation.

The circumferential stress ($\sigma_{\phi\phi}$) as a function of radial position on the surface is shown in Figure 5-3a for a top-hat temperature distribution. For radial positions within the initial temperature distribution, the stress is compressive and has a maximum value of 0.1-0.5 σ_{max} on the axis (r = 0). For a radial position at the temperature distribution boundary, the stress becomes tensile and reaches a peak value of between 0.1-0.3 σ_{max} . The circumferential stress for a Gaussian temperature distribution is shown in figure 5-3b. As before, the stresses are smaller in magnitude.

Figure 5-4a shows the shear stress (σ_{rz}) just below the surface (z = 0.02 D) as a function of radial position for a top-hat temperature distribution. As demanded by the boundary conditions, the shear stress is zero on the surface. For radial positions near the temperature distribution boundary, a significant shear stress develops. The shear stress much deeper below the surface (z = 0.2 D) is shown in figure 5-4b for a Gaussian distribution.

The circumferential stress as a function of depth into the material at a fixed radius r = 0 is shown for both a top-hat and Gaussian distribution in figure 5-5a (for R = 1). After reaching a peak compressive stress at or near the surface, the stress for the two distributions decreases monotonically into the sample. The circumferential stress as a function of depth at a fixed radius r = 1.01w is shown in figure 5-5b (for R = 1). A radius slightly larger than w was chosen because of the sharp discontinuity caused by the initial temperature distribution. For the top-hat distribution, the peak tensile stress reaches one third σ_{max} just below the surface. Note that the depth at which the stress reaches a maximum value (z = 0.03 D for r = 1.01w) decreases as r approaches w.

5.4.1.3 Thermal Diffusion

The quasi-steady state thermoelastic stresses discussed in the previous section are a direct result of the laser-induced non-uniform temperature distribution within the material. As thermal diffusion progresses, the temperature distribution becomes uniform and these stresses will decay to zero. The characteristic time scale of this decay can be estimated from [Carslaw and Jaeger, 1947] :

$$\tau_d = \frac{D^2}{\kappa} \qquad [5\text{-}53]$$

where κ is the thermal diffusivity. For a penetration depth of 200 μm and a thermal diffusivity of biological tissue in the range [Chen and Saha, 1987; Jacques and Prahl, 1987] of 0.1 - 0.15 mm^2/s, this characteristic time is on the order of 400 milliseconds.

5.4.2 Dynamic Fracture

In the simplest photomechanical picture, ablation occurs if the laser-induced stresses exceed the strength of the irradiated material. Experimental evidence, however, shows that both the amplitude of the stress and the time the stress operates for are important [Tuler and Butcher, 1968]. Based on experimental results on the spallation of aluminum and using the concept of cumulative damage, a general dynamic fracture criterion has been introduced given a time dependent tensile stress, $\sigma_{ii}(t)$:

$$\int \left[\sigma_{ii}(t) - \sigma_i\right]^{\lambda} dt = K \qquad [5\text{-}54]$$

where λ and K are constants and σ_i is some stress below which fracture would not occur, even for long times (note that in this reference, tensile stress is defined as negative). For λ = 1, this formula states that fracture occurs when the cumulative product of stress above some threshold (σ_i) and the time this stress operates for reaches some critical value (K). For $\lambda > 1$, as in the aluminum experiments [Tuler and Butcher, 1968] where $\lambda = 2$, the stress above threshold is weighted more heavily than the time during which the stress operates.

The results from the previous section showed that although the quasi-steady state thermoelastic stresses were smaller than the peak acoustic transients, they persisted for over eight orders of magnitude longer in time. Given the dynamic fracture criterion (eq. 5-54), this suggests that the smaller amplitude, long-lived stresses may play an important role in ablation.

5.4.3 Laser-Induced Displacements and Mechanical Properties

The derived expressions allow one to calculate the initial and quasi-steady state stresses given the optical and mechanical properties of the material. These properties, however, are not always known, especially for biological tissue. The expression for the steady-state axial displacement derived in Section 5.3.3.3 (eq. 5-41) can be helpful in determining these properties. The axial surface displacement for a Gaussian temperature distribution can be found from this equation by setting z = 0 and using eq. 5-50 :

$$u_z = -S_3 g_0(R,r') \qquad [5\text{-}55]$$

where the negative sign indicates motion towards the incoming light and

$$S_3 = \frac{2(1+\sigma)}{3} D\beta T_0 \qquad \text{and} \qquad g_0(R,r') = \int_0^\infty \frac{R^2 y}{2(y+1)} e^{-R^2 y^2/4} J_0(yr')dy \qquad [5\text{-}56]$$

For D ~ 200 μm and T_0 ~ 10-100 °C, S_3 is in the range 50-500 nanometers. Note that S_3 is simply proportional to $D\beta T_0$, the result one would expect from a simple one-dimensional model. The function g_0 is the geometrical correction factor and illustrates the

importance of the aspect ratio. For r' = 0, this correction factor is between zero (R small) and one (R large).

An interferometric technique has recently been used to measure the surface movement of biological tissue after laser irradiation (chapter 3, [Albagli et al., 1994b]). Measuring the surface movement for a given laser fluence (Φ_L) allows one to determine S_3 and thus calculate the stresses without knowing the expansion coefficient or the temperature distribution (and thus the heat capacity) :

$$\sigma_{max}(\Phi_L) = \frac{-E}{(1+\sigma)(1-2\sigma)} \frac{S_3(\Phi_L)}{D} \qquad [5\text{-}57]$$

Expressing the Young's modulus in terms of the longitudinal speed of sound (C_l), the density (ρ) and Poisson's ratio (eq. 4-33) gives :

$$\sigma_{max}(\Phi_L) = \frac{-\rho C_l^2}{(1-\sigma)} \frac{S_3(\Phi_L)}{D} \qquad [5\text{-}58]$$

Thus, given the mechanical properties of density, speed of sound, and Poisson ratio, the stresses can be determined by experimentally measuring the surface movement.

5.5 CONCLUSIONS

The full time-dependent solution to the thermoelastic wave equation was derived in Chapter 4 for a one dimensional geometry. Although this solution gives important

insights into the response of biological tissue to laser irradiation, the assumption of a one dimensional geometry is not appropriate for most cases. In this chapter, an extensive calculation to find the steady-steady solution in three dimensions has been detailed. This solution gives important information into both the spatial location of the stresses and the surface expansion.

Important features in the photomechanical picture of laser ablation only become apparent in the full three-dimensional solution of the thermoelastic equations. This solution shows that, for an axially symmetric system, four different stress components, axial, radial, circumferential, and shear, need to be considered. In addition, besides the short-lived acoustic components of these stresses, there are quasi-steady state thermoelastic stress components which operate over much longer time scales. Since dynamic fracture of materials depends on both the amplitude and time duration of the applied stress, these long-lived stresses may play a significant role in the ablation process. In addition, some components of the quasi-steady state stresses reach tensile and shear peaks at or near the surface, a finding consistent with experimental observations of material failure in biotissues.

An expression for the steady-state surface movement in the z direction was also found (eq. 5-55). Unlike the one dimensional solution, this expression shows that the new equilibrium position of the surface depends on both the optical penetration depth and the laser beam radius. Thus in order to extract any quantitative information from a measurement of the surface expansion, as was described in chapter 3, the full three

dimensional expression is needed. A comparison of experiment and theory will be detailed in chapters 7 and 8.

5.6 CHAPTER 5 APPENDIX - VERIFICATION OF SOLUTION

5.6.1 Verification Of The Particular Solution (r-component)

The equations for the displacement (eqs. 5-41 and 5-42) can be verified by substitution back into the original vector differential equation (eq. 5-6) :

$$\frac{E}{2(1+\sigma)}\nabla^2\mathbf{u}+\frac{E}{2(1+\sigma)(1-2\sigma)}\nabla(\nabla\cdot\mathbf{u})=\frac{E\beta}{3(1-2\sigma)}\nabla T \qquad [5\text{-}59]$$

The r component of this equation can be written in the form :

$$(1-2\sigma)\left(\nabla^2 u_r-\frac{u_r}{r^2}\right)+\frac{\partial}{\partial r}(\nabla\cdot\mathbf{u})=2N(1-\sigma)\frac{\partial T}{\partial r} \qquad [5\text{-}60]$$

In cylindrical coordinates,

$$\nabla^2 u_r=\frac{\partial^2 u_r}{\partial r^2}+\frac{1}{r}\frac{\partial u_r}{\partial r}+\frac{\partial^2 u_r}{\partial z^2} \qquad [5\text{-}61]$$

$$\frac{\partial}{\partial r}(\nabla\cdot\mathbf{u})=\frac{\partial^2 u_r}{\partial r^2}+\frac{1}{r}\frac{\partial u_r}{\partial r}+\frac{\partial^2 u_z}{\partial z\partial r}-\frac{u_r}{r^2} \qquad [5\text{-}62]$$

Making these substitutions, eq. 5-60 takes the form :

$$(2-2\sigma)\left[\frac{\partial^2 u_r}{\partial r^2}+\frac{1}{r}\frac{\partial u_r}{\partial r}-\frac{u_r}{r^2}\right]+(1-2\sigma)\frac{\partial^2 u_r}{\partial z^2}+\frac{\partial^2 u_z}{\partial z\partial r}=2N(1-\sigma)\frac{\partial T}{\partial r} \qquad [5\text{-}63]$$

Let us check the particular solution first. Let us define the short hand notation :

$$I[x] \equiv NT_0 D \int \frac{RJ_1(Ry)}{y^2 - 1} x\, dy \qquad [5\text{-}64]$$

The displacement in the z and r directions are given by eqs. 5-24 and 5-25, and using the notation of eq. 5-64, take the form :

$$\overline{u_z} = -I\left[\left(y e^{-yz/D} - e^{-z/D}\right) J_0\left(\frac{yr}{D}\right)\right] \qquad [5\text{-}65]$$

$$\overline{u_r} = -I\left[y\left(e^{-yz/D} - e^{-z/D}\right) J_1\left(\frac{yr}{D}\right)\right] \qquad [5\text{-}66]$$

The partial derivatives in eq. 5-63 can be calculated from eqs. 5-65 and 5-66 :

$$\frac{\partial^2 \overline{u_z}}{\partial r \partial z} = -I\left[\frac{y}{D^2}\left(y^2 e^{-yz/D} - e^{-z/D}\right) J_1\left(\frac{yr}{D}\right)\right] \qquad [5\text{-}67]$$

$$\frac{1}{r}\frac{\partial \overline{u_r}}{\partial r} = -I\left[y\left(e^{-yz/D} - e^{-z/D}\right)\frac{1}{r}\left(\frac{y}{D} J_0\left(\frac{yr}{D}\right) - \frac{1}{r} J_1\left(\frac{yr}{D}\right)\right)\right] \qquad [5\text{-}68]$$

$$\frac{\partial^2 \overline{u_r}}{\partial r^2} = -I\left[y\left(e^{-yz/D} - e^{-z/D}\right)\left(-\frac{y^2}{D^2} J_1\left(\frac{yr}{D}\right) + \frac{2}{r^2} J_1\left(\frac{yr}{D}\right) - \frac{y}{Dr} J_0\left(\frac{yr}{D}\right)\right)\right] \qquad [5\text{-}69]$$

$$\frac{\partial^2 \overline{u_r}}{\partial z^2} = -I\left[\frac{y}{D^2}\left(y^2 e^{-yz/D} - e^{-z/D}\right) J_1\left(\frac{yr}{D}\right)\right] \qquad [5\text{-}70]$$

Substituting eqs. 5-67 through 5-70 into eq. 5-63 yields :

$$I\left[\left\{y^2\left(e^{-yz/D} - e^{-z/D}\right) - \left(y^2 e^{-yz/D} - e^{-z/D}\right)\right\}\frac{y}{D^2} J_1\left(\frac{yr}{D}\right)\right] = N\frac{\partial T}{\partial r} \qquad [5\text{-}71]$$

In order to evaluate the right hand side of eq. 5-71, an expression for the Laplacian of the potential can be found from eq. 5-11, 5-23, and 5-28 and the temperature from eq. 5-9 :

$$T = \frac{1}{N} I\left[\frac{1}{D}\left(y^2 - 1\right)e^{-z/D} J_0\left(\frac{yr}{D}\right)\right] \qquad [5\text{-}72]$$

From eqs. 5-9 and 5-72, the right hand side of eqs. 5-71 can be simplified :

$$N\frac{\partial T}{\partial r} = -I\left[\frac{y}{D^2}\left(y^2 - 1\right)e^{-z/D} J_1\left(\frac{yr}{D}\right)\right] \qquad [5\text{-}73]$$

Substituting eq. 5-73 into eq. 5-71 and simplifying leads to :

$$I\left[\frac{y}{D^2}\left(y^2 - 1\right)e^{-z/D} J_1\left(\frac{yr}{D}\right)\right] = I\left[\frac{y}{D^2}\left(y^2 - 1\right)e^{-z/D} J_1\left(\frac{yr}{D}\right)\right] \qquad [5\text{-}74]$$

and thus the particular solution satisfies the r component of the original differential equation.

5.6.2 Verification Of The Particular Solution (z-component)

In cylindrical coordinates,

$$\nabla^2 u_z = \frac{\partial^2 u_z}{\partial r^2} + \frac{1}{r}\frac{\partial u_z}{\partial r} + \frac{\partial^2 u_z}{\partial z^2} \qquad [5\text{-}75]$$

$$\frac{\partial}{\partial z}(\nabla \cdot \mathrm{u}) = \frac{\partial^2 u_r}{\partial r \partial z} + \frac{1}{r}\frac{\partial u_r}{\partial z} + \frac{\partial^2 u_z}{\partial z^2} \qquad [5\text{-}76]$$

Making these substitutions, eq. 5-59 takes the form :

$$(1-2\sigma)\left[\frac{\partial^2 u_z}{\partial r^2} + \frac{1}{r}\frac{\partial u_z}{\partial r} + \frac{\partial^2 u_z}{\partial z^2}\right] + \frac{\partial^2 u_r}{\partial r \partial z} + \frac{1}{r}\frac{\partial u_r}{\partial z} + \frac{\partial^2 u_z}{\partial z^2} = 2N(1-\sigma)\frac{\partial T}{\partial z} \qquad [5\text{-}77]$$

Using eqs. 5-65 and 5-66, the partial derivatives can be calculated

$$\frac{1}{r}\frac{\partial \overline{u_z}}{\partial r} = I\left[\frac{y}{D}\left(ye^{-yz/D} - e^{-z/D}\right)\frac{1}{r}J_1\left(\frac{yr}{D}\right)\right] \qquad [5\text{-}78]$$

$$\frac{\partial^2 \overline{u_z}}{\partial r^2} = I\left[\frac{y}{D}\left(ye^{-yz/D} - e^{-z/D}\right)\left(\frac{y}{D}J_0\left(\frac{yr}{D}\right) - \frac{1}{r}J_1\left(\frac{yr}{D}\right)\right)\right] \qquad [5\text{-}79]$$

$$\frac{\partial^2 \overline{u_z}}{\partial z^2} = -I\left[\frac{1}{D^2}\left(y^3e^{-yz/D} - e^{-z/D}\right)J_0\left(\frac{yr}{D}\right)\right] \qquad [5\text{-}80]$$

$$\frac{1}{r}\frac{\partial \overline{u_r}}{\partial z} = I\left[\frac{y}{D}\left(ye^{-yz/D} - e^{-z/D}\right)\frac{1}{r}J_1\left(\frac{yr}{D}\right)\right] \qquad [5\text{-}81]$$

$$\frac{\partial^2 \overline{u_r}}{\partial z \partial r} = I\left[\frac{y}{D}\left(ye^{-yz/D} - e^{-z/D}\right)\left(\frac{y}{D}J_0\left(\frac{yr}{D}\right) - \frac{1}{r}J_1\left(\frac{yr}{D}\right)\right)\right] \qquad [5\text{-}82]$$

Using eqs. 5-78 through 5-82, eq. 5-77 becomes

$$-I\left[\frac{1}{D^2}\left(y^2-1\right)e^{-z/D}J_0\left(\frac{yr}{D}\right)\right] = N\frac{\partial T}{\partial z} \qquad [5\text{-}83]$$

From eq. 5-72, the right hand side of eqs. 5-83 can be simplified :

$$N\frac{\partial T}{\partial z} = -I\left[\frac{1}{D^2}\left(y^2-1\right)e^{-z/D}J_0\left(\frac{yr}{D}\right)\right] \qquad [5\text{-}84]$$

and thus the particular solution satisfies the z component of the original differential equation.

5.6.3 Verification Of The Homogeneous Solution (r-component)

The homogeneous solution for the displacement must satisfy the r-component of the homogeneous equation (see eq. 5-63)

$$(2-2\sigma)\left[\frac{\partial^2 u_r}{\partial r^2}+\frac{1}{r}\frac{\partial u_r}{\partial r}-\frac{u_r}{r^2}\right]+(1-2\sigma)\frac{\partial^2 u_r}{\partial z^2}+\frac{\partial^2 u_z}{\partial z\partial r}=0 \qquad [5\text{-}85]$$

The homogeneous solutions were found in eqs. 5-34 and 5-35 :

$$\overline{\overline{u_z}}=-I_1\left[\left(1-2\sigma+\frac{yz}{D}\right)e^{-yz/D}J_0\left(\frac{yr}{D}\right)\right] \qquad [5\text{-}86]$$

$$\overline{\overline{u_r}}=I_1\left[\left(2-2\sigma-\frac{yz}{D}\right)e^{-yz/D}J_1\left(\frac{yr}{D}\right)\right] \qquad [5\text{-}87]$$

where $I_1[x]$ is defined as

$$I_1[x]=NDT_0\int_0^\infty \frac{RJ_1(Ry)}{(y+1)}x\,dy \qquad [5\text{-}88]$$

The partial derivatives in eq. 5-85 can be calculated from eqs. 5-86 and 5-87 :

$$\frac{\partial^2\overline{\overline{u_z}}}{\partial r\partial z}=I_1\left[\frac{y^2}{D^2}\left(2\sigma-\frac{yz}{D}\right)e^{-yz/D}J_1\left(\frac{yr}{D}\right)\right] \qquad [5\text{-}89]$$

$$\frac{1}{r}\frac{\partial\overline{\overline{u_r}}}{\partial r}=I_1\left[\left(2-2\sigma-\frac{yz}{D}\right)e^{-yz/D}\frac{1}{r}\left(\frac{y}{D}J_0\left(\frac{yr}{D}\right)-\frac{1}{r}J_1\left(\frac{yr}{D}\right)\right)\right] \qquad [5\text{-}90]$$

$$\frac{\partial^2\overline{\overline{u_r}}}{\partial r^2}=I_1\left[\left(2-2\sigma-\frac{yz}{D}\right)e^{-yz/D}\left(-\frac{y^2}{D^2}J_1\left(\frac{yr}{D}\right)+\frac{2}{r^2}J_1\left(\frac{yr}{D}\right)-\frac{y}{Dr}J_0\left(\frac{yr}{D}\right)\right)\right] \qquad [5\text{-}91]$$

$$\frac{\partial^2\overline{\overline{u_r}}}{\partial z^2}=I_1\left[\frac{y^2}{D^2}\left(4-2\sigma-\frac{yz}{D}\right)e^{-yz/D}J_1\left(\frac{yr}{D}\right)\right] \qquad [5\text{-}92]$$

Substituting eqs. 91-95 into eq. 87 yields

$$-(2-2\sigma)\left(2-2\sigma-\frac{yz}{D}\right)+(1-2\sigma)\left(4-2\sigma-\frac{yz}{D}\right)+\left(2\sigma-\frac{yz}{D}\right)=0 \qquad [5\text{-}93]$$

or

$$4-8\sigma+4\sigma^2-2\frac{yz}{D}+2\sigma\frac{yz}{D}=4-8\sigma+4\sigma^2-2\frac{yz}{D}+2\sigma\frac{yz}{D} \qquad [5\text{-}94]$$

Thus, this solution solves the r-component of the homogeneous equation.

5.6.4 Verification Of The Homogeneous Solution (z-component)

The homogeneous solution for the displacement must satisfy the r-component of the homogeneous equation (see eq. 5-77)

$$(1-2\sigma)\left[\frac{\partial^2 u_z}{\partial r^2}+\frac{1}{r}\frac{\partial u_z}{\partial r}+\frac{\partial^2 u_z}{\partial z^2}\right]+\frac{\partial^2 u_r}{\partial r\partial z}+\frac{1}{r}\frac{\partial u_r}{\partial z}+\frac{\partial^2 u_z}{\partial z^2}=0 \qquad [5\text{-}95]$$

Using eqs. 5-86 and 5-87, the partial derivatives can be calculated :

$$\frac{1}{r}\frac{\partial\overline{\overline{u_z}}}{\partial r}=I_1\left[\frac{y}{D}\left(1-2\sigma+\frac{yz}{D}\right)e^{-yz/D}\frac{1}{r}J_1\left(\frac{yr}{D}\right)\right] \qquad [5\text{-}96]$$

$$\frac{\partial^2\overline{\overline{u_z}}}{\partial r^2}=I_1\left[\frac{y}{D}\left(1-2\sigma+\frac{yz}{D}\right)e^{-yz/D}\left(\frac{y}{D}J_0\left(\frac{yr}{D}\right)-\frac{1}{r}J_1\left(\frac{yr}{D}\right)\right)\right] \qquad [5\text{-}97]$$

$$\frac{\partial^2\overline{\overline{u_z}}}{\partial z^2}=I_1\left[\frac{y^2}{D^2}\left(1+2\sigma-\frac{yz}{D}\right)e^{-yz/D}J_0\left(\frac{yr}{D}\right)\right] \qquad [5\text{-}98]$$

$$\frac{1}{r}\frac{\partial\overline{\overline{u_r}}}{\partial z}=-I_1\left[\frac{y}{D}\left(3-2\sigma-\frac{yz}{D}\right)e^{-yz/D}\frac{1}{r}J_1\left(\frac{yr}{D}\right)\right] \qquad [5\text{-}99]$$

$$\frac{\partial^2\overline{\overline{u_r}}}{\partial z\partial r}=-I_1\left[\frac{y}{D}\left(3-2\sigma-\frac{yz}{D}\right)e^{-yz/D}\left(\frac{y}{D}J_0\left(\frac{yr}{D}\right)-\frac{1}{r}J_1\left(\frac{yr}{D}\right)\right)\right] \qquad [5\text{-}100]$$

Equation 5-95 now takes the form :

$$(1-2\sigma)I_1\left[2\frac{y^2}{D^2}e^{-yz/D}J_0\left(\frac{yr}{D}\right)\right]+I_1\left[\frac{y^2}{D^2}(-2+4\sigma)e^{-yz/D}J_0\left(\frac{yr}{D}\right)\right]=0 \qquad [5\text{-}101]$$

Thus, this solution solves the z-component of the homogeneous equation and the equations for the displacement (eqs. 5-41 and 5-42) have been verified by substitution back into the original vector differential equation (eq. 5-6).

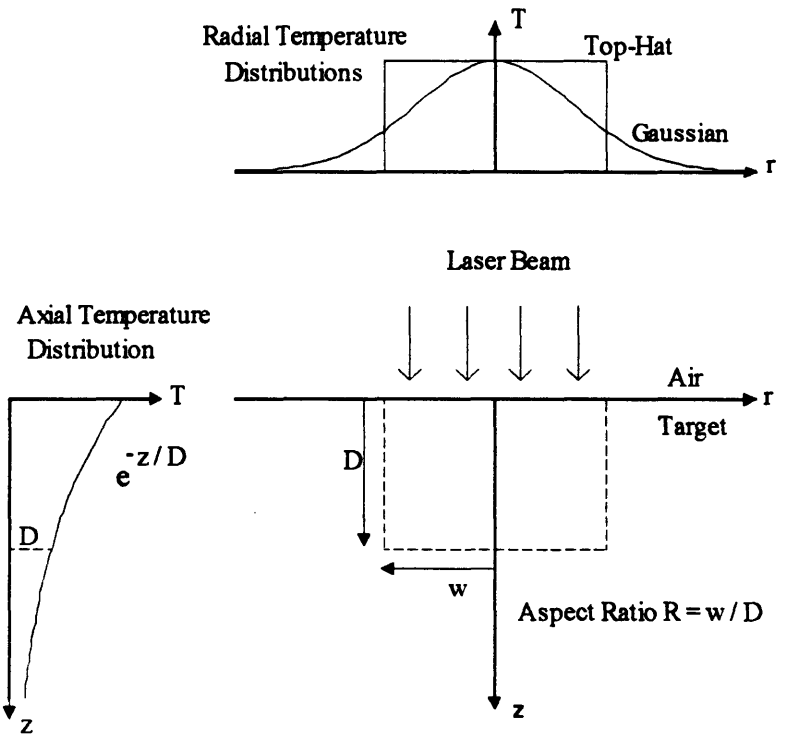

Figure 5-1. A laser beam incident on a target surface creates a non-uniform temperature distribution within the target which is a function of both the spatial distribution of the beam and the optical properties of the material. The resulting deformation and the associated stresses can be determined by solving the thermoelastic equations.

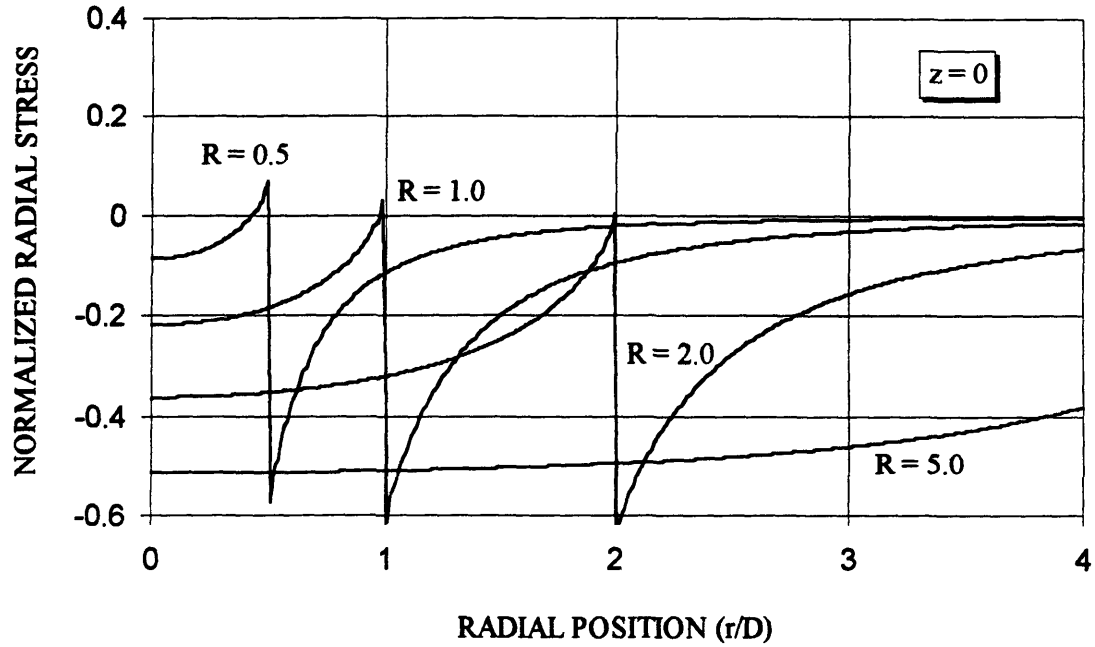

Figures 5-2a. The normalized radial stress (σ_{rr} / σ_{max}) on the surface (z = 0) as a function of radial position caused by a top-hat radial temperature distribution.

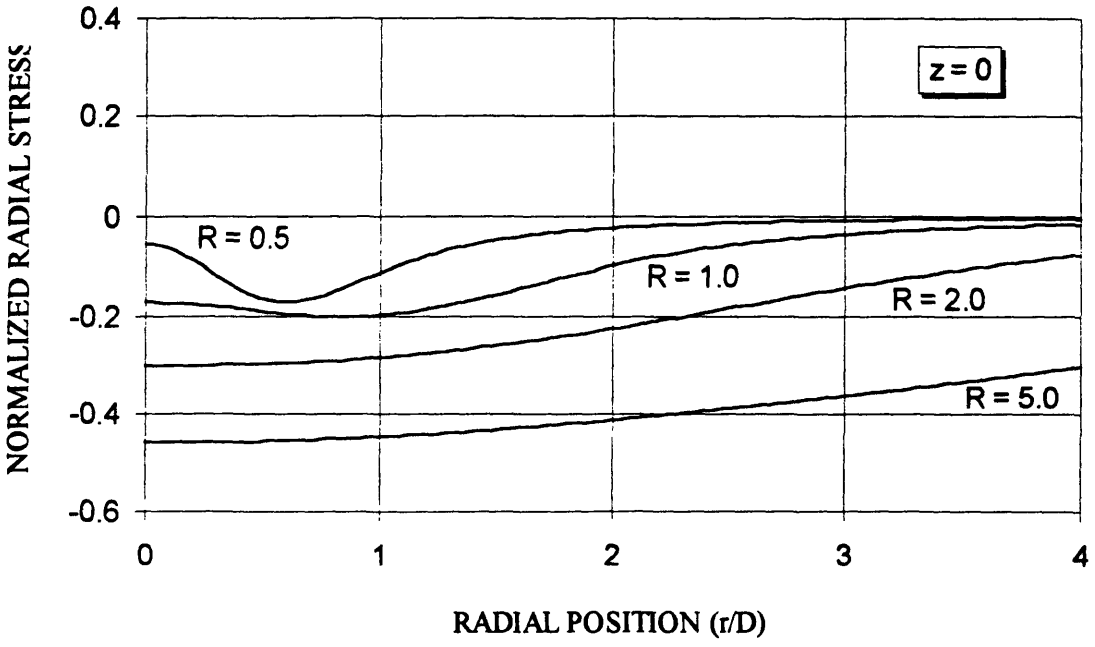

Figures 5-2b. The normalized radial stress (σ_{rr} / σ_{max}) on the surface (z = 0) as a function of radial position caused by a Gaussian radial temperature distribution.

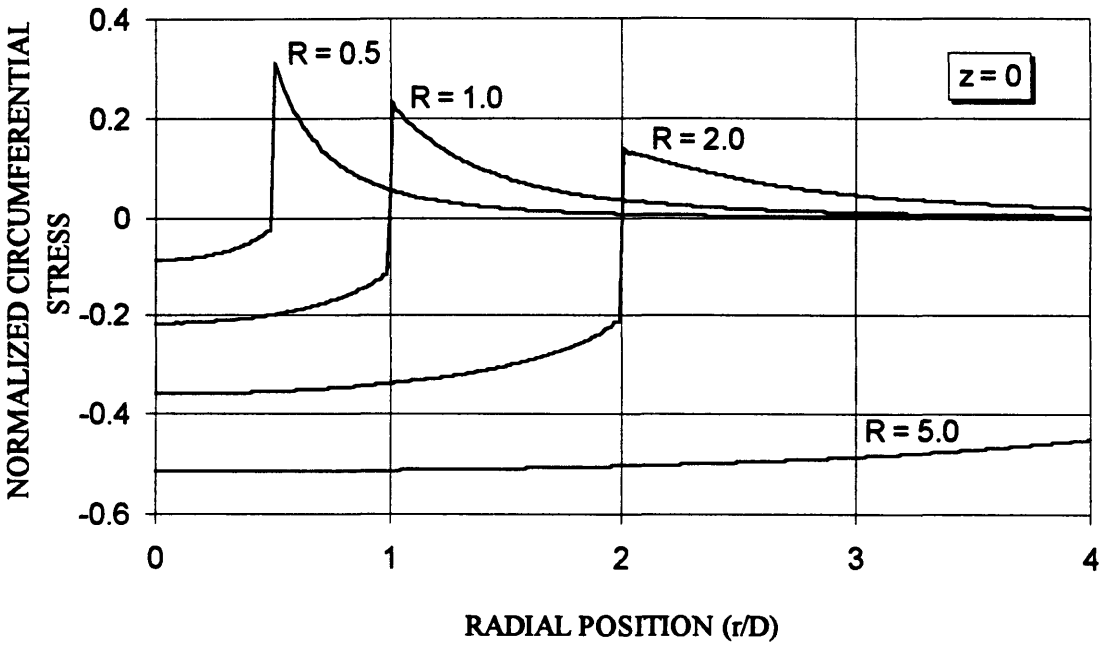

Figure 5-3a. The normalized circumferential stress ($\sigma_{\phi\phi}$ / σ_{max}) on the surface (z = 0) as a function of radial position caused by a top-hat radial temperature distribution. Note that there is a significant tensile stress (at r = RD = w) on the target surface.

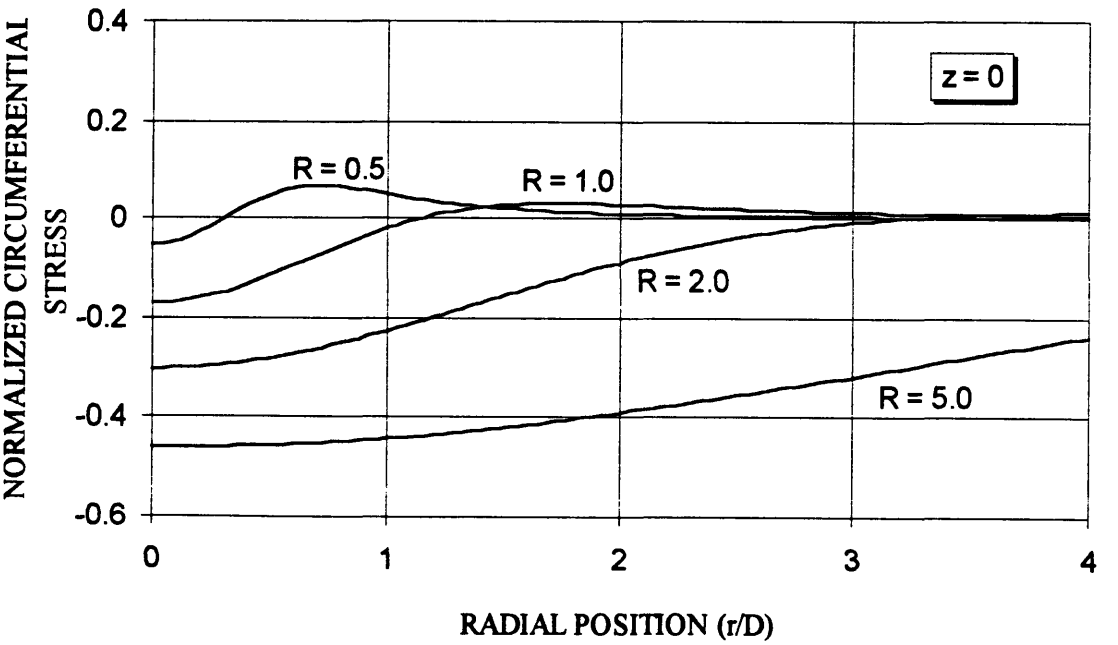

Figure 5-3b. The normalized circumferential stress ($\sigma_{\phi\phi}$ / σ_{max}) on the surface (z = 0) as a function of radial position caused by a Gaussian radial temperature distribution.

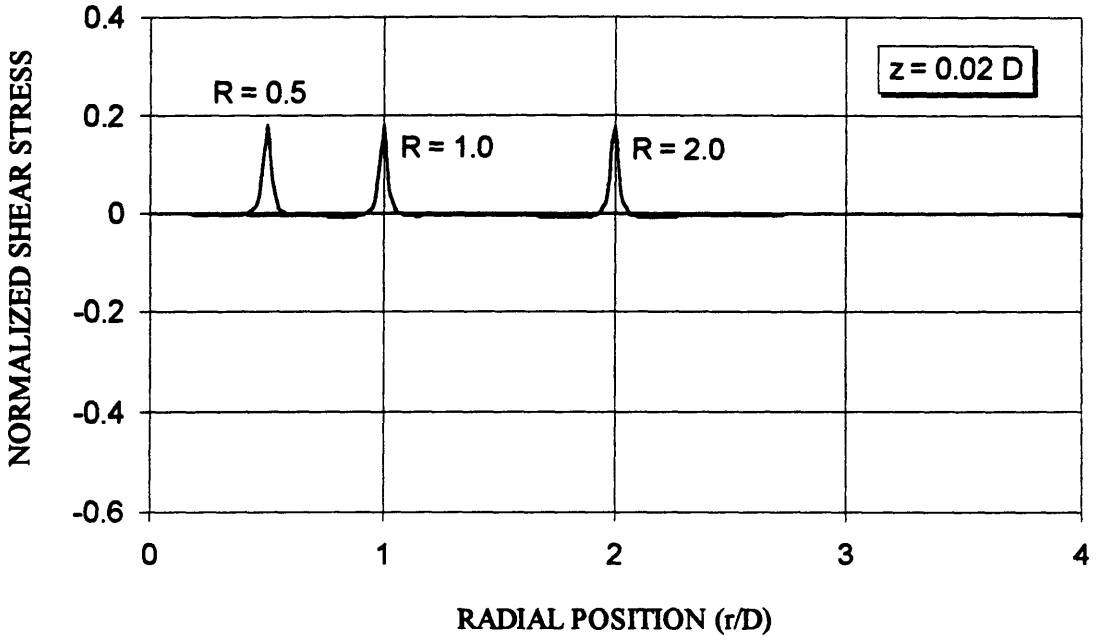

Figure 5-4a. The normalized shear stress (σ_{rz} / σ_{max}) as a function of radial position just below the surface caused by a top-hat radial temperature distribution. The stress is plotted at z = 0.02 D.

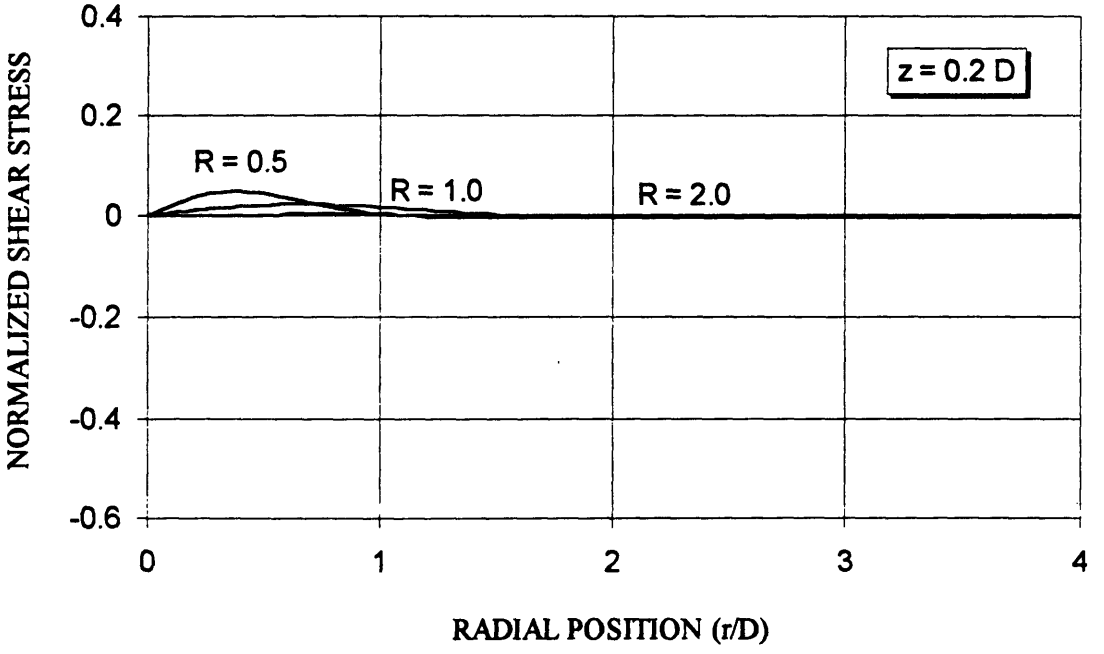

Figure 5-4b. The normalized shear stress (σ_{rz} / σ_{max}) as a function of radial position just below the surface caused by a Gaussian radial temperature distribution. The stress is plotted at z = 0.2 D.

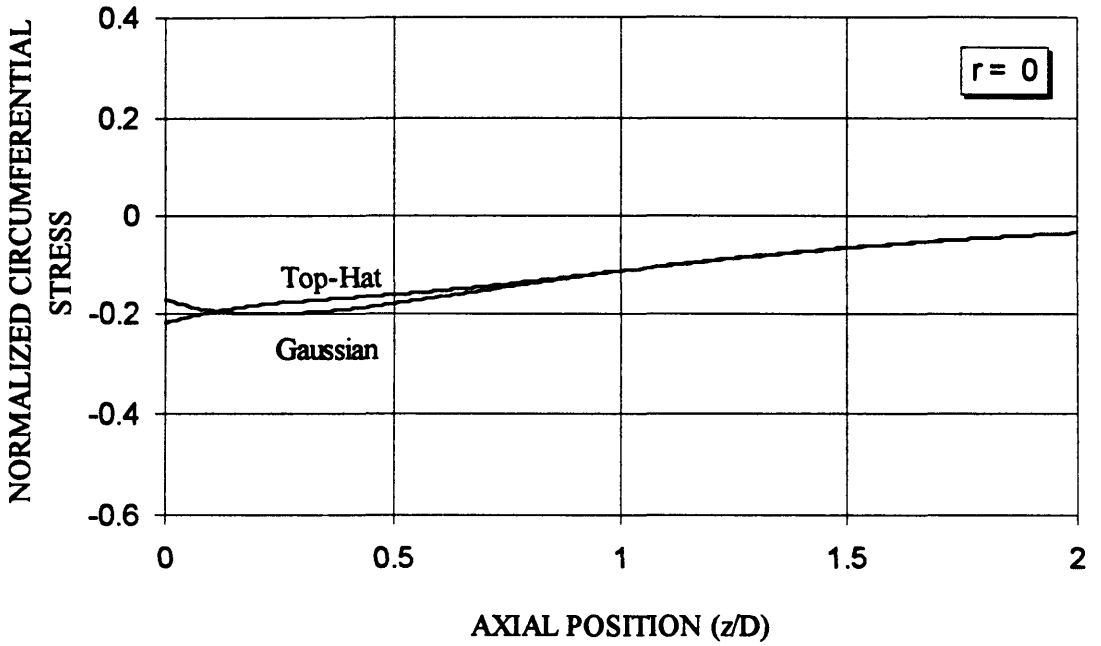

Figure 5-5a. The normalized circumferential stress ($\sigma_{\phi\phi}$ / σ_{max}) as a function of depth into the sample at r = 0 caused by a top-hat and Gaussian radial temperature distribution.

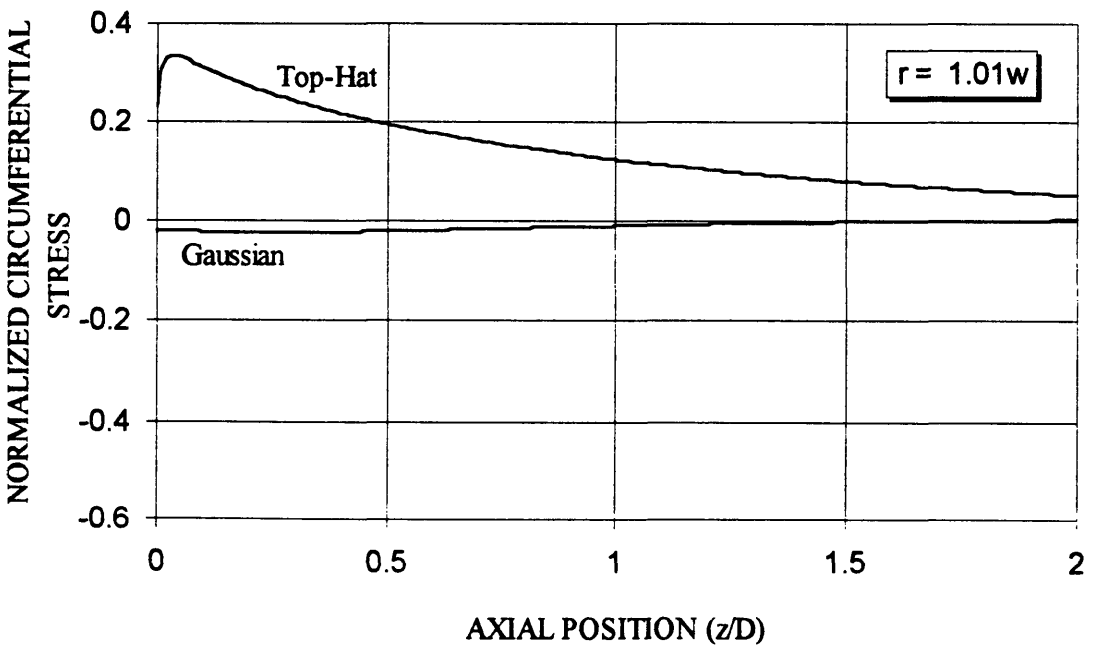

Figure 5-5b. The normalized circumferential stress ($\sigma_{\phi\phi}$ / σ_{max}) as a function of depth into the sample at r = 1.01w caused by a top-hat and Gaussian radial temperature distribution.

CHAPTER 6

Numerical Time Dependent Solution to the Thermoelastic Wave Equation

6.1 OVERVIEW

In the photomechanical model of tissue ablation, it is postulated that the laser-induced stresses initiate the ablation process. In order to quantitatively examine this postulate, the spatial and temporal distributions of the stresses must be known. Although partial solutions have been obtained in the last two chapters, a full three dimensional time dependent solution of these stress distributions is clearly needed. In this chapter, this solution is obtained using numerical methods. The results show the formation of significant transient radial and circumferential tensile stresses on the surface of the laser target, precisely where ablation is observed to occur. In addition, shear stresses are also created near the surface. These results strongly support the photomechanical model of ablation.

This work was presented in part at the 14th Annual Meeting of the American Society for Laser Medicine and Surgery, April 8-10, Toronto, Canada and was submitted to the journal *Optics Letters* in an article entitled "The Photomechanical Basis of Laser Ablation of Biological Tissue" [Albagli et al., 1994d] and in a longer form to *Applied Optics* in an article entitled " Laser-Induced Stress Generation in Solids and its Relation to the Photomechanical Model of the Ablation of Biological Tissue" [Albagli et al., 1994e].

6.2 INTRODUCTION

In chapter 4, a full time dependent analytical solution of the thermoelastic wave equation was presented for a one dimensional geometry. This solution showed the evolution of the initial compressive stress distribution into a traveling bipolar wave with both tensile and compressive components. The tensile components, however, were zero on the surface and became significant only at depths comparable to the optical penetration depth. Thus, although tensile stresses were created, the spatial location of these stresses did not match experimental observations of material failure.

In chapter 5, a steady state analytical solution to the thermoelastic wave equation was found in three dimensions. This solution showed the formation of quasi-steady state circumferential stresses on the surface and shear stresses near the surface. These long-lived stresses may play an important role in the ablation process. The role of the transient stresses, however, cannot be determined from this steady state solution.

In this chapter, the full three dimensional time dependent solution is obtained using numerical methods. Although this solution lacks the obvious benefits of the analytical solutions described above, it has a number of important advantages, including 1) it is the only solution obtained to date for the transient three dimensional stresses; 2) it is needed for a precise comparison to experimental results; 3) solutions can be obtained for arbitrary temperature distributions and laser pulse durations; 4) solutions can be obtained for non-

isotropic materials. The analytical solutions are used in this chapter to check the numerical solutions in the appropriate limiting cases.

6.3 NUMERICAL METHOD OF SOLVING THE THERMOELASTIC WAVE EQUATION

6.3.1 Statement Of Problem And Basic Equations

The problem is to determine the time evolution of the deformation of a solid material due to a laser-induced non-uniform temperature distribution in three dimensions. Cylindrical coordinates are used to take advantage of the axial symmetry of the problem. Let us assume that the laser light has a Gaussian radial profile of radius w, penetrates exponentially into the target with an optical penetration depth D, and has a pulse duration τ. This will lead to a laser-induced temperature distribution of the form :

$$T(r,z,t) = T_0 \frac{t}{\tau} e^{-\frac{z}{D}} e^{-\frac{r^2}{w^2}} \qquad \text{for } t \le \tau$$

$$T(r,z) = T_0 e^{-\frac{z}{D}} e^{-\frac{r^2}{w^2}} \qquad \text{for } t \ge \tau \qquad \text{[6-1]}$$

Since the time regime of interest is only several microseconds, thermal diffusion can be neglected (see section 5.4.1.3).

The equations of motion for an axially symmetric deformation were introduced in chapter 5 (eqs. 5-1 and 5-2) and can be written in the form :

$$\rho \frac{\partial^2 u_r}{\partial t^2} = \frac{\partial \sigma_{rr}}{\partial r} + \frac{\partial \sigma_{rz}}{\partial z} + \frac{\sigma_{rr} - \sigma_{\theta\theta}}{r} \qquad \text{[6-2]}$$

$$\rho\frac{\partial^2 u_z}{\partial t^2} = \frac{\partial \sigma_{zz}}{\partial z} + \frac{\partial \sigma_{zr}}{\partial r} + \frac{\sigma_{zr}}{r} \qquad [6\text{-}3]$$

6.3.2 The Adams-Bashforth Time Stepping Method

The equations of motion described by eqs. 6-2 and 6-3 can each be expressed as two first order equations :

$$\frac{\partial u_r}{\partial t} = \mathrm{v}_r \qquad [6\text{-}4]$$

$$\frac{\partial \mathrm{v}_r}{\partial t} - \frac{1}{\rho}\left[\frac{\partial \sigma_{rr}}{\partial r} + \frac{\partial \sigma_{rz}}{\partial z} + \frac{\sigma_{rr} - \sigma_{\phi\phi}}{r}\right] = 0 \qquad [6\text{-}5]$$

$$\frac{\partial u_z}{\partial t} = \mathrm{v}_z \qquad [6\text{-}6]$$

$$\frac{\partial \mathrm{v}_z}{\partial t} - \frac{1}{\rho}\left[\frac{\partial \sigma_{zz}}{\partial z} + \frac{\partial \sigma_{zr}}{\partial r} + \frac{\sigma_{zr}}{r}\right] = 0 \qquad [6\text{-}7]$$

where u_r and u_z are the components of the velocity in the r and z directions. These components can be found by numerically solving Eqs. 6-5 and 6-7 by using the Adams-Bashforth method [Potter, 1977] :

$$\mathrm{v}_r(t+\Delta t) = \mathrm{v}_r(t) - \left(\frac{3}{2}+\varepsilon\right)G_r(t) + \left(\frac{1}{2}+\varepsilon\right)G_r(t-\Delta t) \qquad [6\text{-}8]$$

$$\mathrm{v}_z(t+\Delta t) = \mathrm{v}_z(t) - \left(\frac{3}{2}+\varepsilon\right)G_z(t) + \left(\frac{1}{2}+\varepsilon\right)G_z(t-\Delta t) \qquad [6\text{-}9]$$

where Δt is the time step, ε is an arbitrary constant (see eq. 6-18), and

$$G_r = \Delta t\left[\frac{\partial A_r}{\partial r} + \frac{\partial B_r}{\partial z} + \frac{A_r - C_\phi}{r}\right] \qquad [6\text{-}10]$$

$$G_z = \Delta t\left[\frac{\partial A_z}{\partial r} + \frac{\partial B_z}{\partial z} + \frac{A_z}{r}\right] \qquad [6\text{-}11]$$

The stress functions A, B and C are related to the stress components via :

$$A_r = -\frac{\sigma_{rr}}{\rho} \qquad A_z = -\frac{\sigma_{zr}}{\rho}$$

$$B_z = -\frac{\sigma_{zz}}{\rho} \qquad B_r = -\frac{\sigma_{rz}}{\rho} \qquad [6\text{-}12]$$

$$C_\phi = -\frac{\sigma_{\phi\phi}}{\rho}$$

and can be expressed in terms of the displacements and temperature distribution by using the stress-strain relation given in chapter 5 (eq. 5-3) :

$$A_r = \frac{-E}{\rho(1+\sigma)(1-2\sigma)}\left[(1-\sigma)\frac{\partial u_r}{\partial r} + \sigma\left(\frac{u_r}{r} + \frac{\partial u_z}{\partial z}\right) - \frac{1+\sigma}{3}\beta T(r,z)\right] \qquad [6\text{-}13]$$

$$B_z = \frac{-E}{\rho(1+\sigma)(1-2\sigma)}\left[(1-\sigma)\frac{\partial u_z}{\partial z} + \sigma\left(\frac{\partial u_r}{\partial r} + \frac{u_r}{r}\right) - \frac{1+\sigma}{3}\beta T(r,z)\right] \qquad [6\text{-}14]$$

$$C_\phi = \frac{-E}{\rho(1+\sigma)(1-2\sigma)}\left[(1-\sigma)\frac{u_r}{r} + \sigma\left(\frac{\partial u_r}{\partial r} + \frac{\partial u_z}{\partial z}\right) - \frac{1+\sigma}{3}\beta T(r,z)\right] \qquad [6\text{-}15]$$

$$A_z = B_r = \frac{-E}{\rho(1+\sigma)}\frac{1}{2}\left(\frac{\partial u_r}{\partial z} + \frac{\partial u_z}{\partial r}\right) \qquad [6\text{-}16]$$

This method is accurate in time to second order and stable providing [Potter, 1977] :

$$\Delta t < \frac{\Delta}{|v_m|} \qquad [6\text{-}17]$$

$$\varepsilon > \frac{1}{4}\left(\frac{\Delta t\, v_m}{\Delta}\right)^2 + \frac{1}{2}\left(\frac{\Delta t\, v_m}{\Delta}\right)^4 \qquad [6\text{-}18]$$

where Δ is the mesh size and v_m is the maximum velocity a disturbance can propagate. In our case, this is the longitudinal speed of sound and we choose $\Delta t = 0.1\ \Delta / C_L$.

At time equal zero, the initial conditions of the problem are that the displacement and velocity are zero everywhere. After the first time step (typically < 1 ns), the laser has deposited some energy in the target creating a non-uniform temperature distribution. The stresses associated with this temperature distribution are determined by eqs. 6-13 through 6-15. These stresses and their spatial derivatives allow one to calculate G_r and G_z, via eqs. 6-10 and 6-11, from which the velocity components can be determined from eqs. 6-8 and 6-9. The radial and axial displacement can then be found by integrating eqs. 6-4 and 6-6 :

$$u_r(t + \Delta t) = u_r(t) + \Delta t\, v_r(t + \Delta t) \qquad [6\text{-}19]$$

$$u_z(t + \Delta t) = u_z(t) + \Delta t\, v_z(t + \Delta t) \qquad [6\text{-}20]$$

6.3.3 Application of the Boundary Conditions and the Laser-induced Temperature Distribution.

In order to solve the differential equations which were derived in the previous section, one must specify the laser-induced temperature distribution and finite boundaries

over which the numerical solution is calculated. In this case, boundaries must be set at r = 0, r = r_{max}, z = 0, and z = z_{max} and special consideration must be given to each boundary.

6.3.3.1. Application to Non-boundary Points

The differential equations describing the stresses (eqs. 6-13 through 6-16) can be simplified using the longitudinal (C_l) and transverse (C_t) speeds of sound [Landau and Lifshitz, 1986] :

$$C_l^2 = \frac{E(1-\sigma)}{\rho(1+\sigma)(1-2\sigma)} \qquad [6\text{-}21]$$

$$C_t^2 = \frac{E}{2\rho(1+\sigma)} \qquad [6\text{-}22]$$

Rewriting eqs. 6-13 through 6-16 using the laser-induced temperature distribution (eq. 6-1) gives :

$$A_r = a_1\Delta\frac{\partial u_r}{\partial r} + 2a_0\Delta\frac{u_r}{r} + a_2\Delta\frac{\partial u_z}{\partial z} + a_3 e^{-\frac{r^2}{w^2}} e^{-\frac{z}{D}} \qquad [6\text{-}23]$$

$$B_z = a_2\Delta\frac{\partial u_r}{\partial r} + 2a_0\Delta\frac{u_r}{r} + a_1\Delta\frac{\partial u_z}{\partial z} + a_3 e^{-\frac{r^2}{w^2}} e^{-\frac{z}{D}} \qquad [6\text{-}24]$$

$$C_\phi = 2a_{00}\Delta\frac{u_r}{r} + a_2\Delta\left(\frac{\partial u_r}{\partial r} + \frac{\partial u_z}{\partial z}\right) + a_3 e^{-\frac{r^2}{w^2}} e^{-\frac{z}{D}} \qquad [6\text{-}25]$$

$$A_z = B_r = a_4\Delta\left(\frac{\partial u_r}{\partial z} + \frac{\partial u_z}{\partial r}\right) \qquad [6\text{-}26]$$

where

$$a_{00} = -\frac{C_l^2}{2\Delta} \qquad a_0 = -\frac{C_l^2}{2\Delta}\left(\frac{\sigma}{1-\sigma}\right)$$

$$a_1 = -\frac{C_l^2}{\Delta} \qquad a_2 = -\frac{C_l^2}{\Delta}\left(\frac{\sigma}{1-\sigma}\right)$$

$$a_3(t \le \tau) = C_l^2 \frac{1+\sigma}{3(1-\sigma)}\beta T_0 \frac{t}{\tau} \qquad a_3(t \ge \tau) = C_l^2 \frac{1+\sigma}{3(1-\sigma)}\beta T_0$$

$$a_4 = -\frac{C_t^2}{\Delta} \qquad \text{[6-27]}$$

Note that these constants have been defined in order to minimize calculations. Thus, although the constants a_0 and a_2 differ by only a factor of two, defining separate constants eliminates the step of multiplying a_0 by two each time A_r and B_z are calculated. On a 300 x 400 grid with 4000 time steps, this saves nearly one billion unnecessary multiplications from being done. Note that the factors of two and Δ in eqs. 6-23 through 6-26 will disappear when these equations are converted into difference formulas.

6.3.3.2. Application to Points on the Boundary z = 0

The boundary at z = 0, the only boundary between the semi-infinite target and a different material (air), needs special consideration. For a surface free of tractions, one has (see eq. 5-7) :

$$\sigma_{zz}\big|_{z=0} = 0 \;\Rightarrow\; B_z\big|_{z=0} = 0 \qquad \text{[6-28]}$$

$$\sigma_{rz}\big|_{z=0} = 0 \;\Rightarrow\; B_r\big|_{z=0} = A_z\big|_{z=0} = 0 \qquad \text{[6-29]}$$

Since neither σ_{rr} nor $\sigma_{\phi\phi}$ is specified on the boundary at z = 0, we must calculate the value of A_r and C_ϕ on the surface from Eqs. 6-23 and 6-25. However, both of these

equations contain a term which is the derivative of u_z in the z-direction, an unknown quantity on the surface. Since we know $B_z = 0$ on the surface from the boundary conditions, this problem can be avoided by solving Eq. 6-24 for this term :

$$\Delta\frac{\partial u_z}{\partial z} = -\frac{a_2}{a_1}\Delta\frac{\partial u_r}{\partial r} - \frac{2a_0}{a_1}\Delta\frac{u_r}{r} - \frac{a_3}{a_1}e^{-\frac{r^2}{w^2}} \qquad [6\text{-}30]$$

Substituting this expression into Eqs. 6-23 and 6-25 yields :

$$A_r\big|_{z=0} = c_1\Delta\frac{\partial u_r}{\partial r} + 2c_3\Delta\frac{u_r}{r} + c_2 e^{-\frac{r^2}{w^2}} \qquad [6\text{-}31]$$

$$C_\phi\big|_{z=0} = c_4\Delta\frac{\partial u_r}{\partial r} + 2c_5\Delta\frac{u_r}{r} + c_2 e^{-\frac{r^2}{w^2}} \qquad [6\text{-}32]$$

where

$$c_1 = a_1 - \frac{a_2^2}{a_1} \qquad c_2 = a_3 - \frac{a_2 a_3}{a_1}$$

$$c_3 = a_0 - \frac{a_2 a_0}{a_1} \qquad c_4 = a_2 - \frac{a_2^2}{a_1} \qquad [6\text{-}33]$$

$$c_5 = a_{00} - \frac{a_2 a_0}{a_1}$$

Since Eqs. 6-31 and 6-32 only contain derivatives in the radial direction, they can be calculated on the boundary at z = 0.

6.3.3.3. Application to Points on the Boundary r = 0

Although there is no boundary condition on the radial axis, special consideration is needed because several terms (eqs. 6-10, 6-11, 6-23, 6-24, 6-25, 6-31 and 6-32) are inversely proportional to the radial position. For these terms, the values are calculated

close to the axis and then extrapolated back to r = 0. The details of this process will be explained in section 6.2.4.

6.3.3.4. Application to Points on the Boundary $z = z_{max}$ and $r = r_{max}$

In order to obtain a numerical solution, a maximum value of r and z must be chosen within the semi-infinite target and artificial boundaries must be applied. For $r = r_{max}$ and $z = z_{max}$, the displacements u_r and u_z have been chosen to be fixed at zero. This artificial boundary will cause any acoustic waves reaching it to be reflected back towards the original interaction region. Since this return wave is an unphysical artifact, r_{max} and z_{max} must be chosen large enough to insure these effects do not influence the area of interest during the time of interest.

6.3.4 Finite Difference Algorithm

In order to numerically solve the system of differential equations described above, the displacements (u_r and u_z) and stress functions (A, B, and C) are calculated at each point on a two-dimensional grid in r and z (figure 6-1) and a finite difference algorithm is used to calculate the needed derivatives. In this figure, gridpoints at which the displacements are calculated are denoted with squares and stress gridpoints are denoted with circles. Using a finite difference algorithm, derivatives are represented as the difference between the value of a variable at two adjacent grid points divided by the distance between them (Δ). Since this procedure gives the value of the derivative at the midpoint of the two gridpoints, the stress functions A, B, and C are defined at the

midpoints of the grid for the displacement variables. In particular, since only the radial derivatives of A and C are needed (eqs. 6-10 and 6-11), the gridpoints for these functions are defined to be at the same z values as the displacements but at intermediate r values (see figure 6-1). Likewise, the gridpoints for B are defined at the same r values and intermediate z values since only derivatives in the z direction are required (eqs. 6-10 and 6-11). Gridpoints denoted by an "x" are locations where the value of the displacement is needed in order to calculate an adjacent stress. These points, labeled u_D, are calculated by averaging the four diagonal nearest displacement gridpoints.

In the equations that follow, the subscripts i and j are integers which represent the location of the grid point ($r = i\Delta$, $z = j\Delta$). Note that since the grids for different variables are interlaced, the indices i and j do not represent the same physical point for different variables. For instance, A (i = 0, j = 0) written as $A_{0,0}$ in the text or A(0,0) in figure 6-1, is defined at $r = \Delta/2$, $z = 0$, while $B_{0,0}$ is defined at $r = 0$, $z = \Delta/2$ (see figure 6-1). Note also that in the equations below, the first subscript for the variables refers to its component (r, z, or ϕ) and the second and third subscripts give the values of i and j.

6.3.4.1. Difference Equations For Non-Boundary Points

The difference equations for the components of G (see eqs. 6-10 and 6-11) can be written as :

$$G_{r\,i,j} = a_5\left(A_{r\,i,j} - A_{r\,i-1,j} + B_{r\,i,j} - B_{r\,i,j-1}\right) + \frac{a_8}{i}\left(A_{r\,i,j} + A_{r\,i-1,j} - C_{\phi\,i,j} - C_{\phi\,i-1,j}\right) \qquad [6\text{-}34]$$

$$G_{z\,i,j} = a_5\left(A_{z\,i,j} - A_{z\,i-1,j} + B_{z\,i,j} - B_{z\,i,j-1}\right) + \frac{a_8}{i}\left(A_{z\,i,j} + A_{z\,i-1,j}\right) \qquad [6\text{-}35]$$

where two new constants have been defined :

$$a_5 = \frac{\Delta t}{\Delta} \qquad a_8 = \frac{\Delta t}{2\Delta} \qquad [6\text{-}36]$$

The equations for the stresses (eq. 6-23 through 6-26) now become

$$A_{r\,i,j} = a_1\left(u_{r\,i+1,j} - u_{r\,i,j}\right) + \frac{a_0}{i+1/2}\left(u_{r\,i+1,j} + u_{r\,i,j}\right) + a_2\left(u_{zD\,i,j} - u_{zD\,i,j-1}\right) + a_3 e^{Rnorm(i+1/2)^2} e^{Znorm\cdot j} \qquad [6\text{-}37]$$

$$A_{z\,i,j} = a_4\left(u_{rD\,i,j} - u_{rD\,i,j-1} + u_{z\,i+1,j} - u_{z\,i,j}\right) \qquad [6\text{-}38]$$

$$B_{z\,i,j} = a_2\left(u_{rD\,i,j} - u_{rD\,i-1,j}\right) + \frac{a_0}{i}\left(u_{rD\,i,j} + u_{rD\,i-1,j}\right) + a_1\left(u_{z\,i,j+1} - u_{z\,i,j}\right) + a_3 e^{Rnorm\cdot i^2} e^{Znorm(j+1/2)} \qquad [6\text{-}39]$$

$$B_{r\,i,j} = a_4\left(u_{r\,i,j+1} - u_{r\,i,j} + u_{zD\,i,j} - u_{zD\,i-1,j}\right) \qquad [6\text{-}40]$$

$$C_{\phi\,i,j} = a_2\left(u_{r\,i+1,j} - u_{r\,i,j}\right) + \frac{a_{00}}{i+1/2}\left(u_{r\,i+1,j} + u_{r\,i,j}\right) + a_2\left(u_{zD\,i,j} - u_{zD\,i,j-1}\right) + a_3 e^{Rnorm(i+1/2)^2} e^{Znorm\cdot j} \qquad [6\text{-}41]$$

where two new constants have been defined :

$$Rnorm = -\frac{\Delta^2}{d^2} \qquad Znorm = -\frac{\Delta}{D} \qquad [6\text{-}42]$$

and the displacements at the diagonal midpoints of the grid have been defined as :

$$u_{zD\,i,j} = \frac{1}{4}\left[u_{z\,i+1,j} + u_{z\,i-1,j} + u_{z\,i,j+1} + u_{z\,i,j-1}\right] \qquad [6\text{-}43]$$

$$u_{rD\,i,j} = \frac{1}{4}\left[u_{r\,i+1,j} + u_{r\,i-1,j} + u_{r\,i,j+1} + u_{r\,i,j-1}\right] \qquad [6\text{-}44]$$

The algorithm to find G_z at a gridpoint is illustrated in figure 6-2. In order to calculate $G_z(i,j)$, the value of A_z must be known at both (i-1,j) and (i+1,j) as described by eq. 6-35. The value of A_z is calculated from the values of u_z (adjacent on the left and right) and values of u_r (adjacent above and below) via eq. 6-38. Since the latter points do not fall directly on a grid point, the value of u_r at this point (labeled by an x, and denoted u_{rD} in figure 6-2) is found from averaging the values of u_r at the four diagonal adjacent grid points (eq. 6-44). In a similar manner, the values of B_Z are found at the appropriate grid point using eq. 6-39. Note that the value of B_z also depends on the temperature at that point.

6.3.4.2. Difference Equations on the Boundary z = 0

The boundary conditions for A and B are given by eqs. 6-28 and 6-29. Combining this with the difference equation for the r component of G (eq. 6-34) and setting j = 0 gives :

$$G_{r\,i,0} = a_5\left(A_{r\,i,0} - A_{r\,i-1,0} + 2B_{r\,i,0}\right) + \frac{a_8}{i}\left(A_{r\,i,0} + A_{r\,i-1,0} - C_{\phi\,i,0} - C_{\phi\,i-1,0}\right) \qquad [6\text{-}45]$$

Note that $B_{r\,i,0}$ is not equal to zero because it is not located on the surface (see figure 6-1) but one half mesh size below the surface. The factor of 2 in front of this term comes from

the fact that this derivative is found from the difference of two points one half mesh size apart. With the boundary conditions, the difference equation for the z component of G (see eq. 35) simplifies to

$$G_{z\,i,0} = 2a_5 B_{z\,i,0} \qquad [6\text{-}46]$$

The difference equations for the needed stresses on the boundary can be found from eqs. 6-31 and 6-32 :

$$A_{r\,i,0} = c_1\left(u_{r\,i+1,0} - u_{r\,i,0}\right) + \frac{c_3}{i+1/2}\left(u_{r\,i+1,0} + u_{r\,i,0}\right) + c_2 e^{Rnorm(i+1/2)^2} \qquad [6\text{-}47]$$

$$C_{\phi\,i,0} = c_4\left(u_{r\,i+1,0} - u_{r\,i,0}\right) + \frac{c_5}{i+1/2}\left(u_{r\,i+1,0} + u_{r\,i,0}\right) + c_2 e^{Rnorm(i+1/2)^2} \qquad [6\text{-}48]$$

The equations for B near the boundary (at z = Δ/2) can be found from equations 6-39 and 6-40 by setting j = 0 :

$$B_{z\,i,0} = a_2\left(u_{rD\,i,0} - u_{rD\,i-1,0}\right) + \frac{a_0}{i}\left(u_{rD\,i,0} + u_{rD\,i-1,0}\right) + a_1\left(u_{z\,i,1} - u_{z\,i,0}\right) + a_3 e^{Rnorm\cdot i^2} e^{Znorm/2} \qquad [6\text{-}49]$$

$$B_{r\,i,0} = a_4\left(u_{r\,i,1} - u_{r\,i,0} + u_{zD\,i,0} - u_{zD\,i-1,0}\right) \qquad [6\text{-}50]$$

6.3.4.3. Difference Equations on the Radial Axis

Since many variables contain terms which are inversely proportional to the radial position, special care must be taken on the radial axis. Given the grid defined in figure 6-1, only the stress function B and the displacements (and thus the G's) are needed on the

axis. For these variables, an additional gridpoint is introduced at r = Δ/4. The value at r = 0 is then calculated from a linear extrapolation using the values ar r = Δ/4 and r = Δ :

$$F(0) = \frac{1}{3}\left[4F\left(\frac{\Delta}{4}\right) - F(\Delta)\right] \qquad [6\text{-}51]$$

The difference equation for G_r (see eq. 6-34) at r = Δ/4 can be written as :

$$\begin{aligned} G_{r\,j}\left(\frac{\Delta}{4}\right) = a_5\left[2A_{r\,j}\left(\frac{\Delta}{2}\right) - 2A_{r\,j}(0) + B_{r\,j}\left(\frac{\Delta}{4}\right) - B_{r\,j-1}\left(\frac{\Delta}{4}\right)\right] \\ + \frac{a_8}{1/4}\left[A_{r\,j}\left(\frac{\Delta}{2}\right) + A_{r\,j}(0) - 2C_{\phi\,j}\left(\frac{\Delta}{4}\right)\right] \end{aligned} \qquad [6\text{-}52]$$

where the subscript i (which is an integer which refers to a mesh point) has been replaced by the actual radial position of the mesh point (value of r) in parenthesis. The factor of two in the first two terms comes from the fact that the spatial derivative is found from two points separated by one half mesh size. In the second term, the value of C is found directly at r = Δ/4 instead of averaging two adjacent points. Using eq. 6-36, this simplifies to :

$$G_{r\,j}\left(\frac{\Delta}{4}\right) = a_5\left[4A_{r\,j}\left(\frac{\Delta}{2}\right) - 4C_{\phi\,j}\left(\frac{\Delta}{4}\right) + B_{r\,j}\left(\frac{\Delta}{4}\right) - B_{r\,j-1}\left(\frac{\Delta}{4}\right)\right] \qquad [6\text{-}53]$$

The difference equation for the z-component of G (see eq. 6-35) at r = Δ/4 can be found using a similar procedure :

$$G_{z\,j}\left(\frac{\Delta}{4}\right) = a_5\left[4A_{z\,j}\left(\frac{\Delta}{2}\right) + B_{z\,j}\left(\frac{\Delta}{4}\right) - B_{z\,j-1}\left(\frac{\Delta}{4}\right)\right] \qquad [6\text{-}54]$$

The difference equations for the r and z components of G at r = Δ/4 (eqs. 6-53 and 6-54) require the stress variables B and C to be known at r = Δ/4. The value of C is found from a linear extrapolation using the values at r = Δ/2 and r = 3Δ/2 :

$$C_{\phi j}\left(\frac{\Delta}{4}\right) = \frac{1}{4}\left[5C_{\phi j}\left(\frac{\Delta}{2}\right) - C_{\phi j}\left(\frac{3\Delta}{2}\right)\right] \qquad [6\text{-}55]$$

The r-component of B at r = Δ/4 (see eq. 6-40) can be written as

$$B_{r j}\left(\frac{\Delta}{4}\right) = a_4\left[u_{r\,j+1}\left(\frac{\Delta}{4}\right) - u_{r\,j}\left(\frac{\Delta}{4}\right) + 2\left(u_{zD\,j}\left(\frac{\Delta}{2}\right) - u_{zD\,j}(0)\right)\right] \qquad [6\text{-}56]$$

and the z component (see eq. 6-39) takes the form :

$$\begin{aligned} B_{z\,j}\left(\frac{\Delta}{4}\right) = {} & 2a_2\left[u_{rD\,j}\left(\frac{\Delta}{2}\right) - u_{rD\,j}(0)\right] + 4a_0\left[u_{rD\,j}\left(\frac{\Delta}{2}\right) + u_{rD\,j}(0)\right] \\ & + a_1\left[u_{z\,j+1}\left(\frac{\Delta}{4}\right) - u_{z\,j}\left(\frac{\Delta}{4}\right)\right] + a_3 e^{Rnorm/2} e^{Znorm(j+1/2)} \end{aligned} \qquad [6\text{-}57]$$

which simplifies to :

$$\begin{aligned} B_{z\,j}\left(\frac{\Delta}{4}\right) = {} & 4a_2 u_{rD\,j}\left(\frac{\Delta}{2}\right) + a_1\left[u_{z\,j+1}\left(\frac{\Delta}{4}\right) - u_{z\,j}\left(\frac{\Delta}{4}\right)\right] \\ & + a_3 e^{Rnorm/16} e^{Znorm(j+1/2)} \end{aligned} \qquad [6\text{-}58]$$

Thus, in order to find the components of B at r = Δ/4 (see eqs. 6-56 and 6-58), we must know the values of the displacement at r = Δ/4. These are found from extrapolation, using the values at r = 0, and r = Δ :

$$u_j\left(\frac{\Delta}{4}\right) = \frac{1}{4}\left[3u_j(0) + u_j(\Delta)\right] \qquad [6\text{-}59]$$

6.3.5 Description of the Computer Program

A computer program written in Fortran was used to implement the numerical algorithm described above. This program is included in the Appendix of this chapter, section 6.6. The inputs to the program are the optical penetration depth D, the laser pulse duration τ, the thermal expansion coefficient β, the longitudinal speed of sound C_l, the Poisson ratio σ, the density ρ, and the laser-induced temperature distribution T(r,z). Although the equations in the preceding section were derived for temperature distribution with a Gaussian radial profile and an exponential axial profile, any arbitrary distribution may be used.

Of particular interest is a temperature profile with a "top-hat" radial distribution. In order to avoid the problems associated with modeling the sharp edges of the top-hat on a numerical grid, the edges are rounded by using a cosine function :

$$T(r,z) = T_0\, e^{-z/D} \qquad for\ r \le r_1$$

$$T(r,z) = T_0\, e^{-z/D}\, \frac{1}{2}\left\{1 + \cos\left[\frac{\pi}{k_1}(r - r_3)\right]\right\} \qquad for\ r \le r_2 \qquad [6\text{-}60]$$

$$T(r,z) = 0 \qquad for\ r > r_2$$

where r_1, r_2, r_3, and k_1 are chosen to round the edge and keep the total energy the same as a top-hat of radius w. For w = 500 μm, these constants are chosen with the values r_1 = 450 μm, r_2 = 530 μm, r_3 = 460 μm and k_1 = 77 μm.

After choosing the mechanical, optical and thermal constants of the material and the characteristics of the incident laser beam, constants pertaining to the numerical grid must be specified. These include the number of grid points in both the r and z direction (imax and jmax respectively), the grid spacing Δ, and the number of time steps. The duration of each time step, Δt, is determined by the grid spacing and the speed of sound (see eq. 6-17). The number of grid points is usually set equal to the maximum number the computer can handle in a reasonable amount of time and depends on the speed and memory capabilities. A typical grid size is 300 by 400 cells. Note that since the program contains 13 double precision two-dimensional arrays of this size, 12 Mbytes of RAM is required (300 x 400 x 13 x 8 bytes/number). The grid size Δ and the number of time steps are then chosen such that no unphysical reflections from the artificial boundaries reach the region of interest in the time of interest. Typically values are $\Delta \sim 10$ μm, $\Delta t \sim 0.2$ to 0.5 ns and 4000 time steps.

The number of floating point calculations required for the numerical grid specified in the last paragraph is exceedingly high. The number of grid points (300 x 400) times the number of time steps (4000) shows that 480 million cells must be calculated. Since the algorithm requires about 100 calculations per cell, 50 billion floating point calculations are needed for a typical run. The time required to run this code on different computers is summarized in Table 6-1.

As Table 6-1 shows, it is unreasonable to run this code on a 386 based personal computer. For this reason, the code was prepared to run on the MIT Athena workstations and the MIT Cray supercomputer. The acquisition of an inexpensive personal computer based on the Pentium processor, however, ran the code 15 times faster than the 386 and made it possible to run this code on the desktop. For this reason, all calculations presented in this thesis were run on this PC.

Computer	Run Time (hr:min)	Normalized Run-Time	MFLOPs (10^6 op/s)
PC 386 (20 MHz)	60:00	15	0.25
PC 486 (33 MHz)	14:50	3.7	1.0
Workstation IBM RS-6000	5:00	1.25	2.8
PC Pentium (60 MHz)	4:00	1	3.5
CRAY X-MP	0:08	1 / 32	112

Table 6-1. Although a 386 based personal computer takes nearly 3 days (an unreasonable amount of time) to run this code, the advent of the Pentium PC (~ $2500) makes it possible to run this code on the desktop.

6.4 VERIFICATION OF THE NUMERICAL SOLUTION

Although numerical methods can be used to solve equations where analytical solutions cannot be found, one major drawback of these methods is the difficulty in

verifying that the output of the computer program is actually the desired solution. For example, although the steady state analytical solution derived in section 5.2 was quite complex, the solution was verified by substitution back into the original equations (see section 5.6). This technique of verification cannot be used with a computer generated numerical solution.

The verification technique that was used on this numerical solution consisted of two steps. First, the program was hand checked against the difference equations described in section 6.2.4. for a 3 by 3 grid for two time steps. Second, the predictions from the code were compared to the analytical solutions derived in chapter 4 (one dimensional time dependent solution) and chapter 5 (three dimensional steady state solution).

6.4.1 Comparison to the One Dimensional Time Dependent Solution

An analytical time dependent solution of the thermoelastic wave equation was derived in chapter 4 in a one dimensional geometry. This geometry can be simulated in the numerical code by using a temperature distribution with no radial dependence. Figure 6-3 shows a comparison between the analytical solution (solid line, labeled theory) and the numerical solution (data points) for the predicted displacement u_z at the surface ($z = 0$) and at a depth $z = D$. The discontinuity at 200 ns corresponds to the time that the bipolar wave reaches a depth D for C_l = 2000 m/s and D = 400 μm. The grid size used in the numerical simulation was 20 μm ($\Delta = 0.05$ D) and the time step was 1 ns. Although the predictions from the numerical model agree quite well with the analytical solution, there

are discrepancies beginning at 0 ns (for z = 0) and 200 ns (for z = D). Note that these discrepancies begin exactly when the bipolar wave reaches that point.

A comparison of the predicted stress distribution at two different times (100 ns and 400 ns) is shown in figure 6-4. As expected, although the numerical model quantitatively shows the correct bipolar wave, it cannot reproduce the true discontinuous solution. This explains the small discrepancies in the predicted displacements, shown in figure 6-3, which occurred at times corresponding to the passing of the bipolar wave. When solving a problem on a mathematical grid, it is essential that the grid spacing is always smaller than the smallest feature being modeled. Clearly, this will not be possible in a problem where a discontinuous jump is present.

The artifacts associated with the discontinuous nature of the biploar wave can be minimized by reducing the grid spacing. Figures 6-5 and 6-6 show the predicted displacements and stress distributions when the grid spacing and time step are reduced by a factor of 5 (Δ = 0.01 D, Δt = 0.2 ns). With this finer resolution, the predicted displacements at z = 0 and z = D now accurately follow the analytical solution (figure 6-5). Although the predicted stress distribution (figure 6-6) also show a dramatic improvement over the low resolution case, there are still discrepancies between it and the analytical solution.

One standard technique to model wave front discontinuities on a numerical grid entails introducing an artificial viscosity [Potter, 1977]. This reduces the "ringing"

associated with a sharp discontinuity by spreading the wave front over several grid points. We can benefit from this approach without adding an artificial viscosity by considering the duration of the laser pulse. Although the wave front is discontinuous for a delta function laser pulse (as shown by the analytical solution), for a pulse duration of 10 ns the wave front will spread out to a width of 20 μm (for C_l = 2000 m/s). Figure 6-7 shows the numerical prediction for the stress distribution assuming a laser pulse duration of 10 ns. The artificial "ringing" associated with the wave front has been further reduced (see figure 6-6). Note that the discrepancy between the slopes of the wave fronts in figure 6-7 is expected because the analytical solution assumes an infinitely short laser pulse.

6.4.2 Comparison to the Three Dimensional Steady State Solution

A three dimensional analytical steady state solution of the thermoelastic wave equation was derived in chapter 5. This solution can be compared to the numerical solution for times much longer than the characteristic time of motion. For a sound velocity of 2000 m/s and a penetration depth of 400 μm, this time is 200 ns (D / C_l). Thus, after 2000 ns, the numerical solution should agree with the analytical steady state solution. In the following figures, it was assumed that the radial profile of the laser was Gaussian with a radius (w) of 400 μm, the penetration depth (D) was 400 μm, the Poisson ratio (σ) was 0.25, the laser-induced temperature rise was 10^0C, the expansion coefficient was 10 x 10^{-6} /K, the longitudinal sound velocity was 2000 m/s, the grid spacing (Δ) was 10 μm, and the time step (Δt) was 0.5 ns.

The surface displacement in the z direction, u_z, as a function of radial position is shown in figure 6-8 for both the numerical and analytical solutions. There is good agreement between the two solutions with the numerical model overestimating the movement by several percent. Note that the surface displacement resembles the Gaussian radial profile of the incident laser beam. The surface displacement in the r direction, u_r, as a function of radial position is shown in figure 6-9. In this case, there is excellent agreement between the numerical and analytical solutions. The peak radial displacement occurs at r = w, the 1/e radius of the initial Gaussian radial profile of the laser beam.

The radial and circumferential stress distributions on the surface as a function of radial position for both the numerical and analytical solution are shown in figures 6-10 and 6-11. In both cases, the two solutions gives identical results. Note that the surface radial stress is always compressive while the surface circumferential stress becomes tensile at radii greater than w. The circumferential and axial stress as a function of depth into the sample are shown in figures 6-12 and 6-13. The circumferential stress is plotted at a radial position of 10 μm (r = w/40) while the axial stress is plotted on the axis (r = 0). The predictions from the numerical model are in complete quantitative agreement with the analytical solution.

6.5 TIME DEPENDENT THREE DIMENSIONAL DISPLACEMENTS AND STRESSES

The complete quantitative agreement between the numerical and analytical solutions described in the previous section gives a very high level of confidence in the

accuracy of the numerical method. This numerical method can now be extended past the earlier analytical solutions to give new information regarding the time dependent surface expansion and the transient stresses

6.5.1 Time Dependent Surface Expansion

The experimental technique of interferometric surface monitoring (discussed in chapters 3, 7, and 8) uses an interferometer to measure the laser-induced time dependent surface expansion of a target material. By comparing the experimentally measured movement to the theoretically predicted movement, important optical and mechanical properties of the material can be determined. These properties allow the laser-induced stresses to be calculated.

The numerically predicted surface expansion (u_z at $z = 0$) as a function of time for a rounded top-hat laser profile (see eq. 6-60) is shown in figure 6-14. This figure shows a complex surface motion which was absent in the simple one dimensional case which predicted a smooth, exponential approach to a new equilibrium value (see eq 4-52 and figure 4-1). The motion shown in figure 6-14 corresponds to $D = 400$ μm, $w = 500$ μm, $R = 1.25$, $C_l = 3000$ m/s, $\sigma = 0.25$, $T = 10^0$C, $\beta = 10^{-5}$ /K, $\Delta = 10$ μm, and $\Delta t = 0.25$ ns.

The functional dependence of the complex features in the surface expansion is shown in figure 6-15. The location of the first peak at 167 ns corresponds to the time for acoustic waves to reach the center from the edge of the beam radius and thus is only a function of w and C_l. Since w is known, the longitudinal speed of sound can be

determined. The location of the second peak (at 333 ns) is related to the tranverse speed of sound (see eq. 6-22). Thus, given w and C_l, the Poisson ratio can be determined from the second peak. Since the initial slope of the expansion curve is only a function of w, C_l, σ and D, the optical penetration depth can now be determined. Finally, by measuring the equilibrium displacement, the ratio of the expansion coefficient to the heat capacity can be calculated. The physical properties are precisely those needed to calculate the laser-induces stressses, as explained in section 5.4.3.

6.5.2 Transient Stresses

The photomechanical model of ablation depends on the generation of tensile stresses to initiate the ablation process. Although the one dimensional solution predicts the formation of a transient axial tensile stress, this stress occurs well beneath the surface, not in the region where ablation is observed to occur. The three dimensional steady state solution showed the existence of long-lived circumferential tensile stresses at the surface of the material. This was a very important and non-intuitive finding since there is no physical boundary in the r or ϕ directions like the boundary at $z = 0$ which gave rise to the axial tensile stress. This target-air interface at $z = 0$, however, is responsible for the generation of the circumferential surface tensile stress because of a coupling of the surface stresses via the boundary conditions. The fact that this can create tensile stresses on the surface in the steady state implies that transient tensile stresses may also be created. The numerical solution allows us to examine this implication for the first time. In all figures below, it is assumed that the radial profile of the laser is a rounded top-hat (see eq. 6-60)

with a radius of 600 μm. Furthermore, it is assumed that D = 860 μm, R = 0.7, C_l = 2850 m/s, and σ = 0.25.

The numerically predicted circumferential stress on the surface of the target is shown in figures 6-16 and 6-17 for different times. Initially, the stress distribution is just proportional to the laser-induced temperature distribution (rounded top-hat) and is compressive (negative values). After 250 ns, however, the initial stress has evolved into a distribution with significant tensile stresses. Although the surface for r > w remains in tension, for r < w the surface oscillates between compression and tension. The numerical solution at 2500 ns is in agreement with the steady state analytical solution derived in chapter 5. Note that there should be a small discrepancy between these two solutions since the numerical solution uses a rounded top-hat laser profile while the analytical solution uses a true top-hat distribution.

The computed radial stress on the surface of the target is shown in figures 6-18 and 6-19 for different times. As we know from the steady state solution, the initial and steady state surface radial stresses are always compressive and thus are not thought to play a role in the ablation process. The time dependent solution, however, shows that for intermediate times, significant tensile stresses do develop on the surface. In fact, tensile stresses of between 0.25 and 0.40 σ_{max} appear at all radial positions between r = 0 and r = w. In addition, the stress distribution oscillates several times between compression and tension.

The shear stress just below the surface (z = 0.05 D) as a function of radial position is shown for different times in figures 6-20 and 6-21. The shear stress on the surface (z = 0) is zero because of the boundary conditions (eq. 6-29). Since the shear stress has no temperature dependence (eq. 5-3), initially it is zero. After 200 ns, a large shear has developed at the sharp temperature gradient at the laser radius (r = w). Although this shear remains constant, the stress at r < w oscillates in sign several times over the next 200 ns. Note that the sign of the shear stress does not correspond to tension and compression like it did for the other stress components, but only to the direction of the shear. At longer times, the stress approaches the steady state analytical solution (see figure 6-21) but has a slightly smaller amplitude since the analytical solution was found for a top-hat radial laser profile without rounded corners.

The results displayed in figures 6-16 through 6-21 are very significant findings. They show, for the first time, the existence of significant tensile stresses on the surface within the heated region (r < w). This finding lends great support to the photomechanical model of laser ablation.

6.6 CONCLUSIONS

Understanding the thermoelastic response of a target material to the absorption of laser light is essential to investigating the photomechanical model of ablation. In chapters 4 and 5, analytical solutions describing the response of the target were determined for several limiting cases. These solutions provided insight into the role that different parameters (laser fluence, geometry, and optical, thermal, and mechanical properties of the

target material) played in determining the overall response to the laser light. These solutions were lacking, however, in two important respects. First, the transient stresses in a three dimensional geometry could not be studied, a major drawback since it is these stresses which are believed to initiate the ablation process. Secondly, the time dependence of the thermoelastic expansion was not determined. Since the experimental technique of interferometric surface monitoring measures this expansion, a detailed comparison between theory and experiment could not be made.

In this chapter, the full time dependent three dimensional solution to the thermoelastic wave equation was determined via numerical methods. This solution, which was checked extensively with the earlier analytical solutions in the appropriate limiting cases, overcame the two major drawbacks of these analytical solutions. In addition, the numerical solution can be extended to use an arbitrary laser-induced temperature distribution, an adjustable laser pulse duration, and a non isotropic target material.

A significant finding from this numerical solution, which allowed the transient stresses in a three dimensional geometry to be studied for the first time, was the formation of tensile stresses on the surface of the target. In particular, both the radial and circumferential components of the stress oscillated between compression and tension on the surface at radial positions between $r = 0$ and $r = w$. The amplitude of these tensile stresses were quite significant, reaching 40% of the initial peak compressive stress. Thus, for the first time, the photomechanical model predicts large tensile stresses on the surface, precisely where material failure is observed to occur.

A second important result obtained from the numerical solution described in this chapter is the complex time dependence of the thermoelastic expansion in three dimensions. This result is essential in order to quantitatively compare experimental results for the laser-induced thermoelastic expansion of different materials with theoretical predictions, described in the next two chapters. In addition, this solution showed additional features in the expansion curve, which were absent in the one dimensional solution, that allow one to determine several important optical, physical, and mechanical properties of the target material. These physical properties are precisely those needed to calculate the magnitude of the laser-induces stresses.

6.7 CHAPTER 6 APPENDIX : FORTRAN PROGRAM

The numerical method of solving the thermoelastic wave equation described in section 6.2 is implemented below in a computer program written in standard Fortran. A "C" in the first column denotes a comment statement that is ignored by the compiler. Additional comments, which do not appear in the actual code, have been added in curly brackets and bolded.

```
C Def5_rz.f : Fortran program to calculate displacement and stress waves
C in laser heated solid in three dimensions in cylindrical coordinates

    IMPLICIT Integer (t, r, z)
                                    {imx1 is number of cells in r direction, jmx1 in z}
    PARAMETER (imax = 300, jmax = 429, imx1 = imax+1, jmx1 = jmax+1)
                                                    {tmax is number of time cells}
                        {NumDep is how many penetration depths to lower boundary}
    PARAMETER (tmax = 3750, NumDep = 5)
    PARAMETER (Rint = 1, Zint = 1, Tint = 4, NumTim = 5)
```

```
      DOUBLE PRECISION  Ur(0 :imx1,0:jmx1),  Uz(0 :imx1,0:jmx1)
      DOUBLE PRECISION  Vr(0 :imax,0:jmax),  Vz(0 :imax,0:jmax)
      DOUBLE PRECISION  Gr(0 :imax,0:jmax),  Gz(0 :imax,0:jmax)
      DOUBLE PRECISION  Ar(0 :imax,0:jmax),  Az(0 :imax,0:jmax)
      DOUBLE PRECISION  Br(0 :imax,0:jmax),  Bz(0 :imax,0:jmax)
      DOUBLE PRECISION UrD(0 :imax,0:jmax), UzD(0 :imax,0:jmax)
      DOUBLE PRECISION  Cp(0 :imax,0:jmax)

      DOUBLE PRECISION Ur1_4(0:jmax), Uz1_4(0:jmax)
      DOUBLE PRECISION UrD1_4(0:jmax), UzD1_4(0:jmax)
      DOUBLE PRECISION Br1_4(0:jmax), Bz1_4(0:jmax), Cp1_4(0:jmax)

      DOUBLE PRECISION  Stor_Us(0:NumTim*2, 0:imax/Rint)
      DOUBLE PRECISION  Stor_Ut(0:2      , 0:tmax/Tint)
      DOUBLE PRECISION  Stor_Sz(0:NumTim*2, 0:jmax/Zint)
      DOUBLE PRECISION  Stor_Sr(0:NumTim*2, 0:imax/Rint)
      DOUBLE PRECISION  Time(1:5)
      DOUBLE PRECISION  dumr(0:imx1), dumz(0:imx1)

      DOUBLE PRECISION GzNEW, VzNEW, UzNEW, GrNEW, VrNEW, UrNEW
      DOUBLE PRECISION dum0, dum5, dum6, dum7, onethird
      DOUBLE PRECISION a1, a2, a3, a4, a5, a6, a7, c1, c2
      DOUBLE PRECISION i2, Rnorm, Znorm, Znorm2, Snorm, Smax, rho
      DOUBLE PRECISION eps, deltaT, sigma, alpha, temp0
      DOUBLE PRECISION PenDep, LasRad, Del, Zmax, Ct, Cl
      DOUBLE PRECISION Peakj, Peakval, a3_old, c3_old, pulse
      DOUBLE PRECISION a0, a00, a8, c3, c4, c5, Rnorm1
      DOUBLE PRECISION dUrdr, rUr, Temp, Guas_con, Cos_con, G_p

      INTEGER i, j, t, k, loop, loop1, tophat

      Time(1) = 250          {Sets the 5 times at which output will be given}
      Time(2) = 375          {Note that these numbers represent the number}
      Time(3) = 500          {of time steps. To get the actual time, you must}
      Time(4) = 750          {multiply by deltaT (Δt) }
      Time(5) = 3750

C Initialize starting array variables to zero

      loop = 0
      DO 10, j = 0, jmax
        Ur1_4(j) = 0
        Uz1_4(j) = 0
        DO 20, i = 0, imax
          Ur(i,j) = 0
```

```
        Uz(i,j) = 0
        Gr(i,j) = 0
        Gz(i,j) = 0
        Vr(i,j) = 0
        Vz(i,j) = 0
20     CONTINUE
10   CONTINUE

     DO 24, j = 0, jmx1
       Ur(imx1,j) = 0
       Uz(imx1,j) = 0
24   CONTINUE

     DO 28, i = 0, imax
       Ur(i,jmx1) = 0
       Uz(i,jmx1) = 0
28   CONTINUE

C Define Constants

     PenDep = 860                    {Optical Penetration Depth, D, in μm}
     LasRad = 500                    {Laser radius, w, in μm}
     Alpha = 1e-5                    {Thermal Expansion Coefficient, β, in /K}
     temp0 = 10                      {Peak Laser-Induced Temperature, in °C}
     Cl = 2.85                       {Longitudinal Sound Velocity, Cl, in nm / ns}
     Sigma = 0.25                    {Poisson Ratio, σ, unitless}
     Pulse = 10.0                    {Laser pulse Duration, τ, in ns}
                          {Constant Describing the Radial Laser Profile}
     Gaus_con = 1/93.0               {1/e of Gaussian in Gaussian Top-Hat}
     Cos_con = 3.1415926535/14.0     {Cosine Function for Rounding Top-Hat}
     G_p = 1.16                      {Amplitude for Gaussian Top-Hat}

     Snorm = -3*(1-sigma)/(alpha*temp0*Cl*Cl*(1+sigma))  {Normalizes stress to σmax}
     rho = 1200                      {Density, ρ, in Kg/m3}
     Smax = 10 * rho / Snorm         {Value of σmax, not used}
     Zmax = NumDep * PenDep          {Maximum size of grid in z direction, in μm}
     Del = Zmax / (jmax+1)           {Δ is based on z parameters, not r params.}

C Denominator should be close to the speed of sound
     deltaT = 0.1 * del / 2.5        { Choose denominator close to Cl so that Δt }
                                     { has a reasonable value like 0.25 or 0.4 }
    dum0 = (deltaT * Cl / Del)**2
     eps = 1.5 * (0.25*dum0 + 0.5*dum0**2)
     Ct = Cl * SQRT( (1.0 - 2.0*sigma) / (2.0 - 2.0*sigma) )
```

```
      tophat = Nint(LasRad / Del)
      Rnorm = -1.0 * (Del / LasRad)**2
C 1D    Rnorm = 0
      Znorm = -1.0 * Del / PenDep
      Znorm2 = Znorm / 2.0

      a0 = -0.5 * Cl**2 * (sigma / (1.0 - sigma)) / Del
      a00 = -0.5 * Cl**2 / Del
      a1 = -1.0 * Cl**2 / Del
      a2 = a1 * sigma / (1.0 - sigma)
      a3 = Cl**2 * alpha * temp0 * (1.0 + sigma) / (3.0*(1.0-sigma))
      a4 = -1.0 * Ct**2 / del
      a5 = deltaT / del
      a6 = 1.5 + eps
      a7 = 0.5 + eps
      a8 = 0.5 * deltaT / Del

      c1 = a1 - (a2**2)/a1
      c2 = a3 * (1 - a2/a1)
      c3 = a0 * (1 - a2/a1)
C     c3 = a0 * (1 - a2/a1) / Del
      c4 = a2 * (1 - a2/a1)
      c5 = (a00 - a2 * a0 / a1 )
C     c5 = (a00 - a2 * a0 / a1 ) / Del
      onethird = 1 / 3.0
      a3_old = a3
      c3_old = c3
                              {Output Files : increment .d31 each time program is run}
      OPEN(Unit = 3, File =  'Tdef_hea.d31', Status = 'New')      {Header information}
      OPEN(Unit = 4, File =  'Tdef_Us.d31', Status = 'New')       {u_r, u_z vs radial pos.}
      OPEN(Unit = 5, File =  'Tdef_Ut.d31', Status = 'New')       {u_r, u_z vs time}
      OPEN(Unit = 7, File =  'Tdef_Sz.d31', Status = 'New')       {σ_zz, σ_rz vs axial pos.}
      OPEN(Unit = 8, File =  'Tdef_Sr.d31', Status = 'New')       {σ_rr, σ_θθ vs radial pos.}

      Write(3, 901) ' All units are in microns and nanoseconds'
      Write(3, 901) ' '
      Write(3, 902) ' R Cells   = ',imax+1,'   Z Cells   = ',
     $       jmax+1,'   Time Cells = ',tmax
      Write(3, 903) ' Grid Size  = ',del, '   Time Step  = ',
     $       deltaT,'   Eps *1000  = ',eps*1000
      Write(3, 901) ' '
      Write(3, 903) ' Pen Depth  = ',PenDep,'   Beam Rad   = ',
     $       Lasrad,'   Aspect Rat = ',Lasrad/PenDep
      Write(3, 903) ' Poisson    = ',sigma, '   Cs (long)  = ',
     $       Cl,   '   Cs (trans) = ',Ct
```

```
      Write(3, 903) ' Expan *1e6 = ',alpha*1e6, '    Peak Temp  = ',
     $       temp0,    ' Pulse Duration = ',pulse
      Write(3, 901) ' '
      Write(3, 904)' a1 = ',a1,'   a2 = ',a2,'   a3 = ',a3,'   a4 = ',a4
      Write(3, 904)' a5 = ',a5,'   a6 = ',a6,'   c1 = ',c1,'   c2 = ',c2

      Write(3, 901) ' '
      Write(3, 913)' Rint = ',Rint,'    Zint = ',Zint,'    Tint = ',Tint
      Write(3, 901) ' '
      DO 29 k = 1, NumTim
        Write(3, 914)' Time ',k,' = ',deltaT * Time(k)
 29   CONTINUE

      Write(3, 901) ' '
      Write(3, 901) 'Temperature Dist. : Gaussian + cos'
      Write(3, 915) ' Guass_peak = ',G_p, '    Guass div  = ',
     $    1/Gaus_con,    '    Cos pi div = ',3.1415926535/Cos_con

  901 Format( A)
  902 Format( A, I9, A, I9, A, I9)
  903 Format( A, F9.4, A, F9.4, A, F9.4)
  904 Format( A, F9.5, A, F9.5, A, F9.5, A, F9.5)
  913 Format( A, I5, A, I5, A, I5)
  914 Format( A, I1, A, F6.0)
  915 Format( A, F6.2, A, F6.0, A, F6.1)

C ****************************************************************
C                   Main Time Loop
C ****************************************************************

      DO 30, t = 1, tmax

C Laser pulse duration is 10 nanoseconds
      If (t*deltaT.LE.10.0) Then
        a3 = a3_old * (t*deltaT/10.0)
        c3 = c3_old * (t*deltaT/10.0)
      Else
        a3 = a3_old
        c3 = c3_old
      Endif

C Find all the UrD and UzD, each is the sum of 4 diagonal neighbors
        DO 50, j = 0, jmax
          DO 60 i = 0, imx1
            dumz(i) = Uz(i,j) + Uz(i,j+1)
```

```
          dumr(i) = Ur(i,j) + Ur(i,j+1)
 60       CONTINUE

          UzD1_4(j) = 0.5 * dumz(0)
          UrD1_4(j) = 0.5 * dumr(0)

          DO 62 i = 0, imax
            UzD(i,j) = 0.25 * (dumz(i) + dumz(i+1))
            UrD(i,j) = 0.25 * (dumr(i) + dumr(i+1))
 62       CONTINUE
C 1D          UzD(imax,j) = UzD(imax-1,j)
C 1D          UrD(imax,j) = UrD(imax-1,j)
C 1D          Uz(imax+1,j) = Uz(imax,j)
C 1D          Ur(imax+1,j) = Ur(imax,j)
 50     CONTINUE

C ************** APPLY BOUNDARY CONDITIONS ***************

C **** BC for Ur ****    dUz/dz at boundary is found from Bz(i,0) = 0

C Find Ar and Cp for all r.
        DO 70, i = 0, imax
          i2 = i + 0.5
          dUrdr = Ur(i+1,0) - Ur(i,0)
          rUr = ( Ur(i+1,0) + Ur(i,0) ) / i2
          IF (i2.LE.44) THEN
            temp = c2 * G_p * exp(-1*(Guas_con*i2)**2)   {Comment out for Top-Hat}
C             temp = c2 * G_p                          {Comment out for Gaussian Top-Hat}
          ELSE IF (i2.LE.56) THEN
            temp = c2 * 0.5 *(1+COS(Cos_con*(i2-42)))        {Rounds Top-Hat}
          ELSE
            temp = 0
          ENDIF
          {For Gaussian profile, use line below, comment out 8 lines above}
C           temp = c2 * Exp(i2*i2*Rnorm)
          Ar(i,0) = c1*dUrdr + c3*rUr + temp
          Cp(i,0) = c4*dUrdr + c5*rUr + temp
 70     CONTINUE
        Cp1_4(0) = 0.25 * (5.0 * Cp(0,0) - Cp(1,0) )

C Find Br for all r
        DO 71, i = 1, imax
          Br(i,0) = a4*( Ur(i,1) - Ur(i,0) + UzD(i,0) - UzD(i-1,0) )
 71     CONTINUE
        Br1_4(0) = a4*( Ur1_4(1) - Ur1_4(0) + 2*(UzD(0,0)-UzD1_4(0)) )
```

```
      Br(0,0) = onethird * ( 4.0 * Br1_4(0) - Br(1,0) )

C Find the new Ur's for r > 0
      DO 72, i = 1, imax
        GrNEW = a5*( 2.0 * Br(i,0) + Ar(i,0) - Ar(i-1,0) ) +
     $          (a8/i) * (Ar(i,0) + Ar(i-1,0) - Cp(i,0) - Cp(i-1,0))
        VrNEW = Vr(i,0) - a6 * GrNEW + a7 * Gr(i,0)
        UrNEW = Ur(i,0) + deltaT * VrNEW

        Gr(i,0) = GrNEW
        Vr(i,0) = VrNEW
        Ur(i,0) = UrNEW
 72     CONTINUE

C Find the new Ur for r = 0                    {By symmetry, u_r is zero at r = 0}
C       GrNEW = a5*( 2.0 * Br1_4(0) + 4.0*(Ar(0,0) - Cp1_4(0)) )
C       GrNew = onethird * (4.0 * GrNew - Gr(1,0))
C       VrNEW = Vr(0,0) - a6 * GrNEW + a7 * Gr(0,0)
C       UrNEW = Ur(0,0) + deltaT * VrNEW
C       Ur1_4(0) = 0.25 * (3.0 * UrNew + Ur(1,0))
      Ur1_4(0) = 0.25 * Ur(1,0)          {Since u_r = 0 at r = 0, u_r at r = Δ/4 is}
                                         {just 1/4 of u_r at r = Δ}
C       Gr(0,0) = GrNEW
C       Vr(0,0) = VrNEW
C       Ur(0,0) = UrNEW

C **** BC for Uz ****   Az=Bz=0 on surface.  Find Bz below surface
      DO 74, i = 1, imax
C       temp = a3*exp(i*i*Rnorm + Znorm2)          {For Gaussian Profile}
       IF (i.LE.44) THEN
         temp = a3*exp(Znorm2) * G_p * exp(-1*(Guas_con*i)**2) {For Top-Hat}
C          temp = a3*exp(Znorm2) * G_p    { For Top-Hat Gaussian Profile}
       ELSE IF (i.LE.56) THEN
         temp = a3*exp(Znorm2) * 0.5*(1+COS(Cos_con*(i-42)))
       ELSE
         temp = 0
       ENDIF
       Bz(i,0) = a1*(Uz(i,1) - Uz(i,0)) + a2*(UrD(i,0) - UrD(i-1,0))
     $    + temp + (a0/i)*(UrD(i,0)+UrD(i-1,0))
 74    CONTINUE

      i = 0
C       temp = a3 * exp( 0.0625 * Rnorm + Znorm2 )     {For Gaussian Profile}
      temp = a3*exp(Znorm2) * G_p                      {For Top-Hat Profiles}
      Bz1_4(0) =    a1 * ( Uz1_4(1) - Uz1_4(0) ) +
```

```
     $          4.0 * a2 * UrD(0,0) + temp

        Bz(0,0) = onethird * ( 4.0 * Bz1_4(0) - Bz(1,0) )

        DO 76, i = 0, imax
          GzNEW = a5 * 2.0 * Bz(i,0)
          VzNEW = Vz(i,0) - a6 * GzNEW + a7 * Gz(i,0)
          UzNEW = Uz(i,0) + deltaT * VzNEW

          Gz(i,0) = GzNEW
          Vz(i,0) = VzNEW
          Uz(i,0) = UzNEW
 76     CONTINUE
        Uz1_4(0) = 0.25 * ( 3.0 * Uz(0,0) + Uz(1,0) )

C ***************************************************************
C ********************  Main loop  ******************************
C ***************************************************************

C Find all non-boundary Az's, Ar's, and Cp's
        DO 80, j = 1, jmax
         DO 82, i = 0, imax
          Az(i,j) = a4*( Uz(i+1,j) - Uz(i,j) + UrD(i,j) - UrD(i,j-1))
          i2 = i + 0.5
          dUrdr = Ur(i+1,j) - Ur(i,j)
          rUr = ( Ur(i+1,j) + Ur(i,j) ) / i2
          dUzdz = UzD(i,j) - UzD(i,j-1)
C           temp = a3 * Exp(i2*i2*Rnorm + j*Znorm)          {For Gaussian Profile}
          IF(i2.LE.44) THEN
            temp = a3 * exp(j*Znorm)*G_p*exp(-1*(Guas_con*i2)**2) {For Top-Hat}
C             temp = a3 * exp(j*Znorm)*G_p          { For Top-Hat Gaussian Profile}
          ELSE IF (i2.LE.56) THEN
           temp = a3*exp(j*Znorm)*0.5*(1+COS(Cos_con*(i2-42)))
          ELSE
            temp = 0
          ENDIF
          Ar(i,j) = a1*dUrdr + a0*rUr + a2*dUzdz + temp
          Cp(i,j) = a2*(dUrdr + dUzdz) + a00*rUr + temp
 82      CONTINUE
        Cp1_4(j) = 0.25 * (5.0 * Cp(0,j) - Cp(1,j) )
 80     CONTINUE

C Find all non-boundary Bz's and Br's

        DO 84, j = 1, jmax
```

```
      DO 86, i = 1, imax
C       temp = a3 * exp(i*i*Rnorm + j*Znorm + Znorm2)  {For Gaussian Profile}
        IF(i.LE.44) THEN
          temp = a3*exp(j*Znorm+Znorm2)
     $          * G_p * exp(-1*(Guas_con*i)**2)    {For Top-Hat Profile}
C           temp = a3*exp(j*Znorm+Znorm2)*G_p  { For Top-Hat Gaussian Profile
        ELSE IF (i.LE.56) THEN
          temp = a3*exp(j*Znorm + Znorm2) *
     $          0.5 * (1+COS(Cos_con*(i-42)))
        ELSE
          temp = 0
        ENDIF
        Bz(i,j) = a1*( Uz(i,j+1) - Uz(i,j) ) + temp
     $          + a2*( UrD(i,j) - UrD(i-1,j) )
     $          + a0*( UrD(i,j) + UrD(i-1,j) ) / i
        Br(i,j) = a4*(Ur(i,j+1) - Ur(i,j) + UzD(i,j) - UzD(i-1,j))
 86     CONTINUE

C i = 0
C       temp = a3 * exp( 0.0625*Rnorm + j*Znorm + Znorm2 ) {For Gaussian Profile}
        temp = a3 * exp( j*Znorm + Znorm2 ) * G_p          {For Top-Hat Profiles}
        Bz1_4(j) = a1 * ( Uz1_4(j+1) - Uz1_4(j) ) +
     $          4.0 * a2 * UrD(0,j) + temp
        Bz(0,j) = onethird * ( 4.0 * Bz1_4(j) - Bz(1,j) )

        Br1_4(j) = a4*(Ur1_4(j+1)-Ur1_4(j) + 2*(UzD(0,j)-UzD1_4(j)))
        Br(0,j) = onethird * ( 4.0 * Br1_4(j) - Br(1,j) )

 84     CONTINUE

C ******* Main loop for Ur and Uz

      DO 90, j = 1, jmax
       DO 100, i = 1, imax

C Find Uz
        GzNEW = a5*( Az(i,j) - Az(i-1,j) + Bz(i,j) - Bz(i,j-1) ) +
     $          (a8/i) * ( Az(i,j) + Az(i-1,j) )
        VzNEW = Vz(i,j) - a6*GzNEW + a7*Gz(i,j)
        UzNEW = Uz(i,j) + deltaT * VzNEW

        Gz(i,j) = GzNEW
        Vz(i,j) = VzNEW
        Uz(i,j) = UzNEW
```

```
C Find Ur
        GrNEW = a5*( Br(i,j) - Br(i,j-1) + Ar(i,j) - Ar(i-1,j) ) +
     $        (a8/i) * (Ar(i,j) + Ar(i-1,j) - Cp(i,j) - Cp(i-1,j))
        VrNEW = Vr(i,j) - a6*GrNEW + a7*Gr(i,j)
        UrNEW = Ur(i,j) + deltaT * VrNEW

        Gr(i,j) = GrNEW
        Vr(i,j) = VrNEW
        Ur(i,j) = UrNEW

 100    CONTINUE

C Find Ur and Uz on the radial axis
        GzNEW = a5*( 4.0 * Az(0,j) + Bz1_4(j) - Bz1_4(j-1) )
        GzNEW = onethird * ( 4.0 * GzNEW - Gz(1,j) )
        VzNEW = Vz(0,j) - a6*GzNEW + a7*Gz(0,j)
        UzNEW = Uz(0,j) + deltaT * VzNEW

        Gz(0,j) = GzNEW
        Vz(0,j) = VzNEW
        Uz(0,j) = UzNEW
        Uz1_4(j) = 0.25 * ( 3.0 * Uz(0,j) + Uz(1,j) )

C       GrNEW = a5*(4.0*(Ar(0,j) - Cp1_4(j)) + Br1_4(j) - Br1_4(j-1))
C       GrNEW = onethird * ( 4.0 * GrNEW - Gr(1,j) )
C       VrNEW = Vr(0,j) - a6*GrNEW + a7*Gr(0,j)
C       UrNEW = Ur(0,j) + deltaT * VrNEW

C       Gr(0,j) = GrNEW
C       Vr(0,j) = VrNEW
C       Ur(0,j) = UrNEW
C       Ur1_4(j) = 0.25 * ( 3.0 * Ur(0,j) + Ur(1,j) )
        Ur1_4(j) = 0.25 * Ur(1,j)

 90     CONTINUE

C ********* End main loop for Ur and Uz ************

C Output Values

      if ( (t.eq.Time(1)) .or. (t.eq.Time(2)) .or. (t.eq.Time(3))
     $     .or. (t.eq.Time(4)) .or. (t.eq.Time(5)) ) THEN
        if (t.eq.Time(1)) THEN
          k = 1
        endif
```

```
      if (t.eq.Time(2)) THEN
        k = 2
      endif
      if (t.eq.Time(3)) THEN
        k = 3
      endif
      if (t.eq.Time(4)) THEN
        k = 4
      endif
      if (t.eq.Time(5)) THEN
        k = 5
      endif

      loop1 = -1
      DO 42, i = 0, imax, Rint              {Outputs values vs radial position}
        loop1 = loop1 + 1
        Stor_Us(k,loop1)      = -1e3 * Uz(i,0)        {Outputs -u_z in nm}
        Stor_Us(numTim+k,loop1) =  1e3 * Ur(i,0)      {Outputs u_r in nm}
        Stor_Sr(k,loop1)      =  Snorm * Ar(i,0)      {Outputs Normalized σ_rr}
        Stor_Sr(numTim+k,loop1) =  Snorm * Cp(i,0) {Outputs Normalized σ_θθ}
C         Stor_Sr(numTim+k,loop1) =  1e4 * Az(i,nint(PenDep/Del))
 42     CONTINUE

      loop1 = -1
      DO 44, j = 0, jmax, Zint              {Outputs values vs axial position}
        loop1 = loop1 + 1
C         Stor_Sz(k,loop1)      = Snorm * Bz(0,j)
        Stor_Sz(k,loop1)      = Snorm * Ar(10,j)
        Stor_Sz(numTim+k,loop1) = Snorm * Ar(25,j)
C         Stor_Sz(numTim+k,loop1) = Snorm * Br(nint(LasRad/Del),j)
 44     CONTINUE

     Endif

      if(MOD(t,Tint).eq.0) then             {Outputs values vs time}
        loop = loop + 1
        Stor_Ut(0,loop) = t * deltaT
        Stor_Ut(1,loop) = -1e3 * Uz(0,0)
        Stor_Ut(2,loop) = -1e3 * Uz(6,0)
C         Stor_Ut(2,loop) =  1e3 * Ur(Nint(LasRad/Del),0)
      endif

 30  CONTINUE
C *** End of Main Time loop ***
```

```
C Write Ur and Uz vs r/D to output file Tdef_Us

    Write(4, 905) '   r/D  ',('; Uz ',Time(k)*deltaT,k=1,NumTim),
   $                  ('; Ur ',Time(k)*deltaT,k=1,NumTim)
    loop1 = -1
    DO 150, i = 0, imax, Rint
      loop1 = loop1 + 1
     Write(4,906) i*Del/PenDep,';',(Stor_Us(k,loop1),';',k=1,NumTim*2)
 150  CONTINUE

C Write Ur and Uz vs Time to output file Tdef_Ut

    Write(5, 901) '   Time ns ; Uz(0,0) ; Uz(6,0) '
    loop1 = 0
    DO 160, t = 1, tmax, Tint
      loop1 = loop1 + 1
      Write(5, 907) (Stor_Ut(k,loop1),';',k=0,2)
 160  CONTINUE

C Write Szz and Spp vs z/D to output file Tdef_Szz

    Write(7, 905) '   Z/D  ',('; Sr10',Time(k)*deltaT,k=1,NumTim),
   $                  ('; Sr25',Time(k)*deltaT,k=1,NumTim)
    loop1 = -1
    DO 170, j = 0, jmax, Zint
      loop1 = loop1 + 1
C     Write(7,906) (j+0.5)*Del/PenDep,';',
     Write(7,906) j*Del/PenDep,';',
   $          (Stor_Sz(k,loop1),';',k=1,NumTim*2)
 170  CONTINUE

C Write Srr and Spp vs r/D to output file Tdef_Srr

    Write(8, 905) '   r/D  ',('; Srr',Time(k)*deltaT,k=1,NumTim),
   $                  ('; Spp',Time(k)*deltaT,k=1,NumTim)
    loop1 = -1
    DO 180, i = 0, imax, Rint
      loop1 = loop1 + 1
     Write(8,906) (i+0.5)*Del/PenDep,';',(Stor_Sr(k,loop1),';',
   $           k=1,NumTim*2)
 180  CONTINUE

 905  Format( 1X, A, 10 (A, F5.0) )
 906  Format( 1X, F7.3, A, 10 (F9.4, A) )
 907  Format( 1X, 3 (F9.4, A) )
```

```
CLOSE(3)
CLOSE(4)
CLOSE(5)
CLOSE(7)
CLOSE(8)
STOP
END
```

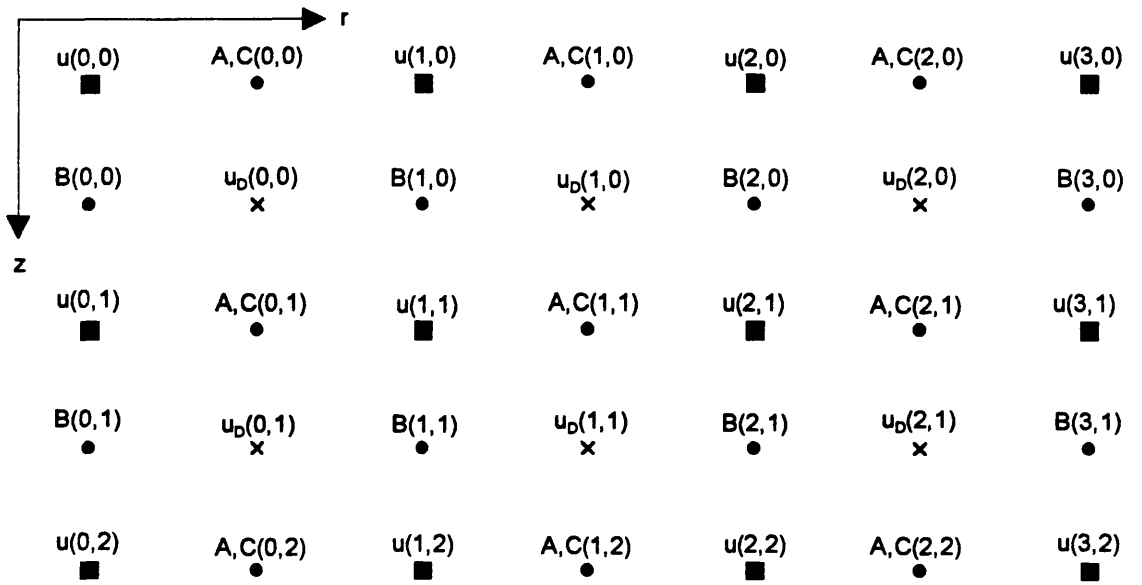

Figure 6-1. In order to solve the thermoelastic wave equation numerically, the displacements (squares) and stress function (circles) must be calculated at each point on a two dimensional grid. These points are indexed by (i,j) where $r = i\Delta$ and $z = j\Delta$.

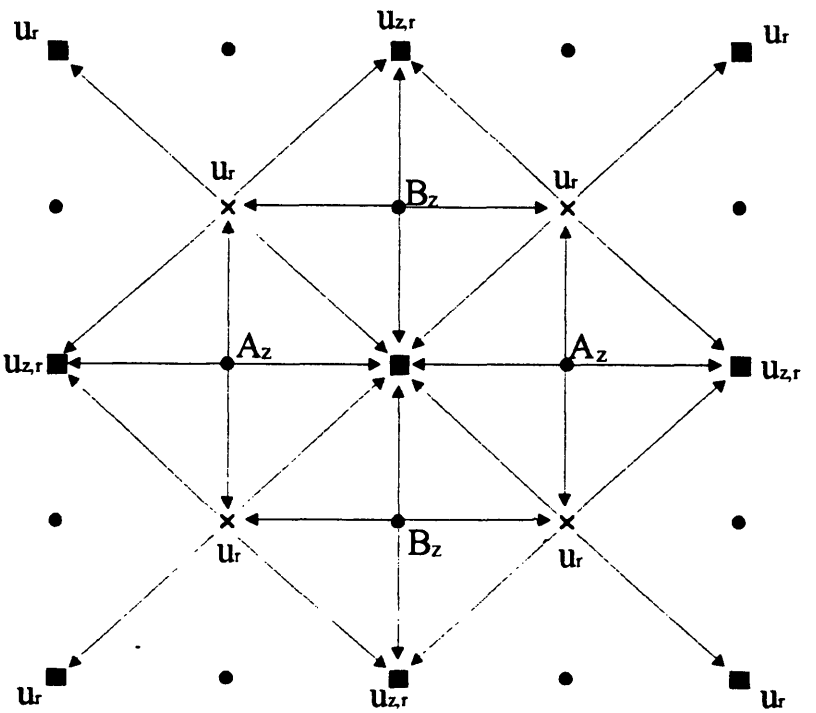

Figure 6-2. A graphical illustration of the finite difference algorithm used to calculate G_z at the center point. Note that the value of G_z will depend on the values of the displacements u_r and u_z on a 3 by 3 surrounding grid.

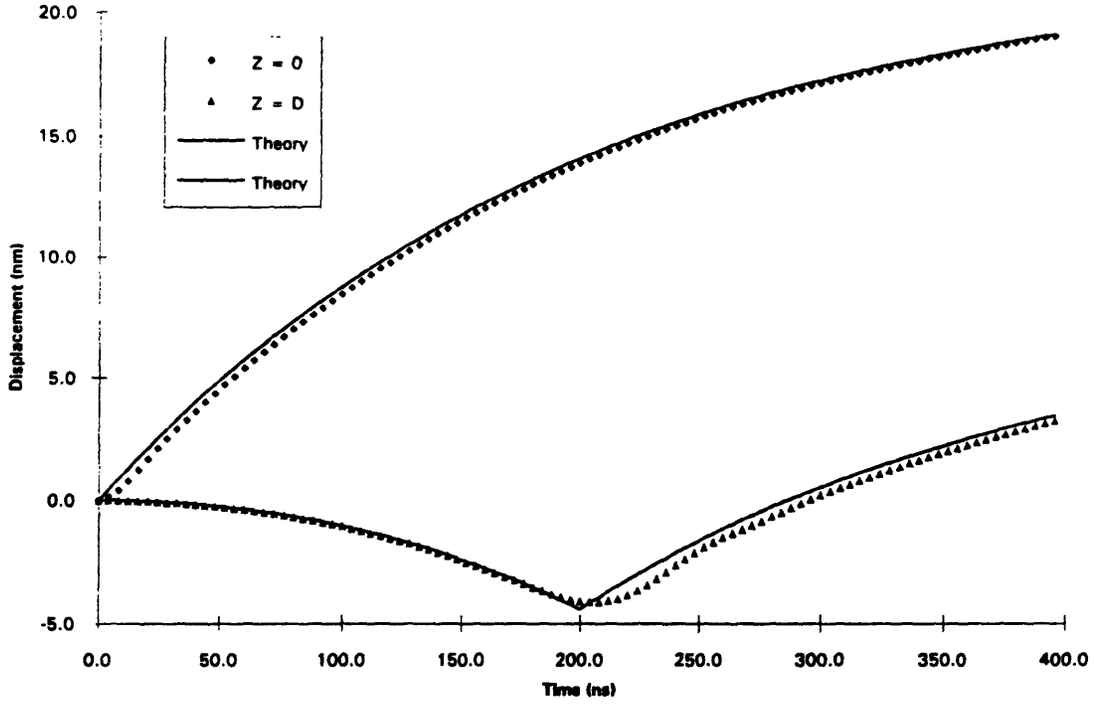

Figure 6-3. With a grid spacing of $\Delta = 0.05$ D, the predicted displacement from the numerical model shows only small discrepancies with the analytical solution.

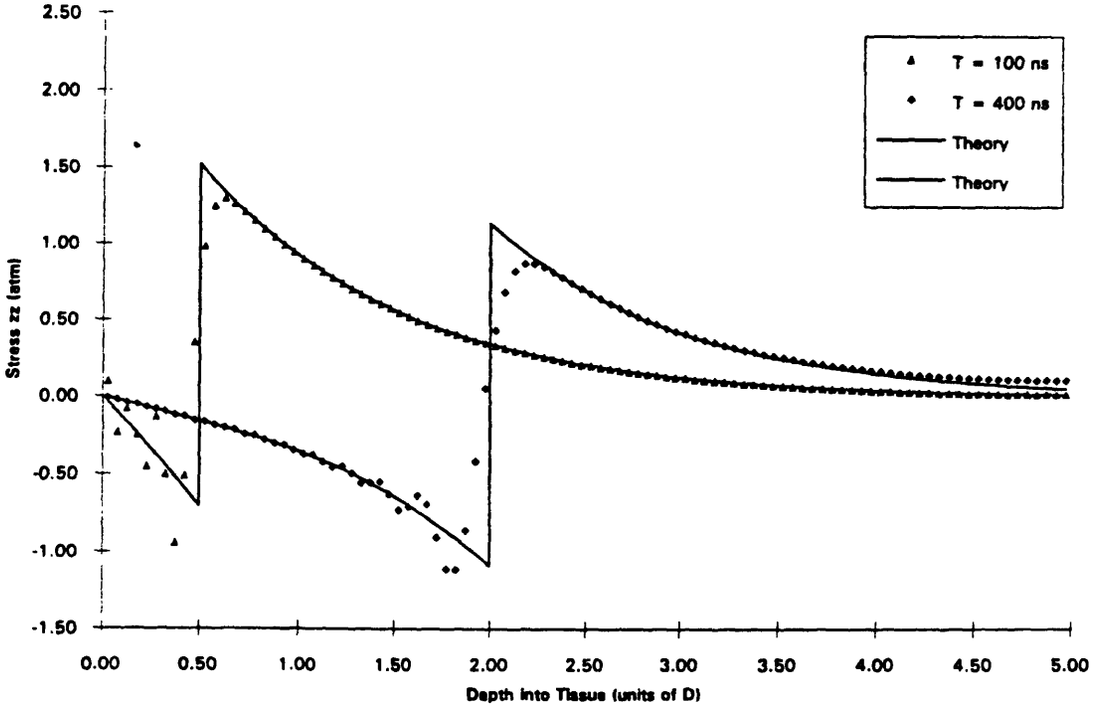

Figure 6-4. With a grid spacing of $\Delta = 0.05$ D, the predicted stress from the numerical model shows discrepancies with the analytical solution at the acoustic wave front.

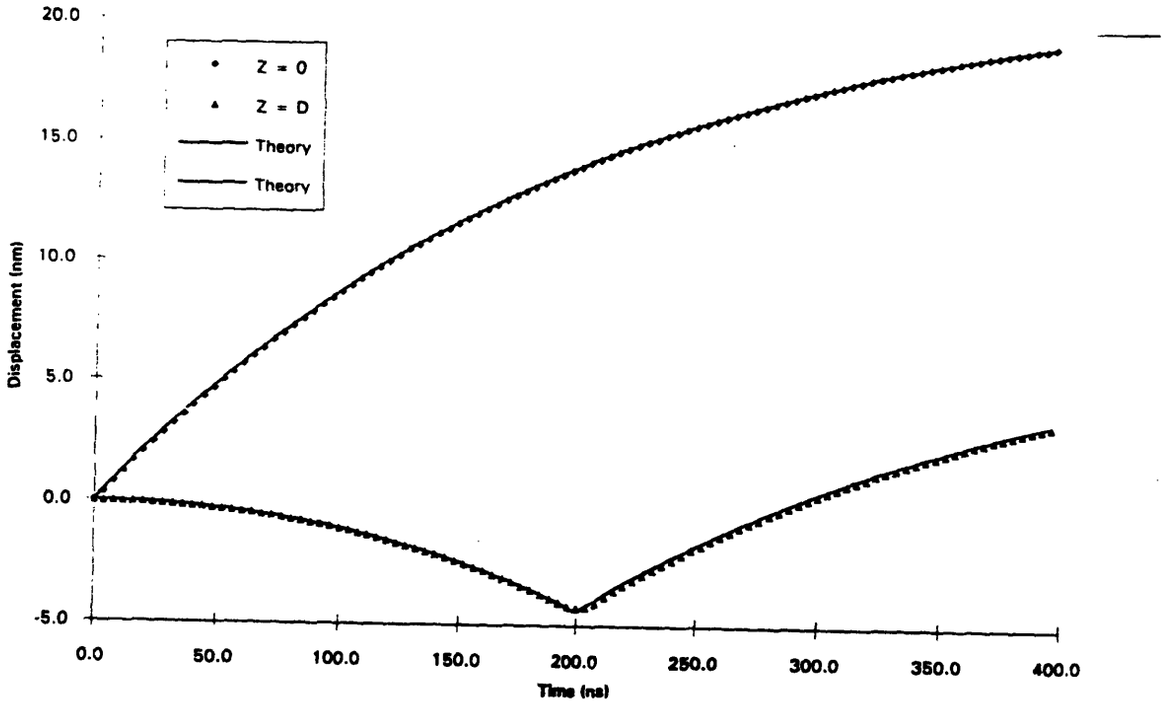

Figure 6-5. By decreasing the grid spacing to $\Delta = 0.01$ D, the predictions from the numerical code show complete agreement with the analytical solution.

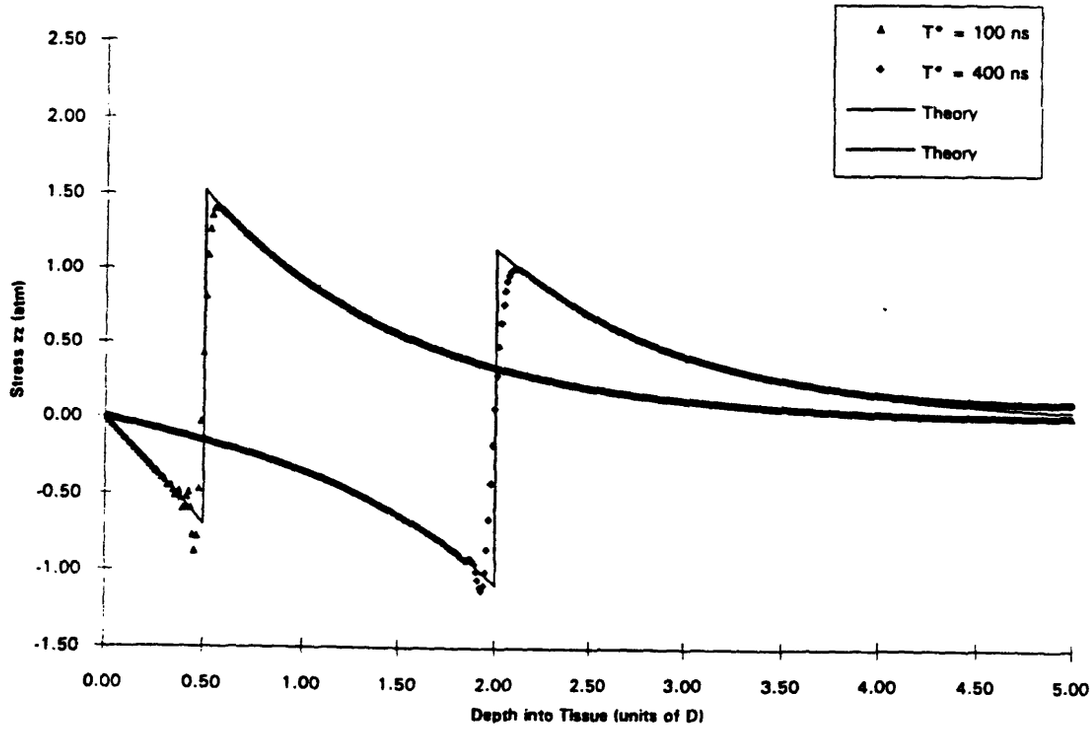

Figure 6-6. By decreasing the grid spacing to $\Delta = 0.01$ D, the discrepancies between the numerical code and the analytical solution are decreased.

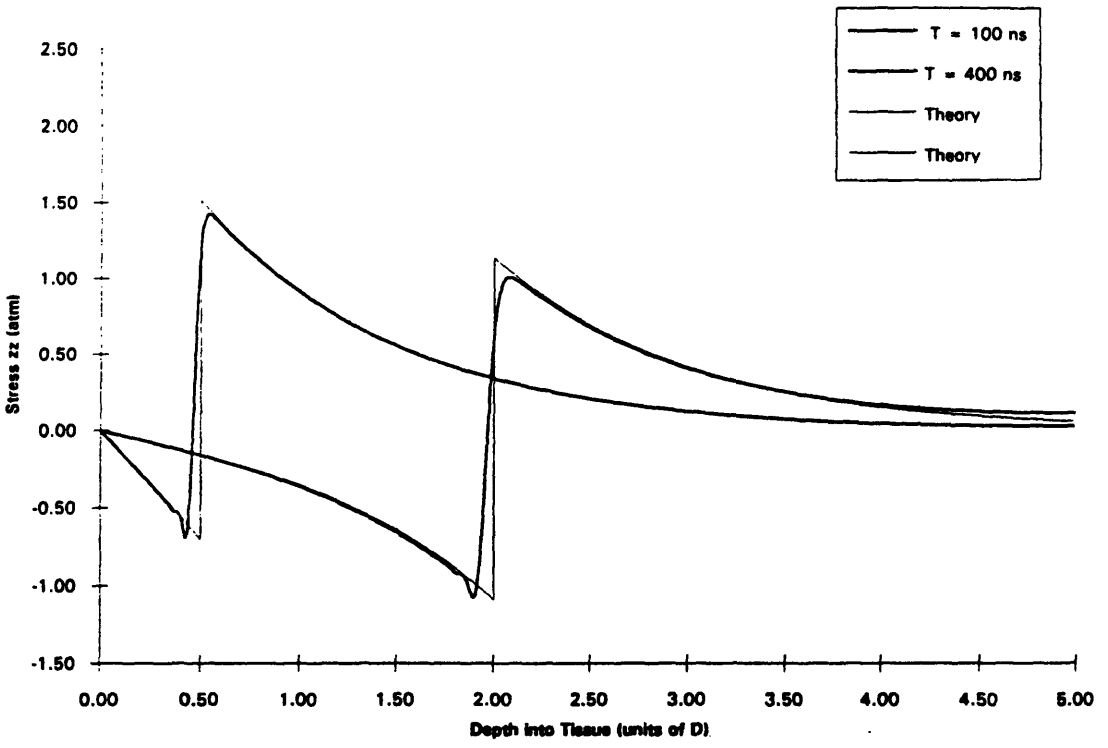

Figure 6-7. By depositing the laser energy over a 10 ns period, the numerical artifact associated with instantaneous deposition is minimized. Note that the slope of the wave front also decreases.

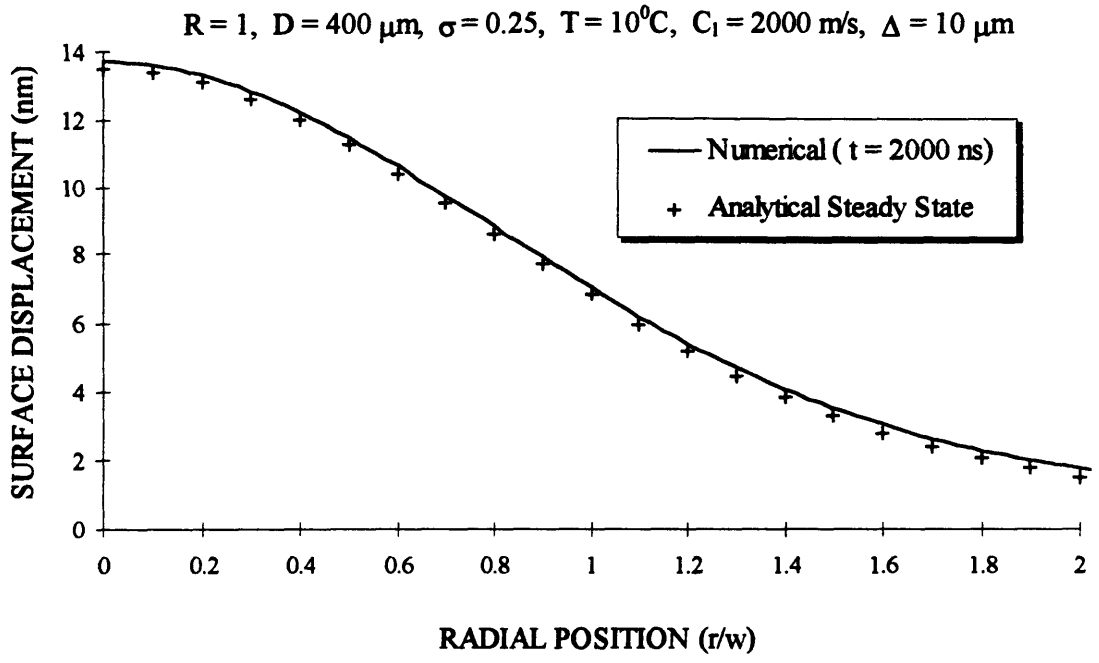

Figure 6-8. The numerically predicted displacement u_z at 2000 ns is several percent greater than the steady state analytical solution. The displacement as a function of radial position resembles the Gaussian radial profile of the incident laser beam.

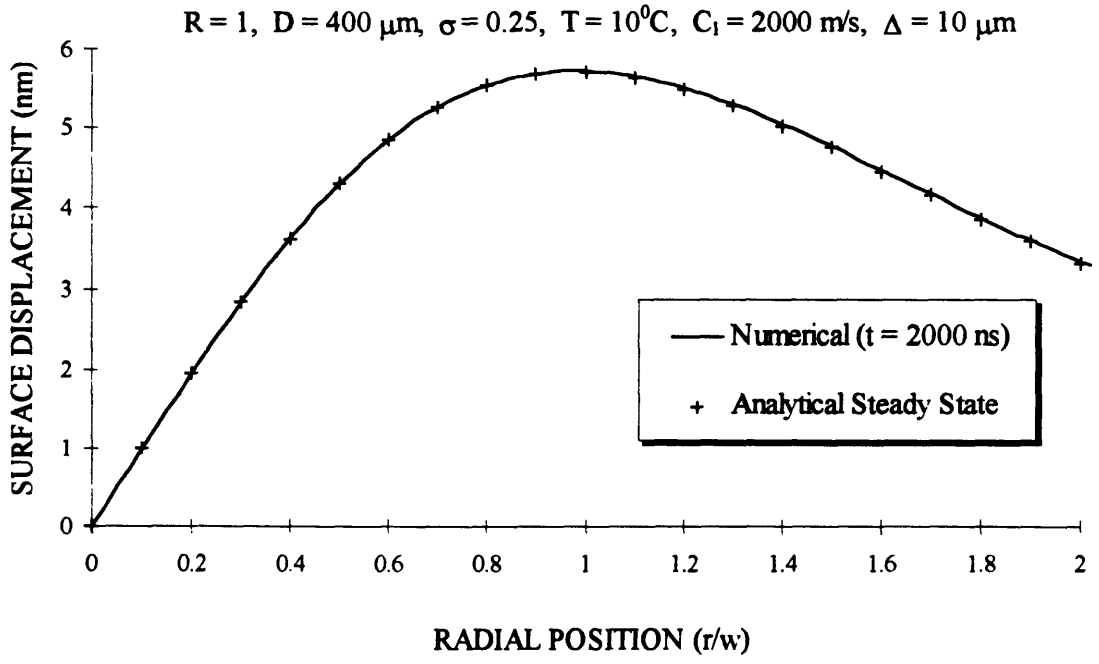

Figure 6-9. The numerically predicted displacement u_r at 2000 ns is identical with the steady state analytical solution. The peak radial displacement occurs at r = w, the 1/e radius of the initial Gaussian radial profile of the laser beam.

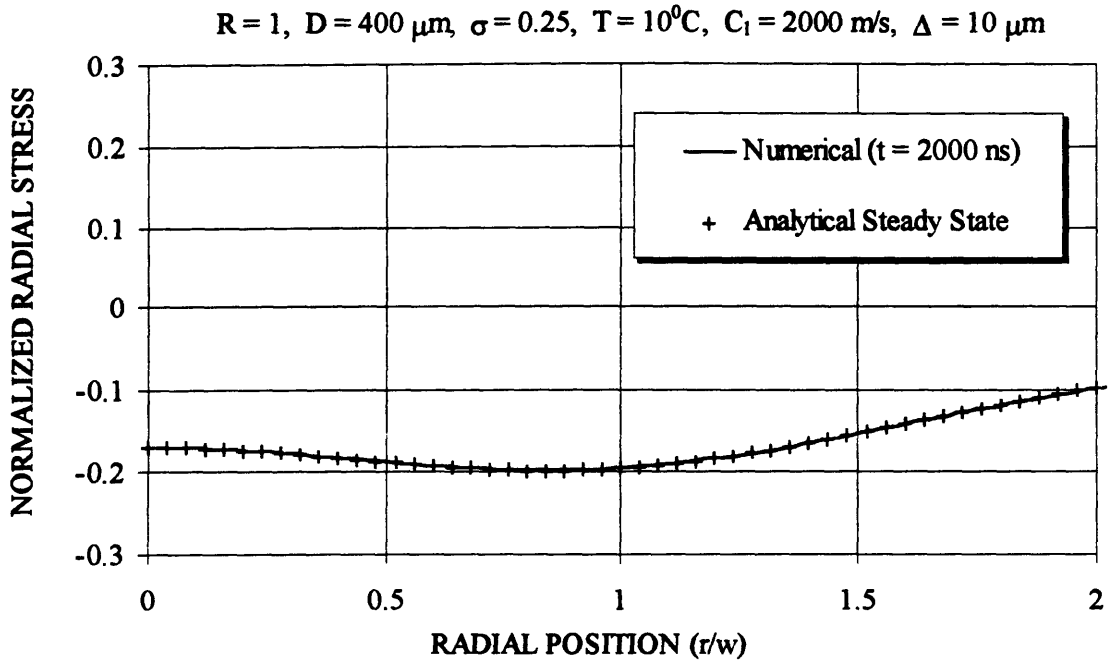

Figure 6-10. The numerically predicted radial stress as a function of radial position at t = 2000 ns is in quantitative agreement with the steady state analytical solution for a laser beam with a Gaussian radial profile.

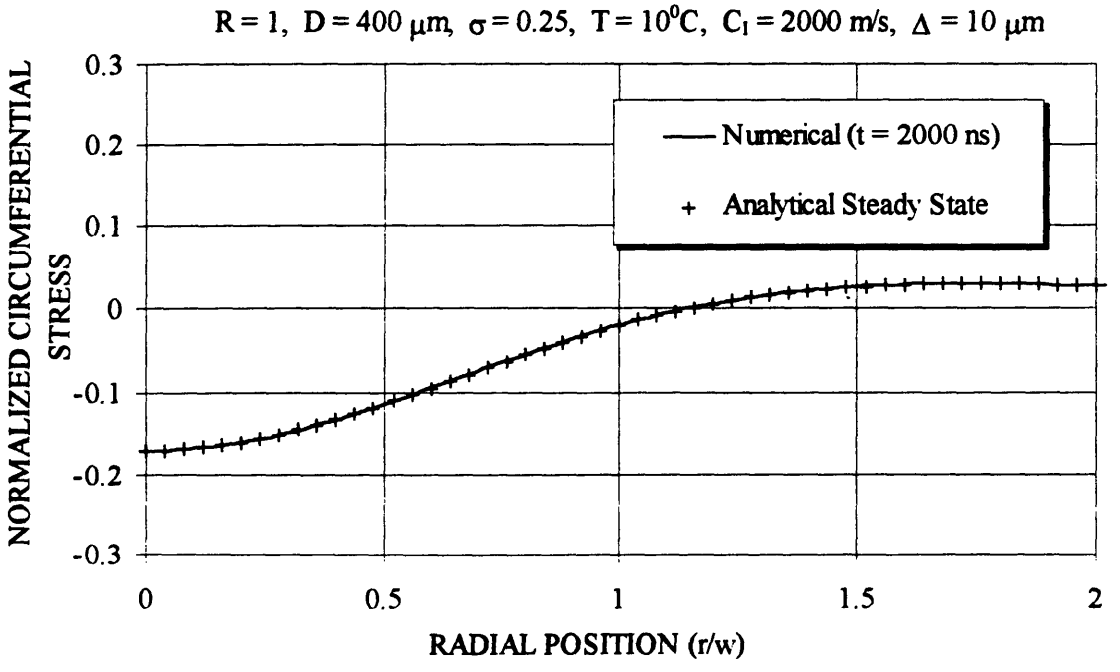

Figure 6-11. The numerically predicted circumferential stress as a function of radial position at t = 2000 ns is in complete agreement with the steady state analytical solution for a laser with a Gaussian radial profile.

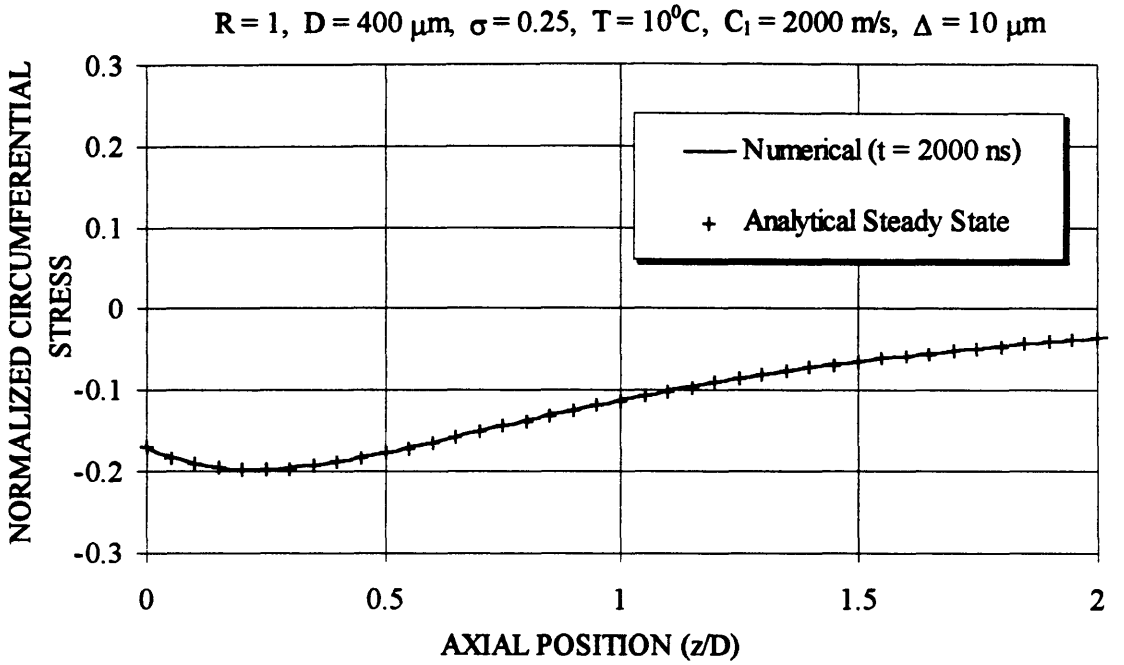

Figure 6-12. The numerically predicted circumferential stress at r = w/40 as a function of axial position at t = 2000 ns is in quantitative agreement with the steady state analytical solution for a laser beam with a Gaussian radial profile.

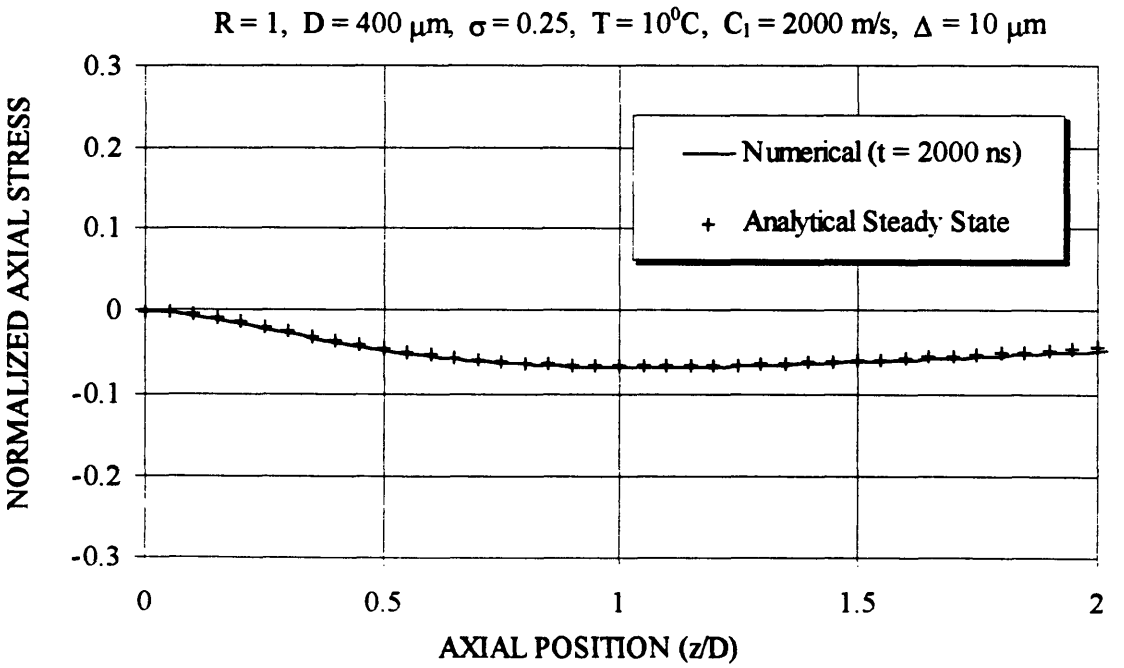

Figure 6-13. The numerically predicted axial stress as a function of axial position at t = 2000 ns is in quantitative agreement with the steady state analytical solution for a laser beam with a Gaussian radial profile.

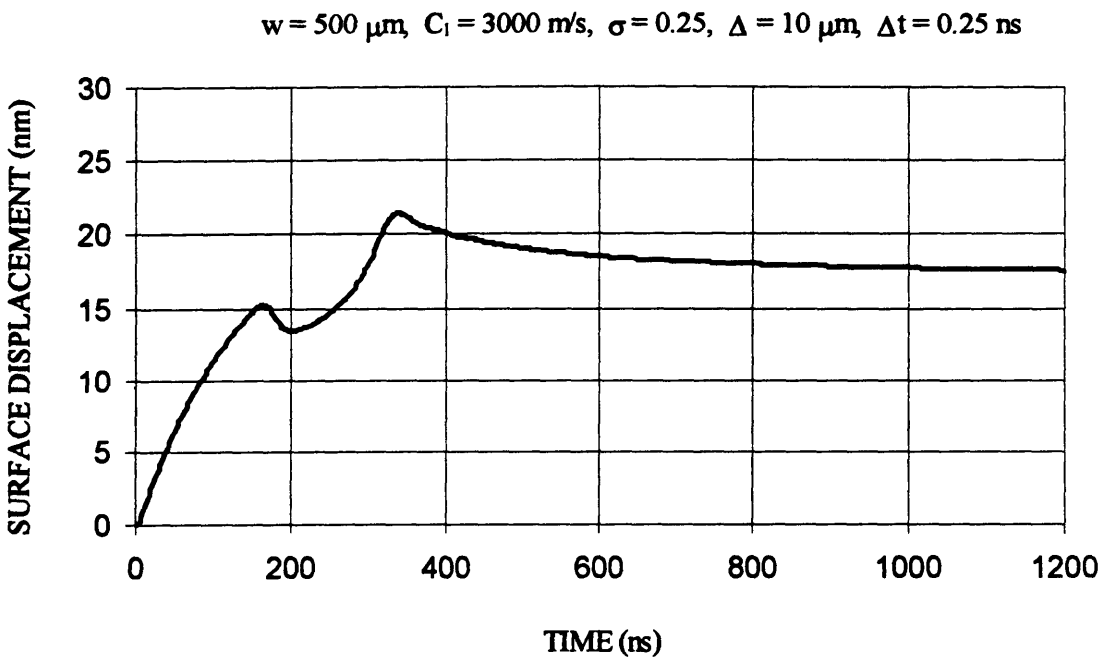

Figure 6-14. The numerically predicted time dependent surface displacement shows additional features which are not present in the one dimensional solution. These features include three direction reversals before a steady state position is reached.

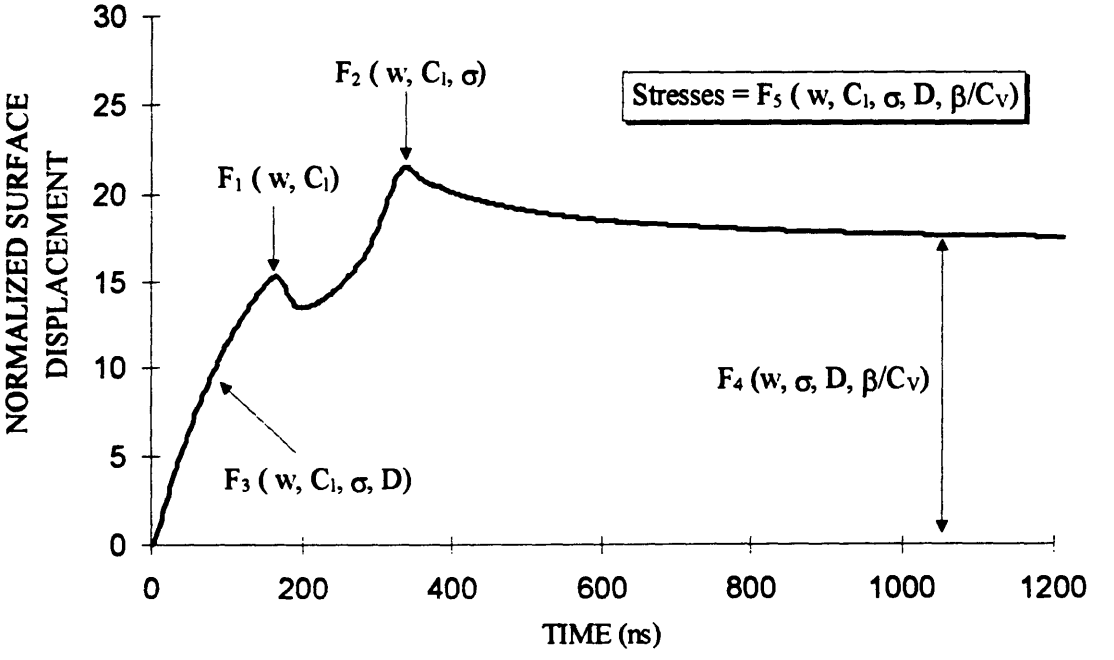

Figure 6-15. The complex features in the surface expansion curve are uniquely related to the optical, mechanical, and thermal properties of the material. Measuring these features allow all the physical properties to be determined which are needed to calculate the laser-induced stresses.

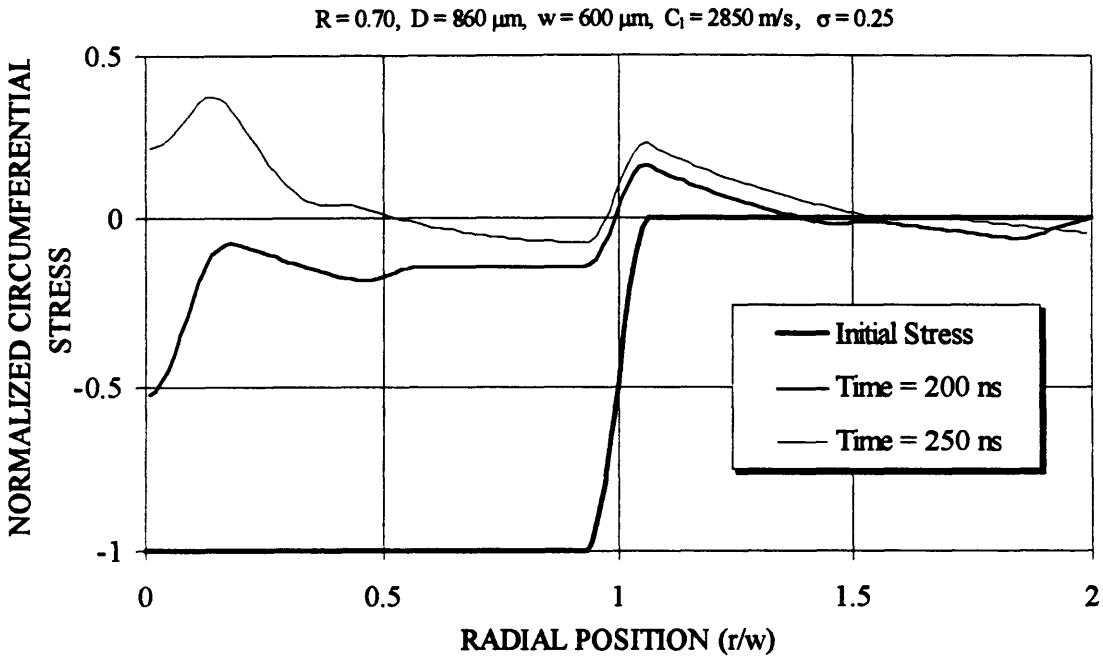

Figure 6-16. The computed circumferential stress as a function of radial position on the target surface. Initially, the laser-induced stress is compressive and mirrors the radial profile of the laser. After 250 ns, tensile stresses have developed on the surface.

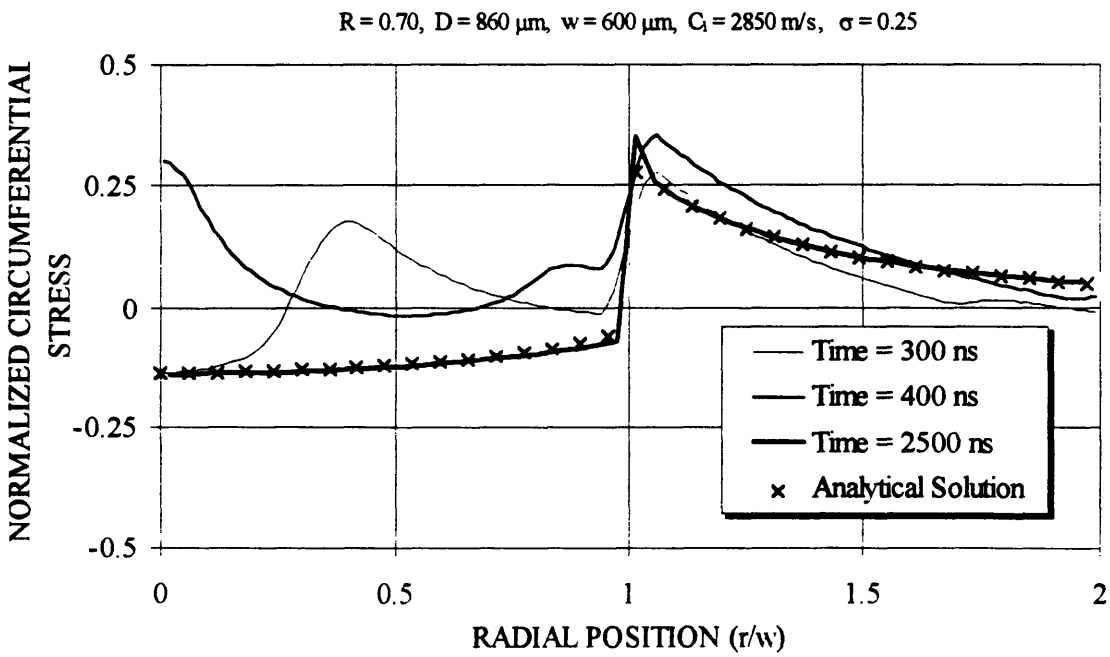

Figure 6-17. The computed circumferential stress distribution on the surface oscillates between compressive and tensile stress for $r < w$. The numerical solution at 2500 ns agrees with the analytical steady state solution.

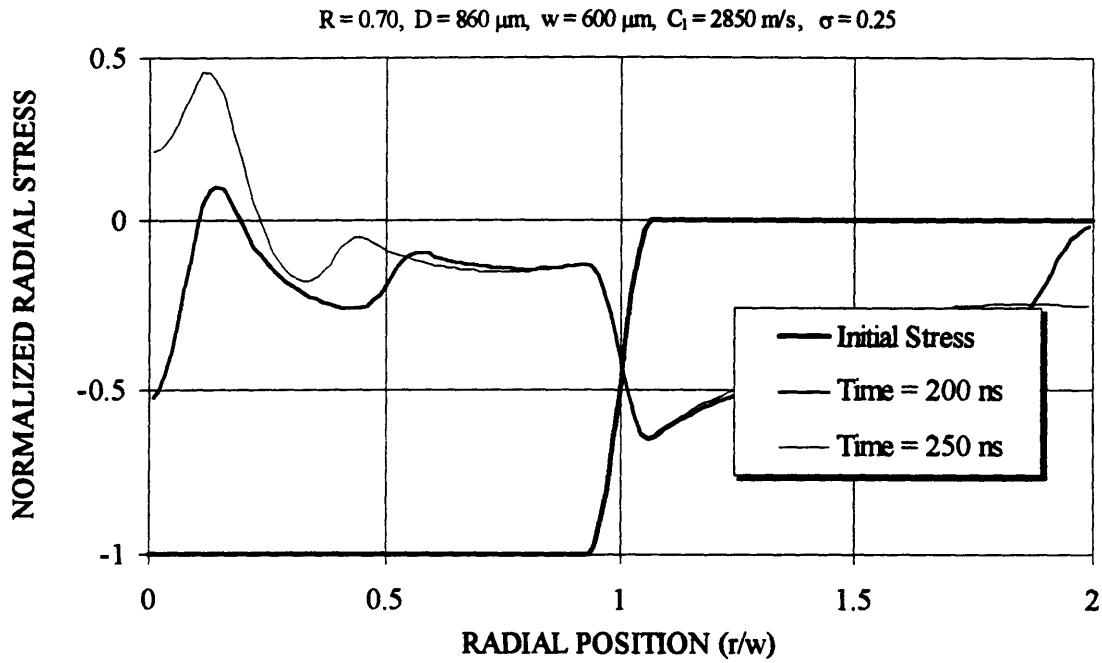

Figure 6-18. The computed radial stress as a function of radial position on the target surface. Initially, the laser-induced stress is compressive and mirrors the radial profile of the laser. Like the circumferential stress, after 250 ns tensile stresses have developed on the surface.

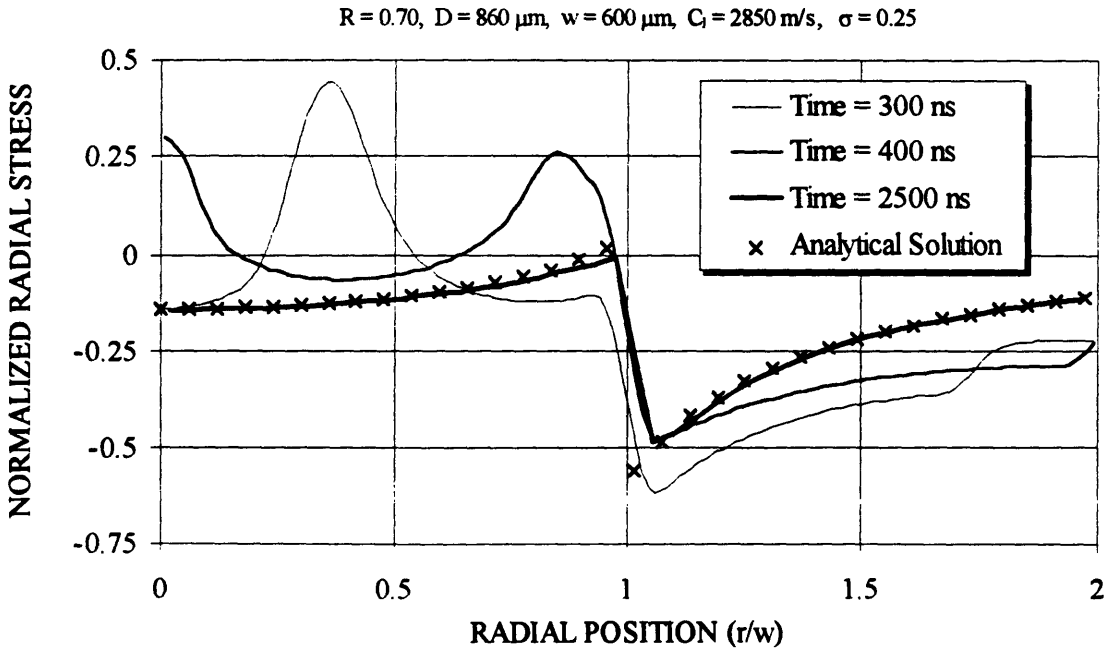

Figure 6-19. The computed surface radial stress also oscillates between tension and compression. The numerical solution at 2500 ns agrees with the analytical steady state solution.

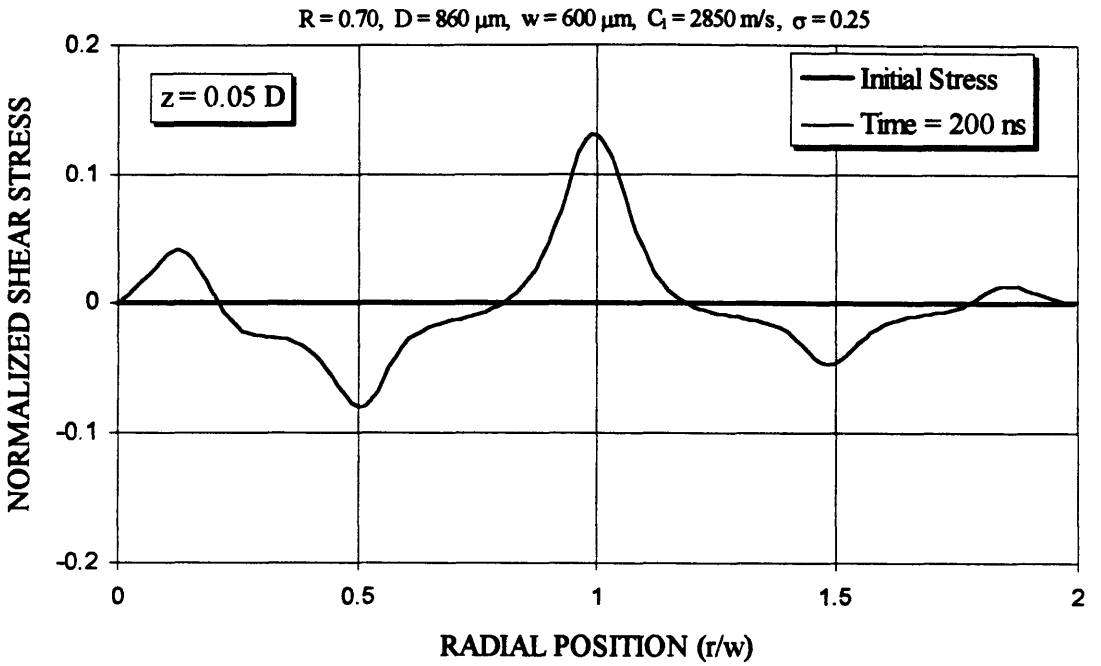

Figure 6-20. The computed shear stress as a function of radial position just below the target surface (z = 0.05 D). The maximum laser-induced shear stress occurs at the sharp temperature gradient at the edge of the laser beam (r = w).

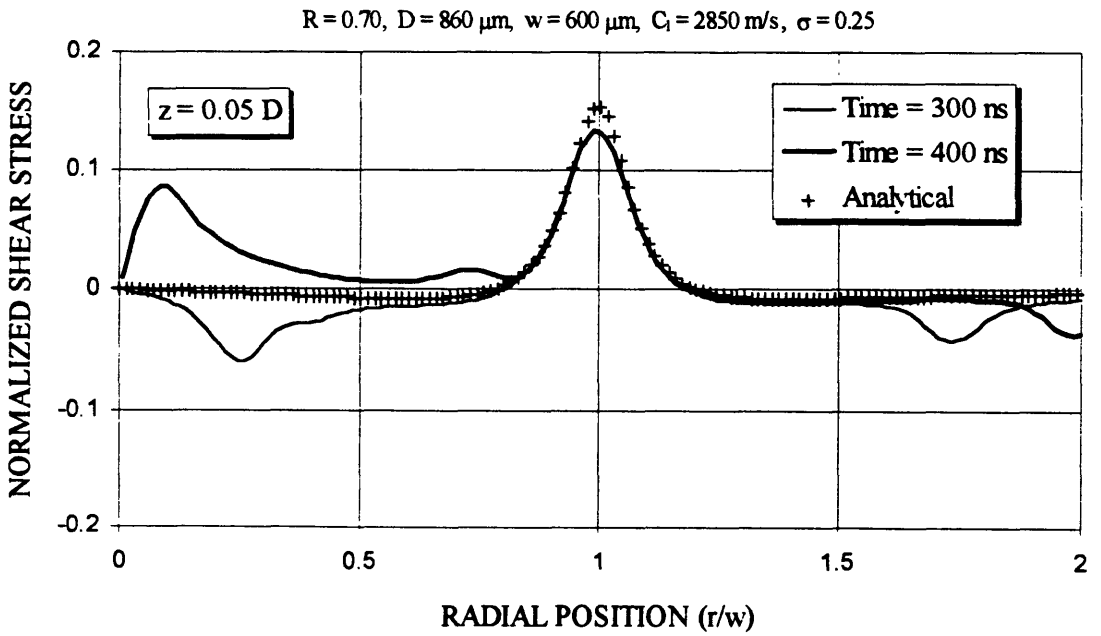

Figure 6-21. At later times, the shear stress within the heated region (r < w) oscillates in magnitude while the shear stress at r = w remains constant. At longer times, the stress approaches the steady state analytical solution (+) but has a slightly smaller amplitude since the analytical solution is for a top-hat radial distribution without rounded corners.

CHAPTER 7

Development of an Interferometric Method for the Measurement of Laser Induced Stresses in Solids

7.1 OVERVIEW

A quantitative determination of the laser induced stress distribution within a solid is of great importance to the understanding of laser ablation. In the previous three chapters, the theory of elasticity has been used to develop a detailed three dimensional model which calculates this stress distribution. For this model to be useful, however, two issues must be examined in detail. First, it must be experimentally verified that the model is correct and complete. In deriving the model, a number of assumptions were made which must be checked. Second, the theoretical model predicts the time dependent stress distribution given the thermal, mechanical, and optical properties of the target material. The magnitude of the stresses cannot be calculated if these properties are not accurately known, as in the case of biological tissue.

In this chapter, an experimental technique is described which addresses both of these issues. This technique is based on an interferometric surface monitoring of the target surface which allows the laser induced thermal expansion of the target to be measured with nanometer accuracy on a nanosecond time scale. Experimental data

collected from glass and acrylite samples, which were irradiated with sub ablation threshold fluences, is in detailed quantitative agreement with our theoretical model and validates the assumptions of this model. In addition, the complex time dependent features in the surface expansion of the target allow one to determine important physical parameters including the longitudinal speed of sound, Poisson's ratio, Gruneisen coefficient, and the optical penetration depth of the laser light. Given these parameters, the laser induced stress distribution as a function of time can be calculated from the model. Results using this experimental technique to study biological tissue will be discussed in chapter 8.

This work was presented in part at the 14th Annual Meeting of the American Society for Laser Medicine and Surgery, April 8-10, Toronto, Canada and was submitted to the journal *Optics Letters* in an article entitled "The Photomechanical Basis of Laser Ablation of Biological Tissue" [Albagli et al., 1994d] and in a longer form to *Applied Optics* in an article entitled "An Interferometric Method for the Measurement of Laser Induced Stresses in Solids and its Implications to Laser Ablation" [Albagli et al., 1994e].

7.2 INTRODUCTION

In order to quantitatively evaluate the photomechanical model of ablation, the magnitude and spatial distribution of the laser induced stresses must be determined. Although a simple one dimensional model was adequate for metals because the depth of light penetration was much smaller than the radius of the beam, a full three dimensional model is required for other materials (including biological tissue) where the light

penetrates more deeply. We have developed an experimental technique which, when coupled with the full time dependent three dimensional model described in chapter 6, allows the determination of the magnitude and spatial distribution of the laser induced stresses in a target material.

This experimental technique, based on Michelson interferometry, is a modified version of the experiment described in chapter 3. In that earlier version, the surface of the target material was used as the end mirror in one arm of the interferometer. When a short pulse of laser light was fired at the target, the resulting expansion changed the path length in the interferometer arm. When the light from this arm was combined with the light reflected from a stationary mirror in the other arm of the interferometer, a time dependent interference pattern was created. An analysis of this pattern allowed one to determine the speed of the surface expansion.

Although this technique provided valuable information, there were two serious limitations. First, the direction of the motion could not be determined. Since the theory predicts that the surface movement changes its directions several times (see chapter 6), it is essential that the experimental apparatus be modified so that it can determine these direction changes. Secondly, the spatial resolution of this technique must be improved by over an order of magnitude. As shown in chapter 3, since the surface movement of bone corresponded to less than one interference fringe shift (158 nm), it could only be estimated. In order to study the complex features in the surface expansion predicted by the theory, a spatial resolution of ~ 10 nm is needed.

The new experimental technique, described in detail in section 7.3, overcomes these two difficulties. In the modified interferometer, the stationary mirror in the reference arm is replaced by an optical system which changes the path length of the arm at a constant rate. If the target surface in the other arm remains stationary, a fixed frequency interference pattern is produced. If the target surface moves, this pattern is modulated. By demodulating the fringe pattern, both the direction and magnitude of the surface movement can be determined. In addition, a careful analysis of the fringe modulation allows one to quantitatively determine movements corresponding to a small fraction of a fringe shift. With these improvements, the new interferometer can measure the position of the surface with a spatial resolution of < 3 nm and a time resolution of < 3 ns.

A detailed comparison of the predicted surface expansion, based on the theoretical model of chapter 6 and briefly reviewed in section 7.4, and the experimentally measured surface expansion, using the modified interferometric technique, is presented in section 7.5 for glass and plastic targets. The detailed quantitative agreement verifies our theoretical model and its assumptions. The time dependent expansion exhibits several complex features which are uniquely related to the thermal, optical and mechanical properties of the material. By comparing the data to the theory, the values of several important physical properties including the longitudinal speed of sound, Poisson's ratio, Gruneisen coefficient, and the optical penetration depth of the laser light can be

extracted. Given these experimentally measured properties, both the magnitude and spatial location of the laser induced stress distribution can be determined.

7.3 EXPERIMENTAL DESCRIPTION OF INTERFEROMETRIC SURFACE MONITORING TECHNIQUE

This section describes the development of a pump-probe technique which can measure the laser induced surface movement of a target material with a spatial resolution of < 3 nm and a temporal resolution of < 3 ns. A schematic of the experimental set-up is shown in figure 7-1. When a short pulse of laser light is absorbed by the target, it causes the material to undergo thermoelastic expansion. Our technique used to measure this expansion is based on a Michelson interferometer which uses the target as the end mirror in one arm of the interferometer and a rotating corner cube prism in the other arm. Using this arrangement, both the velocity and direction of the target movement is measured and thus the surface position as a function of time can be determined. The results from this technique are compared to the theoretical predictions and are presented in section 7.5.

7.3.1 Laser Delivery System

The pump light in this experiment (i.e. the light of sufficient intensity to cause measurable thermoelastic motion by the target) is supplied by a frequency tripled Q-switched Nd:YAG laser (wavelength = 354.7 nm, pulse duration = 7.5 ns, beam diameter = 6 mm). A uniform portion of the beam is chosen with a 3 mm aperture. A 25 cm lens is used to re-image and demagnify the beam at the aperture onto a 1 mm spot on the target surface (concentric with the 100 μm diameter interferometric probe beam) with a top-hat

radial profile. The laser energy is controlled via a half-wave plate and Glan polarizing prism.

Since all quantitative measurements will depend on the fluence of the incident pump beam, careful considerations must be given to its measurement. In particular, under typical experimental conditions, one cannot obtain a smooth top-hat radial profile from a Q-switched, frequency tripled Nd:YAG pulse. Two steps were taken to address this problem. First, a passive beam homogenizer was developed and built. A schematic of the beam homogenizer is shown in figure 7-2. A laser pulse enters from the top left and is incident on a 50 / 50 beamsplitter causing half of the light to travel along path A and half to travel along path B. When these two pulses reach the second beamsplitter, they are each divided again so that the light entering path C (and D) has components from both paths A and B. Since the light that travelled along path B underwent two reflections while that in path A only made one, the light distribution in B will be reflected 180 degrees relative to that in A. When the light from paths C and D is combined at the third beam splitter, the light entering path E (and F) will consist of four pulses (which have travelled paths AC, AD, BC, and BD respectively). The mirrors in path D are arranged to rotate the spatial orientation of the beam by 90^0. This is accomplished by reflecting the beam by 45^0 out of the plane and then back into the plane. Due to the rotations set up in paths B and D, the four pulses of light entering paths E and F will be spatially averaged. The light in these two paths is directed to cross at an aperture which is demagnified and reimaged onto the target surface. The overlap of these two beams is adjusted to give the most uniform profile, as measured on the laser beam analyzer.

It is essential that the eight different path lengths through the homogenizer are all of different lengths by at least the coherence length of the laser or large intensity fluctuations due to interference effects will occur after recombination. In our case, the path length difference was chosen to be at least 5 cm, while the coherence length of the laser is estimated to be 5 mm.

In addition to this beam averaging, a portion of the beam is directed to a laser beam analyzer (Big Sky Software) which stores the energy profile of the pulse in a 240 by 240 array. Figure 7-3 shows the average profile of 9 shots which were taken before, during, and after the experiment. Due to the significant differences between the beam profile and the top-hat distribution, the measured profile was fit to a combination of a Gaussian and cosine function (figure 7-3) and this was used as an input to the numerical model. The details of this fit are described in more detail in section 7.4 (see equations 7-4 and 7-5).

7.3.2 Modified Michelson Interferometer

In the interferometric surface monitoring apparatus, light from a cw Helium Neon laser is electronically shuttered to a 6 millisecond pulse duration and passed to a 50/50 beamsplitter in a Michelson interferometer (outlined by a dotted line in figure 7-1). In the sample arm of the interferometer, a 5 cm lens focuses the light onto the target. The target is adjusted to be normal to the incoming light so that the small fraction of light (typically

several percent) reflected from the index of refraction mismatch at the air-target interface is recollimated by the lens and travels back toward the beamsplitter.

In an earlier version of this experiment (described in chapter 3), the light from the sample was combined with the light from the reference arm of the interferometer to produce interference fringes. Although the time dependent changes in the fringe pattern could be related to the speed of the sample surface, the direction of this motion could not be determined. In this new experimental set-up, the path length of the reference arm is changed at a constant rate, creating a constantly changing fringe pattern. Since the motion of the sample produces a modulation in the fringe pattern, a demodulation of this pattern allows one to determine both the direction and the speed of the sample surface.

In the modified reference arm of the interferometer (figure 7-1), the light passes through a 10 cm lens, reflects from a moving corner cube and comes to focus on a reflecting mirror. The angle of the mirror is adjusted so that the reflected light returns to the corner cube, is recollimated by the lens and travels back toward the beamsplitter. An additional neutral density filter is placed in the reference arm to compensate for the lower specular reflection in the sample arm. The corner cube prism has the property that a light beam incident on it will be reflected 180 degrees (and displaced) independent of the angle of incidence. When the corner cube is used in conjunction with a flat mirror, as in our experimental design, a light beam can be reflected back onto itself (collinear but traveling in the opposite direction) regardless of the angle between the corner cube and the incident light beam. By placing the corner cube on a wheel rotating at 10 Hz., the corner cube will

rotate into the appropriate position every 100 ms. For a small portion of this rotation (θ = +/- 2 degrees), the tangential velocity of the corner cube will remain essentially constant and this retro-reflecting optical system will maintain perfect alignment.

The light from both arms of the interferometer is combined by the beamsplitter and directed towards a red sensitive photomultiplier tube (Hammamatsu R928). An interference filter centered at 632.8 nm is used to filter out stray light. The signal from the photomultiplier tube is captured and digitized at a rate of 1 gigasample/second by a digital oscilloscope (Tektronix model 601A) and transferred to a computer for analysis. For incoherent light, the signal from the PMT would consist of equal contributions from both arms of the interferometer and would be constant in time. For coherent light (the difference in path lengths of the two arms in the interferometer must be within the coherence length of the laser), however, interference effects will take place. Depending on the relative path lengths of the two arms, the light measured by the PMT will be between zero (destructive interference) and two (constructive interference) times the light observed in the incoherent case.

7.3.3 Analysis of Interference Pattern

Experimental data is collected for a time period of 10 μs, during which the angular position of the corner cube is θ = +/- 0.02 degrees and the tangential velocity (v_{cc}) is 2.78 m/s. A subset of this data is shown in figure 7-4 for the case when the target in the sample arm is stationary. This figure shows the sinusoidal voltage pattern created by the alternating constructive and destructive interference of the light. Since the path length in

the reference arm of the interferometer changes at a rate four times greater than the corner cube velocity, the half-period (time between a minimum and maximum) of the reference interference pattern is :

$$P_r = \frac{\lambda/2}{4v_{cc}} = 28.5ns \qquad [7\text{-}1]$$

where λ is the wavelength of the Helium-Neon laser (632.8 nm). If the target in the sample arm moves as a function of time, however, the interference half-period (P_i) will change:

$$P_i = \frac{\lambda/2}{(4v_{cc} - 2v_s)} \qquad [7\text{-}2]$$

where v_s is the average velocity of the sample over the half-period (the direction of v_s is defined as positive for movements towards the beamsplitter). Note that the factor of two difference in the multipliers of the velocities comes from the fact that the light only strikes the sample once but the corner cube twice. The surface movement of the sample (S_s) during the period can be found by multiplying the sample velocity (found from solving eqs. 7-2) by the correspondingly observed half-period, P_i :

$$S_s = \frac{\lambda}{4}\left(\frac{P_i}{P_r} - 1\right) \qquad [7\text{-}3]$$

Note that a positive value of S_s indicates motion towards the beamsplitter. Thus the surface motion of the sample can be determined each half-period (28.5 ns) and the total trajectory can be found by summing all the motions. Note that this time represents the

time interval at which the half-period is determined and does not represent the intrinsic time resolution of the experiment, determined by the 2-3 ns rise time of the PMT.

All timing in the experiment is controlled by two pulse generators (Stanford Research Systems, DG535) which provide triggering for the Nd:YAG laser, electronic shutter, laser beam analyzer, and digital oscilloscope. A pin diode, which is monitoring the rotating wheel, triggers the pulse generators when the corner cube has moved into the appropriate position. In all experiments, data is collected for a 10 μs period with the pump light striking the sample exactly 2 μs into this period (with a jitter of +/- 2 ns). The reference half-period (P_r) is determined from the first 2 μs of interference fringes when the target is stationary. The laser-induced thermoelastic motion of the sample over the next 8 μs is then determined from the remaining interference fringes and eq. 7-3.

In order to determine the spatial resolution of this technique, the surface movement as a function of time of a stationary sample has been calculated from the interference fringes (see figure 7-4) and is shown in figure 7-5. Since the sample is stationary, any calculated motion is a measure of the system resolution. The data in figure 7-5 shows no movement with a standard deviation of +/- 2 nm. The scatter of the data is related to the error in measuring the interference period due to the random noise on the sinusoidal voltage pattern. This noise has contributions from both shot noise (there are only 3000 photoelectrons) and background electronic noise.

7.4 THEORETICAL MODEL OF LASER INDUCED EXPANSION

The experimental technique of interferometric surface monitoring, described in the previous section, measures the time dependent thermoelastic expansion of a target material that has absorbed a short pulse of laser light. Assuming axial symmetry and neglecting scattering within the target, the laser light will be attenuated exponentially with a 1/e depth given by the optical penetration depth (D) leading to a temperature distribution within the target of

$$T(r,z) = \frac{\Phi}{\rho C_V D} L(r) e^{-z/D} \qquad [7\text{-}4]$$

where Φ is the peak incident laser fluence (energy per unit area), L(r) is the radial distribution of this fluence, ρ is the density of the target and C_V is the heat capacity. The measured laser profile (see figure 7-3) can be fit to the form :

$$L(r) = L_0 e^{-r^2/r_4^2} \qquad for \quad r \le r_1$$

$$L(r) = \frac{L_0}{2}\left\{1 + COS\left[\frac{\pi}{k_1}(r - r_3)\right]\right\} \qquad for \quad r_1 < r \le r_2 \qquad [7\text{-}5]$$

$$L(r) = 0 \qquad for \quad r > r_2$$

Using the parameters $L_0 = 1.16$, $r_1 = 440$ μm, $r_2 = 560$ μm, $r_3 = 420$ μm, $r_4 = 930$ μm and $k_1 = 140$ μm, an excellent fit was obtained (see figure 7-3). This fit was used as an input to the numerical model.

As discussed in chapters 4-6, the thermoelastic expansion due to this non-uniform temperature distribution can be found from the theory of elasticity by solving the thermoelastic wave equation:

$$\rho\frac{\partial^2\mathbf{u}}{\partial t^2}-\frac{E}{2(1+\sigma)}\nabla^2\mathbf{u}-\frac{E}{2(1+\sigma)(1-2\sigma)}\nabla(\nabla\cdot\mathbf{u})=-\frac{E\beta}{3(1-2\sigma)}\nabla T \qquad [7\text{-}6]$$

where **u** is the displacement vector, E is Young's modulus, σ is Poisson's ratio, and β is the thermal expansion coefficient. The full time dependent solution of this equation was obtained by numerical methods and was described in detail in chapter 6. This solution will be compared with experimental data in section 7.5.

In applying this model to the calculation of the laser induced surface movement, it is important to keep in mind the additional assumptions that were made. First, it is assumed that the target is isotropic and has negligible viscosity. Furthermore, it is assumed that over the range of temperature rises and deformations, the thermal, mechanical, and optical parameters defined above are constant. As will be shown in section 7.5, a comparison of experiment and theory validates these assumptions.

7.5 COMPARISON OF EXPERIMENTAL RESULTS WITH THEORY

A detailed comparison of the theoretically predicted and experimentally measured thermoelastic expansion caused by sub-ablation threshold laser fluences is presented in this section. Experimental data was collected from plastic (Cyro, acrylite FF) and two different types of glass filters (Schott GG 375, BG 18). In section 7.5.1, the time

dependent thermoelastic expansion will be discussed. The complex behavior of the expansion curve allows the values of important physical properties of the target to be determined. In section 7.5.2, the steady state thermoelastic expansion will be discussed. From this expansion, the final physical constant which is needed to calculate the magnitude of the laser induced stresses can be determined.

7.5.1 Time Dependent Expansion

Figure 7-6 shows a typical result for the surface movement of acrylite as a function of time when a single 10 ns pulse of 10.2 mJ/mm^2 of 355 nm light strikes it at 2000 ns. The target expands rapidly for 195 ns, contracts a small amount, expands again, and then slowly contracts to a new equilibrium level, 275 nm above its original position. The sample surface will remain at its new equilibrium position until thermal diffusion dissipates the energy on a millisecond time scale. The surface movement for a range of fluences from 4.2 to 12.4 mJ/mm^2 is shown in figure 7-7. Although the magnitude of the surface displacement increases as the fluence increases, the temporal features of the curve, described above, remain constant. Thus, as shown in figures 7-6 and 7-7, the interferometric surface monitoring tool can measure the time dependent expansion of a target material with nanometer spatial resolution and nanosecond time resolution. A careful comparison of experimental measurements and theoretical predictions is presented below.

7.5.1.1 Comparison of Theory and Experiment for Glass

Since all of the required physical properties of Schott glass filter GG375 are well known, it is an ideal material to compare theory and experiment. Figure 7-8 shows the first 1000 ns of the time-dependent thermoelastic expansion of this glass after irradiation with a single 10 ns pulse of light for a range of fluences. For each fluence, the total movement has been normalized to 100 units. The time dependent behavior is identical throughout the fluence range, indicating that the optical, thermal, and mechanical properties are constant over this range. Note that the highest fluence corresponds to a laser induced temperature increase of 30^0C. The predicted movement, based on the pulse duration (τ = 10 ns), laser radius (w = 500 μm), optical penetration depth (D = 480 μm, measured with a spectrophotometer), and the manufacturer's values of the Poisson ratio (σ = 0.235) and the longitudinal speed of sound (C_l = 5225 m/s) is in excellent agreement with the data. Note that the time dependent behavior depends on C_l and not on Young's modulus (E) and the density (ρ) individually (see eq. 6-21) and that the expansion coefficient (β), heat capacity (C_v), and density only effect the overall displacement.

As explained in section 6.5.1, the complex time dependent features in the surface movement have a unique relationship to the mechanical, optical, and thermal properties of the material. As shown in figure 7-8, the initial expansion stops and contraction begins at a time of 95 ns. The time of this contraction corresponds exactly to the ratio of the laser beam radius to the longitudinal speed of sound and represents the time at which the finite size of the laser induced temperature distribution is communicated to the center point (where the interferometric probe beam is located). After a brief period of contraction, the expansion continues until a second peak is reached and a slow contraction to the

equilibrium position begins. As learned from the numerical model, the location of the second peak is related to the transverse speed of sound in the material (see eq. 6-22) and thus is a sensitive measure of the Poisson ratio. For the glass sample, where $\sigma = 0.235$, this second peak occurs at 200 ns, just about twice the time of the first peak.

As described in the last paragraph, given the radius of the laser beam, the longitudinal speed of sound and Poisson's ratio can be determined from the location of the two peaks in the expansion curve. Since the initial slope of the expansion curve is only a function of these three parameters and the optical penetration depth, D can now be determined. This is of great significance because D is the 1/e depth of the laser induced temperature distribution and can be determined using this method at a laser fluence near the value needed to initiate ablation. Thus, it represents the "hot" penetration depth which may be different from the value measured using standard techniques and low light levels for a host of reasons including bleaching, triplet state absorption and other non linear effects.

7.5.1.2 Comparison of Theory and Experiment for Plastic

The normalized time dependent surface movement for acrylite for several different fluences is shown in figure 7-9. As with the glass sample, the data indicates that the physical properties of the acrylite do not change for laser induced temperature increases of up to 7^0C. The location of the first peak (t = 195 ns) corresponds to a longitudinal sound velocity of 2550 m/s. This is within 5% of the value reported in the literature for acrylic (2670 m/s) [Ritchie, 1965]. Unlike the data from the glass sample, the location of the 2nd

peak in the expansion curve occurs at a time significantly greater than twice the first peak. Using the numerical model, it was found that the only way to fit this peak was to use a value of 0.32 for the Poisson ratio. The values reported in the literature for similar plastics were between 0.32 and 0.35 [Ritchie, 1965]. From the slope of the initial expansion curve ($2000 < t < 2150$), the optical penetration depth was determined to be 1000 μm.

7.5.2 Equilibrium Displacement

7.5.2.1 Methodology for Determining Laser Induced Stresses

As described above, given the laser radius w, the normalized time dependent expansion curve can be used to determine C_l, σ, and D (and thus R). These parameters allow one to determine the stress distribution using the numerical model to within a multiplicative constant. This constant, labeled σ_{max} and described in section 5.4.1.1 (eq. 5-51), can be written in the form

$$\sigma_{max} = \frac{1+\sigma}{3(1-\sigma)} \rho C_l^2 \beta T\big|_{r=0,z=0} \qquad [7\text{-}7]$$

and describes the maximum stress generated in the target material. Expressing the temperature distribution in terms of the laser fluence (eq. 7-4), this becomes :

$$\sigma_{max} = \frac{1+\sigma}{3(1-\sigma)} \Gamma \frac{\Phi}{D} L_0 \qquad [7\text{-}8]$$

where Γ is the Gruneisen coefficient and

$$\Gamma = \frac{\beta C_l^2}{C_v} \qquad [7\text{-}9]$$

Thus, the maximum stress is simply proportional to the peak energy per unit volume ($L_0\Phi/D$) with a proportionality constant related to σ and Γ. In order to calculate the magnitude of the laser induced stresses, the Gruneisen coefficient (and thus the ratio of the expansion coefficient to the heat capacity) must be known.

The steady state equilibrium position can be used to determine this final parameter. The analytical expression for the steady state equilibrium position S_0 (for a point at z = 0, r = 0 and assuming a top-hat radial laser profile) was found in chapter 5 (see eq. 5-41, 7-4) and can be written as :

$$S_0 = \frac{2(1+\sigma)}{3}\frac{\beta}{\rho C_v} g_0(R)\Phi L_0 \qquad [7\text{-}10]$$

where R is the aspect ratio (equal to w / D) and g is a geometrical correction factor given by

$$g_0(R) = n\int_0^\infty \frac{RJ_1(Ry)}{y+1}dy \qquad [7\text{-}11]$$

where J_1 is a first order Bessel function and n is a laser profile correction factor. The predicted equilibrium position, based on the numerical model described in chapter 6, is in complete quantitative agreement with eq. 7-10 for a top-hat radial laser profile (n = 1). For the experimentally measured laser profile (figure 7-3, eq. 7-5) the value n = 0.96 was

found by dividing the predicted movement from the real profile by the predicted movement for the top-hat profile.

By measuring the equilibrium displacement S_0 for a fluence Φ, the Gruneisen coefficient (and thus σ_{max}) can then be completely determined (see eqs. 7-9, 7-10) :

$$\Gamma = \frac{3}{2(1+\sigma)} \frac{\rho C_l^2}{g_0(R)} \frac{S_0}{\Phi L_0} \qquad [7\text{-}12]$$

given the density of the material (a parameter which is either well known or easily measured). Thus all the mechanical, optical and thermal parameters needed to calculate the time dependent laser induced stress distribution within a material can be determined from a detailed analysis of the thermoelastic expansion.

7.5.2.2 Comparison of Theory and Experiment for Glass

Experimental results for the equilibrium position as a function of laser fluence for two different types of glass filters are shown in figure 7-10. As seen from eq. 7-12, the data should be linear with a slope (S_0 / Φ) proportional to the Gruneisen coefficient. Since all of the physical properties of these glass filters are known, we can compare the computed value of Gruneisen coefficient based on the data with the actual value calculated from eq. 7-12. A least squares fit to the data gives values of the slope 6.3 % and 5.8 % higher than the predicted values. For GG 375, the value of the Gruneisen coefficient is found to be 1.02. Using eq. 7-7, the maximum stress induced by a laser fluence of 25 mJ/mm^2 is σ_{max} = 310 bars. For GG 375, the input parameters were σ = 0.235 and R =

1.04 which were given above, and the manufacturer's values (C_V = 0.72 J/gm K, β = 27 x 10^{-6} /K, and ρ = 2.61 gm/cm^3. Given n = 0.96, the geometrical correction factor (eq. 7-11) was 0.452. For BG 18, the aspect ratio was measured to be R = 0.39 and the manufacturer's values for the other parameters were σ = 0.224, C_V = 0.70 J/gm K, β = 20.4 x 10^{-6} /K, and ρ = 2.68 gm/cm^3. The geometrical correction factor (eq. 7-11) was 0.243.

As a final comparison between experiment and theory, the equilibrium displacement as a function of radial position was determined by translating the HeNe probe beam (100 μm diameter) with respect to the pump light (1000 μm diameter). The results of this experiment along with the theoretical prediction is shown in figure 7-11. Once again, there is quantitative agreement between theory and experiment. As expected, the maximum surface movement occurs at the center of the laser induced temperature distribution. Note that although this temperature distribution has a steep boundary at r = 500 μm, the expansion of the heated material (r < 500 μm) pulls some of the unheated material (r > 500 μm) above its initial position.

7.5.2.3 Comparison of Theory and Experiment for Plastic

Experimental results for the equilibrium displacement of acrylite along with the theoretical predictions from the numerical model are shown in figure 7-12. The input parameters were σ = 0.32 and R = 0.5 which were given above, and the manufacturer's values (C_V = 1.47 J/gm K, β = 192 x 10^{-6} /K, and ρ = 1.2 gm/cm^3). Given n = 0.96, the geometrical correction factor (eq. 7-11) was 0.291. The data marked by solid points refer

to experiments done at virgin sites while the open points represent data taken at sites which had already received irradiation. At low fluences, there is agreement between the data and theory, and the Gruneisen coefficient is found to have the value 0.85.

Although there is agreement between theory and experiment at low fluences, the two diverge as the fluence is increased. In addition, at higher fluences there is a higher spread in the data with each subsequent shot producing less thermoelastic expansion. Unlike in the glass samples, in acrylite small permanent defects, which can be seen with a microscope, are created by the laser pulse. These defects and their relation to the ablation process will be discussed in the next chapter.

7.6 CONCLUSIONS

A determination of the magnitude and spatial distribution of the time dependent laser induced stresses in a solid material is of importance to understanding the mechanism of laser ablation. By combining a theoretical model, described in chapter 6, and an experimental technique, based on interferometric surface monitoring and described in this chapter, we have developed a methodology to determine the laser induced stress distribution within a material. By measuring the time dependent thermoelastic expansion of the target and comparing it to theoretical predictions, the longitudinal speed of sound, Poisson ratio, Gruneisen coefficient and optical penetration depth can be determined. These physical properties can then be used to calculated the stress distribution within the material. Experimental data from glass and acrylite samples, whose physical properties are

well known, are in quantitative agreement with the theoretical predictions and verify the accuracy of our technique. This methodology is of great importance to the study of the photomechanical model of ablation of biological tissue and is presented in the next chapter.

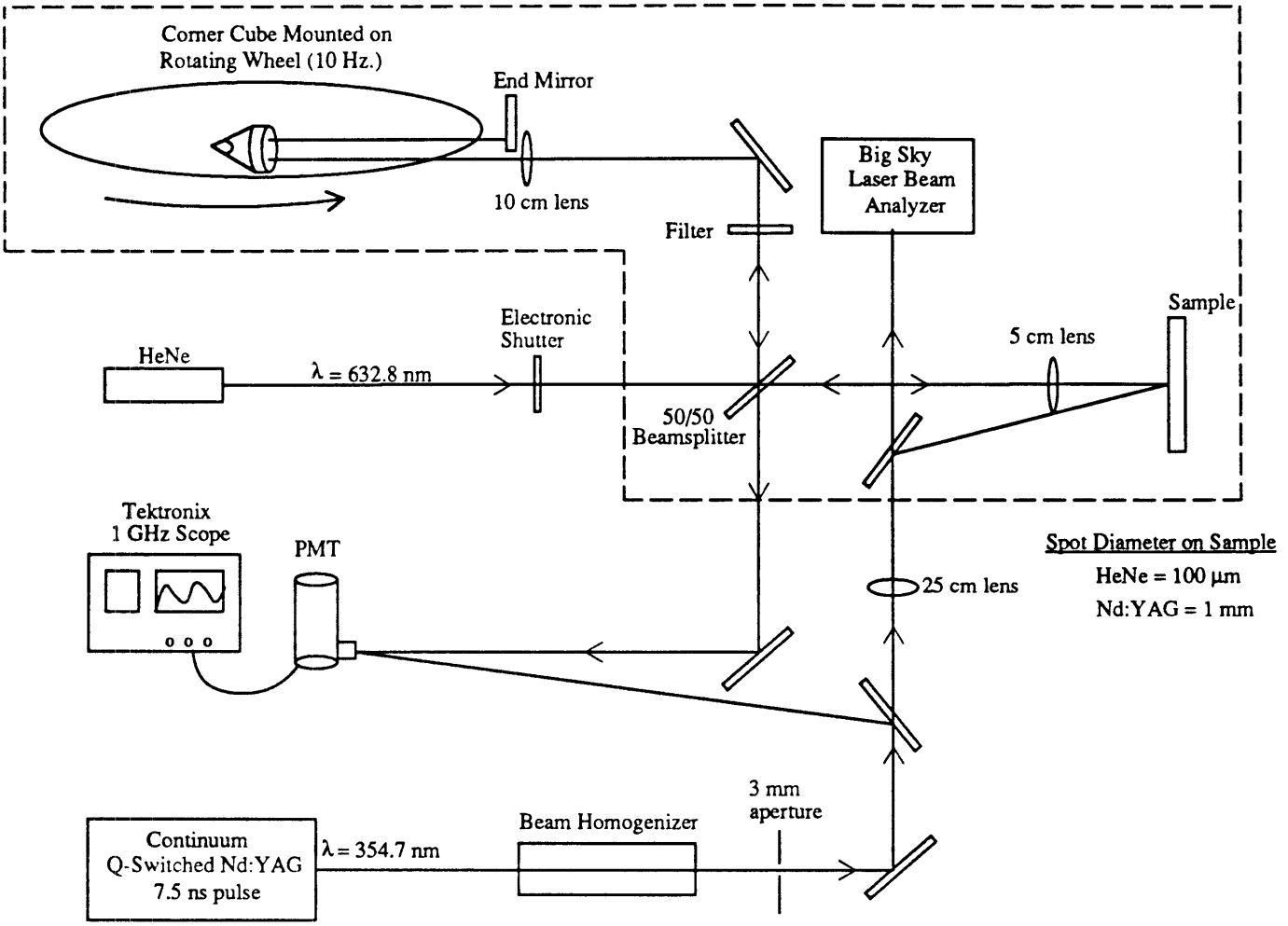

Figure 7-1. Experimental setup of the pump-probe interferometric surface monitoring technique. Thermoelastic expansion of the target caused by the absorption of the pump light can be measured by the interferometer with a spatial resolution of < 3 nm and a time resolution < 3 ns.

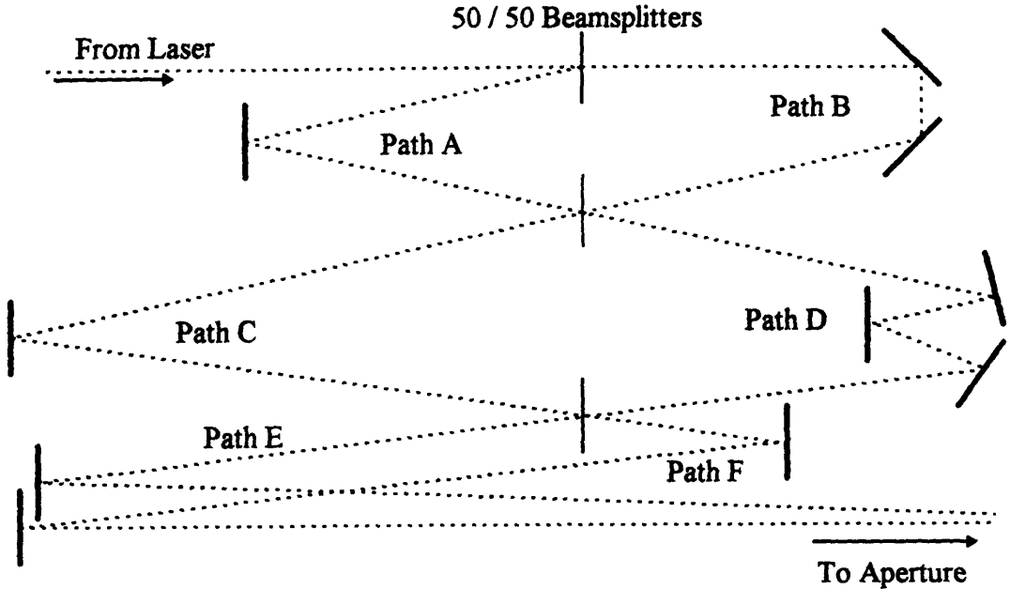

Figure 7-2. Schematic of the Beam Homogenizer

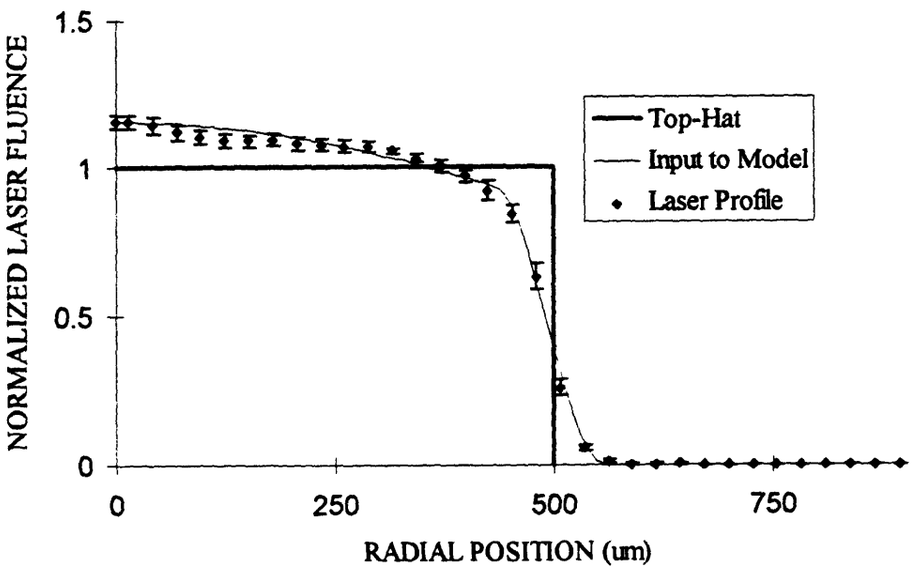

Figure 7-3. The average radial laser beam profile, L(r), was obtained by averaging nine profiles taken before, during, and after the experiments. Due to the significant deviations from a top-hat profile (heavy line), a fit to the data (light line) was used as input to the numerical model.

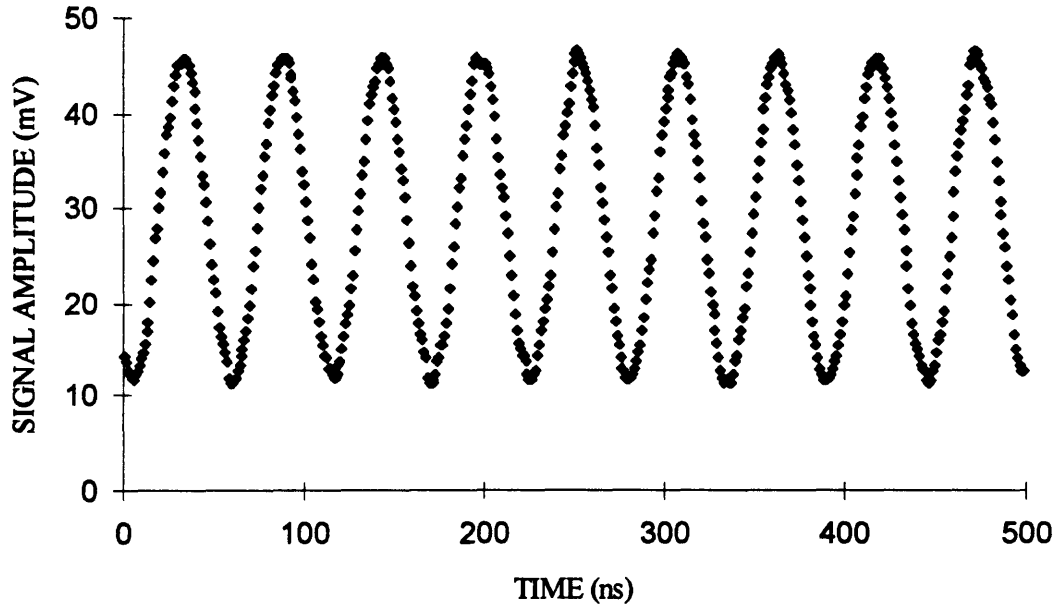

Figure 7-4. Since the relative path length of the arms in the interferometer is changing at a constant rate due to the rotating wheel (for a stationary target), the light intensity on the PMT varies sinusoidally due to the alternating constructive and destructive interference.

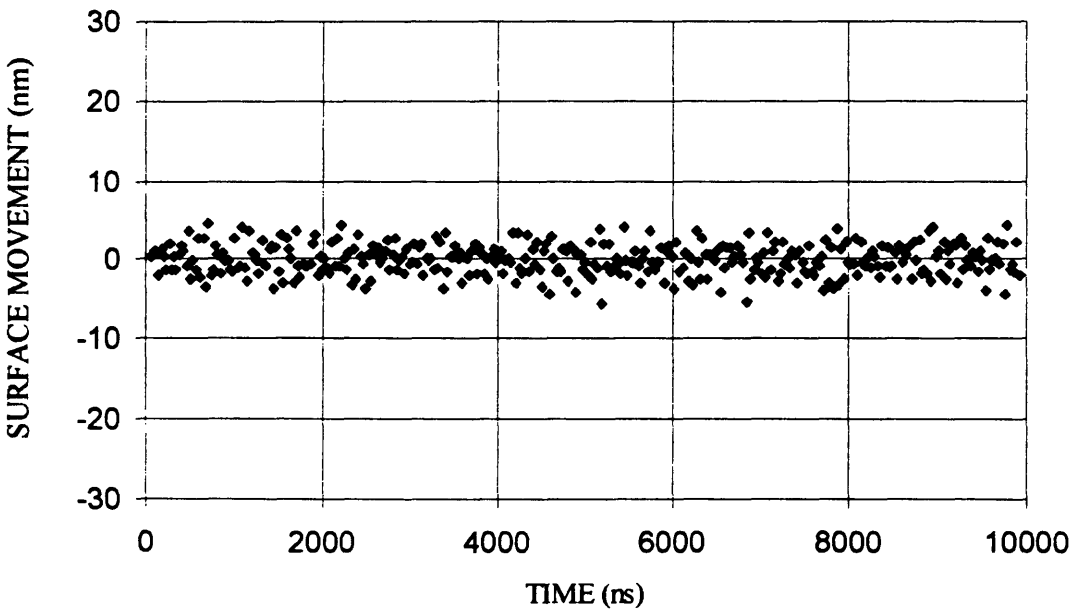

Figure 7-5. The calculated surface movement of a stationary target shows that the spatial resolution of the interferometric surface monitoring tool is +/- 2 nm. The fact that there is no drift indicates that the tangential velocity of the corner cube is essentially constant during the 10 μs experiment.

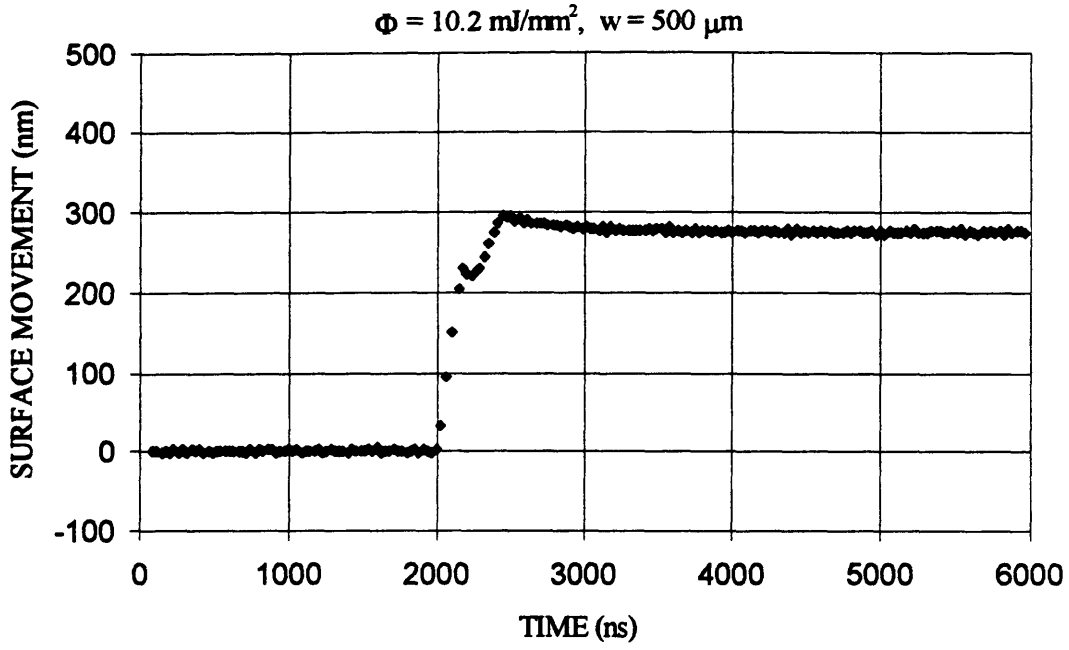

Figure 7-6. The surface movement of acrylite as a function of time after absorbing a short pulse of light at 2000 ns. The surface movement undergoes a series of expansions and contractions before approaching a new equilibrium position at 275 nm.

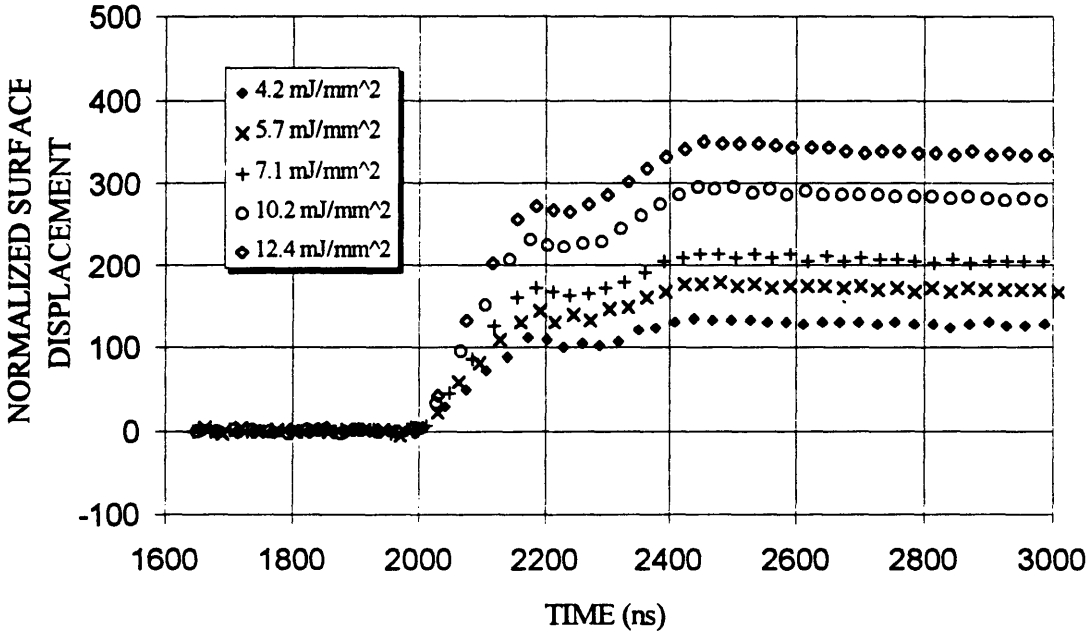

Figure 7-7. As the fluence is increased, the material undergoes more expansion leading to a greater surface movement. The time dependent features of the expansion curve, however, appear to remain constant.

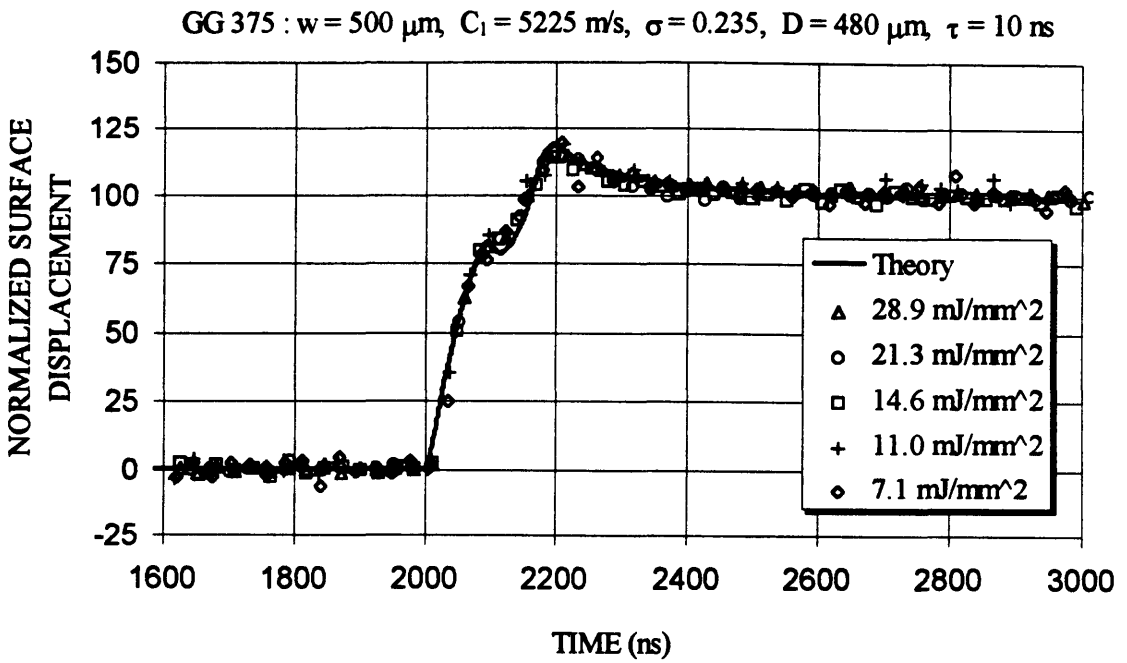

Figure 7-8. The normalized thermoelastic expansion of glass as a function of time shows that over this range of fluences, the optical, thermal and mechanical properties are constant. The theoretical prediction is in excellent agreement with the experimental data, including the fine details.

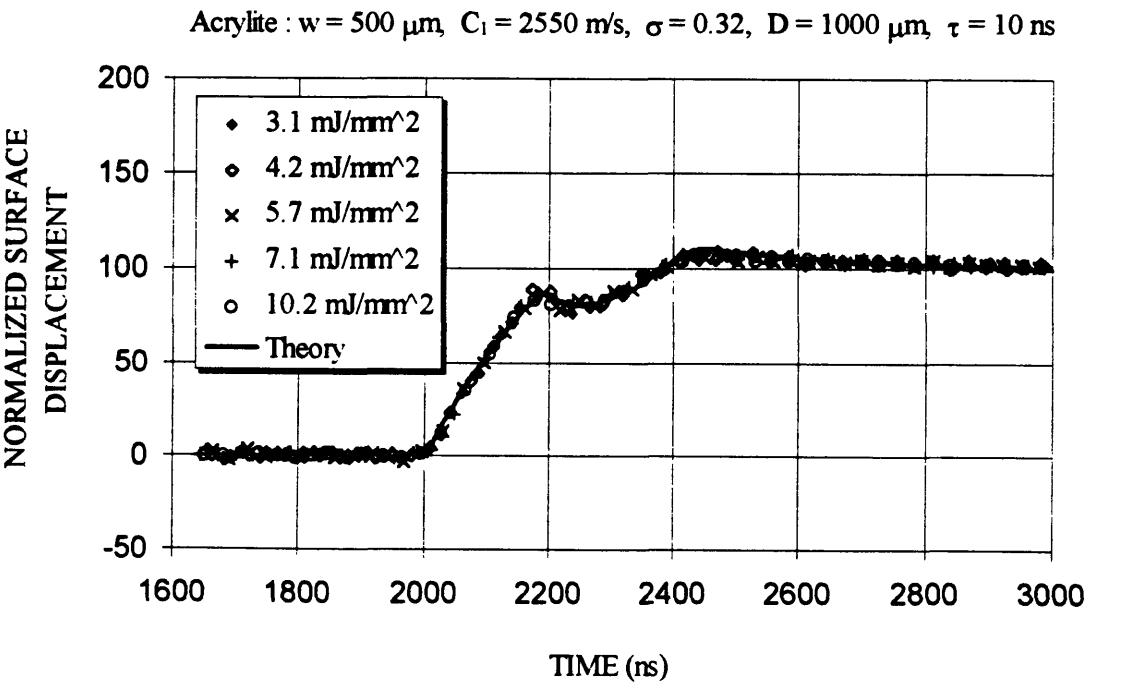

Figure 7-9. The location of the two peaks allow the longitudinal speed of sound and Poisson ratio to be determined. The slope of the initial expansion curve can then be used to determine the optical penetration depth. As with glass, this data implies that the physical properties of acrylite are not changing over this range of fluences.

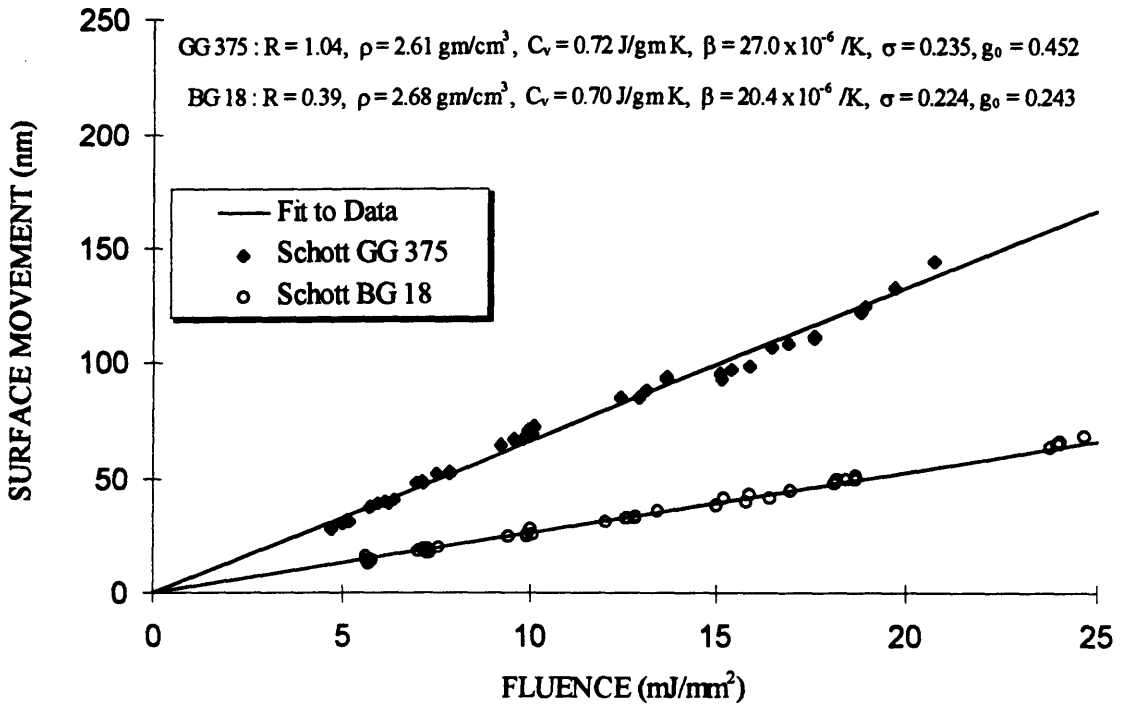

Figure 7-10. The laser-induced thermoelastic expansion of two different glasses as a function of laser fluence is in agreement with the theoretical predicted expansion based on the known optical, thermal, and mechanical properties of the glasses.

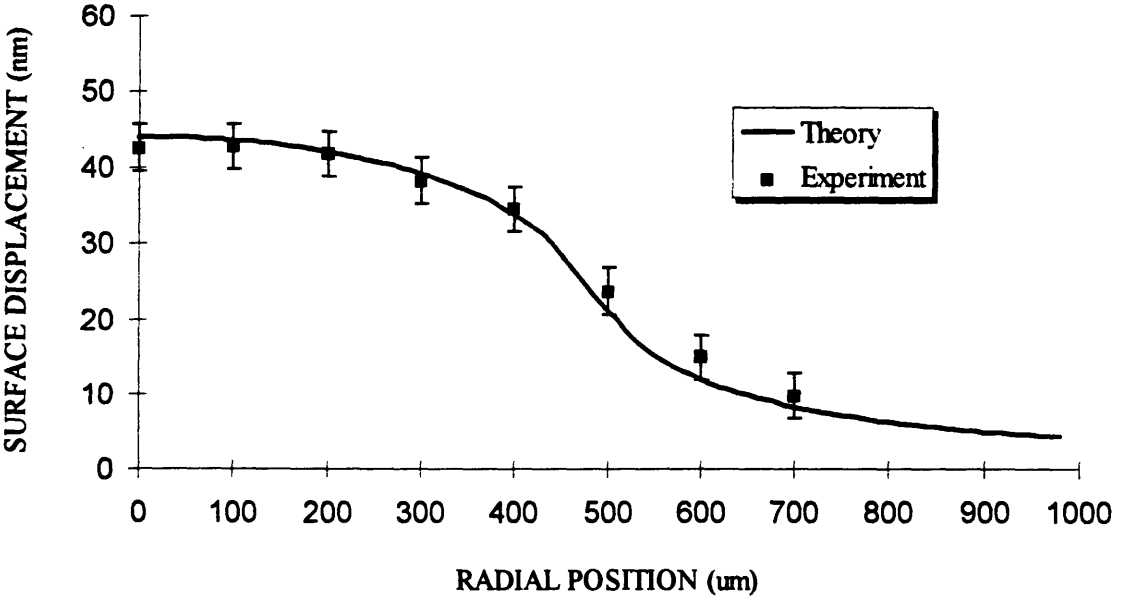

Figure 7-11. A comparison of the measured equilibrium displacement as a function of radial position to the prediction from the numerical model. Note that when the heated material ($r < 500$ μm) expands, it drags the unheated material ($r > 500$ μm) with it. The errors bars are set at + / - 3 nm, the resolution of the experimental technique.

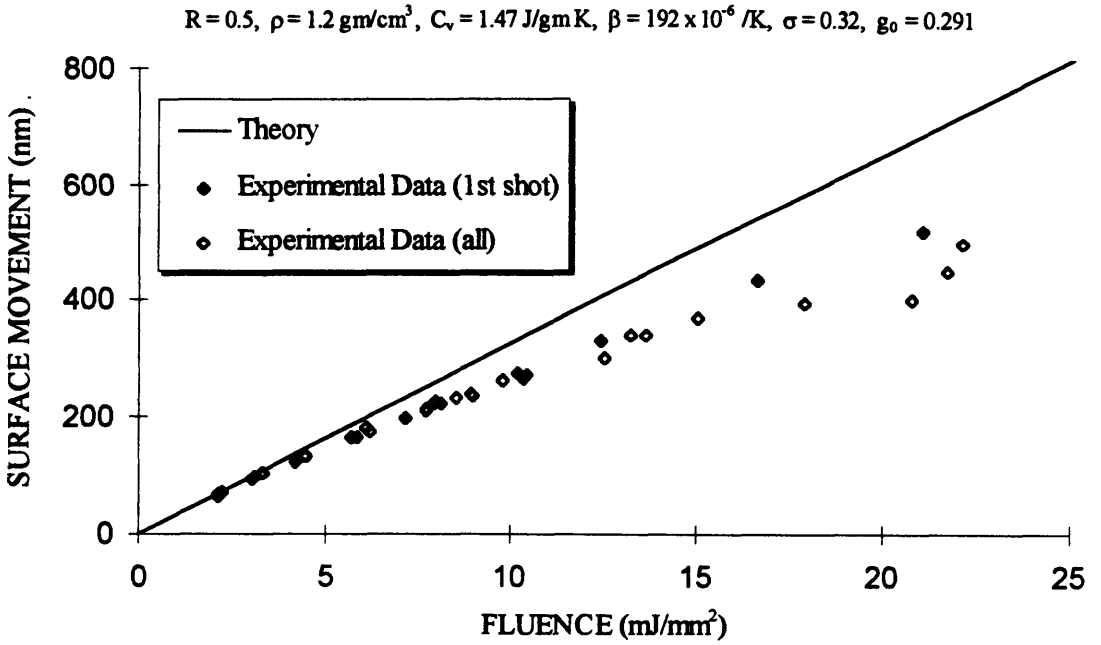

Figure 7-12. The laser-induced thermoelastic expansion of acrylite as a function of laser fluence is in agreement with theory for at low fluences. At higher fluences, permanent defects created by the laser pulse change the response of the target.

CHAPTER 8

Application of Interferometric Surface Monitoring to Study the Physical Properties of Biological Tissue and the Initiation of Ablation

8.1 OVERVIEW

A quantitative determination of the laser induced stress distribution within a solid is of great importance to the understanding of laser ablation. In chapters 4-6, the theory of elasticity has been used to develop a detailed three dimensional model which calculates this stress distribution. The theoretical model predicts the time dependent stress distribution given the thermal, mechanical, and optical properties of the target material. Since these properties are not accurately known for biological tissue, it is difficult to make quantitative predictions. In chapter 7, an experimental technique was described which overcomes this problem. This technique is based on an interferometric surface monitoring of the target surface which allows the laser induced thermal expansion of the target to be measured with nanometer accuracy on a nanosecond time scale. As demonstrated on glass and plastic, the complex time dependent features in the surface expansion of the target allow one to determine the important physical parameters necessary to calculate the stress at the ablation threshold.

In this chapter, experimental results using this technique are presented for both beef shank bone, a characteristic "hard" biological tissue, and human meniscus, a characteristic "soft" biological tissue. The data collected from bone allows the longitudinal speed of sound, Poisson's ratio, Gruneisen coefficient, optical penetration depth, and effects of scattering to be measured. From this data, the magnitude of the laser-induced stress can be calculated. The data collected from meniscus shows the anomalous behavior deduced from earlier experiments (section 3.5) in unprecedented detail. This behavior is consistent with the formation, growth, and collapse of cavitation bubbles within the tissue.

Besides measuring the physical properties of the target material which are necessary to calculate the stresses, this experimental technique can also be used to study the ablation process itself. Results for the ablation of acrylite and bone are presented which are consistent with the photomechanical model of ablation. In particular, these results show although the laser-induced temperature rise at ablation threshold is only ~ 20 ^{0}C, stresses of several hundred bars are generated. Furthermore, at the fluences studied, ablation in both bone and acrylite does not occur on the first shot but after several shots - implying that the material is being gradually altered. Photomicrographs of acrylite show an accumulation of microscopic defects during laser irradiation. These results support the photomechanical model of ablation and will be discussed in greater detail in chapter 9.

This work was presented in part at the 1994 Gordon Conference on Lasers in Biology and Medicine, July 4-8, Meriden, NH by my colleague Dr. Irving Itzkan. Some of this work will be published in the journals *Proceedings of the National Academy of Sciences* [Itzkan et al., 1994] and *Clinical Orthopedics* [Schaffer et al., 1994] by my colleague Dr. Itzkan and Dr. Schaffer.

8.2 INTRODUCTION

In chapter 6, it was shown that laser irradiation of a target surface led to the development of significant tensile stresses on the surface of the target. The magnitude of these stresses were reported as a fraction of σ_{max}, the maximum initial compressive stress. In order to quantitatively evaluate the photomechanical model of ablation, the magnitude of the laser induced stress, and thus the value of σ_{max}, must also be determined. Using the experimental technique of interferometric surface monitoring described in chapter 7 and the full time dependent three dimensional model described in chapter 6, the physical properties necessary to calculate σ_{max} in biological tissue can be determined.

After a brief review of this technique in section 8.3, a detailed comparison of the predicted and experimentally measured surface expansion is presented for beef shank bone in section 8.4. The time dependent expansion exhibits several complex features which are uniquely related to the thermal, optical and mechanical properties of the material. By comparing the data to the theory, the values of several important physical properties including the longitudinal speed of sound, Poisson's ratio, Gruneisen coefficient, and the optical penetration depth of the laser light can be extracted. In

addition, deviations between theory and experiment show the importance of scattering within the target and is addressed in section 8.4.3. Given these experimentally measured properties, σ_{max} can be determined.

With a slight modification of the experimental geometry, the time dependent expansion of the target surface can be determined for laser fluences above the threshold for ablation. Although most of the data presented in chapter 7 and section 8.4 was collected with the HeNe probe beam concentric with the laser pump beam, experimental data can also be collected when the probe is adjacent to the laser heated region. Although the ablation event will completely destroy the surface of the target within the irradiated region, the unaffected adjacent region will allow the results to be monitored interferometrically. Experimental data for the expansion of acrylite and bone during ablation is presented in section 8.5 and is shown to be in support of the photomechanical model of ablation.

Experimental data from meniscus tissue and an aqueous solution is presented in section 8.6. The results show long-lived surface motion which is not consistent with predictions based only on thermoelastic motion. Although this behavior prevents the measurement of some important physical properties, estimates of the peak temperatures (~ 5 ^{0}C) and stresses (20-30 bars) can be made. As deduced in section 3.5, the dynamics of this behavior and the values of temperature and stress are consistent with cavitation phenomena.

8.3 INTERFEROMETRIC SURFACE MONITORING TECHNIQUE

As described in detail in chapter 7, interferometric surface monitoring is a pump-probe technique which can measure the laser induced surface movement of a target material with a nanometer spatial resolution and a nanosecond temporal resolution. The pump light is a short pulse of 355 nm light which is directed onto the target surface. The absorption of this light by the target causes the material to undergo thermoelastic expansion. Our technique used to measure this expansion is based on a modified Michelson interferometer which uses the target as the end mirror in one arm of the interferometer and a rotating corner cube prism in the other arm. Using this arrangement, both the velocity and direction of the target movement is measured and thus the surface position as a function of time can be determined.

A comparison of the experimentally measured time dependent surface expansion to the theoretically predicted movement allows one to determine the optical, thermal and mechanical properties of the target material (see section 7.5). The predicted movement is obtained by a numerical solution of the thermoelastic wave equation for the given non-uniform laser induced temperature distribution and was discussed in detail in chapter 6. Assuming axial symmetry and neglecting scattering within the target, the laser induced temperature distribution within the target will have the form

$$T(r,z) = \frac{\Phi}{\rho C_v D} L(r) e^{-z/D} \qquad [8\text{-}1]$$

where Φ is the peak incident laser fluence (energy per unit area), L(r) is the radial distribution of this fluence, ρ is the density of the target and C_V is the heat capacity.

The assumptions made in the theoretical model and their validity for describing glass and plastic targets were described in section 7.4 and 7.5. In describing biological tissue, there are two additional complications. First, since biological tissue is a turbid media, the assumption of negligible scattering is no longer completely justified. This is discussed in greater detail in section 8.4.3 where it is shown that a first order correction which includes scattering leads to better agreement between experiment and theory. Secondly, some biological tissues, including bone, are known to be non-isotropic. In future work, this effect can be accounted for by replacing the isotropic mechanical constants with nonisotropic tensors in the numerical code.

8.4 EXPERIMENTAL RESULTS ON BONE : MEASUREMENT OF PHYSICAL PROPERTIES

In this section, the technique of interferometric surface monitoring is used to measure the thermoelastic expansion of beef shank bone caused by sub-ablation threshold laser pulses. The laser beam profile and target preparation will be described in section 8.4.1. In section 8.4.2, the time dependent thermoelastic expansion will be discussed. The complex behavior of the expansion curve allows the values of important physical properties of the target to be determined. In section 8.4.3, important deviations between experiment and theory are shown to be caused by scattering within the bone. The steady state thermoelastic expansion is discussed in section 8.4.4. From this expansion, the final

physical constant which is needed to calculate the magnitude of the laser induced stresses can be determined.

8.4.1 Experimental Preliminaries.

The laser beam profile used in this experiment was measured by a laser beam analyzer (see section 7.3.1) before, during and after the experiment and is shown in figure 8-1. Since there are significant deviations between the measured profile and a top-hat distribution, the measured profile was fit to an analytic function of the form :

$$L(r) = L_0 e^{-r^2/r_4^2} \qquad for \quad r \le r_1$$

$$L(r) = \frac{L_0}{2}\left\{1 + COS\left[\frac{\pi}{k_1}(r - r_3)\right]\right\} \qquad for \quad r_1 < r \le r_2 \qquad [8\text{-}2]$$

$$L(r) = 0 \qquad for \quad r > r_2$$

Using the parameters L_0 = 1.16, r_1 = 440 μm, r_2 = 560 μm, r_3 = 420 μm, r_4 = 930 μm and k_1 = 140 μm, an excellent fit was obtained (see figure 8-1). This fit was used as an input to the numerical model.

The spatial resolution of this technique is completely determined by the signal to noise ratio of the interference fringes measured by the photomultiplier tube. For the glass and plastic samples described in chapter 7, the smooth surfaces of these targets allowed large signals to be obtained leading to a standard deviation of +/- 2 nm for the spatial resolution. The signals from the rough surface of bone were smaller in amplitude and significantly more difficult to obtain. The bone surface was prepared by using a razor

blade to remove surface refuse and the periosteum from the cortical surface. The samples were then polished in a three step process which ended with a 0.05 μm grit alumina oxide polish. The interferometric probe beam was translated across the bone surface until a reasonable signal was obtained. Experimental data was collected when the amplitude of the interference fringes was between 15 and 30 mV. The calculated surface motion of a stationary bone sample when the fringe amplitude is 30 mV is shown in figure 8-2. Since the sample is stationary, any calculated motion is a measure of the system resolution. The data in figure 8-2 shows that the spatial resolution is less than 10 nm with a standard deviation of +/- 3 nm. When the fringe amplitude is 15 mV, the standard deviation rises to nearly +/- 5 nm.

8.4.2 Time Dependent Expansion

The dramatic improvement of this experimental technique over that described in chapter 3 is illustrated in figure 8-3. In chapter 3, the surface motion of bone corresponded to less than one fringe of motion (158 nm) and therefore could only be estimated (figure 3-2). With the modified interferometer, small fractions of a fringe shift can easily be determined, as demonstrated in figure 8-3 which shows a 25 nm surface motion of bone. This figure is a ten shot average where each pulse was fired at 2000 ns and had a fluence of 1.4 mJ/mm^2.

The surface movement for a range of fluences from 7.5 to 13.2 mJ/mm^2 is shown in figure 8-4. As with the glass and acrylite surface, the target expands rapidly immediately after absorbing the laser pulse, stops expanding, and then undergoes a

second expansion before reaching a new equilibrium level. The sample surface will remain at its new equilibrium position until thermal diffusion dissipates the energy on a millisecond time scale. Although the magnitude of the surface displacement increases as the fluence increases, the temporal features of the curve, described above, remain constant Thus, as shown in figures 8-3 and 8-4, the interferometric surface monitoring tool can measure the time dependent expansion of a target material with nanometer spatial resolution and nanosecond time resolution. A careful comparison of experimental measurements and theoretical predictions is presented below.

Figure 8-5 shows the first 1200 ns of the experimentally measured time-dependent thermoelastic expansion of bone after irradiation with a single 10 ns pulse of light for a range of fluences. For each fluence, the total movement has been normalized to 100 units. The time dependent behavior is identical throughout the fluence range, indicating that the optical, thermal, and mechanical properties are constant over this range. Note that the highest fluence corresponds to a laser induced temperature increase of 7.8 ^{0}C. As described in chapter 7, the complex time dependent features in the surface movement have a unique relationship to the mechanical, optical, and thermal properties of the material. The time of the first contraction corresponds exactly to the ratio of the laser beam radius (w) to the longitudinal speed of sound (C_l) and represents the time at which the finite size of the laser induced temperature distribution is communicated to the center point (where the interferometric probe beam is located). The time at which the second expansion ends is related to the transverse speed of sound in the material (see eq. 6-22) and thus is a sensitive measure of the Poisson ratio (σ). Since the initial slope of the expansion curve is

only a function of w, C_l, σ and the optical penetration depth, D can now be determined. This is of great significance because D is the 1/e depth of the laser induced temperature distribution and can be determined using this method at a laser fluence near the value needed to initiate ablation.

Using this technique, the values of C_l, σ, and D were determined. The location of the first peak (t = 2167 ns) corresponds to a longitudinal sound velocity of 3000 m/s. This speed was also measured by irradiating the back of the sample and using the interferometer to determine the time of flight of the acoustic wave to reach the front surface. The result of this experiment gave an identical value for the sound velocity. The end of the second contraction at t = 2400 ns corresponds to a value of 0.35 for the Poisson ratio. In order to determine D, the initial expansion curve ($2000 < t < 2100$) from many different experiments (both single shot and 10 shot averages) was compared to predictions from the numerical model for different values of D. By minimizing the least squares fit between theory and experiment, the optical penetration depth was determined to be 325 μm (figure 8-6).

The theoretically predicted movement, based on the values of C_l, σ, and D determined above, is compared to the measured movement in figure 8-5. Although there is general agreement between the two curves, the predicted alternating contractions and expansion are washed out in the data. For a turbid media such as bone, scattering within the target will change the temperature distribution and wash out the sharp temperature gradient at the radial edge of the laser beam. Since it is known that a Gaussian radial

temperature distribution will produce a smooth expansion curve, scattering may produce the measured deviation. This hypothesis is investigated in the next section.

8.4.3 Effects of Scattering in the Thermoelastic Expansion of Bone

The thermoelastic expansion of a material is driven by the temperature distribution within that material. In non-scattering media such as glass and acrylite, the laser-induced temperature distribution will depend on the absorption properties of the material and the laser beam profile. In turbid media, light scattering will also effect this distribution and must be accounted for. Given the optical properties of a material, the temperature distribution can be obtained numerically using a Monte Carlo technique. This technique was originally proposed by Metropolis and Ulam to simulate physical processes using a stochastic model [1949] and has been used by many researchers to study light transport through turbid media [e.g. Prahl et al., 1989]. In this simulation, photon packets are propagated through a three dimensional numerical grid and are subjected to scattering and absorption events. The probability of these events are determined by the absorption coefficient (μ_a) and the scattering coefficient (μ_s). Given a scattering event, the angle of scattering is determined by a probability function called the phase function. For biological tissue, the Henyey-Greenstein phase function is used [Jacques et al., 1987]. The average cosine of the scattering angle is called the anisotropy and is denoted by the symbol g.

Given μ_a, μ_s, g and the phase function, the monte carlo program can simulate the propagation of photon packets through tissue and record where every photon was absorbed or scattered out of the tissue boundaries. By simulating a large number of

photons, an accurate map can be made of the energy per unit volume as a function of spatial position which is directly proportional to the temperature distribution.

In order to examine the effects of scattering on the thermoelastic expansion of bone, a first order correction was made by using the approximate temperature distribution obtained by a monte carlo simulation as the input to the numerical model for thermoelastic expansion described in chapter 6. The optical penetration depth D, which has been used throughout this thesis and is equal to the "1/e" penetration depth of the light within the tissue, can be expressed in terms of the optical parameters discussed above :

$$D = \frac{1}{\sqrt{3\mu_a\left(\mu_a + \mu_s'\right)}} \qquad [8\text{-}3]$$

$$\text{where } \mu_s' = \mu_s(1-g) \qquad [8\text{-}4]$$

and is called the effective scattering coefficient. In order to estimate the values of these optical parameters, I will start with the value D = 325 μm obtained in the previous section. The values of μ_a and μ_s' where previously measured for beef shank bone using an integrating sphere and spectrophotometer and a penetration depth of 220 μm was obtained [Izatt, 1991b]. In order to collect this data, a milling machine was used to thin a 3 mm thick bone sample to several hundred microns. I will assume that this process is more likely to change the scattering properties of the bone than the absorption properties. Thus, using the value of μ_a = 0.7 mm^{-1} obtained by Izatt and D = 325 μm, the effective scattering coefficient can be found from eq. 8-3 and has the value 3.7 mm^{-1}. Since the

anisotropy of most biological tissues is between 0.7 and 0.95 [Cheong et al., 1990], I will choose a value g = 0.8 which leads to a scattering coefficient of 18.6 mm^{-1} (see eq. 8-3).

Using these parameters, a monte carlo program developed in our laboratory [Wu et al., 1993] was used to determine the temperature distribution within the tissue. Three million photon packets were used and a three dimensional mesh which divided the tissue into bins 40 μm on a side was used. A top-hat radial profile was assumed for the incident laser light. The resulting temperature distribution as a function of radial position for the first bin (depth = 0 to 40 μm) is compared to the result for no scattering (for the same penetration depth) in figure 8-7. As expected, scattering of the light from within the laser beam boundary leads to a reduction of peak temperature in the center and an increased temperature at larger radii. The peak temperature at the center is only 51 % of that obtained without scattering. The calculated temperature distribution as a function of depth on the radial axis is shown in figure 8-8 along with the exponentially decaying function obtained in the case where scattering is absent. The curves have been normalized so that the depth dependence could be compared.

The numerical solution of the thermoelastic wave equation, described in chapter 6, requires analytical functions for the initial temperature distribution. Therefore, as a first approximation, I will use an analytical function which fits the radial temperature distribution from the monte carlo model (see figure 8-7) which has the form :

$$L(r) = L_0 e^{-r^2/r_1^2} \qquad for \quad r \le r_1$$

$$L(r) = 0.2L_0 + 0.31L_0\left\{1 + COS\left[\frac{\pi}{k_1}(r - r_3)\right]\right\} \qquad for \quad r_1 < r \le r_2 \qquad [8\text{-}5]$$

$$L(r) = 0.62L_0 e^{-r^2/r_5^2} \qquad for \quad r > r_2$$

where $L_0 = 0.5$, $r_1 = 460$ μm, $r_2 = 540$ μm, $r_3 = 460$ μm, $r_4 = 1000$ μm, $r_5 = 500$ μm and $k_1 = 80$ μm. Due to the similarity of the axial temperature distributions for the cases of scattering and no scattering (see figure 8-8), an exponentially decaying axial temperature distribution is used.

The predicted thermoelastic motion of the bone surface caused by the temperature distribution described by eq. 8-5 is plotted against experimental data in figure 8-9. The agreement between theory and experiment is significantly better when the effects of scattering are included (figure 8-9) than when scattering is neglected (figure 8-5). This confirms the hypothesis put forward in the last section that scattering is responsible for the "washing out" of the alternating expansions and contractions originally predicted. In future work, the computer program which determines the thermoelastic motion should be modified so that the full three dimensional temperature distribution from the monte carlo program can be directly used.

Thus, the strong agreement between the predicted and measured surface motion gives a high level of confidence in the ability of this technique to measure the longitudinal speed of sound, Poisson ratio, and optical penetration depth described in section 8.4.2. In addition, since the scattering properties of the material also effect the shape of the

expansion curve in a known way, as described in this section, information regarding the scattering coefficient can also be obtained.

8.4.4 Equilibrium Displacement

As described above, given the laser radius w, the normalized time dependent expansion curve can be used to determine C_l, σ, and D (and thus R). Given these values, along with the heat capacity and density, the thermal expansion coefficient can be determined from the equilibrium displacement as a function of fluence. The analytical expression for the steady state equilibrium position S_0 (for a point at z = 0, r = 0 and assuming a top-hat radial laser profile) was given in chapter 7(see eq. 7-10) and can be written as :

$$S_0 = \frac{2(1+\sigma)}{3}\frac{\beta}{\rho C_V} g_0(R) L_0 \Phi \qquad [8\text{-}6]$$

where R is the aspect ratio (equal to w / D) and g is a geometrical correction factor given by

$$g_0(R) = n\int_0^\infty \frac{RJ_1(Ry)}{y+1}dy \qquad [8\text{-}7]$$

where J_1 is a first order Bessel function and n is a laser profile correction factor. For the radial profile given be eq. 8-5, the value n = 0.96 was found. Given w = 500 μm and D = 325 μm, the aspect ratio is 1.54 and g_0 is 0.545. Thus, by measuring S_0 as a function of fluence, β can be found since all the other parameters in eqs. 8-6 and 8-7 are known.

Experimental results for the equilibrium position as a function of laser fluence for bone are shown in figure 8-10. As seen from eq. 8-6, the data should be linear with a slope (S_0 / Φ) proportional to the thermal expansion coefficient. Using the values given above and the additional values ρ = 2.0 gm/cm^3 and C_V = 1.33 J/gm K [Duck, 1990], a least squares fit to the data gives β = 163 x 10^{-6} /K. This is consistent with the value of 197 x 10^{-6} /K reported by Duck [1990}.

As described in section 7.5.2.1, the peak laser-induced stress in a target is proportional to the laser fluence (see eq. 7-8) :

$$\sigma_{max} = \frac{1+\sigma}{3(1-\sigma)}\Gamma\frac{\Phi}{D}L_0 \qquad \text{where} \qquad \Gamma = \frac{\beta C_l^2}{C_V} \qquad [8\text{-}8]$$

and Γ is the Gruneisen coefficient. For bone, the value of the Gruneisen coefficient is found to be 1.1. Using eq. 8-5, the maximum stress induced by a laser fluence of 25 mJ/mm^2 is σ_{max} = 300 bars. Thus all the mechanical, optical and thermal parameters needed to calculate the time dependent laser induced stress distribution within a material can be determined from a detailed analysis of the thermoelastic expansion.

As a final comparison between experiment and theory, the equilibrium displacement as a function of radial position was determined by translating the HeNe probe beam (100 μm diameter) with respect to the pump light (800 μm diameter). The results of this experiment along with the theoretical prediction is shown in figure 8-11. The theoretical prediction is based on a radial temperature distribution of the form given by eq. 8-5 with L_0 = 0.5, r_1 = 360 μm, r_2 = 440 μm, r_3 = 360 μm, r_4 = 900 μm, r_5 = 400

μm and k_1 = 80 μm. Once again, there is quantitative agreement between theory and experiment. As expected, the maximum surface movement occurs at the center of the laser induced temperature distribution.

8.5 RESULTS FROM ACRYLITE AND BONE : NEAR ABLATION THRESHOLD

The experimental data described in the last section and in chapter 7 was obtained at laser fluences below the threshold for ablation. When ablation occurs, the explosive removal of material destroys the surface of the target and prevents interferometric data from being collected. As shown in figures 7-11 and 8-11, there is measurable surface movement at radial positions greater than the radius of the incident laser beam. Thus, by translating the interferometric probe beam off to the side of the laser-target interaction, interferometric data can be collected even above ablation threshold. In this section, experimental results for the surface movement of acrylite and bone will be presented for fluences near the ablation threshold. The implications of these results to the mechanism of ablation will also be discussed.

8.5.1 Thermoelastic Expansion of Acrylite During Ablation

In order to use the interferometric surface monitoring technique to study the ablation process, the probe beam must be translated to a position outside of the laser beam radius. In acrylite, where scattering is negligible, the unheated material in front of the probe beam will still undergo thermoelastic motion as the adjacent, laser-heated material expands. Comparisons of the measured and predicted time dependent expansion for

fluences well below ablation threshold are shown in figures 8-12 and 8-13. In figure 8-12, the motion is monitored at a radial distance of 400 μm, slightly outside the laser beam radius of 375 μm. In figure 8-13, the motion is monitored at an even greater radius of 600 μm. The same time dependent features in the surface expansion which were seen when the center of the temperature distribution was monitored are present in these figures. After an initial expansion, the surface contracts, expands again, and then slowly approaches a new equilibrium position. As expected, however, there are quantitative differences between the off center and on center curves. As shown in figure 7-11, the magnitude of the expansion decreases significantly for radii outside the laser beam radius. At a radial position of r = 600 μm, the surface motion is only about one tenth of that expected at r = 0. On center, the expansion begins immediately after the laser pulse is fired. Off center, the expansion begins after the laser pulse, at a time which corresponds to the travel time of an acoustic wave to reach the probe position from the edge of the distribution. Due to the acoustic travel time, the timing of the other features in figures 8-12 and 8-13 is also changed. However, as seen by the excellent fits, these features change in the theoretically predicted way and thus the methodology of determining the optical, thermal, and mechanical properties of the target material is still valid.

In the following experiments, the laser fluence was increased to values near the ablation threshold. The laser radius was set to 400 μm and the probe beam was set to monitor the expansion at a radius of 600 μm. The measured radial temperature distribution has the form given by eq. 8-2 with $L_0 = 1.15$, $r_1 = 340$ μm, $r_2 = 460$ μm, $r_3 = 318$ μm, $r_4 = 730$ μm and $k_1 = 150$ μm. The laser was fired at 2000 ns. The predicted (solid line) and

measured (data points) laser induced surface expansion of acrylite, after irradiation with a fluence of 39 mJ/mm^2, is shown in figure 8-14a. As can be seen in the figure, the agreement between theory and experiment is still quite good. Since the total movement at this high fluence cannot be predicted due to the non linear fluence dependence (see figure 7-12), the theoretical prediction has been normalized to the measured steady state displacement. The deviation between theory and experiment is consistent with the trend discovered at moderate fluences (~ 20 mJ/mm^2) while monitoring at the center.

After the fifth shot is fired at the same location, the features of the expansion curve begin to change dramatically (see figure 8-14b). As noted earlier, subsequent shots at the same site cause less expansion than the first shot (see figure 7-12). After the fifth shot, there are additional changes including a deepening of the depression after the first peak followed by a sharper rise to the second peak. The subsequent shot causes major deviations in the expansion curve. As can be seen in the figure, the surface motion caused by the sixth shot rises more quickly and then undergoes a contraction to a position 70 nm below the original level. This is followed by a sharp rise and a second sharp contraction. As will be discussed below, the new features of this curve corresponds to a fracturing of the surface (see figure 8-18, photograph C).

Similar behavior is seen in figures 8-15a and 8-15b which show the surface expansion of acrylite after irradiation with a fluence of 60 mJ/mm^2. At this fluence, there is still agreement between theory and experiment, indicating that the speed of sound and penetration depth have not changed significantly. As before, the major deviation is a

reduction in the first depression. The second shot at the same location (figure 8-15b) shows a further reduction in the depression and an overall decreased displacement but otherwise shows the same temporal location of the peaks and the same initial slope (when the two curves are normalized to the same total displacement). After the fourth shot, the unusual features seen in figure 8-14b and discussed above appear, including a surface contraction of 250 nm below its original position (see figure 8-18, photograph D).

8.5.2 Thermoelastic Expansion of Bone During Ablation

Using similar experimental conditions, the interferometric surface monitoring technique can be used to study the ablation of bone. In bone, where scattering is not negligible, the material in front of the probe beam (at $r > w$) will undergo thermoelastic motion as the result of both the expansion of the adjacent, laser-heated material and the small heating caused by the scattered light. In the following, the theoretical predictions are based on a radial temperature distribution of the form given by eq. 8-5 with $L_0 = 0.5$, $r_1 = 360$ μm, $r_2 = 440$ μm, $r_3 = 360$ μm, $r_4 = 900$ μm, $r_5 = 400$ μm and $k_1 = 80$ μm. The predicted (solid line) and measured (data points) laser induced surface expansion of bone, at a radius of 500 μm from the center of the laser beam ($w = 400$ μm), is shown in figure 8-16a. In this experiment, 19.2 mJ/mm^2 of light was fired at 2000 ns. As with acrylite, the same time dependent features in the surface expansion which were seen when the center of the temperature distribution was monitored are present in figure 8-16a.

After the second shot is fired at the same location (with a fluence of 29.4 mJ/mm^2), the features of the expansion curve begin to change (figure 8-16b). In particular, the

amplitude of the second expansion peak increases dramatically. The fourth shot causes major deviations in the expansion curve. As can be seen in the figure, the surface motion caused by this shot undergoes a large contraction to a position 110 nm below the original level. Similar behavior is seen in figure 8-17 which shows the surface expansion of bone for a fluence of 34 mJ/mm^2 and a radius of 700 μm. After the fourth shot at the same location, a contraction to 200 nm below the original surface position is seen.

8.5.3 Implications to the Mechanism for Ablation

Photographs of the acrylite surface after various numbers of laser shots are shown in figure 8-18 (A-D). All photographs were taken through a microscope and were back illuminated. After eight shots at a fluence of 26 mJ/mm^2, a large number of defects have accumulated in the laser irradiated region (photograph A). The diameter of the effected region is equal to the laser beam diameter (800 μm). A high magnification of these defects is shown in photograph B. An examination of these defects reveals that the dark circles are actually fracture patterns that are out of focus. These fracture patterns, or microcracks, are also visible in photograph B. These microcracks are concentrated near the surface and the number of them increases with each subsequent laser pulse. The formation of these defects also correlates with the non linear fall off of the equilibrium displacement as a function of fluence that was reported in chapter 7 (figure 7-12). Furthermore, since these defects will weaken the overall strength of the material, their accumulation may play an important role in the ablation process and is discussed in chapter 9. Photograph C shows the acrylite surface after 6 shots at a fluence of 40 mJ/mm^2 and corresponds to the data shown in figure 8-14b. The appearance of a large

fracture (lower center, circular in shape) correlates with the appearance of the anomalous surface motion which was measured (see figure 8-14b). The acrylite surface after five shots at a fluence of 60 mJ/mm^2 is shown in photograph D and corresponds to one shot beyond the experimental data of figure 8-15b. This photograph shows the complete destruction of the acrylite surface that occurs during ablation.

The data presented in figures 8-14, 8-15, and 8-18 provide valuable information on the mechanism of ablation. Using eq. 7-4, the peak temperature rise in acrylite caused by a laser fluence of 40.0 mJ/mm^2 can be calculated. This temperature, equal to 26.4 ^0C, is well below that required to cause vaporization. As discussed in chapter 2, it has been postulated that much higher temperatures may be present do to a substantial dynamic decrease in the penetration depth. The data in figures 8-14a and 8-15a imply that the penetration depth does not become substantially smaller at fluences sufficient to cause ablation. Although the laser-induced temperature rise is small, at this fluence the maximum stress is significant ($\sigma_{max} \sim 250$ atm).

The thermoelastic response of bone was very similar to that of acrylite (see figure 8-16 and 8-17). As with acrylite, the peak temperature rise after irradiation with a fluence of 35 mJ/mm^2 is only 20.7 ^0C and is well below that required for vaporization. The experimental data in figure 8-16a shows that there is not a dramatic reduction in the optical penetration depth at fluences near those sufficient to cause ablation. Although the laser-induced temperature rise is small, at this fluence the maximum stress is significant ($\sigma_{max} \sim 420$ atm).

The significance of these findings and their relation to the mechanism of ablation will be discussed in greater detail in chapter 9.

8.6 INTERFEROMETRIC SURFACE MONITORING OF MENISCUS AND WATER

8.6.1 Experimental Results

The tool of interferometric surface monitoring can also be used to study the laser-tissue interaction in "soft" biological tissue [Schaffer et al., 1994]. Data collected with an earlier version of this tool (see section 3.5) implied that a complex surface motion, which was not consistent with theoretical predictions, was taking place. Since this earlier tool was not sensitive to the direction of the motion, however, this motion was indirectly deduced by the complex interference pattern. A preliminary study of this surface motion using the new interferometric tool which is sensitive to the direction of motion is presented below. In this preliminary study, it is assumed that the radial profile has a top-hat distribution with a measured radius of 500 μm. Since the laser beam homogenizer was not used and the radial profile was not measured with the laser beam analyzer, the error bars associated with knowing the laser fluence are large (~ +/- 25 %). As in section 3.5, data is presented for both a $FeCl_3$ aqueous solution and human meniscus tissue.

As with the bone samples, it was very difficult to get a good specular reflection from the surface of meniscus. The smaller signals led to a reduction in the signal to noise ratio and thus poorer spatial resolution. The measured surface movement of a stationary

meniscal target is plotted in figure 8-19 and shows a scatter of +/- 25 nm and a standard deviation of +/- 8 nm. This resolution, however, is a significant improvement over that from chapter 3 and, coupled with the ability to detect the direction of motion, should provide unprecedented detail of the thermoelastic response of the tissue.

The thermoelastic surface motion of meniscus after irradiation with a fluence of 1.5 mJ/mm^2 is shown in figure 8-20. The short pulse of laser light was fired at 2000 ns. As expected, the tissue undergoes thermoelastic expansion for several hundred nanoseconds before reaching a new equilibrium position. As shown in figure 8-21, the surface motion shows an additional unexpected feature after irradiation at a higher fluence (4.4 mJ/mm^2). The surface initially expands to almost 200 nm, before settling back to the equilibrium position of 140 nm. This feature, although much smaller, is also present in the previous figure (8-20). As the fluence is increased to 7.2 mJ/mm^2, this feature begins to dominate the motion (figure 8-22). As shown in this figure, motion takes place for nearly 5 μs, over an order of magnitude longer than theoretically predicted. For this fluence, the meniscus surface moves over 900 nm, before returning to its equilibrium position 260 nm above its original level.

The surface motion of an aqueous solution after laser irradiation was also monitored to determine whether this anomalous behavior in meniscus could be attributed to the water which comprises 70 % of the tissue. Figure 8-23 shows this motion of an $FeCl_3$-doped solution after irradiation with a 5.4 mJ/mm^2 pulse at t = 2000 ns. As with meniscus, the surface motion is dominated by the same long-lived anomalous behavior.

8.6.2 Analysis

The experimental results presented in section 8.6.1 are entirely consistent with the earlier results reported in section 3.5. The new technique, however, directly shows both the expansion and contraction of the material in unprecedented detail. As discussed in section 3.6, this motion is consistent with the formation, growth, and collapse of cavitation bubbles within the target material.

Although the complex features of the time dependent expansion curve are hidden by the effects of cavitation, the equilibrium displacement can be measured at times after the collapse of the bubbles. Figure 8-23 shows an equilibrium displacement of the aqueous solution of 218 nm after irradiation with a fluence of 5.4 mJ/mm^2. Using eq. 8-6, the measured constants D = 200 μm and w = 500 μm, the calculated value $g_0(R) = 0.68$ and the known values of water ($\rho = 1.0$ gm/cm^3, $C_V = 4.18$ J/gm K and $\sigma = 0.5$) gives a measured value of the expansion coefficient of 245×10^{-6} / K. This value is within 20 % of the known value of water (206×10^{-6} / K). Using data for the surface motion of meniscus (figures 8-20 through 8-22), the expansion coefficient of this tissue can also be calculated. Given D = 350 μm [Banish, 1992], w = 500 μm, $g_0 = 0.55$, $\rho = 1.1$ gm/cm^3 [Duck, 1990], and assuming similar values of the heat capacity and Poisson ratio as water gives $\beta = 293 \times 10^{-6}$ / K. This value is consistent with the fact that the expansion coefficient of soft biological tissues is generally greater than that of pure water [Duck, 1990].

A calculation of the associated stresses and temperatures rises verifies that cavitation is the cause of the rapid surface expansion and contraction. Using eq. 8-1 and the parameters given above, the peak temperature rise of the aqueous solution is only 6.4 ^{0}C for the experimental conditions shown in figure 8-23. For meniscus, the temperature rise is between 1 and 4.5 ^{0}C (figures 8-20 through 8-22). Although these temperature rises are too small to cause any effects associated with vaporization, the associated stresses are large enough to rupture the water. Using eq. 8-8 and the value C_l = 1500 m/s, the maximum stress in the aqueous solution is 30 bars (figure 8-23). In meniscus, the maximum stress is 20 and 33 bars, respectively, for figures 8-21 and 8-22. As discussed in section 3.6, this is in the range where one would expect cavitation to begin.

This is a significant finding because the collapse of cavitation bubbles has been shown to be capable of destroying any adjacent solid material. Although this phenomena needs to be studied in much greater detail, the finding of a destructive mechanical effect which is initiated by very low laser fluences (and thus low temperature rises) lends support to the photomechanical model of ablation

8.7 CONCLUSIONS

A determination of the magnitude and spatial distribution of the time dependent laser induced stresses in a solid material is of importance to understanding the mechanism of laser ablation. Although the spatial distribution of stresses was calculated in chapter 6 (showing the significant finding that tensile stresses formed on the surface of the target),

the magnitude of the stresses could not be calculated without knowledge of the physical properties of the material. By combining a theoretical model, described in chapter 6, and an experimental technique, based on interferometric surface monitoring and described in chapter 7, I have developed a methodology to determine the magnitude of laser-induced stresses within biological tissue. By measuring the time dependent thermoelastic expansion of the target and comparing it to theoretical predictions, the longitudinal speed of sound, Poisson ratio, Gruneisen coefficient, and optical penetration depth were determined. Deviations between theory and experiment showed the important effects of scattering within the tissue. The ability to theoretically account for the effects of this scattering imply a future use of this technique to study light propagation within turbid media. Experimental data that demonstrates this methodology was presented in this chapter on beef shank bone.

Experimental data collected on human meniscus tissue and an aqueous solution showed additional, long-lived motion which was not consistent with purely thermoelastic motion. The dynamic behavior, low temperatures, and moderate stresses associated with this motion is consistent with the formation, growth, and collapse of cavitation bubbles (see section 3.6). This is an important finding since the collapse of cavitation bubbles is a mechanically destructive event and may play an important role in the ablation of soft biological tissues with a high water content.

In addition, a slight modification in the experimental geometry allowed the ablation event itself to be studied. Experimental results for bone and acrylite near ablation

threshold were presented. Although there were minor deviations in the expansion curve at fluences sufficient to cause ablation, there was no evidence that a significant reduction in the optical penetration depth was taking place. At ablation threshold, the peak laser induced temperature within the samples was only ~ 20^0C, a value not consistent with photothermal models of ablation. Instead, the data shows that ablation does not occur after the first shot at the fluences studied but only after several shots. This implies that the material is changing during these initial shots to make it more susceptible to ablation. Photomicrographs of acrylite show an accumulation of laser-induced microcracks after each laser pulse until ablation occurs. The peak laser-induced stresses associated with these fluences in both bone and acrylite were several hundred bars, corresponding to a significant fraction of the static tensile strength of the material. As will be discussed in greater detail in chapter 9, these results strongly imply a photomechanical model of ablation.

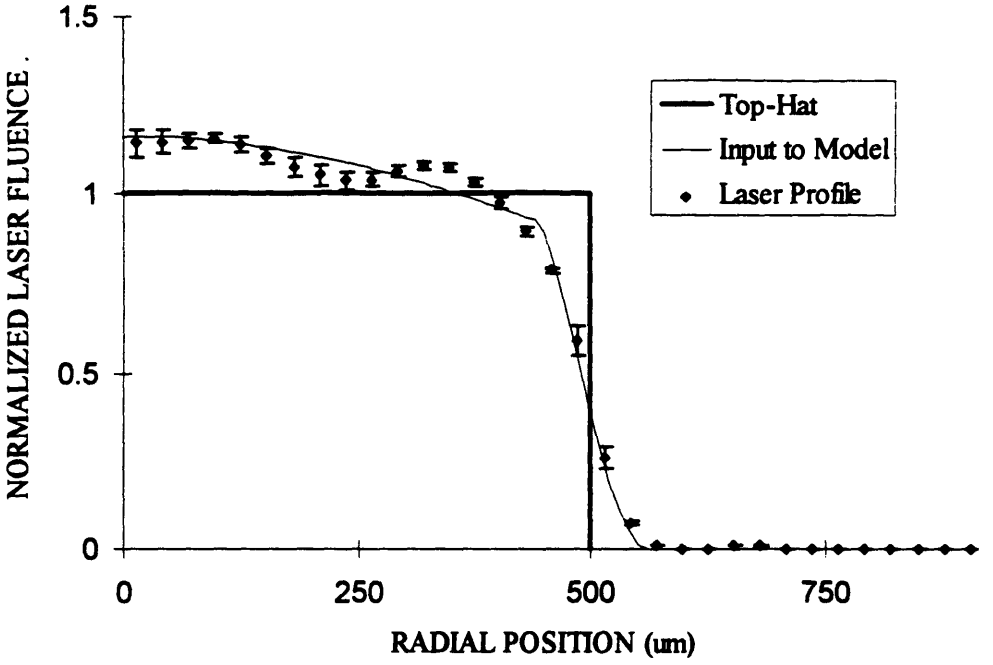

Figure 8-1. The average radial laser beam profile, L(r), was obtained by averaging five profiles taken before, during, and after the experiments. Due to the significant deviations from a top-hat profile (heavy line), a fit to the data (light line) was used as input to the numerical model.

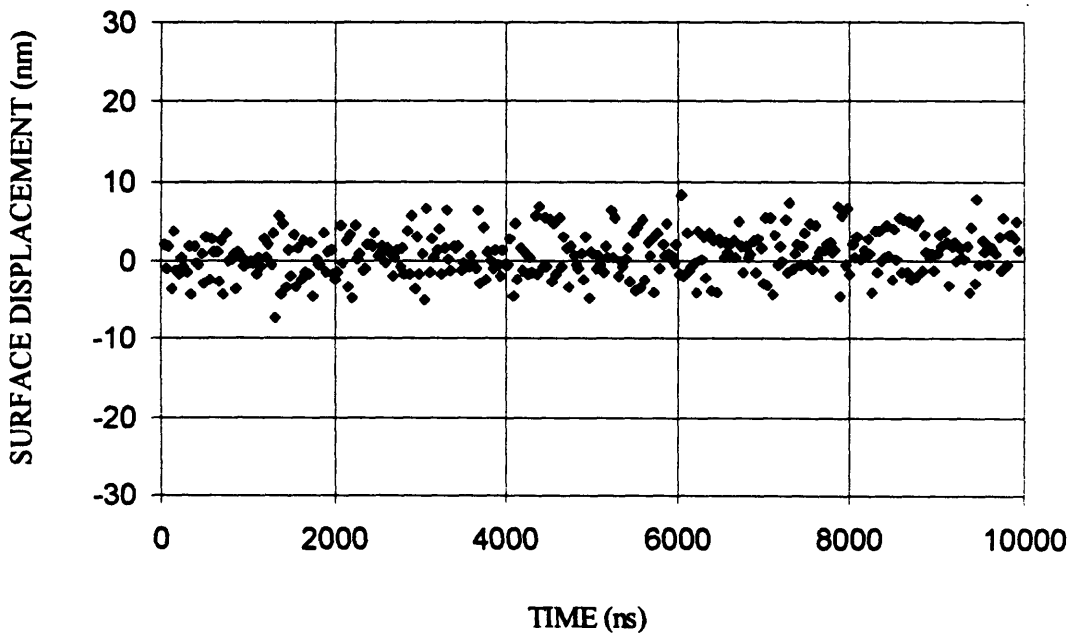

Figure 8-2. The calculated surface movement of a stationary bone target shows that the spatial resolution of the surface monitoring tool is less than 10 nm (with a standard deviation of +/- 3 nm) when the amplitude of the interference fringes is 30 mV. For an amplitdue of 15mV, the standard deviation increased to about +/- 5 nm.

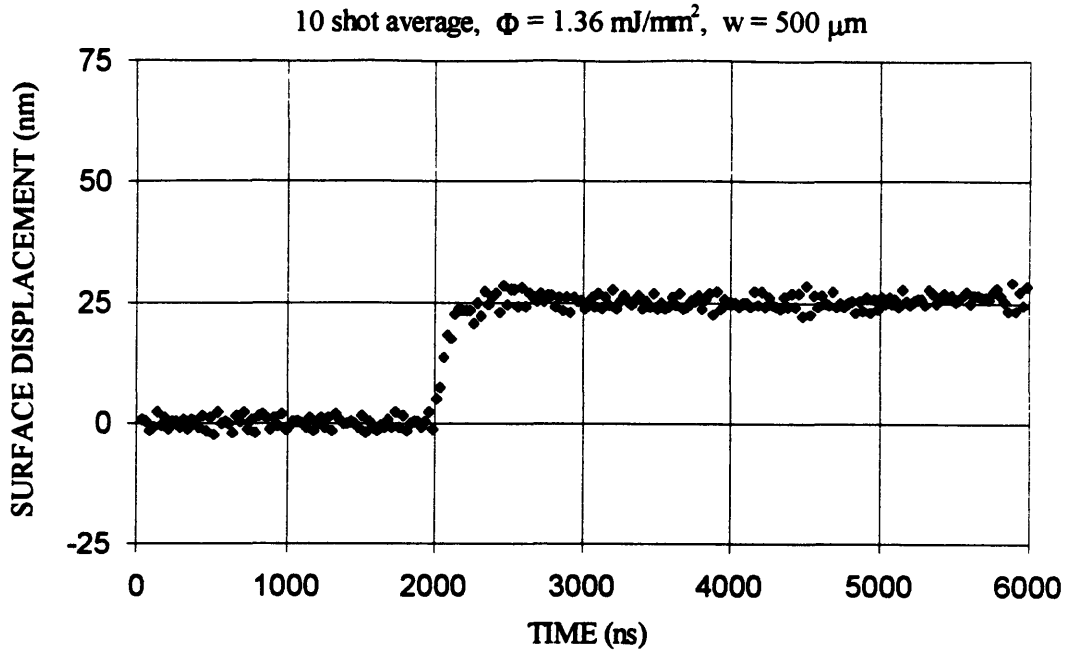

Figure 8-3. The surface movement of bone as a function of time after absorbing a short pulse of light at 2000 ns. This ten shot average shows a bone movement of only 25 nm and demonstrates the dramatic improvements over the original bone data presented in chapter 3.

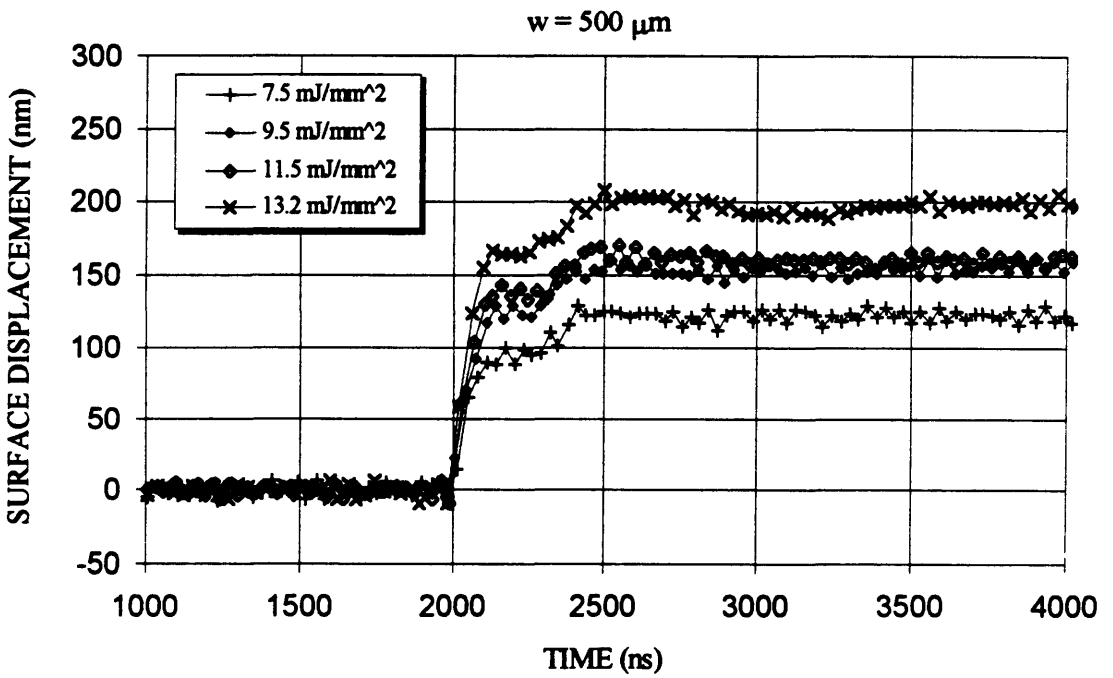

Figure 8-4. As the fluence is increased, the material undergoes more expansion leading to a greater surface movement. The time dependent features of the expansion curve, however, appear to remain constant.

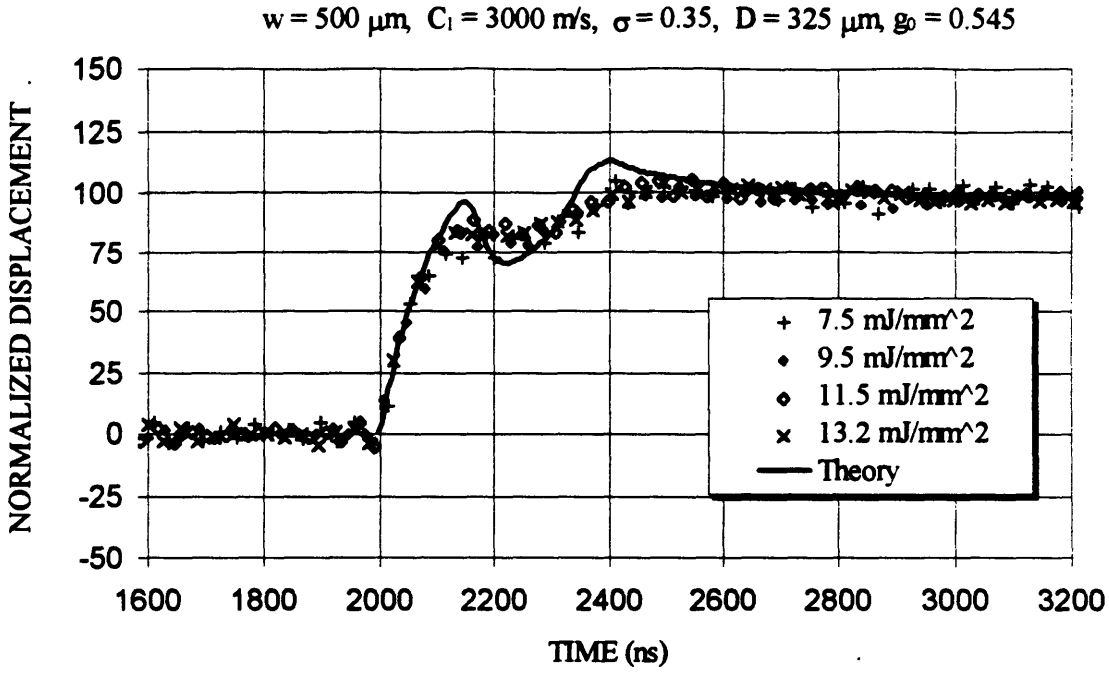

Figure 8-5. The normalized thermoelastic expansion of bone as a function of time shows that over this range of fluences, the optical, thermal and mechanical properties are constant. The deviations between theory and experiment may be due to the more complex light distribution within the bone due to scattering..

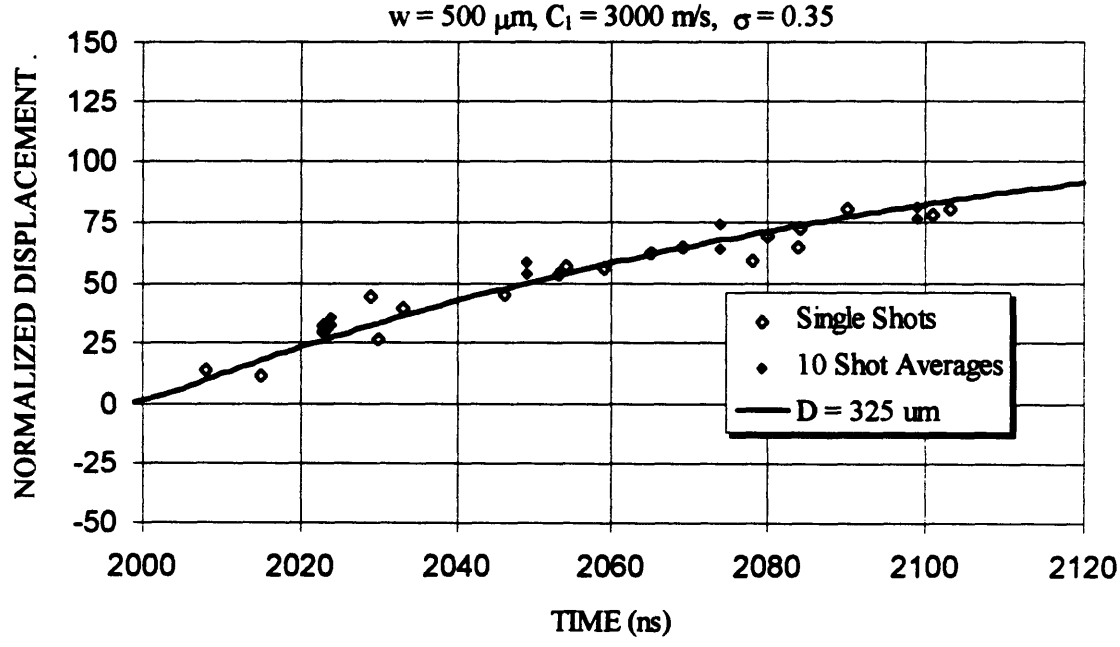

Figure 8-6. The slope of the initial expansion curve can then be used to determine the optical penetration depth. Using data from a range of fuences, the value D = 325 μm was found from a least squares fit of the numerical prediction.

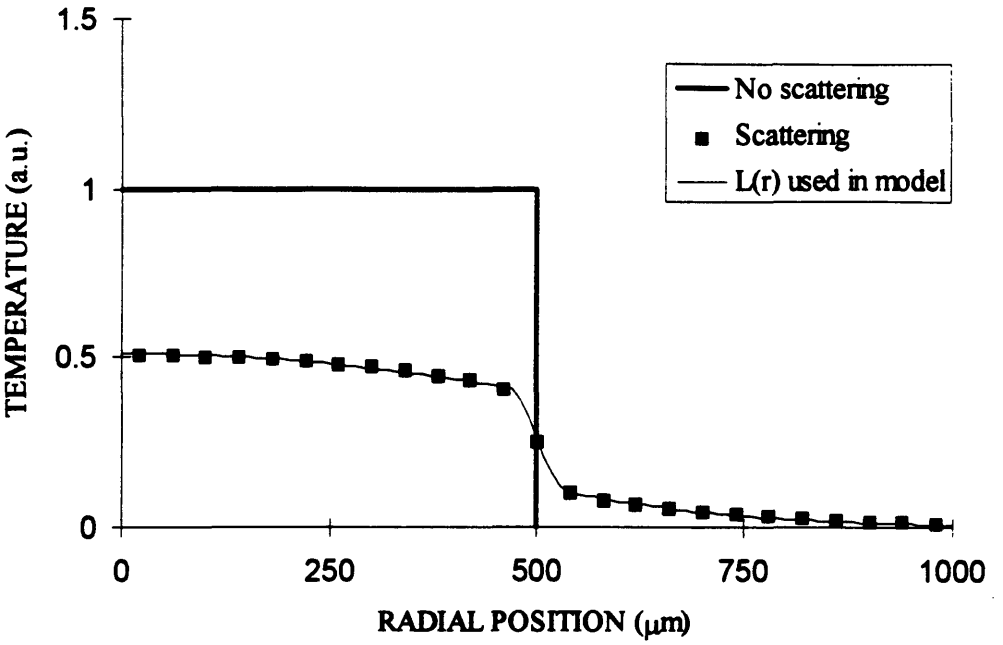

Figure 8-7. Comparison of the temperature distribution near the surface as a function of radial position for the case when scattering is present (dark squares) and absent (heavy line) shows that scattering causes a redistribution of energy from within the laser profile to larger radii. A monte carlo technique was used to determine the profiles. An analytical fit to the scattering profile (light line) is used as input to the thermoelastic expansion model.

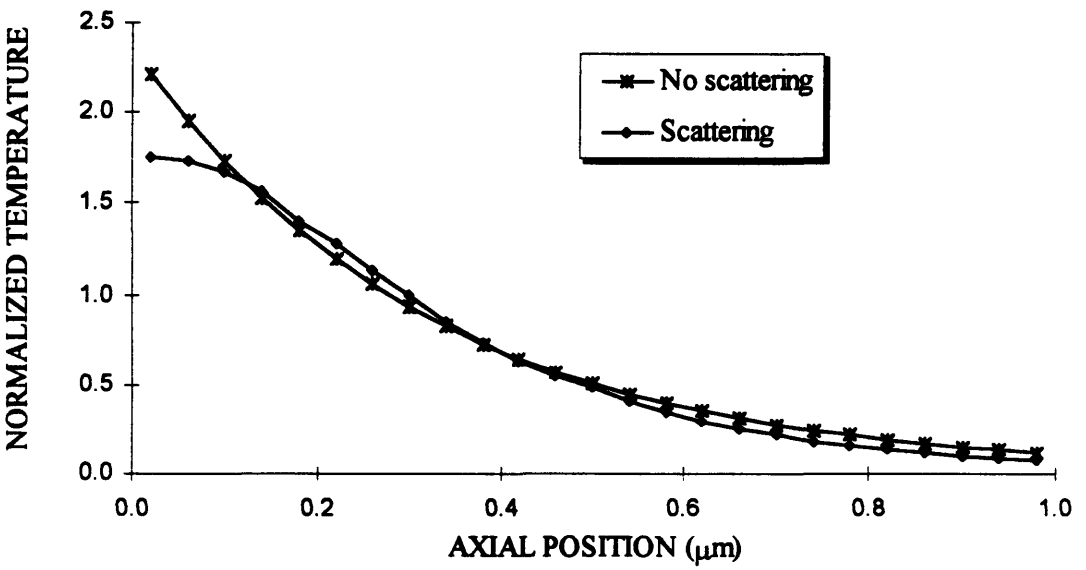

Figure 8-8. Comparison of the normalized temperature distribution on the radial axis as a function of depth into the tissue for the case when scattering is present and absent.

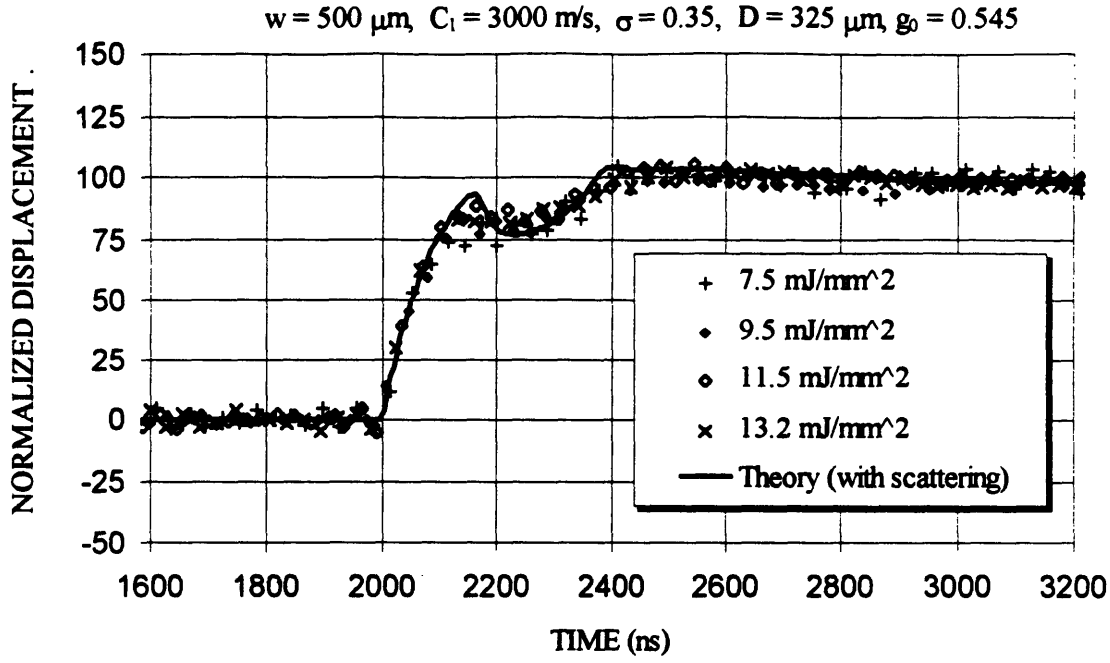

Figure 8-9. When the effects of scattering are included, the deviations between theory and experiment are significantly reduced (compare to fig 8-5). Thus, besides allowing C_l, σ, and D to be determined, the time dependent surface expansion provides important information on the scattering within the target.

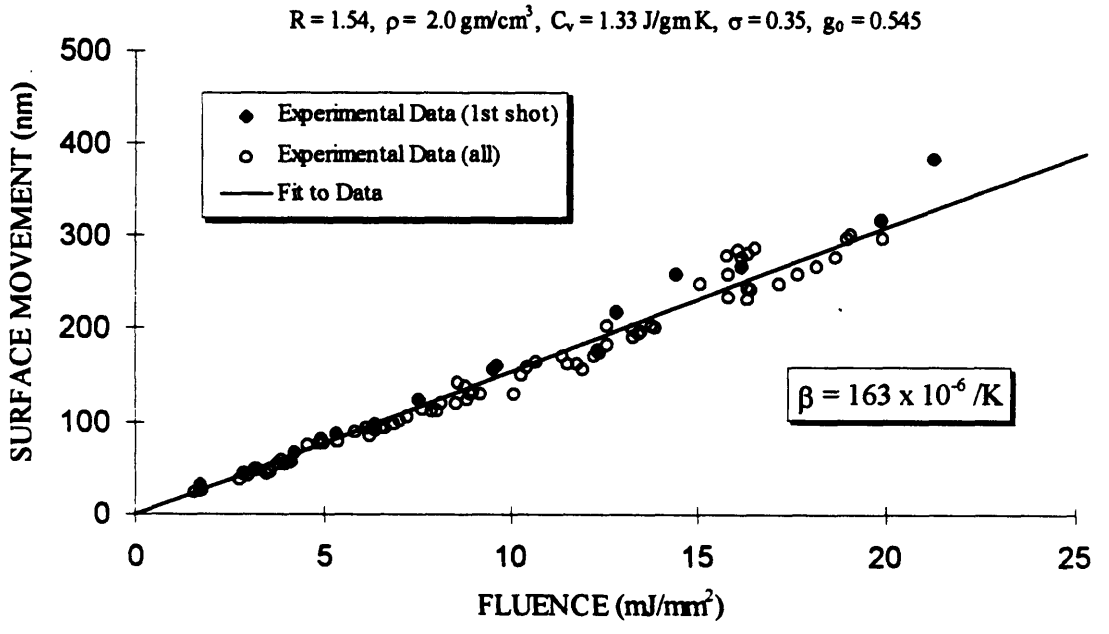

Figure 8-10. The laser-induced thermoelastic expansion of bone as a function of laser fluence. The linear dependence between surface movement and fluence allow the thermal expansion coefficient (and thus the Gruneisen coefficient) to be determined.

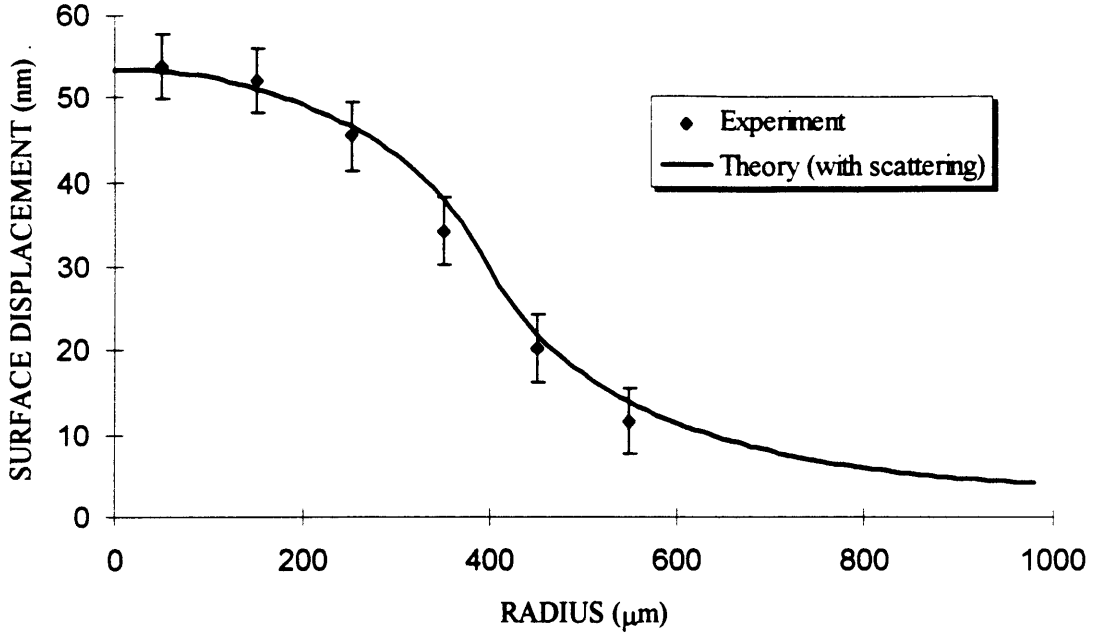

Figure 8-11. Comparison of theory and experiment for the laser-induced thermoelastic expansion of bone as a function of radial position. Note that there is still significant expansion of material at radii greater than the laser beam radius (w = 400 μm) due to both the adjacent expansion of heated material and heating due to light scattering.

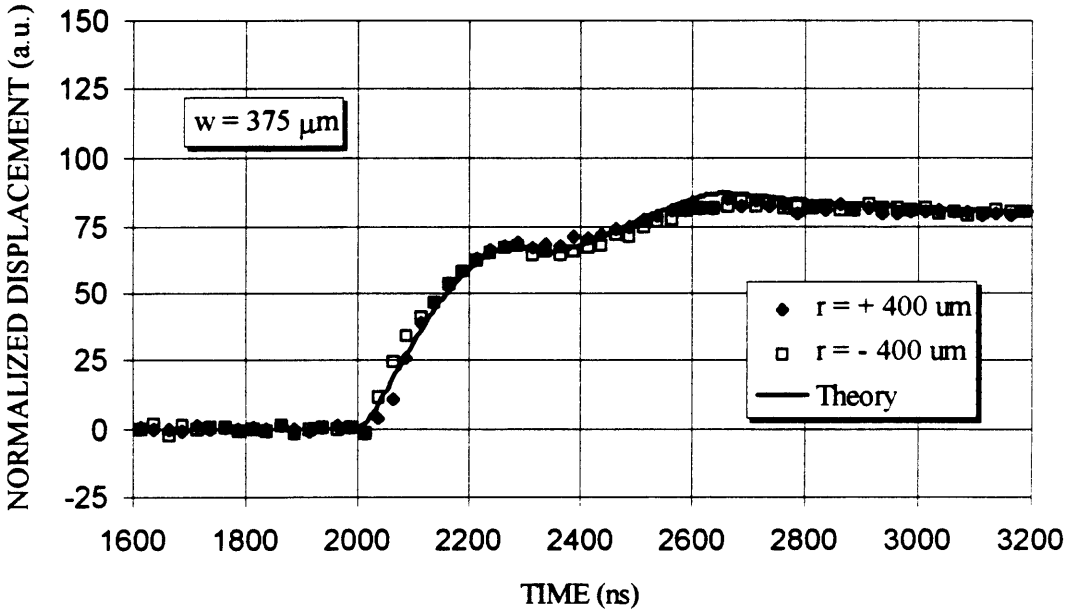

Figure 8-12. The surface movement of acrylite just outside of the laser beam radius has the same characteristic features as the surface movement at the center. As the theoretical fit shows, the same information concerning the physical properties of the target can be extracted at this location.

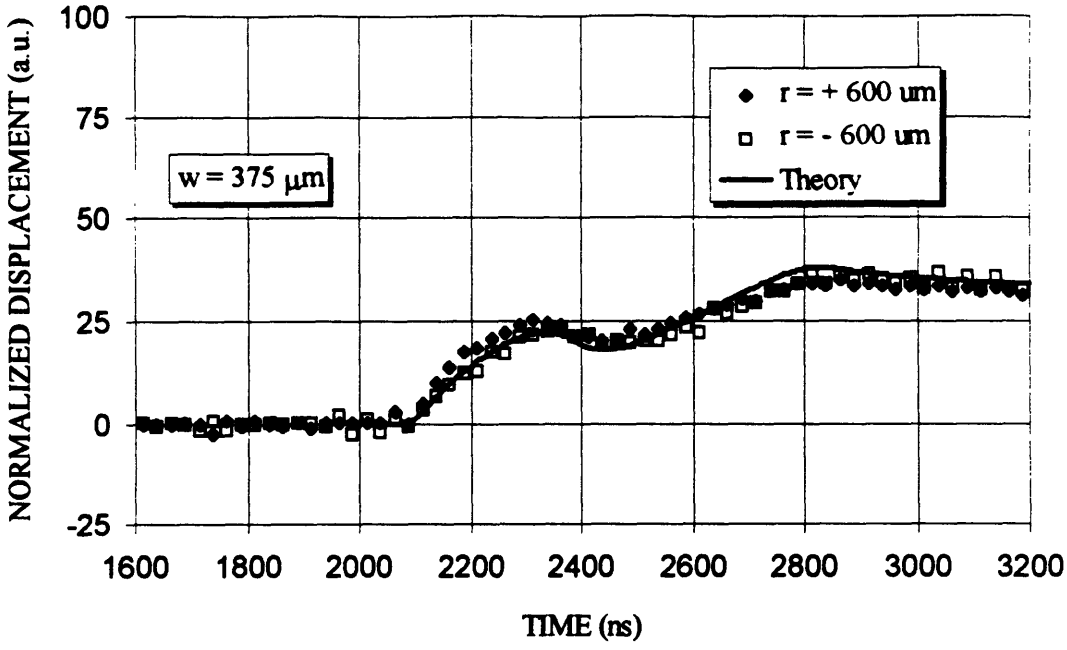

Figure 8-13. The surface movement of acrylite at a radius of 600 μm has the same characteristic features as the surface movement at the center. Although the ablation process will destroy the surface of the target within the laser beam radius, it can be safely monitored at large radii.

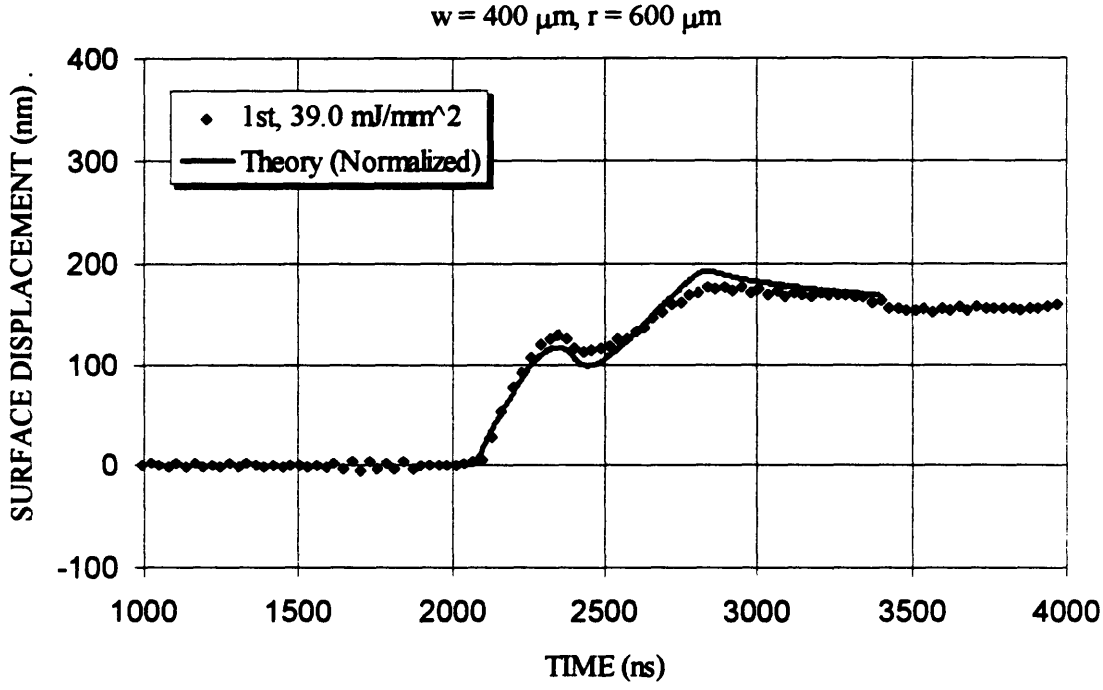

Figure 8-14a. The surface movement at r = 600 μm as a function of time after the first laser shot has the same characteristic features of expansions and contractions as the surface movement in the center. At high fluences, the magnitude of the first contraction (t = 2400 ns) is reduced.

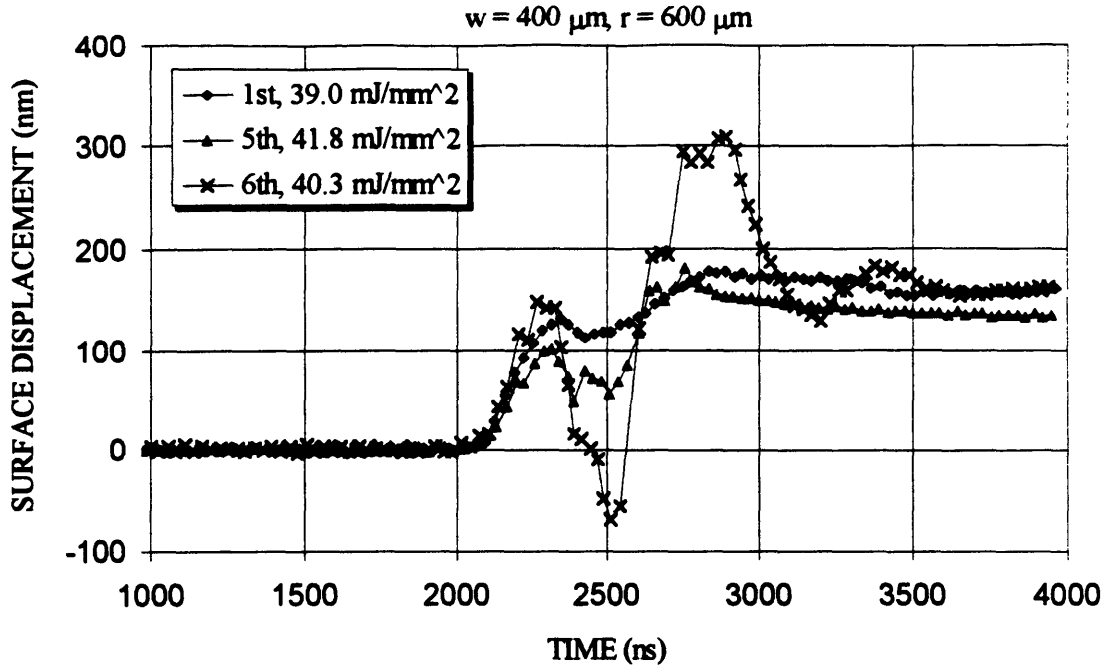

Figure 8-14b. After 5 shots at the same site, the features of the expansion curve begin to change dramatically. On the sixth shot, significant deviations occur including a contraction of the surface to a position 70 nm below its original level.

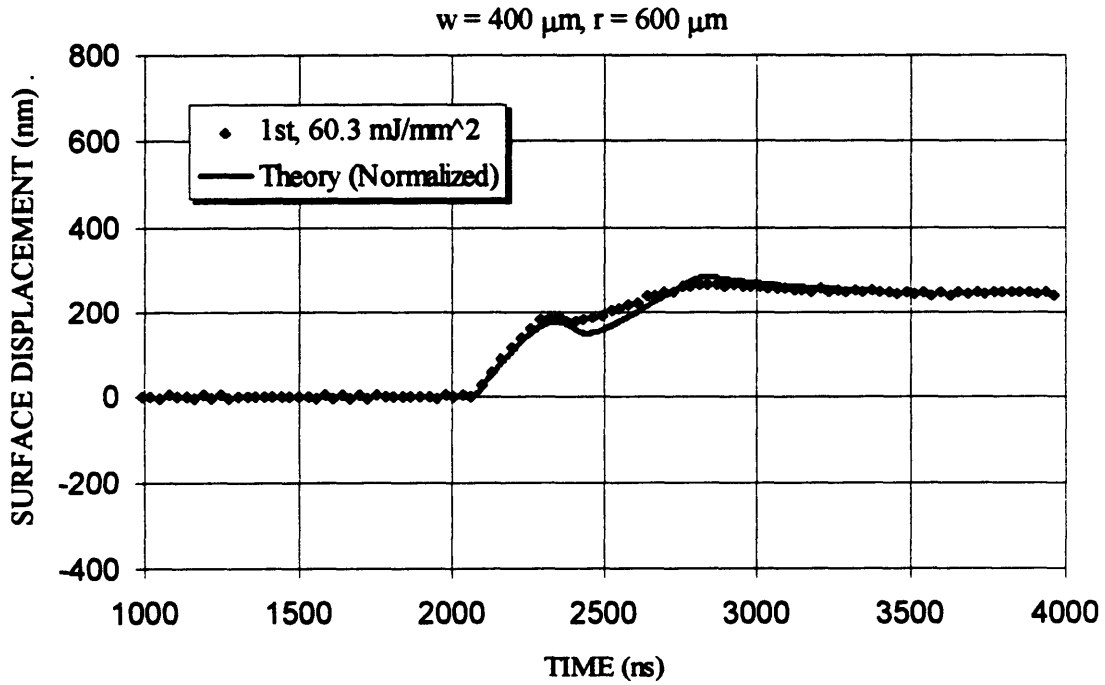

Figure 8-15a. At a fluence of 60.3 mJ/mm2, the surface movement at r = 600 μm as a function of time after the first laser shot exhibits small deviations from the predicted movement, indicating that there are not major changes in the optical or mechanical properties.

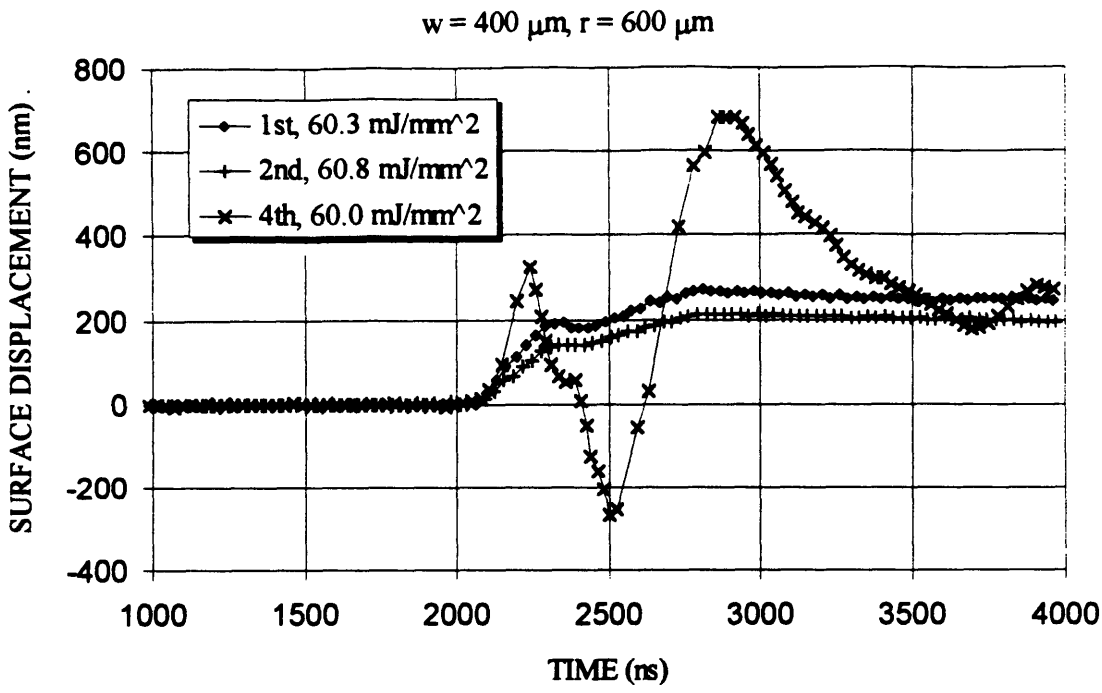

Figure 8-15b. The second shot at the same sight shows less total movement and a smoothing of the first contraction. At this fluence, ablation begins on the fourth shot.

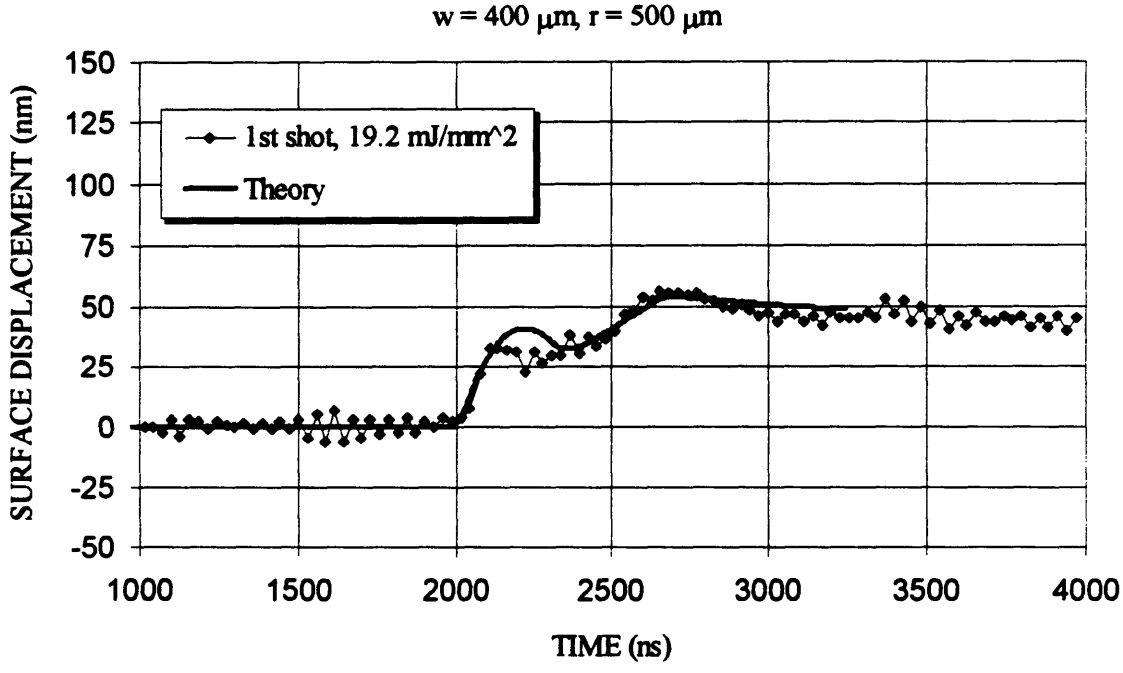

Figure 8-16a. Although high fluences will alter the bone surface and prevent interferometric surface monitoring, this problem can be alleviated by translating the probe beam 500 μm off center. The surface movement off center shows the same complex features as the surface movement at r = 0, although the timing of these features is altered due to the travel time of the acoustic waves. The agreement between theory and measurement is still quite good.

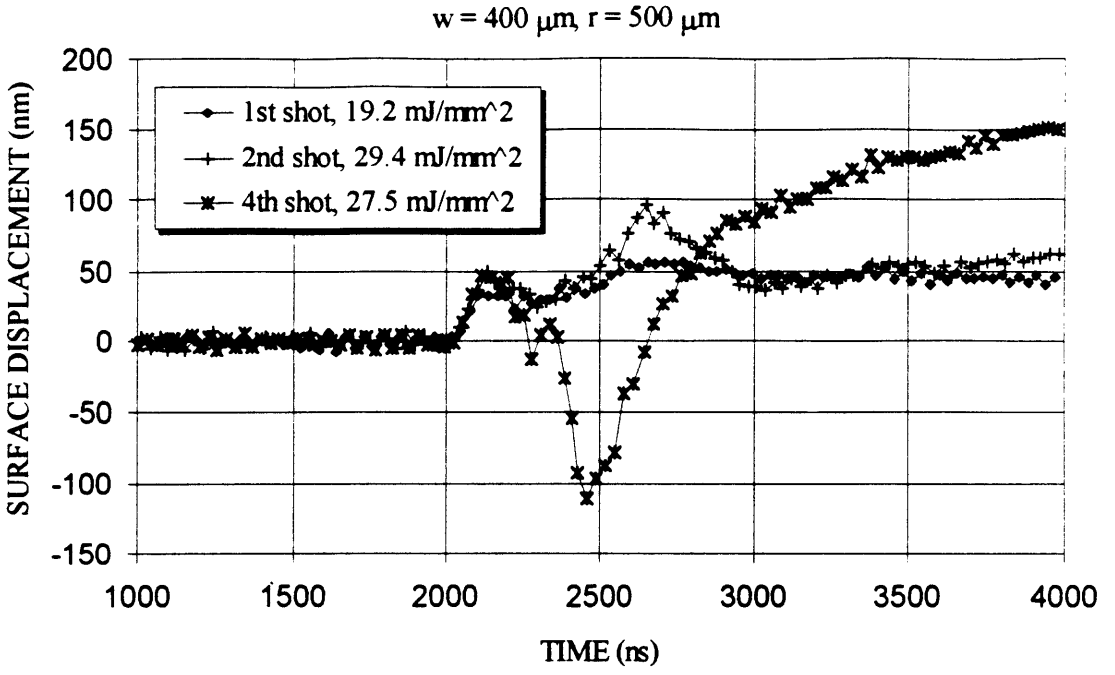

Figure 8-16b. As subsequent laser shots are fired at the the same site on the bone surface, the movement begins to change. After the second shot, there is an increased expansion at the second peak (t = 2600 ns). After the fourth shot, there is a large negative motion after the first peak. Both of these features are similar to those found in acrylite on the shots before and during ablation.

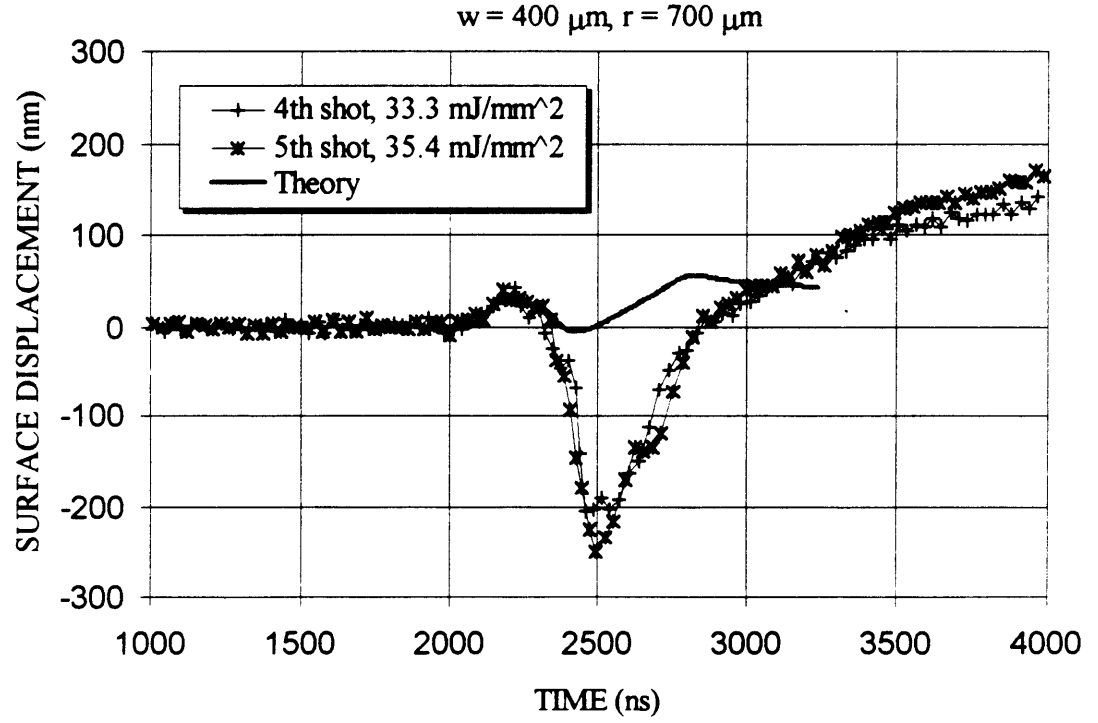

Figure 8-17. The surface movement of bone at a radial position of 700 μm shows that after several shots, the characteristic signature of the ablation process appears.

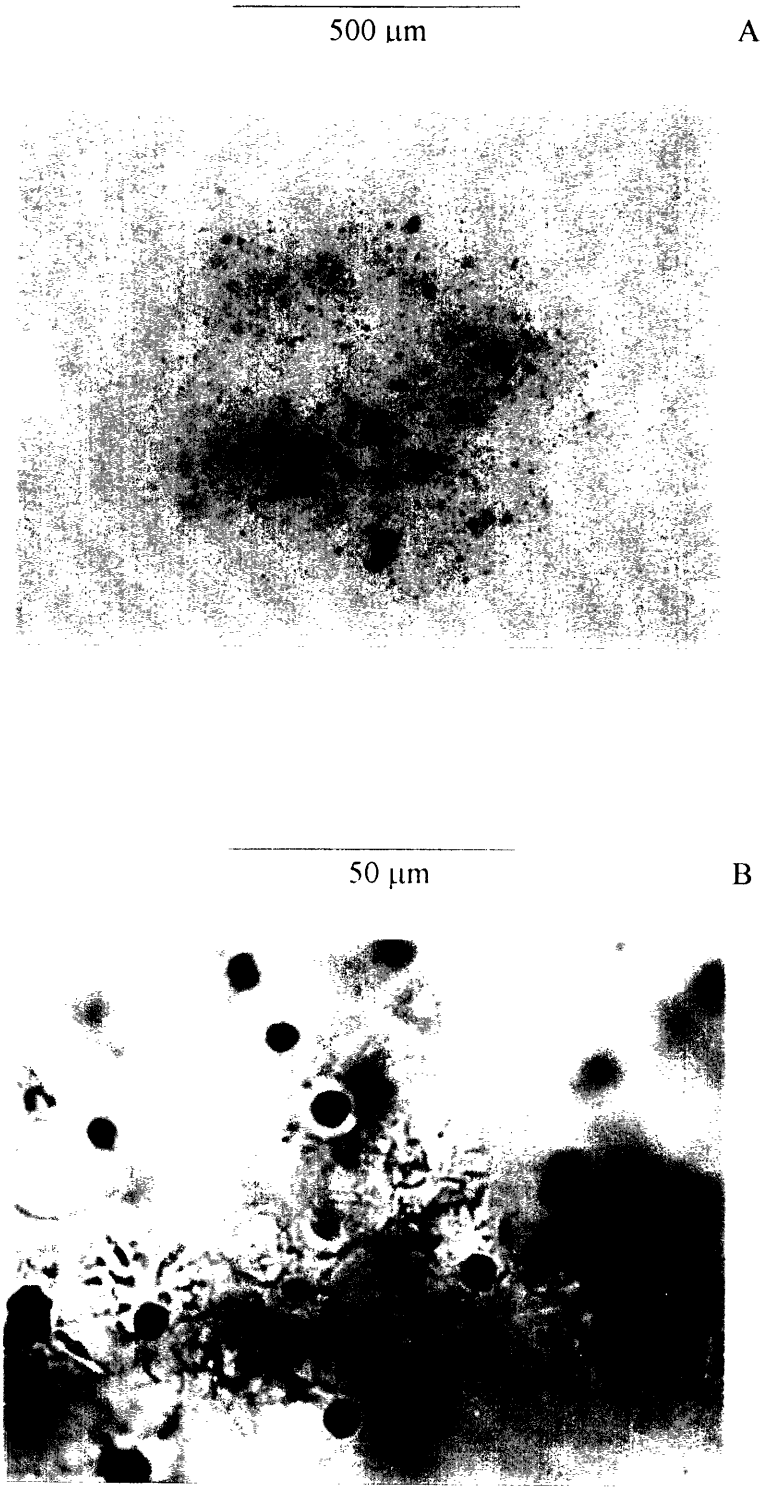

Figure 18 (A,B). Back-illuminated photomicrograph of the acrylite sample after irradiation with 8 shots at a fluence of 26 mJ/mm^2 shows the formation of permanent light scattering defects (A). In the high magnification photograph, fracture-like patterns are visible (B). The dark circles represent these same patterns which are out of focus.

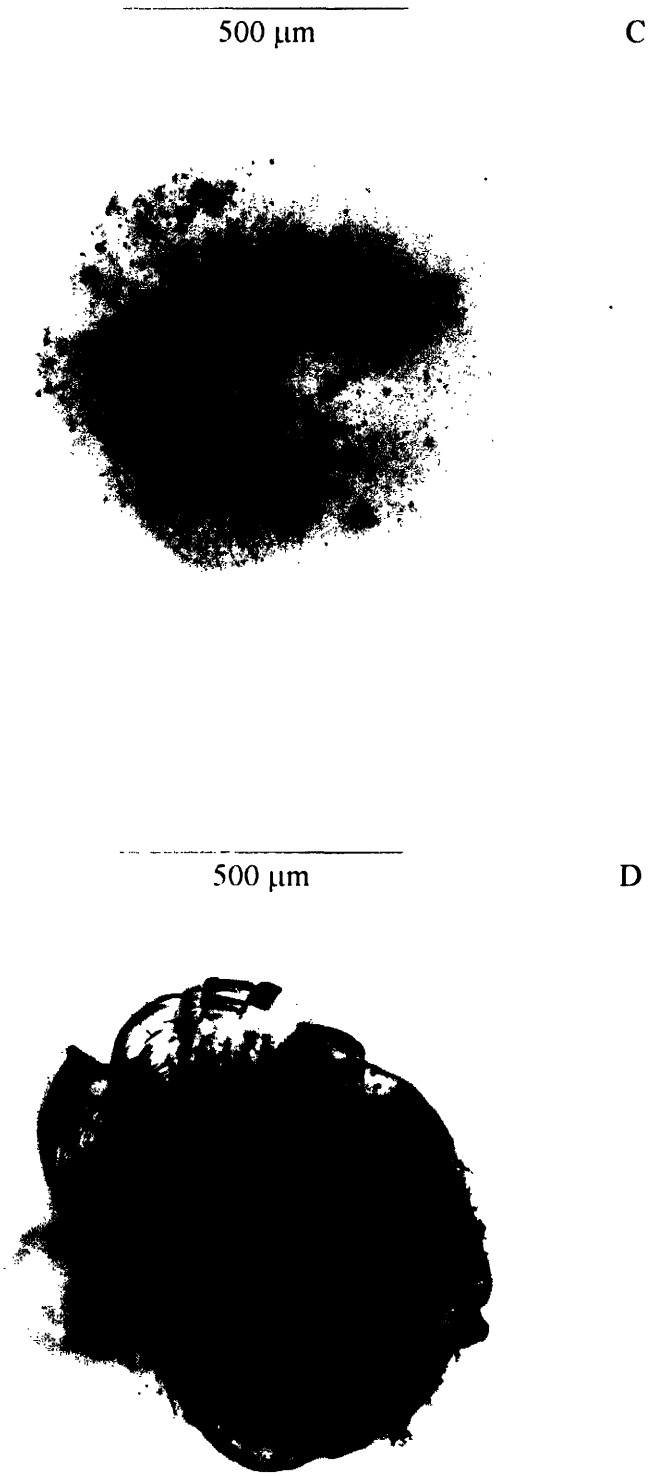

Figure 18 (C,D). Back-illuminated photomicrograph of the acrylite sample after irradiation with 6 shots at a fluence of 40 mJ/mm^2 (see figure 14b) shows the formation of a large fracture (C). After 5 shots at a fluence of 60 mJ/mm^2 (see figure 15b), ablation occurs (D).

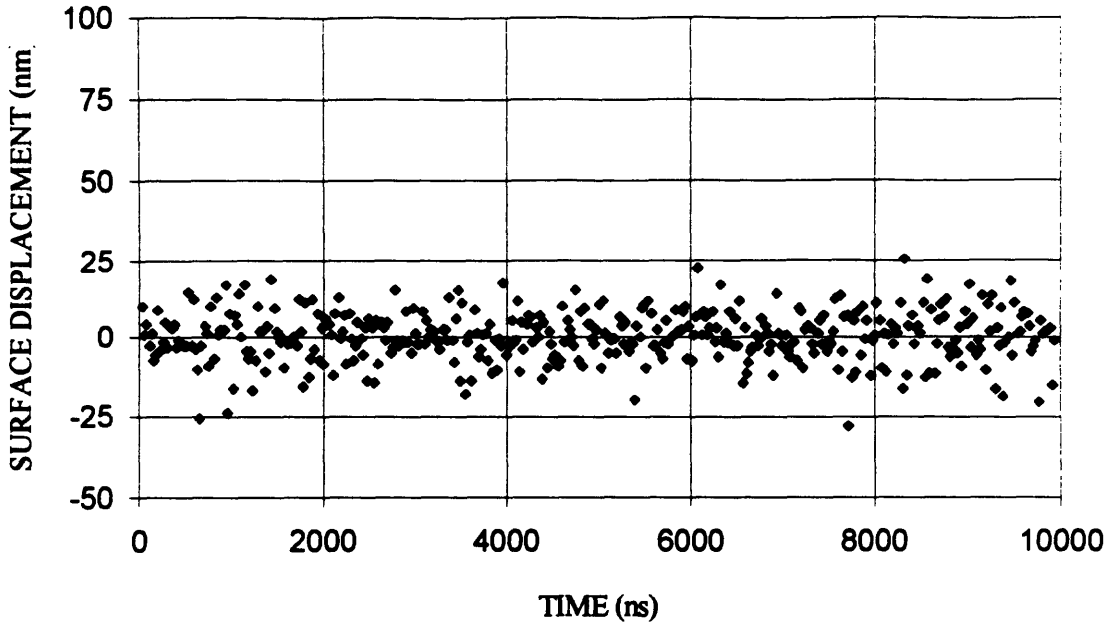

Figure 8-19. The measured surface movement of stationary human meniscus shows a total scatter of the data of +/- 25 nm and a standard deviation of +/- 8 nm.

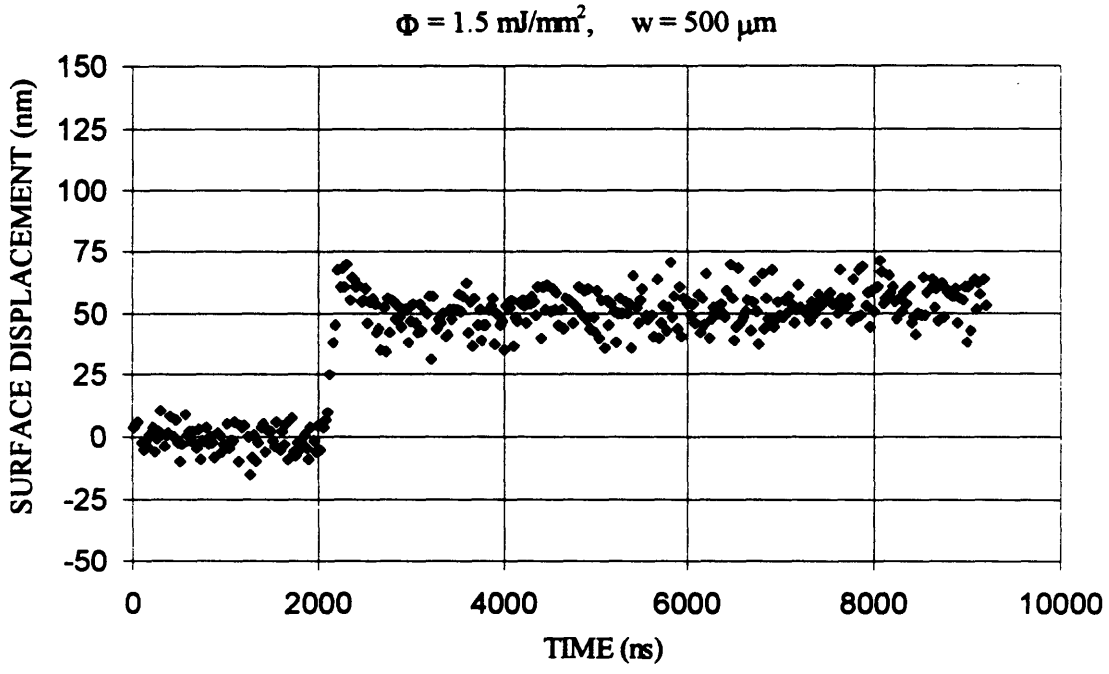

Figure 8-20. The surface movement of human meniscus as a function of time when 1.5 mJ/mm^2 of 355 nm laser light was fired at 2000 ns. Qualitatively, the 200 ns expansion to a new equilibrium position is in agreement with the expected movement.

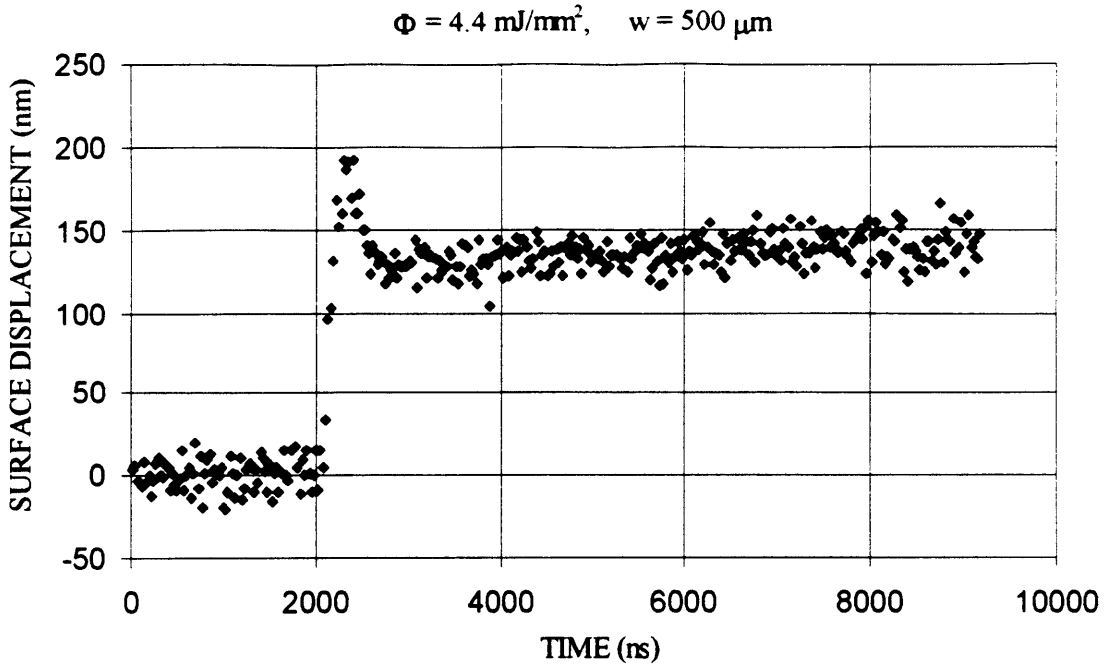

Figure 8-21. At a fluence of 4.4 mJ/mm^2, the time dependent surface movement of meniscus shows dramatic deviations from the expected behavior. The displacement overshoots the equilibrium position by 33 % and motion continues for over 500 ns. This overshoot is barely visible in figure 8-20 as well.

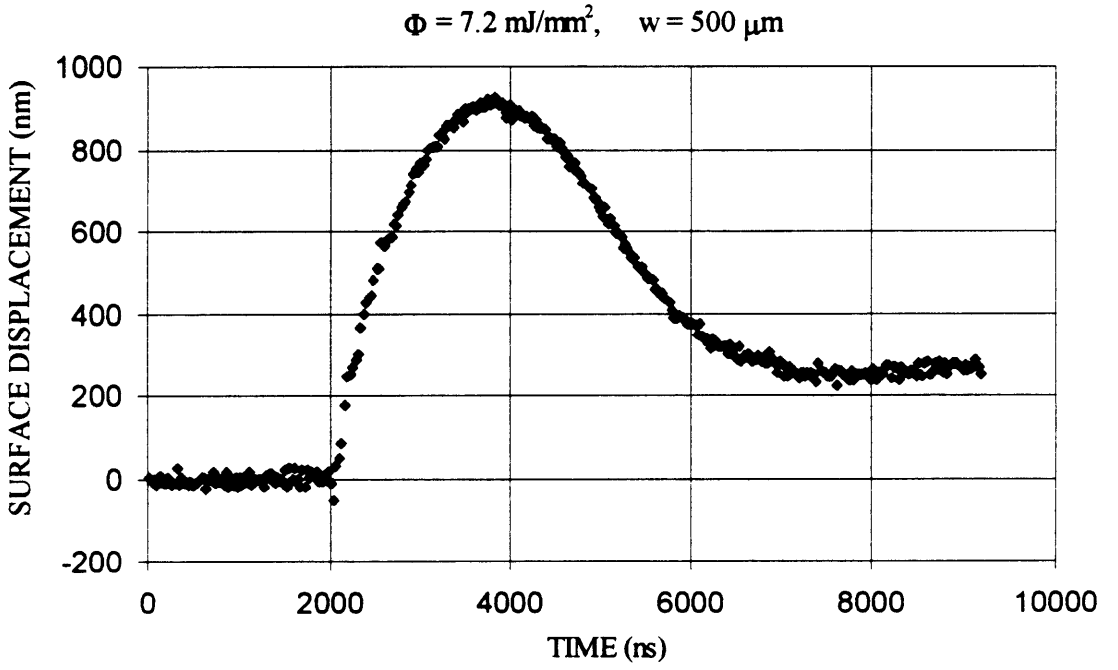

Figure 8-22. At a higher fluence, the anomalous behavior increases in magnitude and in duration. Here, over 900 nm of motion occurs before the surface returns to an equilibrium position of 260 nm.

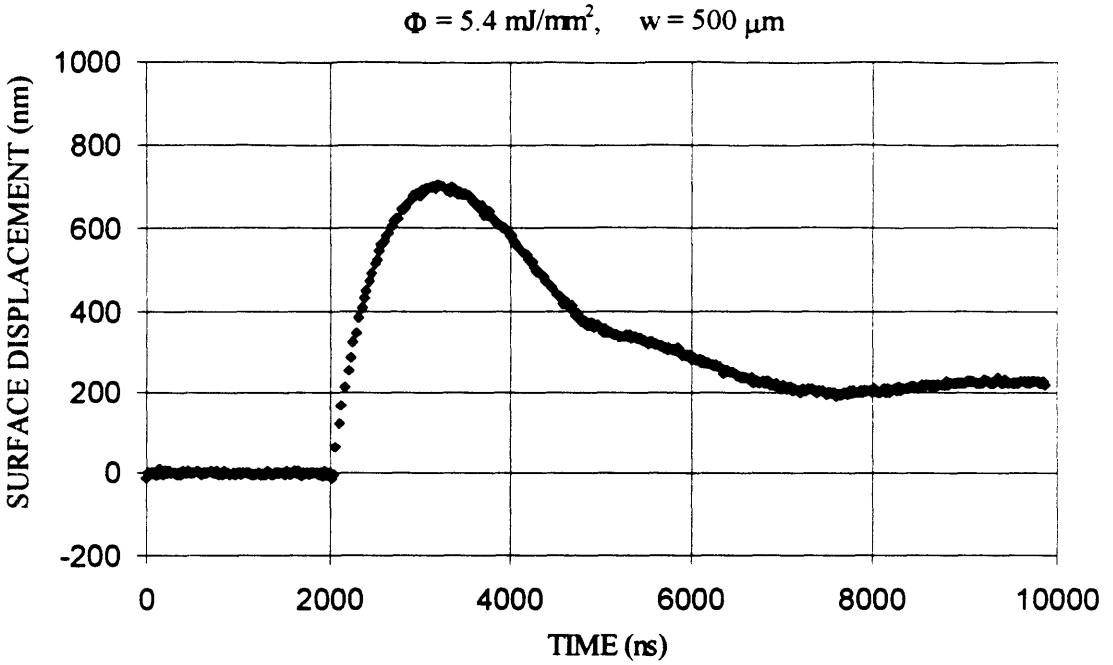

Figure 8-23. The surface movement of an aqueous solution shows the same characteristic features as seen from meniscus. The final equilibrium position of 218 nm is consistent with the expected level based on the thermal expanison coefficient of water. The anomalous behavior in the expanison curve is caused by the growth and collapse of cavitation.

CHAPTER 9

Conclusions and Future Directions

9.1 OVERVIEW

At the beginning of this thesis, no theoretical model was consistent with the experimental results. The photothermal model postulated that ablation was initiated when the laser deposited the heat of vaporization into the material. As discussed in chapter 1, there was experimental evidence that the amount of energy within tissue at the initiation of ablation was over an order of magnitude too low. The photochemical model was proposed to explain this discrepancy, proposing that the absorption of photons led to a direct dissociation of molecular bonds. This process, it was argued, was more efficient than vaporization and thus could occur given the small laser fluences necessary to cause ablation. Although this process may explain some effects in the deep ultraviolet, experimental data in the near ultraviolet, visible, and infrared clearly show that this explanation is not viable (section 1.3.3). Finally, the photomechanical model of ablation was also proposed to explain the occurrence of ablation at such a low energy density. This model postulated that laser-induced tensile stresses caused a mechanical rupture of the material, leading to ablation. The theoretical models that calculated the stress distribution showed that the tensile stresses on the surface were zero and did not become significant until a depth approximately equal to the optical penetration depth of the light.

Since the penetration depth of light in biological tissue in this wavelength regime is several hundred to several thousand microns, there are negligible tensile stresses where ablation is observed to occur (typically several to several tens of microns deep).

This thesis has added significant experimental results and theoretical findings to the current body of knowledge. In this chapter, I will summarize the experimental and theoretical methods used in this thesis (section 9.2) and then review the results for these methods and their implications to our understanding of ablation (section 9.3). These results provide strong evidence for the photomechanical model of ablation and against a photothermal one. The development of a quantitative photomechanical model of ablation will be discussed in section 9.4. Finally, some future directions and experimental improvements will be proposed in section 9.5.

9.2 EXPERIMENTAL AND THEORETICAL METHODS OF THIS THESIS

I have used a variety of techniques to investigate the underlying mechanism of the ablation process. As discussed in section 1.2, a parametric study correlating the depth of the ablation crater to the irradiation conditions was used to determine important parameters including the fluence threshold. In chapter 2, this work was combined with a survey of data from the literature to determine the energy density within tissue necessary to initiate ablation. The dependence of this energy density threshold was investigated as a function of wavelength, pulse duration and tissue type.

An extensive theoretical effort was also undertaken in this thesis. In order to investigate the photomechanical model of ablation, a model describing the thermoelastic response of material to short pulsed laser irradiation is required. One-dimensional models for this have been reported in the literature, and are valid in the limiting case that the diameter of the incident laser beam is much greater than the optical penetration depth (large aspect ratio). For most wavelengths studied in this thesis, this assumption is not valid in biological tissue. I have developed a three-dimensional model to describe the thermoelastic response of material to short pulsed laser irradiation which is valid for an arbitrary aspect ratio. This model has both a steady state and time-dependent component. In the steady state, analytical solutions for the quasi-steady state stresses and equilibrium displacement have been obtained. A numerical technique has been used to find a time-dependent solution. Both of these solutions have proved to be invaluable in this investigation of the underlying mechanism of ablation.

A novel experimental technique to study the thermoelastic response of tissue to laser irradiation has also been developed. This technique is based on a Michelson interferometer which uses a moving end mirror in one arm and the tissue surface as the other end mirror. Using this technique, the absolute position of the surface of the tissue can be determined as a function of time with a spatial resolution of a few nanometers and a time resolution of a few nanoseconds. This experiment has been used to verify the theoretical model, study the optical, mechanical, and thermal properties of tissue after sub-threshold laser irradiation, and study the ablation process itself.

9.3 IMPLICATIONS OF RESULTS FOR THE MECHANISM OF ABLATION

9.3.1 Photothermal Model of Ablation

The results presented in this thesis are not consistent with a photothermal model for short pulsed laser ablation. In chapter 2, data relating to the ablation of both "soft" and "hard" tissue was collected from a wide range of published studies (including our own work) and analyzed. It was found that throughout the near ultraviolet, visible, and infrared, the energy density necessary to initiate ablation in both aorta and bone was constant and was an order of magnitude less than that required for vaporization. This trend was valid as long as the pulse duration was less than the characteristic time for the laser-induced stress to dissipate. For longer pulse durations, an energy density comparable to the heat of vaporization was required to initiate ablation.

The explanation for this energy density discrepancy for short pulsed lasers that the optical penetration depth is reduced by an order of magnitude is not consistent with our results. The optical penetration depth measured in an integrating sphere ($I = 10^{-5}$ W/cm^2) and by the interferometric surface monitoring technique near ablation threshold ($I = 10^{8}$ W/cm^2) showed no evidence of a reduction in the penetration depth over 13 orders of magnitude in intensity. Although modest optical changes have been reported for tissue heated in a bath to 60-100 ^{0}C, our data shows that the peak laser-induced temperature rise at ablation threshold is only about 20 ^{0}C. Finally, since the chromophores responsible for the absorption of light in tissue are highly wavelength dependent, the fact that this

discrepancy occurs over such a wide range of wavelengths from the near ultraviolet to the infrared argues against transient optical changes and non-uniformly heated microregions but for a more universal effect.

9.3.2 Photomechanical Model of Ablation

The results presented in this thesis are consistent with a photomechanical model for short pulsed laser ablation. As discussed above, the wide range of wavelengths over which the energy density required to initiate ablation was constant implies that a universal, wavelength-independent effect is responsible. Since the laser-induced stress is proportional to the energy density, this data implies that ablation occurs when a critical stress is reached, the central postulate of the photomechanical model of ablation. This implication led me to study this model in much greater detail.

As mentioned in section 9.1, the central problem with the photomechanical model is that the spatial distribution of the predicted tensile stress is not in agreement with experimental results. These predictions, however, were based on a one-dimensional model. Results from our three dimensional, steady state model yielded several important findings regarding this discrepancy. First, there are three additional stress components (radial, circumferential, and shear) which are necessarily absent in the one-dimensional case. Second, although the one-dimensional stress dissipates quickly, in three dimensions there are quasi-steady state stresses associated with the non-uniform temperature distribution which last for eight orders of magnitude longer in time. Third, and most important, the spatial distribution of stresses is more consistent with experimental

observations. The circumferential stress is found to have a tensile component on the surface of the target and shear stress is produced near the surface.

Although the steady state model yielded important information about the quasi-steady state stresses, it provided no information about the transient stresses which were also believed to play an important role. These stresses were examined through a time-dependent numerical solution of the three-dimensional thermoelastic wave equation. The results from this solution conclusively showed that the apparent major drawback of the photomechanical model was an artifact from the simplifying assumptions of the one-dimensional calculation. The complete solution showed that both radial and circumferential tensile stresses were produced on the surface of the material throughout the entire laser heated region. In addition, shear stresses were produced near the surface. The magnitude of these stresses were a significant fraction of the peak initial laser-induced compressive stress.

Although the existence of tensile stresses on the surface of an irradiated target is a significant theoretical finding, two important issues must be resolved. First, experimental verification of this finding is required to prove that the model is correct. Second, although the predicted normalized stress distributions depend mainly on the laser irradiation geometry, the magnitude of the stress is a function of the optical, mechanical, and thermal properties of the target. These physical properties, which are not accurately known for biological tissue, must be determined in order to calculate the magnitude of the stress. The experimental technique of interferometric surface monitoring resolved both of these

issues. First, the data collected with this apparatus provided a precise time history of the thermoelastic motion of the target. The extraordinary agreement between the measured and theoretically predicted motion of glass and acrylite samples verified that the model was both correct and complete. Second, it was found that the detailed, time-dependent features of the thermoelastic motion were uniquely related to the physical properties of the target. By comparing theory and experiment, all the necessary physical properties could be determined including the longitudinal speed of sound, Poisson's ratio, the optical penetration depth, the role of scattering, the thermal expansion coefficient, the Gruneisen coefficient, and the magnitude of the laser-induced stress.

Experimental results from bone and acrylite (a plastic with similar physical properties to bone) revealed several important findings. First, the peak laser-induced temperature rise within these materials at fluences sufficient to cause ablation was only about 20 ^{0}C. Although this is a modest rise, the stresses associated with this temperature distribution were quite significant, over 250 bars for acrylite and 420 bars for bone. This stress represents a significant fraction of the static tensile strength of these materials (700 bars for acrylite, ~1200 bars for bone [Benedek and Villars, 1973]). In addition, the strength of bone under shear stress is only ~ 500 bars [Duck, 1990]. Second, it was found that ablation did not occur on the first shot, but only after several shots had been fired on the same location. A similar behavior has been observed in the ablation of polymethyl methacrylate in the deep ultraviolet [Srinivasan et al., 1990]. The number of shots required to cause ablation decreased as the incident laser fluence was increased. This implies that a change in the material takes place after each shot which makes it more

susceptible to ablation. An examination of the acrylite sample showed that each laser pulse created a distribution of microscopic fractures or microcracks on and near the surface of the material. Subsequent shots led to an accumulation of these defects until ablation occurred. Although the existence of these features could not be absolutely verified in bone where scattering prevents optical examination, the similarities between the thermoelastic motion of these two materials and the multi-shot ablation threshold strongly implies their existence. The formation of these defects and their effects on the overall strength of the material have been studied by researchers in other fields and are discussed in the next section.

Experimental results in meniscus, a "soft" biological tissue, and an aqueous solution also revealed several important findings. First, it was found that a laser-induced temperature rise of only a few degrees was sufficient to cause cavitation. Although other researchers have measured cavitation in liquid media above the tissue surface using strobe photography, our experiment measured the effects of cavitation within the turbid tissue. Second, an extrapolation to the measured ablation threshold shows a peak temperature rise of only 25 ^{0}C. The large stresses (over 100 bars) associated with this modest temperature rise, however, will cause a significant amount of cavitation. Since cavitation phenomena are known to be capable of destroying any adjacent material, this data implies that laser-induced stresses are responsible for initiating ablation.

9.4 DEVELOPMENT OF A QUANTITATIVE PHOTOTHERMAL MODEL OF ABLATION

Although the evidence presented above gives strong support for a photomechanical model of ablation which is governed by laser-induced stresses, there are many quantitative aspects of this model which are still unresolved. One complex issue concerns the determination of the stress required to initiate ablation. As shown above, the effects of microscopic defects and cavitation bubbles must be accounted for in order to resolve this issue.

The effects of the accumulation of microcracks in solid material has been studied by researchers in other fields. Anisimov et al. [1984] has developed a detailed model for the accumulation of damage caused by tensile stresses. In the model, small defects are created by tensile stresses that exceed a critical value, σ_0, which is smaller than the static tensile strength. A kinetic equation describing the total volume of microcracks (V_c) is given by :

$$\frac{dV_c}{dt} = \begin{cases} k_1\left(\sigma_m - \dfrac{\sigma_0 k_2}{k_2 + V_c}\right)\left(V_c + k_3\sigma_m^{k_4}\right), & \sigma_m > \dfrac{\sigma_0 k_2}{k_2 + V_c} \\ 0 \quad , & \sigma_m < \dfrac{\sigma_0 k_2}{k_2 + V_c} \end{cases} \qquad [9\text{-}1]$$

where σ_m is the stress component with the maximum value, and k_1, k_2, k_3 and k_4 are constants to be determined experimentally. As can be seen in eq. 9-1, once microcracks are formed, the application of additional stresses increases the density of cracks and reduces the threshold value necessary to create more cracks. This process continues to weaken the material until the applied stress completely fractures the material and the pressure gradient accelerates the debris away from the surface.

This model assumes that cracks are created whenever the tensile stress exceeds a critical value, independent of the temporal duration of the applied stress. As discussed in section 5.4.2, Tuler and Butcher [1968] have developed a dynamic fracture criterion which assigns a weight to both the magnitude of the stress and its duration. Due to the long-lived quasi-steady state stresses produced by laser irradiation, this additional complication should also be included in a model of ablation.

This model is entirely consistent with all the results from this thesis. A similar model can be proposed for the ablation of "soft" tissue where the laser-induced stresses create cavitation bubbles which damage the structural protein matrix of the tissue. However, significant theoretical analysis and new experimental measurements are needed in order to firmly establish this model. The development of a complex computer simulation which models this dynamic fracture constitutes one possible future direction for this research.

9.5 FUTURE DIRECTIONS AND EXPERIMENTAL IMPROVEMENTS

9.5.1 Proposed Experiments

The interferometric surface monitoring tool developed in this work can be used to study many other aspects relating to the ablation of biological tissue. As discussed in chapter 8, information regarding the ablation process can be studied by monitoring the thermoelastic response of the tissue next to the zone of laser irradiation. Preliminary data showed a strong recoil associated with the ejection of debris. Many features of this

movement are not quantitatively understood including both its magnitude and temporal location. The removal of a thin layer of material can be incorporated into the numerical model. A comparison of numerical predictions and further experimental data should allow additional information to be extracted from this feature.

The importance of scattering within turbid biological tissue was discussed in chapter 8 and must be properly accounted for in a quantitative model of ablation. The interferometric surface monitoring apparatus offers a new technique to study light propagation within tissue. In a non-scattering medium, the thermoelastic motion at a radius r_1 outside the zone of laser irradiation (radius w) should not begin until a time given by

$$t_1 = \frac{r_1 - w}{C_l} \qquad [9\text{-}2]$$

where C_l is the longitudinal speed of sound. In a scattering medium, some light will propagate and be absorbed in the region around r_1. Thermoelastic motion associated with the laser-induced temperature in this local region will begin immediately after the laser pulse. Thus, by measuring this motion before time t_1, the local temperature distribution can be determined allowing the effects of scattering to be determined.

Experimental data collected in this thesis implies that the ablation of soft biological tissue cannot be properly understood without studying cavitation. Other researchers have studied cavitation in transparent liquids through the use of fast strobe photography. Although this technique has provided valuable information, it has several limitations.

First, it is limited to non-scattering medium and thus is used to study water and not biological tissue itself. Second, it provides only snapshots in time and cannot show the time evolution of a single event. Third, it is difficult to extract quantitative information of the bubble size. Our technique, based on interferometric surface monitoring, overcomes all three of these limitations. As demonstrated in chapter 8, a quantitative determination of the total bubble volume as a function of time can be directly measured in biological tissue. This technique is also an excellent tool for studying cavitation in water. Since the characteristic signature of cavitation can be measured when the bubbles radii are only a few nanometers, accurate experiments to determine the cavitation threshold can be performed. Additional experiments to study cavitation can be done in gelatin and other similar materials. These materials have the advantage of having physical properties which can be accurately controlled and which are in between that of water and soft tissue.

Although cavitation is an important phenomena which needs further study, valuable information concerning the physical properties of soft tissue can be obtained by studying the thermoelastic motion below the cavitation threshold. As shown in chapter 8, however, cavitation begins after only several tens of nanometers of motion. In order to study the details of the thermoelastic motion, significant improvements in the signal to noise ratio for soft tissue must be made. As discussed in the next section, I believe a substantial improvement is possible.

The interferometric surface monitoring tool may also be used as a diagnostic instrument. Since the measured thermoelastic motion is related to the optical, mechanical,

and thermal properties of a material as well as the spatial distribution of these properties, it should be possible to detect a sub surface region of material whose physical properties are different. This could include a tumor imbedded within tissue or a defect within a manufactured item. One advantage of this technique over ultrasound is that it would be sensitive to a changes in optical properties, while ultrasound is primarily sensitive to mechanical changes.

9.5.2 Experimental Improvements

The spatial resolution of the interferometric monitoring tool developed in this thesis is quite remarkable. The resolution obtained in the experiments (< 2 nm in glass and plastic, 3-5 nm in bone, and 8 nm in meniscus) represents measuring less than one part in one hundred of the wavelength of the interferometric light (632.8 nm). Although this experiment has allowed exquisitely sensitive measurement to be made, future experiments will require improvements to be made. In particular, an order of magnitude improvement would be highly desirable to monitor the thermoelastic motion of soft tissue below the cavitation threshold and to monitor motion at locations well outside the laser-irradiated zone (to study both ablation and light scattering).

I believe that the spatial resolution of the interferometric monitoring tool can be increased by an order of magnitude. Currently, this experiment is designed around a 5 mW HeNe laser, which is electronically shuttered to a 6 millisecond pulse, and a red-sensitive photomultiplier tube. The signal to noise can be improved by both increasing the laser power and the efficiency of the detector. Two problems must be overcome to

implement these improvements. First, the output current from the photomultiplier tube is near its maximum rated value. Second, because the HeNe probe beam is focused onto a 100 μm spot size on the tissue, the total energy delivered to the tissue by the probe beam must be considered. In order to keep this energy well below that delivered by the pump beam, any increase in the power of the probe beam must be offset by a decrease in its exposure time.

Improvements in the experiment can be made in the following way. First, the current photomultiplier tube needs to be replaced by one with a higher maximum output current or by a fast photodiode. The quantum efficiency of the new detector should be an order of magnitude higher than the current value of ~ 6 %. If a pmt is used, this improvement can be easily obtained by using a blue or green probe laser. The laser power can also be increased from 5 mW to 50 mW. In order to keep the total energy delivered to the tissue constant, this increase in laser power should be coupled with a reduction in the electronic shuttering of this beam from six milliseconds to less than one. With these improvements, the signal should increase by a factor of 100 yielding an order of magnitude improvement in the signal to noise ratio and the spatial resolution of the apparatus.

REFERENCES

[Albagli et al., 1994a] D. Albagli, L.T. Perelman, G.S. Janes, C. von Rosenberg, I. Itzkan and M.S. Feld. "Inertially confined ablation of biological tissue," *Lasers in the Life Sciences*, **6**(1), 55-68 (1994).

[Albagli et al., 1994b] D. Albagli, B. Banish, M. Dark, G.S. Janes, C. von Rosenberg, L.T. Perelman, I. Itzkan and M.S. Feld. "Interferometric Surface Monitoring of Biological Tissue to Study Inertially Confined Ablation," *Lasers in Surgery and Medicine*, **14**(4), 374-385 (1994).

[Albagli et al., 1994c] D. Albagli, M. Dark, C. von Rosenberg, L.T. Perelman, I. Itzkan, M.S. Feld. "Laser-Induced Thermoelastic Deformation : A Three Dimensional Solution and its Application to the Ablation of Biological Tissue", *Medical Physics*, **21**(8), 1323-1331 (1994).

[Albagli et al., 1994d] D. Albagli, M. Dark, L.T. Perelman, C. von Rosenberg, I. Itzkan and M.S. Feld. 'The Photomechanical Basis of Laser Ablation of Biological Tissue", *Optics Letters*, accepted (1994).

[Albagli et al., 1994e] D. Albagli, M. Dark, L.T. Perelman, C. von Rosenberg, I. Itzkan and M.S. Feld. 'Laser-Induced Stress Generation in Solids and its Relation to the Photomechanical Model of the Ablation of Biological Tissue", *Applied Optics*, submitted (1994).

[Anisimov et al., 1984] S.I. Anisimov, A.V. Bushman, G.I. Kanel', A.B Konstantinov, R.Z. Sagdeev, S.G. Sugak and V.E. Fortov. 'Physics of the damage from high-velocity impact", *JETP Lett.* **39**, 8-11 (1984).

[Banish, 1993] B. Banish. 'Investigation of Laser Ablation of Biological Tissue Using Short Pulses of 355 Nanometer Light", Bachelor of Science Thesis, MIT (1993).

[Barker and Hollenbach, 1972] L.M. Barker and R.E. Hollenbach. "Laser Interferometer for Measuring High Velocites of any Reflecting Surface", *J Appl Phys* **43**, 4669-4675 (1972);

[Benedek and Villars, 1973] G.B. Benedek and F.M.H. Villars. Physics with Illustrative Examples from Medicine and Biology, Addison-Wesley Publishing Company, Reading, MA (1973).

[Boley and Weiner, 1985] B.A. Boley and J.H. Weiner. Theory of Thermal Stresses, Robert E. Krieger Publishing Company, Malabar, FL (1985).

[Buchelt et al., 1992] M. Buchelt, H.P. Kutschera, T. Katterschafka, H. Kiss, B. Schneider and Robert Ullrich. "Erb:YAG and Hol:YAG Laser Ablation of Meniscus and Intervertebral Discs", *Lasers in Surgery and Medicine* **12**, 375-381 (1992).

[Bushnell and McCloskey, 1968] J.C. Bushnell and D.J. McCloskey, "Thermoelastic Stress Production in Solids," *Jour Appl Phys*, **39**(12), 5541-5546 (1968).

[Carome et al., 1964] E.F. Carome, N.A. Clark and C.E. Moeller. "Generation of Acoustic Signals in Liquids by Ruby Laser-Induced Thermal Stress Trnasients", *Applied Physics Letters* **4**(6), 95-97 (1964).

[Carslaw and Jaeger, 1947] H.S. Carslaw and J.C. Jaeger, Conduction of Heat in Solids, Clarendon Press, Oxford (1947).

[Chen and Saha, 1987] I.I.H. Chen and S. Saha, "Thermal Analysis of the Bone Surface Induced by Laser Radiation," *Annals of Biomedical Eng.*, **15**, 457-466 (1987).

[Cheong et al., 1990] W.F. Cheong, S.A. Prahl and A.J. Welch. "A Review of the Optical Properties of Biological Tissues", *IEEE Jour. Qaunt. Elec.* **26**(12), 2166-2185 (1990).

[Cilesiz and Welch, 1993] I.F. Cilesiz and A.J. Welch. "Light dosimetry: effects of dehydration and thermal damage on the optical properties of the human aorta", *App. Opt.* **32**, 477-487 (1993).

[Collins, 1925] J.R. Collins. "Change in the Infrared Absorption Spectrum of Water with Temperature", *Phys. Rev.* **26**, 771-779 (1925).

[Cothren et al., 1986] R.M. Cothren, C. Kittrell, G.B. Hayes, R.L. Willet, B. Sacks, E.G. Malk, R.J. Ehmsen, C. Bott-Silverman, J.R. Kramer and M.S. Feld. "Controlled Light Delivery for Laser Angiosurgery", *IEEE J. Quant. Elec.* **22**, 4-7 (1986).

[Cowin, 1989] S.C. Cowin (ed.). Bone Mechanics. Florida : CRC Press. 80-124 (1989).

[Cross et al., 1987] F.W. Cross, R.K. Al-Dhahir, P.E. Dyer and A.J. MacRobert. "Time-Resolved Photoacoustic Studies of Vascular Tissue Ablation at Three Laser Wavelengths", *Appl. Phys. Lett.* **50**(15), 1019-1021 (1987).

[Cross et al., 1988] F.W. Cross, R.K. Al-Dhahir and P.E. Dyer. "Ablative and Acoustic Response of Pulsed UV laser-irradiated Vascular Tissue in a Liquid Environment", *Jour. Appl. Phys.* **64**(4), 2194-2201 (1988).

[Cummings and Walsh, 1992] J.P. Cummings and J.T. Walsh. "Q-switched Laser Ablation of Tissue : Plume Dynamics and the Effect of Tissue Mechanical Properties", *Laser-Tissue Interaction III, SPIE* **1646**, 242-253 (1992).

[Cummings and Walsh, 1993] J.P. Cummings and J.T. Walsh. "Erbium Laser Ablation : The Effect of Dynamic Optical Properties", *Applied Physics Letters* **62**(16), 1988-1990 (1993).

[Cummings and Walsh, 1993b] J.P. Cummings and J.T. Walsh. "Tissue Tearing Caused by Pulse Laser-Induced Ablation Pressure", *Applied Optics* **32**(4), 494-503 (1993).

[Curcio and Petty, 1951] J.A. Curcio and C.C. Petty. "The near infrared absorption spectrum of liquid water". *Jour. of the Opt. Soc. of Amer.* **41**, 302-304 (1951).

[de la Torre and Gregory, 1992] R. de la Torre R and K.W. Gregory. "Cavitation bubbles and acoustic transients may produce dissections during laser angioplasty", *J Am Coll Cardiol*; **19**, 48A (1992).

[Deckelbaum, 1994] L.I. Deckelbaum. "Coronary Laser Angioplasty", *Lasers in Surgery and Medicine* **14**, 101-110 (1994).

[Dingus and Scammon, 1991a] R.S. Dingus and R.J. Scammon. "Ablation of Material by Front Surface Spallation", (Ed) J.C. Miller and R.F. Haglund Jr., *Laser Ablation, Mechanisms and Applications*, Springer-Verlag, **389**, 180-190 (1991).

[Dingus and Scammon, 1991b] R.S. Dingus and R.J. Scammon. "Gruneisen-Stress Induced Ablation of Biological Tissue", *Laser-Tissue Interaction II*, SPIE **1427**, 45-54 (1991).

[Doukas et al., 1990] A.G. Doukas, R. Birngruber and T.F. Deutsch. "Determination of Shock Wave Pressures Generated by Laser Induced Breakdown in Water", *Laser-Tissue Interactions, SPIE* **1202**, 61-70 (1990).

[Doukas and Zweig, 1992] A.G. Doukas and A.D. Zweig. "Characterization of Plasma Induced Shock Waves", *Laser-Tissue Interaction III, SPIE* **1646**, 275-283 (1992).

[Dubovik, 1981] A. Dubovik. The Photographic Recording of High Speed Processes, John Wiley & Sons, New York, p. 313 (1981).

[Duck, 1990] F.A. Duck, Physical Properties of Tissue, Academic Press, London (1990).

[Duffy et al., 1992] S. Duffy, M. Davis, F. Sharp, J. Stamp and R. Ginsberg. "Preliminary Observations of Holmium:YAG Laser Tissue Interaction Using Human Uterus", *Lasers in Surgery and Medicine* **12**, 147-152 (1992).

[Dyer and Srinivasan, 1986] P.E. Dyer and R. Srinivasan. "Nanosecond Photoacoustic Studies on Ultraviolet Laser Ablation of Organic Polymers", *Appl. Phys. Lett.* **48**(6), 445-447 (1986).

[Dyer and Al-Dhahir, 1990] P.E. Dyer and R.K. Al-Dhahir. "Transient Photoacoustic Studies of Laser Tissue Ablation", In : Laser-Tissue Interaction, SPIE **1202**, 46-60 (1990).

[Edigar et al., 1993] M.N. Edigar, G.H. Pettit, R.P. Weiblinger and C.H. Chen. "Transmission of Corneal Collagen During ArF Excimer Laser Ablation", *Lasers in Surgery and Medicine* **13**, 204-210 (1993).

[Esenaliev et al., 1989] R.O. Esenaliev, A.A. Oraevsky and V.S. Letokhov. "Laser ablation of atherosclerotic blood vessel tissue under various irradiation conditions", *IEEE Trans on Biomed. Eng.* **36**, 1188-1194 (1989).

[Feld et al., 1991] M.S. Feld, J.R. Kramer, D. Albagli, R.M. Cothren, R.R. Dasari, G.B. Hayes, J.A. Izatt, I. Itzkan, G.S. Janes, R.P. Rava. "LAS II : An Integrated System for Spectral Diagnosis, Guidance, and Ablation in Laser Angiosurgery", in Future Directions in Interventioanl Cardiology, J.H.K. Vogel, ed., C.V. Mosby & Co., St Louis (1991).

[Garrison and Srinivasan, 1984] B.J. Garrison and R. Srinivasan. "Microscopic Model for the Ablative Decomposition of Polymers by Far Ultraviolet Radiation (193 nm)", *Appl. Phys. Lett.* **44**(9), 849-851 (1984).[Furzikov, 1987] N.P. Furzikov. "Different lasers for angioplasty: thermooptical comparison", *IEEE Jour. Quant. Elect.* **QE-23**, 1751-1755 (1987).

[Gijsbers et al., 1990] G.H.M. Gijsbers, R.L.H. Sprangers, M. Keijzer, J.M.T. De Bakker, T.G. Van Leeuwen, R.M. Verdaasdonk, C. Borst and M.J.C. Van Gemert. "Some Laser-Tissue Interactions in 308 nm Excimer Laser Coronary Angioplasty", *Jour. of Interven. Card.* **3**, 231-241 (1990).

[Golovlyov and Letokhov, 1993] V.V. Golovyov and V.S. Letokhov. "Ablation of an Optically Homogeneous Absorbing Medium by Scattered pulsed Laser Radiation", *Appl. Phys.* **B 57**, 451-457 (1993).

[Golovlyov et al., 1993] V.V. Golovyov, R.O. Esenaliev and V.S. Letokhov. "Laser Ablation of Absorbing Liquids", *Appl. Phys.* **B 57**, 417-423 (1993).

[Goodier, 1937] J.N. Goodier, "On the Integration of the Thermo-elastic Equations," Phil Mag, **23**, 7th series, 1017-1032 (1937).

[Gradshteyn and Ryzhik, 1965] I.S. Gradshteyn and I.M. Ryzhik, Table of Integrals Series and Products, 4th ed., Academic Press, New York (1965).

[Haar et al., 1984] L. Haar, J.S. Gallagher and G.S. Kell. NBS/NRC Steam Tables, Washington : Hemisphere Publishing Corporation (1984).

[Haase et al., 1993] K.K. Haase, H. Hanke, A. Baumbach, S. Hassenstein, M. Wehrmann, S. Duda, C. Rose, W. von Munch and K.R. Karsch. "Occurrence, Extent, and Implications of Pressure Waves During Excimer Laser Ablation of Normal Arterial Wall and Atherosclerotic Plaque", *Las. Surg. Med.* **13**, 263-270 (1993).

[Hynynen, 1991] K. Hynynen. "The threshold for thermally significant cavitation in dog's thigh muscle in vivo", *Ultrasound in Medicine and Biology*; **17**, 157-169 (1991).

[Itzkan et al., 1994] I. Itzkan, D. Albagli, B.J. Banish, M. Dark, C. von Rosenberg, L.T. Perelman, G.S. Janes and M.S. Feld, "Pressure Generation During Inertially Confined Ablation," (Ed) J.C. Miller and D.B. Geohegan, *Laser Ablation : Mechanisms and Applications II*, AIP Conf. Proc. **288**, 491-506 (1994).

[Izatt et al., 1990a] J.A. Izatt, N.D. Sankey, F. Partovi, M. Fitzmaurice, R.P. Rava, I. Itzkan and M.S. Feld. "Ablation of Calcified Biological Tissue Using Pulsed Hydrogen Flouride Laser Radiation", *IEEE J. Quant. Elec.* **QE-26**, 2261-2270 (1990).

[Izatt et al., 1990b] J.A. Izatt, D. Albagli, I. Itzkan and M.S. Feld. "Pulsed Laser Ablation of Calicified Tissue : Physical Mechanisms and Fundamental Parameters", *Laser-Tissue Interactions, SPIE* **1202**, 133-140 (1990).

[Izatt et al., 1991a] J.A. Izatt, D. Albagli, M. Britton, J.M. Jubas, I. Itzkan and M.S. Feld. "Wavelength Dependence of Pulsed Laser Ablation of Calcified Tissue", *Las. in Sur. and Med.* **11**, 238-249 (1991).

[Izatt, 1991b] J.A. Izatt. "Pulsed Laser Ablation of Calcified Biological Tissue: Physical Mechanisms and Clinical Applications", Ph.D. Thesis, MIT (1991).

[Jacques and Prahl, 1987] S.L. Jacques and S. Prahl, "Modeling Optical and Thermal Distributions in Tissue During Laser Irradiation," *Las. Surg. Med.*, **6**, 494-503 (1987).

[Jacques et al., 1987] S.L. Jacques, C.A. Alter and S.A. Prahl. "Angular Dependence of HeNe Laser Light Scattering by Human Dermis", *Lasers in the Life Sciences* **1**, 309-333 (1987).

[Jacques et al., 1992] S.L. Jacques, G. Gofstein and R.S. Dingus. "Laser-flash Photography of Laser-Induced Spallation in Liquid Media", *Laser-Tissue Interaction III, SPIE* **1646**, 284-294 (1992).

[Jansen et al., 1993] E.D. Jansen, T.G. van Leeuwen, R.M. Verdaasdonk, TH. Le, M. Motamedi, A.J. Welch and C. Borst. "Influence of Tissue Mechanical Strength During UV and IR Laser Ablation in Vitro", *Laser-Tissue Interaction IV, SPIE* **1882**, 139-146 (1993).

[Jansen et al., 1994] E.D. Jansen, T.G. van Leeuwen, M. Motamedi, C. Borst and A.J. Welch. "Temperature Dependence of the Absorption Coefficient of Water for Midinfrared Laser Radiation", *Lasers in Surgery and Medicine* **14**, 258-268 (1994).

[Johnson, 1994] D.E. Johnson. "Use of the Holmium:YAG (Ho:YAG) Laser for Treatment of Superficial Bladder Carcinoma", *Lasers in Surgery and Medicine* **14**, 213-218 (1994).

[Kaufmann and Hibst, 1989] R. Kaufmann and R. Hibst. "Pulsed Er:YAG and 308 nm UV-Excimer Laser : An in Vitro and in Vivo Study of Skin-Ablative Effects", *Lasers in Surgery and Medicine* **9**, 132-140 (1989).

[Kitai et al., 1991] M.S. Kitai, V.L. Popkov, V.A. Semchishen and A.A. Kharizov. "The Physics of UV Laser Cornea Ablation", *IEEE Jour. Quant. Elec.* **27**(2), 302-307 (1991).

[Knapp et al., 1970] R.T. Knapp, J.W. Daily and F.G. Hammitt. Cavitation. New York : McGraw-Hill Book Company. 51-58,97-104 (1970).

[Landau and Lifshitz, 1986] L.D. Landau and E.M. Lifshitz, Theory of Elasticity, 3rd ed., Pergamon Press, Oxford (1986).

[Landau and Lifshitz, 1987] L.D. Landau and E.M. Lifshitz. Fluid Mechanics, 2nd ed., Oxford: Pergamon Press (1987).

[Lane et al., 1987] R.J. Lane, J.J. Wynne and R.G. Geronemus. "Ultraviolet Laser Ablation of Skin : Healing Studies and a Thermal Model", *Las. in Sur. and Med.* **6**, 504-513 (1987).

[Levine et al., 1989] L.M.A. Levine, L.G. Fredin and M.J. Berry. "Infrared absorption spectra of cured epoxy resin and human corneal tissue at temperatures up to 450 ^{o}C", *Thermal and optical interactions with biological and related composite materials*, SPIE **1064**, 131-134 (1989).

[Li et al., 1991] Z. Li, W. Van De Merwe and L. Reinisch. "Comparison of the Excimer Laser and Erbium Yttrium Aluminum Garnet Laser for Applications in Osteotomy", *Laser-Tissue Interactions II,* SPIE **1427**, 152-161 (1991).

[Li et al., 1992] Z. Li, J.E. Code and W.P. Van De Merwe. "Er:YAG :Laser Ablation of Enamel and Dentin of Human Teeth", *Lasers in Surgery and Medicine* **12**, 625-630 (1992).

[Lord Rayleigh, 1917] Lord Rayleigh. "On the pressure developed in a liquid during the collapse of a spherical cavity", *Phi Mag* **34**, 94-98 (1917).

[Love, 1927] A.E.H. Love, Treatise on the Mathematical Theory of Elasticity, 4th ed., Oxford (1927).

[Metropolis and Ulam, 1949] N. Metropolis and S. Ulam. "Monte Carlo Method", *Journal of the American Statistical Association* **44**, 335-341 (1949).

[Morse and Ingard, 1968] P.M. Morse and K.U. Ingard. Theoretical Acoustics. New York : McGraw-Hill Book Company, 227-256 (1968).

[Motamedi et al., 1992] M. Motamedi, S. Rastegar and B. Anyari, "Thermal Stress Distribution in Laser Irradiated Hard Dental Tissue : Implications for Dental Applications," *Laser-Tissue Interaction III,* SPIE **1646**, 315-321 (1992).

[Nowacki, 1962] W. Nowacki, Thermoelasticity, Pergamon Press, Oxford (1962).

[Oraevsky et al., 1988] A.A. Oraevsky, V.S. Letokhov, S.E. Ragimov, V.G. Omel'yanenko, A.A. Belyaev, B.V. Shekhonin and R.S. Akchurin. "Spectral

Properties of Human Atherosclerotic Blood Vessel Walls", *Las. in the Lif. Sci.* **2**, 275-288 (1988).

[Oraevsky et al., 1991] A.A. Oraevsky, R.I. Esenaliev and V.S. Letokhov. "Pulsed Laser Ablation of Biological Tissue: Review of the Mechanisms", (Ed) J.C. Miller and R.F. Haglund Jr., *Laser Ablation, Mechanisms and Applications*, Springer-Verlag, **389**, 112-122 (1991).

[Oraevsky et al., 1991b] A.A. Oraevsky, R.O. Esenaliev and V.S. Letokhov. "Temporal Characteristics and Mechanism of Atherosclerotic Tissue Ablation by Nanosecond and Picosecond Laser Pulses", *Lasers in the Life Sciences* **5**(1-2), 75-93 (1992).

[Oraevsky et al., 1993] A.A. Oraevsky, S.L. Jacques and F.K. Tittel. "Determination of Tissue Optical Properties by Piezoelectric Detection of Laser-Induced Stress Waves", *Laser-Tissue Interaction IV, SPIE* **1882**, 86-101 (1993).

[Paltauf et al., 1992] G. Paltauf, E. Reichel and H. Schmidt-Kloiber. "Study of different ablation models by use of high-speed-sampling photography", Laser-Tissue Interaction III, SPIE; **1646**, 343-352 (1992).

[Partovi et al., 1987] F. Partovi, J.A. Izatt, R.M. Cothren, C. Kittrell, J.E. Thomas, S. Strikwerda, J.R. Kramer and M.S. Feld. "A Model for Thermal Ablation of Tissue Using Laser Irradiation", *Las. Surg. Med.* **7**, 141-154 (1987).

[Perelman et al., 1994] L.T. Perelman, D. Albagli, M. Dark, J. Schaffer, C. von Rosenberg, I. Itzkan and M.S. Feld. "Physics of laser-Induced Stress Wave Propagation, Cracking, and Cavitation in Biological Tissue", *Laser Tissue Interaction V, SPIE* **2134A**, 144-155, in press (1994).

[Pettit and Ediger, 1993] G.H. Pettit and M.N. ediger. "Pump / Probe Transmission Measurements of Corneal Tissue During Excimer Laser Ablation", *Lasers in Surgery and Medicine* **13**, 363-367 (1993).

[Pickering et al., 1993] J.W. Pickering, S. Bosman, P. Posthumus, P. Blokland, J.F. Beek, and M.J.C. van Gemert. "Changes in the optical properties (at 632.8 nm) of slowly heated myocardium", *App. Opt.* **32**, 367-371 (1993).

[Potter, 1977] D. Potter. Computational Physics, John Wiley and Sons, New York (1977).

[Pouchert, 1967] C.J. Pouchert, ed., The Aldrich Library of FT-IR Spectra, Vol. 2, Aldrich Chemical Company., Milwaukee, p. 1267 (1967).

[Prahl et al., 1989] S.A. Prahl, M. Keijzer, S.L. Jacques and A.J. Welch. A Monte Carlo Method of Light Propagation in Tissue", SPIE Institute Series, Vol **IS 5**, 102-111 (1989).

[Preisack et al., 1992] M.B. Preisack, W. Nev, R. Nyga, M. Wehrmann, K. Haase and K.R. Karsch. "Ultrafast Imaging of Tissue Ablation by a XeCl Excimer Laser in Saline", *Las. Surg. Med.* **12**, 520-527 (1992).

[Prince et al., 1988] M.R. Prince, R.R. Anderson, T.F. Deutsch and G.M. LaMuraglia. "Pulsed Laser Ablation of Calcified Plaque", *Optical Fibers in Medicine III*, SPIE **906**, 305-309 (1988).

[Quigley et al., 1992] M.R. Quigley, T. Shih, A. Elrifai, J.C. Maroon and M.L. Lesiecki. "Percutaneous Laser Discectomy with the Ho:YAG Laser", *Lasers in Surgery and Medicine* **12**, 621-624 (1992).

[Reinisch and Ossoff, 1993] L. Reinisch and H. Ossoff. "Acoustic Effects During Bone Ablation", *Laser-Tissue Interaction IV, SPIE* **1882**, 112-121 (1993).

[Ritchie, 1965] P.D. Ritchie. Physics of Plastics, D. Van Nostrand Compnay, Princeton, NJ (1965).

[Robertson and Williams, 1971] C.W. Robertson and D. Williams. "Lambert Absorption Coefficients of Water in the Infrared", *J. Op. Soc. Am.* **61**, 1316 (1971).

[Schaffer er al., 1994] J.L. Schaffer, M. Dark, I. Itzkan, D. Albagli, L.T. Perelman, C. von Rosenberg and M.S. Feld. "Mechanisms of Meniscal Tissue Ablation by Short Pulse Laser Irradiation", *Clinical Orthopedics*, submitted (1994).

[Schlenk et al., 1990] E. Schlenk G. Profeta, J.S. Nelson, J.J. Andrews and M.W. Berns. "Laser Assisted Fixation of Ear Prostheses After Stapedectomy", *Lasers in Surgery and Medicine* **10**, 444-447 (1990).

[Schomacker et al., 1991] K.T. Schomacker, Y. Domankevitz, T.J. Flotte and T.F. Deutsch. "$CoMgF_2$ laser ablation of tissue: Effect of wavelength on ablation threshold and thermal damage", *Las. in Sur. and Med.* **11**, 141-151 (1991).

[Sedov, 1959] L.I. Sedov. Similarity and Dimensional Methods in Mechanics : Academic Press, New York, 213 (1959).

[Singleton et al., 1986] D.L. Singleton, G. Paraskevopoulus, G.S. Jolly, R.S. Irwin and D.J. McKenney. "Excimer lasers in cardiovascular surgery : Ablation products and photoacoustic spectrum of arterial wall", *Appl. Phys. Lett.* **48**, 878-880 (1986).

[Sokolnikoff, 1956] I.S. Sokolnikoff, Mathematical theory of Elasticity, 2nd ed., McGraw-Hill Book Company, New York (1956).

[Spindel et al., 1992] M.L. Spindel, A. Moslem, K.S. Bhatia, B. Jassemnejad, K.E. Bartels, R.C. Powell, C.M. O'Hare and T. Tytle. "Comparison of Holmium and Flashlamp Pumped Dye Lasers for Use in Lithotripsy of Bilary Calculi", *Lasers in Surgery and Medicine* **12**, 482-489 (1992).

[Srinivasan, 1986] R. Srinivasan. "Ablation of Polymers and Biological Tissue by Ultraviolet Lasers", *Science* **234**, 559-565 (1986).

[Srinivasan et al., 1987] R. Srinivasan, P.E. Dyer and B. Braren. "Far-Ultraviolet Laser Ablation of the Cornea : Photoacoustic Studies", *Lasers in Surgery and Medicine* **6**, 514-519 (1987).

[Srinivasan et al., 1990] R. Srinivasan, B. Braren and K.G. Casey. "Nature of Incubation Pulses in the Ultraviolet Laser Ablation of Polymethyl Methacrylate", *J. Appl. Phys.* **68**(4), 1842-1847 (1990).

[Taylor et al., 1987] R.S. Taylor, D.L. Singleton and G. Paraskevopoulos. "Effect of optical pulse duration on the XeCl ablation of polymers and biological tissue", *Appl. Phy. Lett.* **50**, 1779-1781 (1987).

[Taylor et al., 1987] R.S. Taylor, L.A.J. Higginson and K. Leopold. "Dependence of the XeCl laser cut rate of plaque on the degree of calcification, laser fluence, and optical pulse duration", *Las. in Sur. and Med.* **10**, 414-419 (1990).

[Torres et al., 1994] J.H. Torres, A.J. Welch, I. Cilesiz and M. Motamedi. "Tissue Optical Property Measurements : Overestimation of Absorption Coefficient With Spectrophotometric Techniques", *Lasers in Surgery and Medicine* **14**, 249-257 (1994).

[Tuler and Butcher, 1968] F.R. Tuler and B.M. Butcher, "A Criterion for the Time Dependence of Dynamic Fracture," *International Journal of Fracture Mechanics*, 4(4), 431-437 (1968).

[Valderrama et al., 1989] G.L. Valderrama, R.F. Menefee, B.D. Krenek and M.J. Berry. "Chemical Laser Interactions With Human Corneal Tissue", *Thermal and Optical Interactions With Biological and Related Composite Materials, SPIE* **1064**, 135-145 (1989).

[Valderrama et al., 1990] G.L. Valderrama, R.F. Menefee, B.D. Krenek and M.J. Berry. "Chemical laser interactions with human cardiovascular tissue", *Laser Tissue Interaction*, SPIE **1202** (1990).

[Van Gemert and Star, 1987] M.J.C. Van Gemert and W.M. Star. "Relations between Kubelka-Monk and Transport Equation Models for Anisotropic Scattering", *Las. in Lif. Sci.* **1**, 287-298 (1987).

[van Leeuwen et al., 1992] T.G. van Leeuwen, L. van Erven, J.H. Meertens, M. Motamedi, M.J. Post and C. Borst. "Origin of arterial wall dissections induced by pulsed excimer and mid-infrared ablation in the pig", *J Am Coll Cardiol* **19**, 1610-1618 (1992).

[van Leeuwen et al., 1993] T.G. van Leeuwen, J.H. Meertens, E. Velema, M.J. Post and C. Borst. "Intraluminal vapor bubble induced by excimer laser pulse causes microsecond arterial dilation and invagination leading to extensive wall damage in the rabbit", *Circulation*; **87**, 1258-1263 (1993).

[van Saarloos and Constable, 1993] P.P van Saarloos and I.J. Constable. 'Improved Excimer Laser Photorefractive Keratectomy System", *Lasers in Surgery and Medicine* **13**, 189-196 (1993).

[Venugopalan et al., 1993] V. Venugopalan, A.D. Zweig, T.F. Deutsch, N.S. Nishioka and B.B. Mikie. 'Physical Mechanisms Controlling the Generation of Laser-Induced Stress", *Laser-Tissue Interaction IV, SPIE* **1882**, 102-111 (1993).

[Vickers et al., 1992] V.A. Vickers, S.L. Jacques, J. Schwartz, M. Motamedi, S. Rastegar and J.W. Martin. "Ablation of Hard Dental Tissues with the Er:YAG Laser", *Laser-Tissue Interaction III, SPIE* **1646**, 46-55 (1992).

[Walsh and Deutsch, 1989] J.T. Walsh and T.F. Deutsch. 'Pulsed C02 Laser Ablation of Tissue : Effect of Mechanical Properties", *IEEE Trans. Biomed. Eng.* **36**, 1195-1201 (1989).

[Weast, 1983] R.C. Weast, editor. CRC Handbook of Chemistry and Physics, CRC Press, Florida (1983).

[Wu et al., 1993] J. Wu, F. Partovi, M.S. Feld and R.P. Rava. 'Diffuse Reflectance from Turbid Media : An Analytical Model of Photon Migration", *Applied Optics* **32**(7), 1115-1121 (1993).

[Yannas, 1972] I.V. Yannas. 'Collagen and Gelatin in the Solid State", *J. Macromol. Sci.-Revs. Macromol. Chem.* **C7**, 49-104 (1972).

[Zel'dovich and Raizer, 1966] Y.B. Zel'dovich and Y.P. Raizer. Physics of Shock Waves and High-Temperature Hydrodynamic Phenomena : Academic Press, New York, Vol. I. (1966) and chapter XII (Vol. II); 1967.

[Zel'dovich and Raizer, 1967] Y.B. Zel'dovich and Y.P. Raizer. Physics of Shock Waves and High-Temperature Hydrodynamic Phenomena : Academic Press, New York, chapter XII, Vol. II (1967).

[Zweig and Weber, 1987] A.D. Zweig and H.P. Weber. 'Mechanical and Thermal Parameters in Pulsed Laser Cutting of Tissue", *IEEE Jour. Quant. Elec.* **23**, 1787-1793 (1987).

[Zweig and Deutsch, 1992] A.D. Zweig and T.F. Deutsch. "Shock Waves Generated by Confined XeCl Excimer Laser Ablation of Polyi mide", *Appl. Phys. B* **54**, 76-82 (1992).